The Dissertation Committee for Justin David Lowrey Certifies that this is the approved version of the following dissertation:

Subsurface Radioactive Gas Transport and Release Studies using the UTEX Model

Committee:

Steven Biegalski, Supervisor

Derek Haas

Mark Deinert

Eric Schneider

Sheldon Landsberger

Subsurface Radioactive Gas Transport and Release Studies using the UTEX Model

by

Justin David Lowrey, B.S.Ast.; B.S.Phy.; M.S.E.

Dissertation

Presented to the Faculty of the Graduate School of

The University of Texas at Austin

in Partial Fulfillment

of the Requirements

for the Degree of

Doctor of Philosophy

The University of Texas at Austin

August, 2013

Dedication

For my Dad, for *always* being there for me, for always giving me confidence, and for never letting me quit.

For my Mom, for always caring and always listening.

For my Brother, for always being my friend.

For Jennifer, for your endless love and passion for life, and for giving me the strength to persevere.

Acknowledgements

I would like to thank Dr. Steven Biegalski as my advisor, teacher, colleague, and friend whose guidance, support and motivation have not only been central to the completion of this project, but have also been an inspiration to me personally. I would like to thank Dr. Derek Haas who has been instrumental in fostering the growth of this project and provided both professional and personal guidance through some challenging times for me. I would like to thank Dr. Mark Deinert for his expertise and advice in support of this project. Additionally, Drs. Andrew Osborne and Geoff Recktenwald were of immense help at various points within this project and showed great patience in working with me. I would like to thank Dr. Erich Schneider for many late afternoon, yet very inspiring, course lectures over the last four years, and for giving me many of the tools that I utilize every day now. I would like to thank Dr. Sheldon Landsberger for introducing me to nuclear engineering more than eight years ago; he is the person responsible for my returning to UT Austin. My colleagues and friends, Drs. Christie Egnatuk and Amanda Prinke have been of immense help with their support, advice and humor, especially in the later parts of the completion of this dissertation.

I would like to thank Dr. Charles Carrigan for the few insightful and encouraging discussions we have had regarding this research and the larger field in general. I would also like to thank Dr. Harry Miley for his support of my work and for many entertaining afternoon discussions over coffee. Drs. James Hayes, Ted Bowyer, and Justin McIntyre have also provided a wealth of advice as well as direct and indirect support of my efforts on this project.

This work would not have been possible without support and funding from the United States Department of Energy, National Nuclear Security Administration, under Award Number DE-AC52-09NA28608 and the Defense Threat Reduction Agency under Award Number HDTRA1-12-1-0018.

Lastly, I would like to thank the Pacific Northwest National Laboratory for the opportunity to work alongside an amazing group of scientists in pursuit of finishing this dissertation, as well as the chance to explore new areas.

Pacific Northwest National Lab Information Release Number: PNNL-22582

Subsurface Radioactive Gas Transport and Release Studies using the UTEX Model

Justin David Lowrey, Ph.D.

The University of Texas at Austin, 2013

Supervisor: Steven Biegalski

Underground nuclear explosions (UNEs) produce anthropogenic isotopes that provide the only definitive means by which to determine whether a nuclear explosion has taken place. Verification of a suspected test under the Comprehensive Nuclear-Test-Ban Treaty (CTBT) includes both on-site and atmospheric sampling of specific noble gas radioisotopes for analysis of origin. It is well-established that the processes of subsurface transport can affect the rate at which such gases will reach the surface. However, the relative abundance of anthropogenic isotopes reaching the surface following transport is currently assumed to rely solely on their direct fission yield, decay rate, and their production from precursor decay, making no account for the influence of transport processes on isotopic ratios.

The Underground Transport of Environmental Xenon (UTEX) model has been developed to examine the possible effects of subsurface transport on radioxenon isotopic ratios as well as to consider a number of on-site inspection-related applications. In this work, background on the UTEX model's development, evolution and vetting is presented. This is followed by the characterization and analysis of a number of applications of the model for consideration of CTBT-relevant scenarios. Specifically, the UTEX model's capability to analyze CTBT on-site inspection concept of operations is

demonstrated. This is accomplished through an examination of generalized UNE source terms, geological stratigraphy, UNE impact on local geology, natural soil-gas radionuclide backgrounds, atmospheric infiltration, and sampling methodology. It is shown that the processes driving noble gas transport through geological media can significantly skew the ratios of key radioxenon isotopes that are used to help verify whether or not a well-contained underground test has taken place. This result emphasizes the need for a broader understanding of radionuclide signatures used for CTBT verification purposes and the mechanisms that can alter them.

Table of Contents

List of Tables

List of Figures

Chapter 1. Introduction

1.1 MOTIVATION

Since the signing of the Limited Test Ban Treaty in 1963, a majority of nuclear explosion tests have been carried out in underground facilities intended to contain the fission products that result, therefore minimizing evidence of the explosions. Three decades later in September 1996, the Comprehensive Nuclear-Test-Ban Treaty (CTBT), an international resolution banning any and all nuclear explosions, was opened for signatures; to date the treaty has been signed by 183 countries and ratified by 159 countries (CTBTO Prepatory Commission, 2013). Implicit in the CTBT is the need for a cooperative, global capacity to reliably detect and verify underground nuclear explosions.

Underground nuclear tests produce anthropogenic radioactive isotopes that provide the only definitive means by which to determine whether a nuclear explosion has taken place. In an underground nuclear explosion (UNE), these radionuclide fission and soil-activation products are directly injected into the surrounding geologic media. What results is a distribution of radionuclides within the geology hundreds of meters below the surface known as the initial contaminant distribution halo. Vertical transport by a number of mechanisms inevitably brings some amount of this contaminant to the surface and into the atmosphere where it can be detected by specific atmospheric monitoring stations. Verification of a suspected test under the CTBT includes both onsite and atmospheric sampling of specific noble gas radioisotopes for analysis of origin signature (CTBTO Preparatory Commission, 1996; Hannon, 1985).

The International Monitoring System (IMS) is a 321-station network spread out around the globe (see Figure 1.1), consisting of seismic, infrasound, hydroacoustic, as well as radionuclide monitoring technologies (CTBTO Prepatory Commission, 2010).

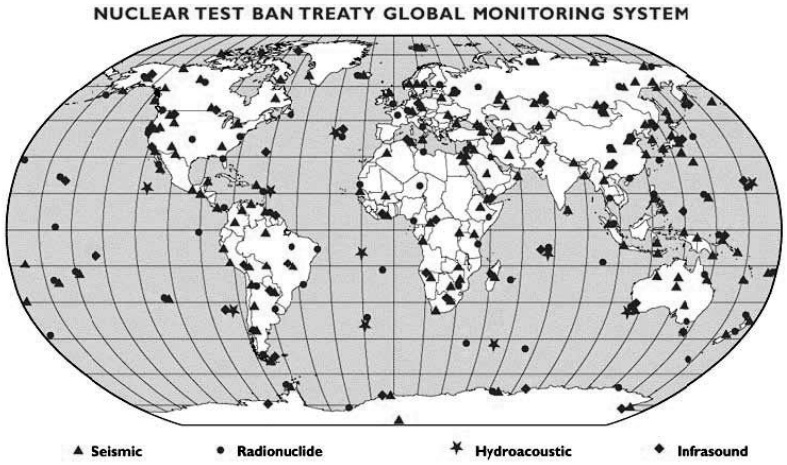

Figure 1.1 Global distribution of IMS stations.

Along with established lines of international consultation, clarification and on-site inspections, the IMS is a major component in the CTBT verification system. Of the 321 stations in the IMS network, 80 serve to monitor radionuclides in the atmosphere (CTBTO Prepatory Commission, 2010). These stations are generally located strategically in areas of rapid wind mixing to facilitate a high volume air sampler, which filters and collects radioactive particulates. These filters are subsequently counted with gamma ray detectors to determine activity levels of various radionuclides that might be present.

Monitoring of radionuclide levels in the atmosphere faces a number of challenges. First and foremost, clandestine nuclear explosions are assumedly conducted with the intent of containing as much of the explosion evidence as possible to prohibit detection. Accordingly, in an effort to increase radionuclide detection efficiency and reliability, the International Noble Gas Experiment (INGE), started in 1999, developed and deployed at IMS stations four different types of xenon detectors (CTBTO Prepatory Commission, 2010). Xenon isotopes, as noble gas fission products, are of special interest in atmospheric monitoring for underground nuclear activity because of their short half-lives, relatively high production yields, and ability to move through geological structures

without reacting (T. W. Bowyer *et al.*, 2011; T. W. Bowyer *et al.*, 2002; Carman *et al.*, 2003; Saey, 2009; Van der Stricht & Janssens, 2001). Xenon is present naturally in the atmosphere at a level of 0.087±0.001 parts per million with the natural isotopic abundances listed in Table 1.1 (Hwang *et al.*, 2005).

Table 1.1 Natural abundance of Xenon Isotopes

Xe Isotope	**Natural Abundance**
^{124}Xe	0.095%
^{126}Xe	0.089%
^{128}Xe	1.91%
^{129}Xe	26.4%
^{130}Xe	4.07%
^{131}Xe	21.2%
^{132}Xe	26.9%
^{134}Xe	10.4%
^{136}Xe	8.86%

Radioactive isotopes of xenon in the atmosphere, however, are largely anthropogenic in origin (Biegalski *et al.*, 1999; Bowyer *et al.*, 1999). So-called radioxenon is primarily produced as release from the commercial nuclear power industry as well as in the medical industry, but radioxenon is also released in nuclear explosions. This leads to a second major challenge to atmospheric monitoring of radionuclides – generally speaking nuclear explosions are far from the only source of radionuclide production in the modern world, thus identifying a particular radioisotope signal as emanating from a nuclear explosion is not trivial. Peaceful nuclear applications, such as for power generation and medical isotope production, have associated with them their own radionuclide signatures that can potentially serve to mimic or obscure more concerning signs of weapons applications; medical isotope production facility signatures can be especially difficult to distinguish from those of nuclear explosions. As such, not just the activity levels of radionuclides in the atmosphere, but their isotopic ratios are of

central importance to atmospheric monitoring and distinguishing sources of nuclear explosions from other anthropogenic sources.

A major objective of IMS atmospheric monitoring is to observe radioxenon signals and examine the ratios of four xenon isotopes, ^{135}Xe, ^{133}Xe, ^{133m}Xe and ^{131m}Xe for comparison with expected values for nuclear explosion sources. On October 3, 2006, the Democratic People's Republic of Korea gave warning of its intention to conduct a nuclear test, and six days later claimed that one had been successfully carried out. Anthropogenic xenon isotopes were the only fission products to be measured off-site afterwards and served as critical evidence that a nuclear explosion had taken place (Ringbom *et al.*, 2009). Being able to predict the isotopic ratio signatures produced by underground nuclear explosions is therefore crucial to the effectiveness of atmospheric monitoring of radionuclides (Carrigan *et al.*, 1996; Hannon, 1985; Zuckerman, 1993).

On-site inspections (OSI) make up another component of the CTBT verification regime. The CTBT provides for an OSI of suspected nuclear activity locations at the request of a member state. Within 96 hours of an inspection request, member countries are required to vote on the request, and the OSI will only be allowed to proceed upon an affirmative vote of 30 or more member countries out of the 51 member states. An OSI is limited to searching an area no greater than 1,000 square kilometers, and the country in question can exclude certain locations within the designated area as restricted areas (RA) (CTBTO Preparatory Commission, 1996).

Various technologies are set to be used in an OSI, including radionuclide monitoring techniques. Just as in IMS atmospheric monitoring for airborne contaminant traces, radionuclide rates of decay and environmental mobility are key to their detection by an OSI effort (see Figure 1.2). However, as it is estimated that an OSI team could not likely reach field locations before about 10 days following a suspected UNE event, the

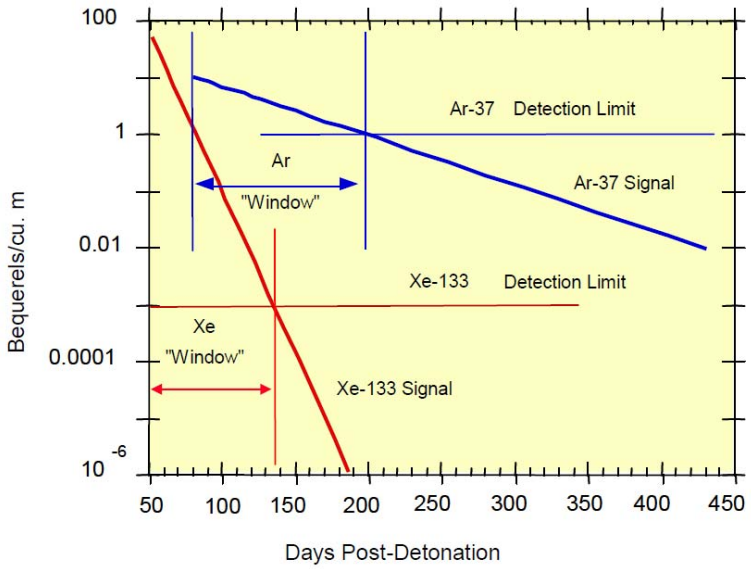

Figure 1.2 Estimated radioxenon and radioargon activity windows at the surface following a UNE event, (Carrigan, 2009).

nature of radionuclide releases relevant to IMS detection and OSI detection are likely somewhat different. Detection by the IMS would require a very significant release or venting of radionuclides from a UNE to overcome both radioactive decay and atmospheric dilution before its being measured. An OSI measurement of radionuclide evidence from a UNE would likely come in a period of two weeks or more following the suspected event, and would more likely be the result of a much slower seepage of contaminant (Carrigan & Sun, 2012).

A list of radionuclides of potential OSI interest is shown in Table 1.2. Radionuclides with half-lives under 9 hours are excluded from consideration due to the unlikelihood that they would exist in detectable quantities in the time frame of potential OSI detection. Of the nuclides listed, radioargon isotopes are the only non-fission products. Within a UNE, radioargon can be expected to be produced through the neutron

activation of the natural soil and rock environment. With a substantially longer half-life than radioxenon and similar environmental mobility, ^{37}Ar in particular is regarded as a significant candidate for OSI detection (Haas *et al.*, 2010; Purtschert *et al.*, 2007).

Table 1.2 Noble gas and volatile radionuclides with potential interest for OSI inspections

Isotope	**Half-Life**	**Production and delectability notes**
^{125}Xe	16.9 hours	Primarily created through ^{124}Xe(n,γ) ^{125}Xe reaction.
^{127}Xe	36.4 days	Primarily created through ^{126}Xe(n,γ) ^{127}Xe reaction.
^{129m}Xe	8.9 days	Primarily created through ^{128}Xe(n,γ) ^{129m}Xe reaction.
^{131m}Xe	11.9 days	Longest lived radioxenon with good fission yield.
^{133m}Xe	2.2 days	
^{133}Xe	5.2 days	
^{135}Xe	9.1 hours	
^{85}Kr	3934.4 days	Hard to detect via classic gamma-ray spectroscopy. Documented environmental background.
^{37}Ar	35.0 days	Produced primarily through ^{40}Ca(n,α)^{47}Ar with secondary production through ^{36}Ar(n,γ) ^{37}Ar reaction.
^{39}Ar	269 years	Produced primarily through ^{38}Ar(n,γ) ^{39}Ar with secondary production through ^{42}Ca(n,α)^{49}Ar reaction.
^{42}Ar	32.9 years	Produced from double neutron capture ^{40}Ar(n,γ) ^{41}Ar(n,γ)^{42}Ar with secondary production from ^{44}Ca(n,γ)^{45}Ca (n,α)^{42}Ar. Low anticipated production.
^{129}I	1.57E7 years	Hard to detect through classical gamma-ray spectroscopy. Low specific activity.
^{131}I	8.0 days	Decays to ^{131m}Xe and ^{131} Xe (stable).
^{133}I	20.8 hours	Decays to ^{133m}Xe and ^{133} Xe (stable).
^{134}Cs	2.1 years	Shielded radionuclide (no radioactive parent).
^{136}Cs	13.2 d	Shielded radionuclide (no radioactive parent).
^{137}Cs	30.1 years	High environmental background due to past fallout and reactor accidents.

Currently, the bulk of the knowledge and methods used to predict UNE radioxenon signatures have focused on simply modeling the production source. Largely neglected in these calculations are the effects of chemical and isotopic mixing that occur as a result of environmental transport of radioxenon and its parent radionuclides. As compared its origin signature hundreds of meters beneath the surface, this mixing can significantly alter the isotopic ratios before radioxenon reaches the surface and atmosphere. Given that atmospheric monitoring and OSI sampling for radionuclides are the only real means by which a nuclear explosion can be positively verified, a greater understanding of the various physical phenomena responsible for subsurface radionuclide transport is essential.

1.2 NPE GAS TRACER EXPERIMENT

1.2.1 The Experiment

Following the signing of the CTBT in 1996, the Comprehensive Test Ban Treaty Research program was initiated for the purpose of researching technologies of potential use for OSI. Within this, the Lawrence Livermore National Laboratory On-Site Inspection project considered four technologies that were considered particularly promising for use in an OSI, yet insufficiently developed. One such technology considered was noble gas transport modeling and sampling, carried out as part of the Non-Proliferation Experiment (Carrigan *et al.*, 1997).

The Non-Proliferation Experiment (NPE), conducted by Lawrence Livermore National Laboratory (LLNL), entailed the September 22, 1993 detonation of a one-kiloton chemical explosion within Rainier Mesa at the Nevada Test Site. Situated at a depth of about 400 m below the surface, the NPE afforded a unique opportunity to

simulate the release and subsequent transport of radionuclides from a nuclear event. As a whole, the NPE consisted of a broad range of goals. First, on-site, pre-shot, shot-time, and post-shot measurements of gas seepage and seismic activity were taken to mimic challenge OSI scenarios. Second, there was the objective of comparing the underground chemical explosion with the measurements of nearby nuclear test explosions within the same geologic medium. Lastly were a number of scientific objectives regarding the structure of the regional crust and upper mantle, examined by seismic stations located across the region (Denny, 1994). The specific aim of the LLNL OSI project was to determine whether a well-contained underground explosion could be detected by gas sampling along nearby geologic faults, and if so, to define a basis for predicting the detectability of quickly decaying radionuclides that could be positively linked to fission products from a nuclear detonation (Carrigan, *et al.,*1997).

The setup of the NPE was as follows: approximately 1.29 kg of ANFO[1] blasting agent was placed within a 15.2 m diameter, 5.5 m tall cylindrical cavity. Within the cavity two samples of tracer gas, 8 m^3 of SF_6 and 1.3 m^3 of ^3He were placed. Sulfur hexafluoride, SF_6, is a relatively inert compound of high molecular weight (146), good thermal stability, and was detected at background levels of only 3 ppt (parts-per-trillion by volume) at the test site. ^3He similarly existed at very low background levels, only 7.34 ppt. To detect the concentration of SF_6 in gas samples, chromatography was used, while mass spectrometry was used to determine ^3He concentrations.

[1] AN/FO, ammonium nitrate/fuel oil; by far the most common type of explosive utilized in North America

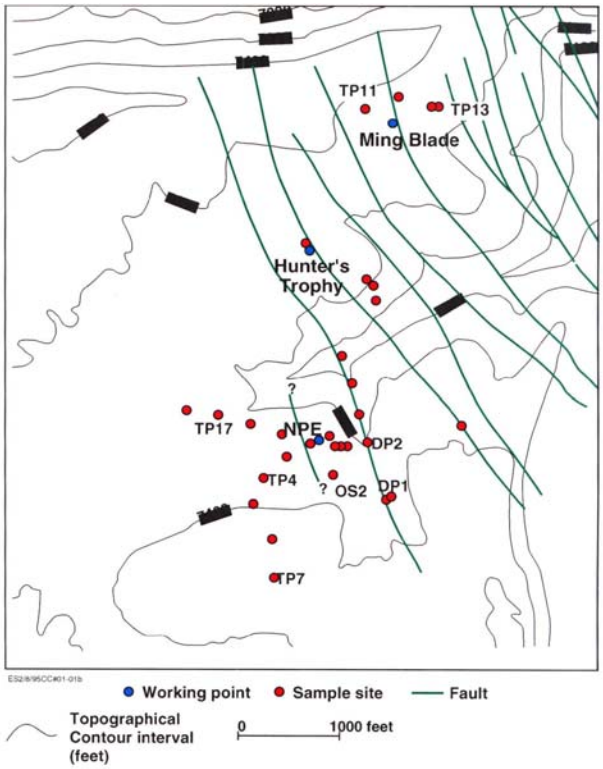

Figure 1.3 Surface distribution of soil gas sampling stations. Stations denoted 'OS' and 'DP' are located on pre-existing faults or fissures. Note also that Hunter's Trophy is the site of a previously conducted underground nuclear explosion (Carrigan *et al.*, 1997; Denny, 1994).

Over a roughly 500-day period following the detonation, 200 gas samples were collected in the region and analyzed for traces of the gases. Figure 1.3 shows an overview of the NPE site at Rainier Mesa (Denny, 1994). A NOAA[2] weather station located at an elevation of 2286m on Rainier Mesa recorded barometric readings throughout the duration of the experiment. Sampling sites as indicated in Figure 1.3 can be broadly categorized as either being located on pre-existing fault lines or near the point of detonation. Fault line stations were sampled most often, but during "barometric events," additional surface samples were collected at stations near the detonation point. It would

[2] National Oceanic and Atmospheric Administration, United States Department of Commerce

turn out that only one ground zero gas sample ever recorded a SF_6 concentration above background. Due to heavy snows, the majority of samples were collected during the fall and spring following the detonation, particularly during periods of deep barometric depressions (Carrigan *et al.*, 1997).

1.2.2 NPE Results

Table 1.3 summarizes the gas sampling observations (Carrigan *et al.*, 1997). Over a period of 508 days, thirteen samples were identified as positive for SF_6, the first of which came 50 days following the detonation at the site OS-6. Like all but one of the locations of positive samples, this station site is located on a pre-existing fault several hundred meters from the point of detonation, near to the site of a previously conducted underground nuclear explosion called Hunter's Trophy. This initial positive sample followed a number of large barometric depressions. Of particular interest is that while SF_6 was subsequently detected well above background in a few other sample suites, no amounts were seen in many additional sample suites, as indicated by the "no detects" in Table 1.3. ^3He was not detected significantly above background levels until day 375 following the detonation, 325 days following the initial detection of SF_6.

An important goal of the LLNL OSI project team was to develop a basis for future prediction of the detectability of rapidly decaying radionuclides unambiguously emanating from nuclear detonations. To this end, a numerical model of tracer transport was developed with two broad points in mind, both of which were strongly supported by the results of the NPE. First, the fact that all but one positive sample came at stations located near pre-existing faults considerable distances from the detonation point lends support to the theory that fractures within an otherwise homogeneous geologic media (matrix) provide "fast tracks" for the migration of contaminants to the surface. The study

Table 1.3 Summary of Rainier Mesa Gas Sampling Observations from the NPE (Carrigan *et al.*, 1997).

Sample Suite	Date	No. Sites F=fracture S=soil	Total Detects (Total Samples)	Locations of SF_6 Detection	SF_6 Conc., ppt	Locations of ^3He Detection	^3He Conc., ppt	Barometric Pressure (mbar)
1	08-Jul-93	3F	0 (3)		ND		-	772.1
2	11-Aug-93	3F	0 (5)		ND		ND	775.2
3	09-Sep-93	3F	0 (6)		ND		ND	777.6
4	22-Sep-93	Tunnel Port	0 (2)		ND		ND	772.5
5	24-Sep-93	3F	0 (3)		ND		-	778.2
6	10-Nov-93	3F	0 (6)	OS-6	340		ND	764.8
7	17-Mar-94	3F	1 (7)	OS-1	540		ND	771.2
		3F		OS-6	580			
		3F		OS-6	280			
8	23-Mar-94	3F	1 (6)	OS-1	580		ND	765.3
		3F		OS-2	450			
		3F		OS-3	400			
9	17-May-94	2F	3 (2)		ND		-	765.2
10	19-May-94	3F	0 (3)		-		ND	770.7
11	11-Aug-94	1F	0 (1)		ND		-	779.1
12	29-Sep-94	5F	0 (9)		ND		ND	771.6
13	04-Oct-94	1F	0 (11)		ND		ND	766.6
14	06-Oct-94	5F	2 (11)	OS-1	13	OS-6	8.42	771.2
15	12-Oct-94	5F	1 (12)	OS-3	18		ND	769.8
16	02-Nov-94	6F	3 (15)	DP-1	45	DP-1	9.22	760.9
		6F		OS-6	45			
17	03-Nov-94	8F	0 (15)		ND		ND	764.5
18	10-Nov-94	13S	3 (41)	DP-1	18	DP-1	21.4	760.8
		6F		TP-4	9			
19	16-Nov-94	18S, 8F	1 (40)		ND	DP-1	14.7	762.8

of continuous and networked fractures and their role as effective contaminant transport was undertaken in the 1970's by a handful of groups including Wilson & Witherspoon (1970), Nelson & Handin (1977), and Gale (1979). A second key element of the NPE migration study was the magnitude of the effect of variations in surface pressure on bringing a tracer contaminant to the surface, a process termed *barometric pumping* first modeled as a source of tracer transport by Nilson & Lie (1990), which will be described in greater detail in the following section and chapter. While large barometric depressions tended to precede the positive sample results in the NPE, smaller amplitude, higher frequency barometric variations seemed to have little effect on the detection of trace gas.

1.3 BAROMETRIC PUMPING

Binary gas diffusion has long been known to be too slow to account for the transport of detectable concentrations of rapidly decaying radionuclides from hundreds of meters underground to the surface. Two well-considered examples are ^{37}Ar and ^{133}Xe, radionuclides of particular interest in atmospheric monitoring having short half-lives of 34.8 days and 5.2 days, respectively. Additionally, long term, highly pressurized subsurface sources are ineffective in pushing gases to the surface – gas flow in this scenario is typically largely horizontal due to the anisotropic permeability of geologic layers (Carrigan *et al.*, 1997). Alternatively, as demonstrated in the results of the NPE, a deep, extended drop in surface pressure can be very effective in the transport of subsurface gas to the surface.

The concept of barometric pumping is simple. Consider a concentration of trace gas located deep beneath the surface within the rock matrix. During periods when the barometric pressure falls below the ambient pressure of the formation, tracer gas within fractures is pulled upwards. The flow is complicated by the fact that, as the gas travels along the fracture it also has the opportunity to diffuse horizontally back into the higher levels of rock matrix. As a result, the concentration of a trace gas moving along a fracture toward the surface during a pressure low will tend to decrease. When the barometric pressure rises higher than the pressure in the formation, gas within the fractures is pushed back downwards, and again the tracer gas escapes into rock matrix through the porous fracture walls. On the next cycle, decreasing pressure again pulls trace gas from the matrix upwards through the fractures. The effect of fracture-matrix diffusion in these cycles is that low/high pressure cycles are not completely reversible – even if pressure variations are perfectly sinusoidal, there is a net upward "ratcheting" of the tracer concentration front.

Models, both numerical and analytical, of subsurface gas transport have been explored well before the NPE-migration model reported on by the LLNL team. Of particular relevance to this thesis are two works by Grisak & Pickens (1980) and Tang *et al.* (1981), which demonstrated the role of fracture-matrix interactions in controlling the rate of contaminant migration in hydrological applications. In the former study, a finite element model was developed for solute transport by advection[3], mechanical dispersion, and diffusion in single-direction flow field. Similarly, the later study considered an analytical solution to tracer transport within a fracture surrounded by saturated porous rock. Additionally, however, the Tang study considered molecular diffusion both along the fracture axis as well as into the surrounding matrix, adsorption[4] in the matrix, and lastly radioactive decay. In 1984, Neretnieks and Rasmuson developed an integrated finite difference scheme to model radionuclide migration that examined variation in both fracture cross section and fluid velocity, which ultimately demonstrated how simplified models of 1D transport could be extended to more complex configurations.

The first actual trace gas vertical transport model based on barometric pumping as the primary transport mechanism was developed by Nilson and Lie (1990). This finite difference based numerical model considers a double-porosity formulation[5] in which fractures are the dominant pathways by which contaminants migrate, and fracture-matrix interactions play a critical role in determining the rate of migration. Finally and somewhat more recently, the **N**on-isothermal **U**nsaturated-Saturated **F**low **T**ransport (NUFT) model was developed by Nitao (1996) and utilized in the NPE-migration model

---

[3] Advection refers to transport of a substance due to the bulk motion of a fluid.

[4] Adsorption refers to the adhesion of atoms or molecules to a surface, as opposed to *absorption* within a permeable liquid or solid

[5] Double-porosity models of fracture and matrix systems were previously looked at in Gringarten (1984) and Chen (1989), referenced in the bibliography.

by the LLNL OSI team (Carrigan, 1994; Carrigan *et al.*, 1996; Nitao, 1998). Using this model and based on the results of the NPE, Carrigan made predictions regarding the vertical transport of ^{37}Ar and ^{133}Xe due to barometric pumping. Beginning with an initial source of 9.7×10^{12} Bq of ^{37}Ar and 6.7×10^{15} Bq of ^{133}Xe, they used the 1D model based on Nilson & Lie (1990) to calculate a resulting surface concentration of 6 Bq/m^3 after 80 days and 41 Bq/m^3 after 50 days for ^{37}Ar and ^{133}Xe respectively.

1.4 STATEMENT OF GOALS

Of utmost importance to the accuracy and reliability of radionuclide monitoring for the purposes of the IMS and OSI procedure is the capacity to unambiguously identify a radioisotope signature as one emanating from an underground nuclear explosion as opposed to from a source of a peaceful nature. In order to distinguish one radioisotope signature from another, the expected isotopic ratios of important radionuclides must be known. It is well established that the processes of subsurface transport can affect the rate at which such gases will reach the surface. However, the relative abundance of anthropogenic isotopes reaching the surface following transport is currently assumed to rely solely on their direct fission yield, decay rate, and their production from precursor decay (Le Petit, *et al.*, 2008), making no account for the influence of transport processes on fluctuations in isotopic ratios. While the ability to well-define such ratios as they are directly produced by nuclear explosions exists, the potential for alteration once radionuclides have transported through hundreds of meters of rock to reach the surface had not been considered before work began that has since culminated in the present body of work (Lowrey, *et al.*, 2012; Lowrey, *et al.*, 2013; Lowrey, 2011). As the effects of vertical transport on isotopic ratios of noble gas are not as well understood, the broad

goal of this work was to develop a vertical transport model for xenon and its parent nuclides as they result from an underground nuclear explosion in an effort to better understand the effects of this transport on the isotopic ratios of xenon.

To accomplish a self-contained transport model, the first task was to define a source term – that is, to calculate an inventory of the concentration or activities of the radionuclides that result from a nuclear explosion. In particular, the source term in this work is time-dependent, and entails tracking the quantities of xenon isotopes ^{131m}Xe, ^{133m}Xe, ^{133}Xe, and ^{135}Xe, as well as their parent radionuclides. Next, a vertical transport model following the scheme defined by Nilson & Lie (1990) was developed, which has been named Underground Transport of Environmental Xenon (UTEX). UTEX considers tracer transport in a 2D double-porosity model. Additionally, it accepts a generalized pressure function, user-defined physical parameters, as well as a time varying source term to calculate the outflow of tracer gas from the surface. Properties of particular gases are specified through the diffusion coefficient.

Major goals of this Ph.D. with a short description of intent and chapter locations are outlined as follows:

1. Model initial source term – (Chapter 2) While the larger goal of this work is to examine how geological transport can influence a given underground source signature, characterization of the initial source has a large effect on how transported radionuclide gas mixes at later times and isotopic ratios can be skewed. A simple, fast fission model of IAEA significant[6] quantities of fissile

[6]The International Atomic Energy Agency (IAEA) defines a *significant quantity* of fissile material as the approximate amount of nuclear material for which the possibility of manufacturing a nuclear explosive device cannot be excluded (Boyer, 2013)

material is used to approximate the source term of a normalized 1 kton, hypothetical underground nuclear explosion.

2. UTEX transport code development – (Chapters 2 and 3) The UTEX model is a numerical code package developed as part of this Ph.D. work that simulates the simultaneous movement, decay and buildup of various radioxenon isotopes as they originate from an underground, time-dependent source. Built upon a simple double porosity framework, UTEX serves as the engine for the work completed in this Ph.D. As such, development of the code itself is an initial major goal.
3. UTEX transport code benchmarking – (Chapter 3) UTEX has undergone a lot of evolution since its creation to make the code faster, more efficient, and more flexible to generalized applications, many of which are considered in the second half of this dissertation. Accordingly, the code must be vetted and optimized. Through comparison with simple analytical case studies, the numerical code can be benchmarked.
4. General geologic parameter sensitivity – (Chapter 4) A handful of physical parameters constitute the UTEX input for defining the modeled geologic system. A natural starting point for simulations of subsurface transport is the consideration of how these various parameters affect noble gas transport. This can be accomplished through a large scale sensitivity study covering an array of parameters to evaluate the resulting effects on gas outflows and isotopic fluctuations.
5. Source term consideration – (Chapter 4) Once being transported, xenon gas produced from different source terms behave the same way. However, the time-dependent source term itself contributes to the character of fluctuations induced by transport processes. This is especially important in *source mixing* wherein

oscillations in gas movement can result in radionuclide signatures that are not indicative of a source of any specific time. How the source specification can influence this transport "smearing" of signatures is considered.

6. Sampling assumptions – (Chapter 4 and 7) Slow transport of well-contained UNE gas, as considered in the UTEX model, has most direct relevance to OSI science. How soil-gas sampling is simulated in UTEX is to be considered in terms of its collection assumptions as well as its location and depth.
7. Cavity and geology characterization – (Chapter 5) The geological environment of a UNE is probably the most important factor in how likely a potential UNE will be to leak and potentially be detected. Effort should be made to study how various geological assumptions affect simulated transport in UTEX. Additionally, consideration should also be made for the fact that a UNE will have a significant local effect on the geology in the creation of an explosion cavity and rubblizing surrounding rock.
8. Soil-gas background estimates – (Chapter 6) Soil-gas background levels of radionuclide gas are becoming ever more important as technology improves and minimum detection limits decrease. Understanding background sources and what can influence them is an important component in being able to distinguish low concentration evidence of a potential UNE from soil-gas background.
9. On-site inspection considerations – (Chapter 7) OSI scenarios provide the most direct application for UTEX simulation of underground transport. A number of open questions remain in the OSI concept of operations, which UTEX could be utilized to study. The dangers of atmospheric infiltration and the barometric effect of sail-sampling in the subsurface are just two.

Chapter 2. Theory

2.1 UNE SOURCE TERM MODEL

This first section concerns the theory and assumptions behind the specification of the source terms that are effectively used in the remainder of this work to approximate a 1 kton UNE. In this context, a source term can be thought of as an approximate inventory of all the radionuclides resulting from a UNE. Of particular importance to this work is radioxenon; among other radionuclides, the source term needs to account for the production of ^{131m}Xe, ^{133m}Xe, ^{133}Xe, and ^{135}Xe, as well as their parent radionuclides as a function of time. This time-varying source term will later serve to determine the amount of a particular radionuclide that gets created and added into the transport model at each step in time considered. In addition to xenon, the production and transport of radioactive ^{37}Ar is considered.

2.1.1 Modeling a UNE

Only a simplified model of a fast fission burnup is considered in this work. This choice is more than adequate considering that the real focus of this work is in examining the potential for underground transport to alter an initial radionuclide signature from an underground anthropogenic source. Furthermore, as a fast pulse fission burnup within a power reactor has a fission product spectrum that is similar to that of a nuclear explosion, this approximation is very suitable for the transport studies in this work. Production of radionuclides by a fission device detonated underground will occur predominantly by two processes. The first is of course the fission reactions that take place in the course of the explosion that yields fission products, such as xenon. A second process of importance yields *activation products* that result from non-fission reactions induced by free neutrons. Neutrons produced by fission reactions during the explosion can escape into the

surrounding media where they may undergo one or more interactions with nuclei. A typical fast neutron that escapes into the surrounding geologic medium can interact with nuclei in that medium in all the following ways: scattering (elastic and inelastic), radiative capture, charged-particle interactions, fast neutron reactions, and in some instances even fission.

The two primary interactions between free neutrons and nuclei within the surrounding geologic media that need be considered here are inelastic scattering and neutron activation through radiative capture. Inelastic scattering is the primary interaction by which a high energy neutron is slowed down, and can be summarized by the simple expression

$$n + {}^{A}Z \rightarrow {}^{A}Z' + n'$$

where ${}^{A}Z'$ and n' denote the same nucleus and neutron but with altered kinetic energies. Fast neutrons scattering from much heavier nuclei will typically lose momentum as a result of the interaction; successive interactions of this type will eventually reduce neutron energies by several orders of magnitude.

Neutron activation by radiative capture occurs when a neutron is captured by a nucleus, ${}^{A}Z$, thus creating an isotope of the nucleus that is heavier by one neutron, which is typically in an excited, meta-stable state, denoted ${}^{A+1}Z^{*}$. Upon de-excitation, a gamma-ray is given off, leaving ${}^{A+1}Z$. Thus radiative capture can be summarized

$$n + {}^{A}Z \rightarrow {}^{A+1}Z^{*} \rightarrow {}^{A+1}Z + \gamma .$$

The final product ${}^{A+1}Z$ of this reaction is often itself radioactive, and subsequently undergoes beta decay to yield other nuclei that are also termed activation products within the source term. Of particular importance to the present work is the production of radioactive ${}^{37}\mathrm{Ar}$ through

$$n + {}^{40}\mathrm{Ca} \rightarrow {}^{37}\mathrm{Ar} + \alpha .$$

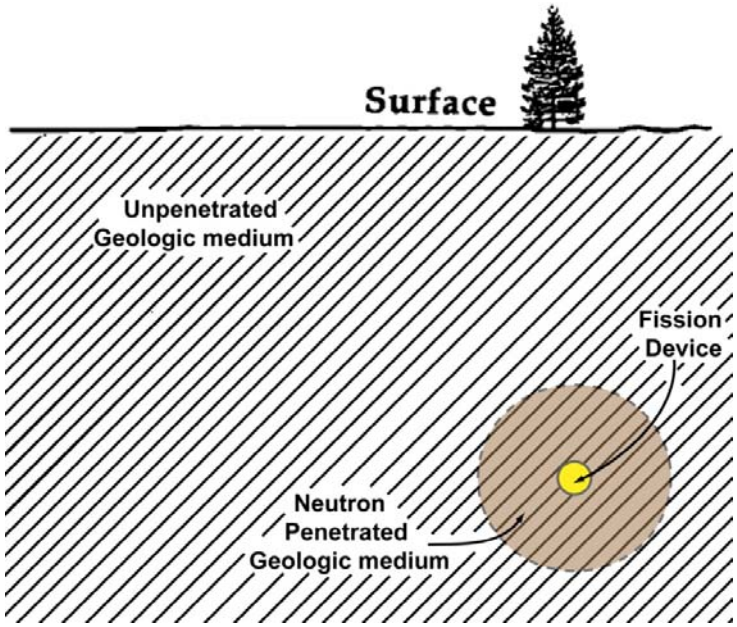

Figure 2.1 Depiction of the simple nuclear explosion model, not drawn to scale. Modified from an illustration in Nilson, *et al.,* (1991).

The simplest possible model of an underground nuclear explosion consists of the 2D configuration depicted in Figure 2.1. In this model, there are only two regions of interest: the fission device and the surrounding neutron-penetrated geologic medium. The fission device can be modeled as a small, spherical, critical assembly of fissile material in which fission occurs to produce a distribution of neutrons. Surrounding the fission core is a spherical region of geologic medium; neutrons that escape the core interact with nuclei of this medium. A basic assumption inherent in this model is that the nuclear detonation occurs at a depth deep enough that all of the free neutrons are eventually absorbed in the geologic medium.

2.1.2 Calculation of the Source Term

To model the neutron flux within the fission core as well as in the surrounding geologic medium, the code MCNP was utilized. MCNP is a general **M**onte **C**arlo

Neutral-**P**article code used for the simulation of neutron, electron, or photon transport (Briesmeister, 1986). This code is capable of modeling an arbitrary 3D configuration of various material cells with specified boundaries. With the neutron flux profiles generated in MCNP as input, the code ORIGEN 2.2 was used to model the resulting material compositions resulting from the various particle interactions (Bell, 1973). To facilitate this functionality, MONTEBURNS was used. MONTEBURNS is essentially a script that takes an MCNP input file with specified system geometry and initial material compositions, calculates and transfers one-group cross-sections and flux values to ORIGEN, which in turn calculates and returns to MCNP the resulting material compositions (Poston & Trellue, 1998). These cycles, or burn steps, are repeated until the desired energy burnup is achieved.

Modeling of the system using MONTEBURNS requires specification of all of the following major parameters: geometry of the system's various cells, initial material composition within those cells, all boundaries and boundary conditions, total time to burn, power output, number of burn steps, and which nuclides are to be explicitly tracked in MONTEBURNS. Two generic compositions of fissile materials were ultimately considered for the fission core, one consisting of highly-enriched uranium (HEU) and the other plutonium, the compositions of which are shown in Table 2.1 (Stacey, 2007). Figure 2.2 represents a simple illustration of the model geometry. Since a true underground explosion scenario would take place hundreds of meters beneath the surface, the radius of the surrounding geologic medium, R, should ideally be of the same order as the depth of the device. However, it is unnecessary to simulate the neutronics in hundreds of meters of geology due to neutron attenuation. As a result, the parameter R is a variable parameter to be determined in such a way that a satisfactory fraction of all neutrons in the

system eventually die within the system without escaping into the vacuum cell surrounding the geometry, as shown in Figure 2.2.

Table 2.1 Fractional composition of generic HEU & Pu for calculation of simple source term (Stacey, 2007).

HEU		Pu	
^{234}U	0.12	^{238}Pu	0.01
^{235}U	94.00	^{239}Pu	93.80
^{238}U	5.88	^{240}Pu	5.80
		^{241}Pu	0.13
		^{242}Pu	0.02
		^{241}Am	0.22

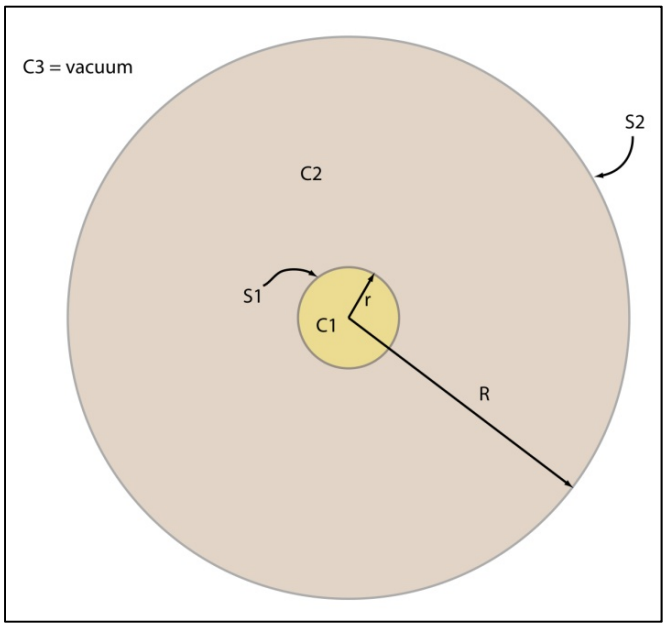

Figure 2.2 Simple model used for source term calculation in MCNP, with C1 (cell 1) being the fission core, and C2 the surrounding geologic medium.

The goal of the source term calculation is to make a rough estimate of an inventory of radionuclide activities resulting from a generic UNE, normalized to a total of 1 kiloton total energy release, or 4.184×10^{12} J. MONTEBURNS requires an average power as one of its input parameters. Estimating the time duration of the explosion to be 1 μs, the average power output can easily be calculated to be

$$P = \frac{4.184\times10^{12}\,\mathrm{J}}{10^{-6}\,\mathrm{s}} = 4.184\times10^{18}\,\mathrm{W} = 4.184\times10^{12}\,\mathrm{MW}.$$

Lastly, the composition of the surrounding geologic medium needs to be defined, element by element. Elemental compositions of five different mediums are presented in Appendix A, three of which constitute rock estimates and two soil estimates. These compositions assume natural isotopic abundances. These five samples have been chosen for consideration in this study in large part because they likely represent upper and lower bounds for the number of activation products produced in the media surrounding the fission device. Note that the five estimates vary little in the concentrations of the majority of elements; the most notable exceptions are in the estimates of H and Fe concentration, the former due mainly to a difference in the treatment of water within the studies. Hydrogen and iron both act as neutron moderators, for they have relatively large inelastic neutron scattering cross-sections. The presence of these nuclei in the medium around the fission device is likely to mean a quicker attenuation of the outward neutron flux, therefore altering the distribution of activation products that result.

2.2 SOURCE TERM RESULTS

With a working compilation of MONTEBURNS, MCNP, and ORIGEN 2.2 and with the major parameters set as described in the previous section, simple burnup calculations were made with the HEU and Pu starting concentrations of Table 2.1. Since

all that is necessary for the basic source term calculation needed in the UTEX model is to simulate enough fissions to produce 4.184×10^{12} J of energy, the burnup model was kept simple. The International Atomic Energy Agency (IAEA) defines a *significant quantity* (SQ) of fissile material as the approximate amount of nuclear material for which the possibility of manufacturing a nuclear explosive device cannot be excluded (Boyer, 2013). Calculations modeled burnups of IAEA SQs of HEU and Pu material for a length of time long enough to produce the desired number of total fissions.

2.2.1 Diagnostics

The first step in the source term calculation was to simply test the implementation on the fission model and then test it with the addition of a thin shell of surrounding geologic media to determine whether the model depicts the neutron physics that are expected. Immediately noticeable in the calculation was that even though no neutron source was present in the geologic medium, the addition of the surrounding medium produced a definite alteration in the neutron flux profile within the "core." The reason for this is obvious; due to inelastic scattering events in the surrounding geologic medium, a certain fraction of neutrons are reflected back into the core where they add to the overall neutron flux.

To get an idea of the magnitude of these effects, a simple analysis of the neutron flux profile was conducted, the results of which are summarized in Table 2.2 and Figure 2.3. In order to determine the number of neutrons passing first out of the core and then back into the core upon reflection, a *flag* within MCNP was set up to flag neutrons that pass the core's surface from the positive (rock) side to the negative (core) side. As seen below, neutron reflection contributes a significant fraction of the neutron flux within the

core; by 50 cm of rock thickness, 20% of the neutrons contributing to the total neutron flux in the core are flagged as having passed from the rock to the core cells.

Table 2.2 Fractional neutron flux profile of HEU fissioning core with various thicknesses of surrounding Wedepohl rock.

Rock thickness	*n* flux from core alone	*n* flux coming from rock
1cm	0.9491	0.0509
10cm	0.8442	0.1558
50cm	0.7972	0.2028
100cm	0.7947	0.2053

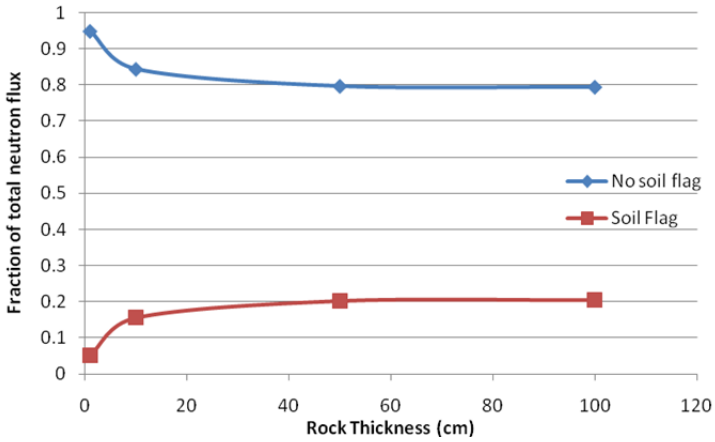

Figure 2.3 Fraction of neutrons in HEU fissioning core flagged and non-flagged as coming from the surrounding medium

In addition to contributing to the overall neutron flux, the backscattered neutrons might also alter the energy flux spectrum within the core, as demonstrated by the data in Table 2.3. Realistically, however, the time for backscattered neutrons to re-enter the fissioning core is likely longer than the time it takes the explosion to occur. As a result, estimates

for products resulting from fissioning in the core were made assuming no backscattered neutrons (in other words, calculated without the surrounding geology). With regard to soil activation, neutrons that escape the core undergo inelastic collisions with nuclei of the surrounding rock, losing energy along their path. As the rock thickness surrounding the fissioning core increases, neutrons penetrate deeper into the rock and lose increasing amounts of energy.

Table 2.3 HEU core neutron energy flux profile for various thicknesses of Wedepohl rock

Rock Thickness(cm)	% flux by energy range		
	Thermal	Intermediate	Fast
0	0	5.39	94.61
1	0	5.54	94.46
10	0	7.02	92.98
25	0	9.92	90.08
50	0.14	12.44	87.42
100	0.34	12.90	86.76

Of secondary importance in Figure 2.3 and Table 2.2 is the asymptotic nature of the variation of neutron flux characteristics with increasing thickness of surrounding rock. For the Wedepohl rock composition used in those analyses, beyond an outer thickness of 80-100 cm, additional amounts of rock media have negligible effects on the physics within the fissioning core. As stated in the previous section and illustrated in Figure 2.2, the explosion model should include a geologic media of thickness, *R*, such that a suitably small fraction of the system neutrons escape into the outer vacuum cell.

Figure 2.4 shows the results of a simple MCNP analysis of the fraction of neutrons that are lost through escape into the outer vacuum as the thickness of surrounding rock is increased. Again, the Wedepohl rock composition was utilized

surrounding a HEU fission core. As depicted in the figure, the neutron escape fraction drops below 1% around R = 125 cm, below 0.1% around 160 cm, and approaches 0.01% by 200 cm. The particular value that constitutes a "suitably small" escape fraction is somewhat arbitrary; the runtime of a MONTEBURNS burn source term calculation involving a fissioning core and 200 cm thickness of surrounding geologic medium was of the order 12 hours on an Intel® Core™ 2 Duo CPU computer, a length of time deemed long enough to devote to a single calculation. As such, an R = 2 m was taken for the thickness of geologic media for all source term calculations. Given that the five compositions studied have some variation, particularly in their hydrogen and iron content, 200 cm of thickness assured that all source term calculations yielded neutron escape fractions of below 0.1%.

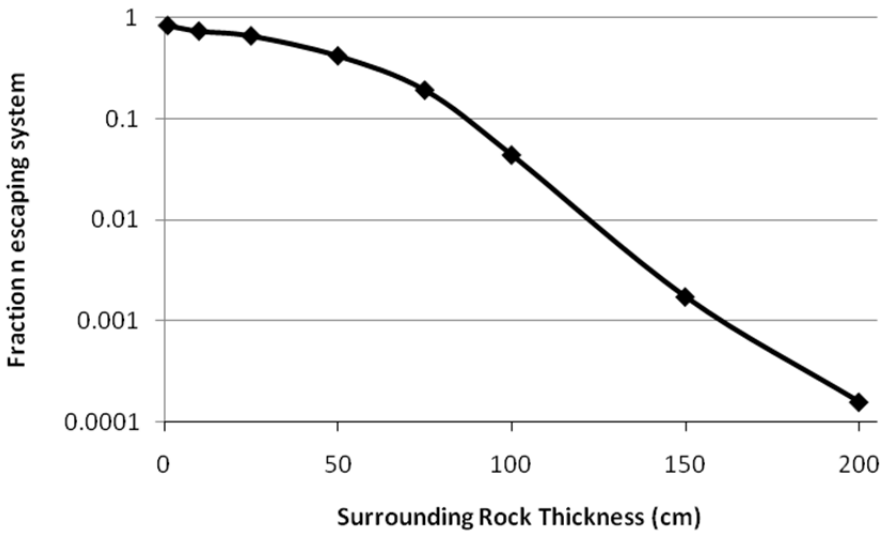

Figure 2.4 Fraction of *n* escaping the system for various thicknesses of Wedepohl rock surrounding HEU core

2.2.2 Source Term Calculation Results

With the input parameters verified and set, calculation of the source term was just a matter of patience while letting the numerical model process. The output of most interest from a burn run of MONTEBURNS is a final inventory of nuclide concentrations within the system. These concentrations represent the initial state of the system immediately following the fission event, assuming one of the five geologic compositions listed in Appendix A. To determine the time-varying source term, this initial inventory was can be fed into ORIGEN 2.2 and decayed for various lengths of time to obtain a database of radionuclide inventories at various times following the detonation. Table 2.4 and Table 2.5 provide a snapshot of the source terms of some of the most pertinent radionuclides.

While ORIGEN 2.2 decay is perfectly sufficient to determine these inventories at any time desired, this strategy grows prohibitively cumbersome in the construction of decay cards and the extraction of data for, say, 10,000 time intervals, as is necessary for use in the UTEX transport code. To really make use of these data in the transport model, an analytical source term was derived, for which an understanding of the physics behind the source term time evolution is necessary.

Figure 2.5, Figure 2.6, and Figure 2.7 show the decay chains of ^{131}Xe, ^{133}Xe, and ^{135}Xe respectively and Table 2.6 provides ORIGEN 2.2 generated activity levels for the relevant radionuclides at several times. Even following the simulated fission event, new radioxenon is continually produced from the decay of its parent radionuclides. As an example, consider the decay chain of ^{135}Xe as shown in Figure 2.7. An analytical source term calculation for ^{135}Xe is relatively simple because in this case the first three parent radionuclides have half-lives of less than 20 seconds – within a few minutes, and certainly within an hour, nearly all of these short-lived parents have decayed away.

Table 2.4 Activities in Ci of Xe radioisotopes following modeled 1 kton explosion at various post-burn decay times, assuming both uranium and plutonium cores.

		Initial	1 hr	10 hr	1 day	10 days	30 days	100 days
Uranium Core	^{131m}Xe	1.361E-01	7.948E-01	2.386E+01	5.972E+01	3.555E+02	2.638E+02	7.439E+00
	^{133}Xe	1.964E+02	6.481E+03	8.824E+04	1.709E+05	1.127E+05	8.120E+03	7.805E-01
	^{133m}Xe	1.560E+03	1.984E+03	7.379E+03	1.208E+04	1.743E+03	3.122E+00	7.441E-10
	^{135}Xe	1.109E+05	6.651E+05	2.000E+06	1.329E+06	1.843E-01	2.334E-17	0.000E+00
Plutonium Core	^{131m}Xe	1.811E-01	9.736E-01	2.705E+01	6.791E+01	4.147E+02	3.094E+02	8.740E+00
	^{133}Xe	6.991E+02	7.171E+03	8.886E+04	1.717E+05	1.134E+05	8.178E+03	7.861E-01
	^{133m}Xe	5.446E+03	5.831E+03	1.078E+04	1.490E+04	1.906E+03	3.425E+00	8.163E-10
	^{135}Xe	2.648E+05	9.930E+05	2.269E+06	1.459E+06	1.988E-01	2.518E-17	0.000E+00

Table 2.5 Activities of ^{37}Ar in Ci resulting from modeled 1 kton explosion and subsequent neutron activation in 2m of various surrounding soil and rock compositions.

		Initial	10 hr	1 day	10 days	30 days	100 days
Uranium Core	Wedepohl	1.014E+03	1.005E+03	9.937E+02	8.316E+02	5.597E+02	1.401E+02
	Taylor	9.455E+02	9.377E+02	9.270E+02	7.757E+02	5.222E+02	1.307E+02
	Mason	4.616E+02	4.579E+02	4.526E+02	3.788E+02	2.549E+02	6.380E+01
	Bowen	3.488E+02	3.460E+02	3.420E+02	2.862E+02	1.926E+02	4.820E+01
	Vinogradov	3.477E+02	3.448E+02	3.409E+02	2.853E+02	1.920E+02	4.805E+01
Plutonium Core	Wedepohl	1.760E+03	1.745E+03	1.725E+03	1.444E+03	9.717E+02	2.432E+02
	Taylor	1.502E+03	1.489E+03	1.472E+03	1.232E+03	8.294E+02	2.075E+02
	Mason	7.241E+02	7.182E+02	7.100E+02	5.941E+02	3.999E+02	1.001E+02
	Bowen	5.021E+02	4.980E+02	4.922E+02	4.119E+02	2.773E+02	6.938E+01
	Vinogradov	5.011E+02	4.970E+02	4.913E+02	4.111E+02	2.767E+02	6.925E+01

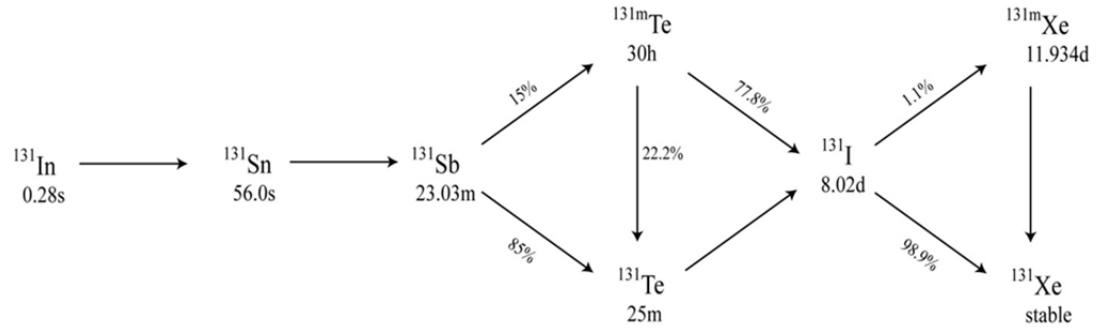

Figure 2.5 The decay chain of ^{131}Xe and its parent radionuclides.

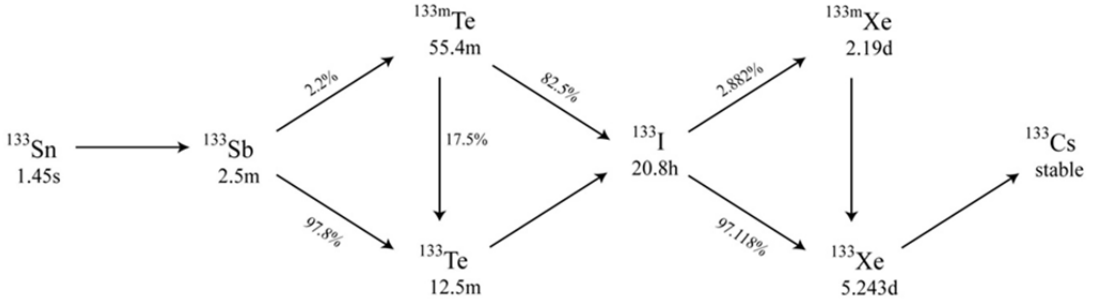

Figure 2.6 The decay chain of ^{133}Xe and its parent radionuclides.

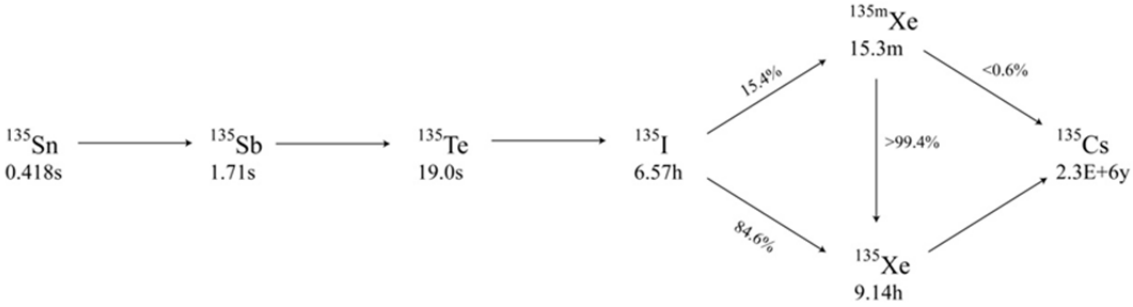

Figure 2.7 The decay chain of ^{135}Xe and its parent radionuclides.

The UTEX model was written to include a Bateman equation solving routine for the determination of the nuclide inventory resulting from an arbitrary specification of the source for the nuclides listed in Table 2.6. The strength of this routine is that any starting source concentrations can be modeled and the resulting xenon inventories as well as instantaneous ingrowth rates can be determined for an arbitrary time step length and at any given time. This greatly facilitates the inclusion of a flexible, time-dependent source term in the UTEX model. The source term for ^{131m}Xe, ^{133m}Xe, ^{133}Xe, and ^{135}Xe carried out to 100 days following the initial simulated fission event is shown in Figure 2.8.

Table 2.6 Activities in Ci of radioxenon and parent radionuclides resulting from 1 kton HEU fission core detonation.

	INITIAL	15.0MI	1.0HR	3.0HR	10.0HR	1.0D	10.0D	100.0D
IN131	2.899E+09	0.000E+00	0.000E+00	0.000E+00	0.000E+00	0.000E+00	0.000E+00	0.000E+00
SN131	4.655E+08	2.400E+04	3.013E-09	0.000E+00	0.000E+00	0.000E+00	0.000E+00	0.000E+00
SB131	2.832E+07	3.257E+07	8.392E+06	2.256E+05	7.181E-01	7.279E-12	0.000E+00	0.000E+00
TE131	3.181E+06	1.434E+07	1.444E+07	1.348E+06	1.636E+04	1.182E+04	8.041E+01	1.703E-20
TE131M	4.729E+04	6.224E+04	8.196E+04	8.511E+04	7.257E+04	5.252E+04	3.572E+02	7.563E-20
I131	3.426E+02	8.821E+03	5.349E+04	9.689E+04	9.966E+04	9.782E+04	4.942E+04	2.115E+01
XE131M	1.361E-01	1.611E-01	7.948E-01	5.252E+00	2.386E+01	5.972E+01	3.555E+02	7.439E+00
IN131	2.899E+09	0.000E+00	0.000E+00	0.000E+00	0.000E+00	0.000E+00	0.000E+00	0.000E+00
SN133	2.967E+09	0.000E+00	0.000E+00	0.000E+00	0.000E+00	0.000E+00	0.000E+00	0.000E+00
SB133	3.431E+08	4.911E+06	1.114E+01	9.895E-15	0.000E+00	0.000E+00	0.000E+00	0.000E+00
TE133	6.012E+07	6.384E+07	6.361E+06	2.809E+05	1.433E+03	3.908E-02	0.000E+00	0.000E+00
TE133M	1.519E+07	1.289E+07	7.345E+06	1.637E+06	8.547E+03	2.330E-01	0.000E+00	0.000E+00
I133	6.203E+04	8.789E+05	1.675E+06	1.868E+06	1.541E+06	9.669E+05	7.233E+02	0.000E+00
I133M	3.895E+08	3.072E-22	0.000E+00	0.000E+00	0.000E+00	0.000E+00	0.000E+00	0.000E+00
XE133	1.964E+02	8.739E+02	6.481E+03	2.582E+04	8.824E+04	1.709E+05	1.127E+05	7.805E-01
XE133M	1.560E+03	1.603E+03	1.984E+03	3.300E+03	7.379E+03	1.208E+04	1.743E+03	7.441E-10
SN135	1.213E+08	0.000E+00	0.000E+00	0.000E+00	0.000E+00	0.000E+00	0.000E+00	0.000E+00
SB135	2.638E+09	0.000E+00	0.000E+00	0.000E+00	0.000E+00	0.000E+00	0.000E+00	0.000E+00
TE135	4.114E+09	3.372E-05	0.000E+00	0.000E+00	0.000E+00	0.000E+00	0.000E+00	0.000E+00
I135	2.519E+06	5.869E+06	5.425E+06	4.399E+06	2.111E+06	4.865E+05	7.108E-05	0.000E+00
XE135	1.109E+05	2.990E+05	6.651E+05	1.275E+06	2.000E+06	1.329E+06	1.843E-01	0.000E+00
XE135M	6.606E+06	3.798E+06	1.241E+06	7.062E+05	3.382E+05	7.793E+04	1.139E-05	0.000E+00

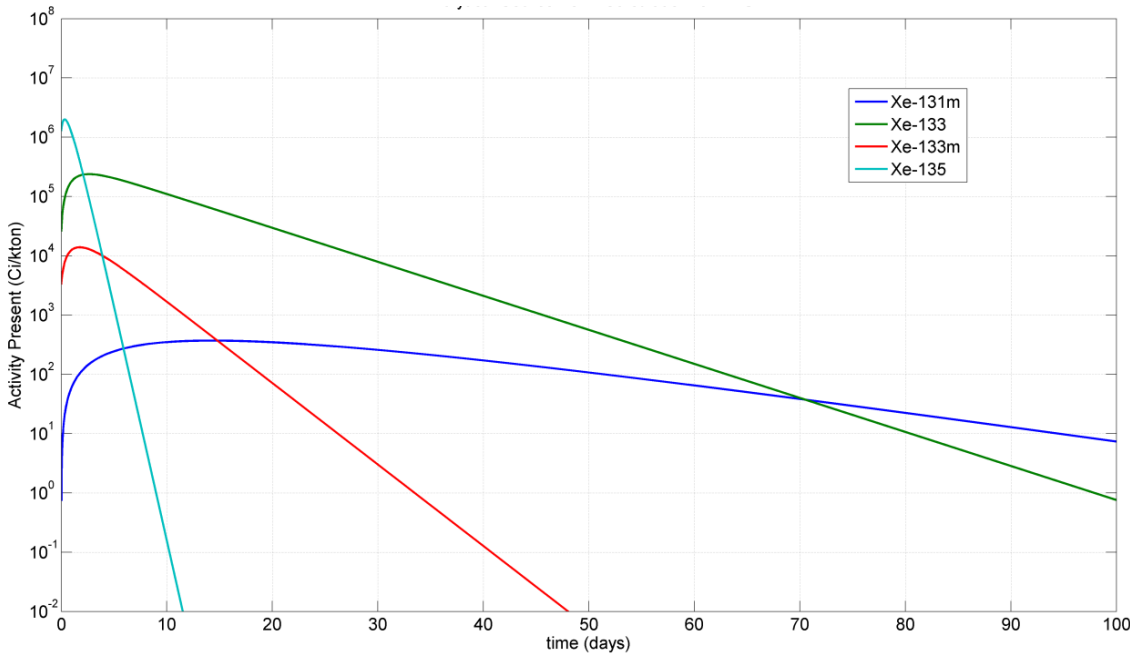

Figure 2.8 Radioxenon source term resulting from HEU core explosion.

2.3 TRANSPORT BASICS

The intent of this section is twofold. First, the basic terminologies and principles underlying the theory of gas transport that are necessary to the forthcoming discussion of the vertical transport model are presented. Second, these basic principles are utilized to characterize two very simple scenarios of subsurface vertical transport of a trace gas. This discussion then leads into the more complex analytical, double-porosity model of gas transport.

2.3.1 Basics of Transport Theory

Diffusion refers to the net migration of particles from regions of higher concentration to regions of lower concentration as a result of random particle motions. Defining $C = C(\mathbf{x})$ as the concentration of a tracer in a system described by the vector

coordinates $\mathbf{x}$, and $\mathbf{J}$ the flux of the tracer, then the above definition for diffusion can be restated mathematically as

$$\mathbf{J} = -D\nabla C. \tag{2.1}$$

This relation is known as Fick's first law of diffusion. The negative sign in Equation (2.1) indicates that a positive flux of particles is directed *down* the concentration gradient. The constant of proportionality, D, is termed the diffusion coefficient, or diffusivity, and accordingly has dimensions in SI units of [m^2/s]. The diffusion coefficient is actually specific to the substance that is diffusing as well as the fluid in which it is located, and is a function of temperature, pressure, and dynamic viscosity (defined below) (Bird, *et al.,* 2006). Considering the one-dimensional isothermal, isobaric, binary diffusion of one substance *i* in another *j*, Eq. (2.1) becomes simply[7]

$$J^i = -D^{ij}\frac{\partial C^i}{\partial x}. \tag{2.2}$$

In a porous medium, the ratio of fluid-filled, void volume V_{void} to the bulk volume V_{bulk} is termed the *porosity*, $\phi = V_{void} / V_{bulk}$.. Diffusion through a porous medium is characterized by the bulk properties of the medium in addition to the properties of the fluid which fills the pores. As such, an *effective diffusion coefficient* D_e^{ij} is defined as

$$D_e^{ij} = \frac{\phi}{\tau} D^{ij} \tag{2.3}$$

where τ is a dimensionless parameter called tortuosity, which has no single, agreed-upon definition, but essentially is a measure of how "twisty" a curve is (Epstein, 1989). Note also that some sources define the tortuosity as $T = \phi / \tau$. While conventions might differ, the effect of the tortuosity factor is to reduce the diffusivity to account for an increase in path lengths as a result of "obstacles" within a porous medium.

---

[7] Note that the superscripts in Eq. (2.2) are indices rather than exponents; or more accurately they are labels.

A*dvection* refers to the transport of a substance by a fluid as a result of the bulk motion of the fluid. Here the term fluid is used loosely, but because advection by definition requires the existence of a *current*, it cannot occur in a solid. One dimensional advection of a fluid through a porous medium is described generally by Darcy's law

$$J = -\frac{k}{\mu}\frac{\partial p}{\partial x}. \tag{2.4}$$

Note that this equation has the same form as Equation (2.2) - the movement of a substance is determined by a pressure gradient in the bulk fluid. The constant of proportionality in this case is determined by the *permeability*, k, and the *dynamic viscosity*, μ. The permeability is a characteristic of a porous medium describing its capability to transmit fluid, and has SI units of [m^2]. Permeability is also commonly given in the literature in terms of millidarcy (mD), equivalent to 10^{-15} m^2. The dynamic viscosity is a measure of a fluid's internal resistance to flow in response to an applied stress, and has SI units of [Pa·s] (Bird *et al.*, 2006).

Nominal values for the parameters described above are given in Table 2.7, adopted from Nilson *et al.* (1991), and unless stated otherwise, these values will be assumed throughout the rest of this chapter.

2.3.2 Gas Flow by Diffusion

It has long been known that diffusion alone cannot account for the vertical transport of contaminant gases from deep underground to the surface. As an example, consider the following scenario considered in Nilson *et al.* (1991), which will be utilized and modified in subsequent sections as well. Assume that a gaseous contaminant is distributed underground throughout an area bounded from below at a depth L = 500 m by an impenetrable floor and initially extends upwards a distance L_0 = 300 m as depicted in Figure 2.9.

Table 2.7 Values assumed for transport theory parameters.

Parameter	Assumed Value
porosity (in matrix)[8]	$\phi_m =$ 0.1
permeability (of matrix)	$k_m =$ 10^{-15} m^2
tortuosity	$\tau =$ 10
dynamic viscosity (air)	$\mu =$ 2×10^{-5} Pa·s

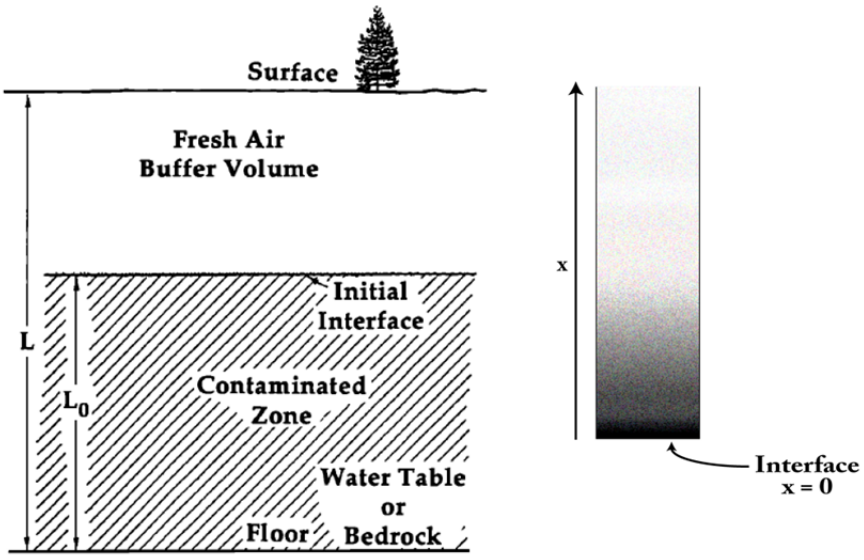

Figure 2.9 Depiction of diffusion transport scenario. Modified from a figure in Nilson *et al.* (1991).

[8] The '*m*' label here is necessary to distinguish parameters as they apply to the bulk matrix medium from later values as they apply to fractures.

Consider one small element of the so-called contamination front, which lies on the initial fresh air-contaminant interface as shown on the right of Figure 2.9. If the contaminated region extends sufficiently far laterally, then the transport of this element can be considered one-dimensional. Discounting adsorption effects, continuity requires that a change in concentration in this element must be due to a flux of contaminant, therefore

$$\frac{\partial C}{\partial t}+\frac{\partial}{\partial x}\left(J\right)=0 \tag{2.5}$$

and upon substitution of Eq. (2.2) for the flux (ignoring the *i* and *j* labels for clarity) this becomes

$$\frac{\partial C(x,t)}{\partial t}=D\frac{\partial^2 C(x,t)}{\partial x^2}. \tag{2.6}$$

Eq. (2.6) is the diffusion equation, the solution of which in this 1D scenario is a quick, easy exercise in the application Laplace transformations. Since the vertical column begins with no concentration inside, the initial condition is $C(x>0,0)=0$. As for boundary conditions, clearly $C(x\to\infty,0)=0$ is one. For the second, assume that diffusion beneath the interface is sufficient to maintain the concentration at $x=0$ at a constant value $C_0=C(0,0)=C(0,t)$. Transforming both sides of Eq. (2.6) with respect to time yields.

$$s\overline{C}(x,s)-\underbrace{C(x,0)}_{=0}=D\frac{\partial^2\overline{C}(x,s)}{\partial x^2}$$

$$\frac{\partial^2\overline{C}(x,s)}{\partial x^2}=\frac{s}{D}\overline{C}(x,s)$$

$$\overline{C}(x,s)=a_1e^{\sqrt{\frac{s}{D}}x}+a_2e^{-\sqrt{\frac{s}{D}}x}.$$

This is the general solution. Based on the first boundary condition above, $a_1 = 0$. The transformed second boundary condition requires that $\overline{C}(0,s)=\int_0^\infty C(0,t)e^{-st}dt=C_0/s$ so

$$\overline{C}(x,s) = \frac{C_0}{s} e^{-\sqrt{\frac{s}{D}}x}$$

the reverse transform of which finally yields

$$C(x,t) = C_0 erfc\left(\frac{x}{\sqrt{4Dt}}\right). \tag{2.7}$$

This result introduces a very important ratio $x/\sqrt{4Dt}$ that is characteristic of solutions to the general diffusion equation. *Erfc* is the complimentary error function, and varies between 1 and 0 as the above ratio varies from 0 to ∞. Since *D* is typically very small, long times *t* are usually required to make the above ratio approach 1 or less. This introduces the notion of the *characteristic timescale* for the migration of the contaminant front by diffusion given *D* and a desired depth of transport *x*, usually written

$$t_D = \frac{x^2}{D}. \tag{2.8}$$

Taking $D(^{133}\text{Xe})$ = 1.24E-5 $m^2 \cdot s^{-1}$, the characteristic time for diffusion of ^{133}Xe up the 200 m separating the interface and surface in Figure 2.9 is $t_D \approx 3.23\text{E}9$ s or 102.3 years! This is much too long of a window for atmospheric monitoring.

2.3.2 Gas Flow in a homogeneous medium

Consider now a simple model of vertical transport of a contaminant in a homogeneous single-porosity medium, driven by atmospheric pumping. The scenario is depicted in Figure 2.10. The flow through this medium is determined by the same parabolic partial differential equation as the diffusion scenario

$$\frac{\partial p}{\partial t} = \alpha \frac{\partial^2 p}{\partial x^2} \tag{2.9}$$

where

$$\alpha = \frac{k p_0}{\mu \phi} \tag{2.10}$$

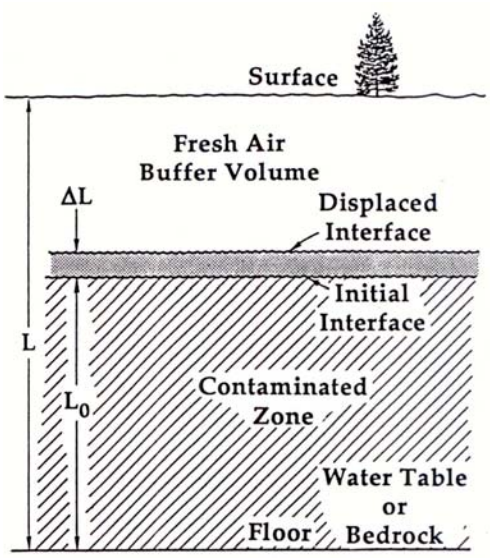

Figure 2.10 Depiction of transport in a homogenous medium by differential volumetric displacement, from Nilson *et al.* (1991).

is known as the bulk pneumatic diffusivity and p_0 is the mean static pressure in the system (Carslaw, *et al.*, 1962). If the surface pressure varies harmonically about p_0 with period T and maximum amplitude Δp, and the system is bounded from below by a water table then the pressure at a depth x responds according to Equation (2.9), the solution of which is given by

$$\frac{p - p_0}{\Delta p} = \frac{\cosh \lambda \sqrt{i} \left(1 - \frac{x}{L}\right)}{\cosh \lambda \sqrt{i}} e^{i\omega t} \tag{2.11}$$

where $\lambda = L\sqrt{\omega / \alpha}$ and $\omega = 2\pi / T$ (Carslaw *et al.*, 1962). If the average static pressure p_0 is taken to be 10^5 Pa, the amplitude of the variation $\Delta p = 2/30\, p_0$, the period T = 200 hours, and the depth to the floor L = 500 m, then using Eq. (2.11) to model the pressure response within the top ten meters of the system yields Figure 2.11.

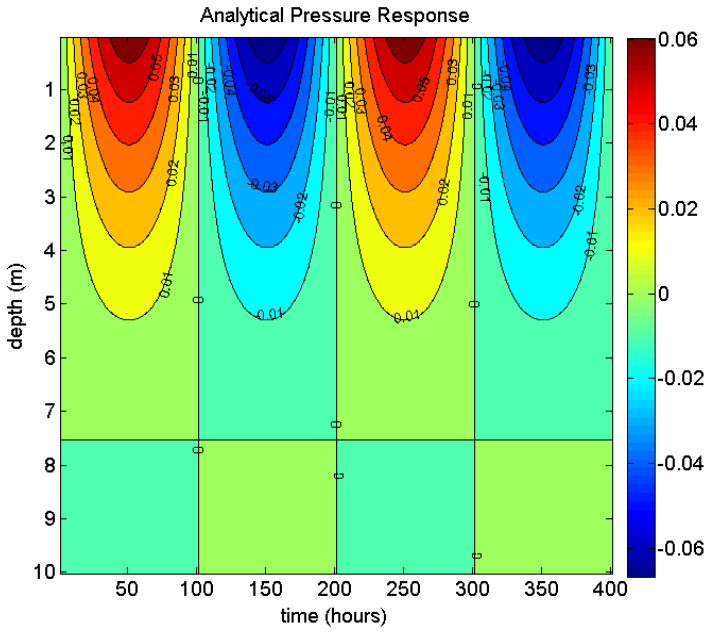

Figure 2.11 The analytical pressure response within the first 10 meters below the surface; given as a fraction of the deviation from the mean static pressure.

Being able to model the underground pressure response to variations in the surface pressure is an important component to the UTEX model. For now, however, assume as a theoretical upper bound that the diffusivity of the porous medium is large enough that the air pressure within the entire system very closely follows any variations at the surface. For isothermal, sinusoidal variations in surface pressure, a piston-like response results in which there is a differential volumetric displacement of the concentration front, as illustrated in Figure 2.10. If L_0 is the depth of contaminant beneath the surface, and A the lateral area of the system, then an isothermal change in pressure $\Delta p/p_0$ results in an incremental shift in volume $\Delta V/V_0$, where $V_0 = \phi A L_0$ and accordingly $\Delta V = \phi A \Delta L$. As a result, the differential displacement in concentration front due to an isothermal shift in pressure can be estimated by

$$\frac{\Delta L}{L_0} = \frac{\Delta p}{p_0}. \tag{2.12}$$

A value of $\Delta p = 2/30 p_0$ as utilized above in Figure 2.11 represents an upper bound variation in surface pressure. Even with this value, for L_0 = 300 m of contaminant, the maximum expected displacement of the concentration front would be

$$\Delta L = \frac{\Delta p}{p_0} L_0 = \frac{2}{30}(300 \text{ m}) \approx 20 \text{ m}.$$

Given that the contaminant lies 200 m below the surface in this example, a shift of 20 m during a deep barometric low will never bring contaminant to the surface. Additionally, by this simple model the front will retreat back down once the pressure rises again.

2.3.3 Gas Flow in a fracture embedded in a homogeneous medium

As a last example before considering the double-porosity model on which the UTEX code is based, consider now the same scenario as described in Section 2.3.2 but with the addition of a narrow fracture embedded within the otherwise homogeneous matrix medium. In contrast to the model without the fracture, consider now that the differential volumetric expansion that results from a barometric low is channeled entirely into the narrow fracture. Assuming for now that there is no further seepage of the contaminant from the fracture into the higher matrix levels, then this addition of the fracture to the system leads essentially to an amplification of the expansion.

If the width of the matrix slab between successive fractures is δ_m and the fracture width is δ_f, then by taking a simple ratio of matrix to fracture volumes, Equation (2.12) now leads to

$$\Delta L = \frac{\Delta p}{p_0} L_0' \frac{\phi_m \delta_m}{\delta_f}. \tag{2.13}$$

Note that the porosity of the fracture, ϕ_f, is taken to be 1, otherwise it too would appear in the denominator. Taking δ_m = 2 m, δ_f = 0.001 m, then the height by which the contaminant can rise within the fracture is

$$\Delta L = \frac{2}{30}(300\text{ m})\frac{(0.1)(1\text{ m})}{(0.001\text{ m})} = 2000\text{ m}\,.$$

Even much more modest pressure variations of 1/100 p_0 would be enough to bring the contaminant up the 200 m to the surface in a single low period within this model.

2.4 DOUBLE-POROSITY MODEL

As a basis for vertical transport of subsurface contaminant implemented in UTEX, the double-porosity model is a 2D model that is locally 1D and builds upon lessons learned from the simpler models described previously. By *double-porosity* and *1D* it is meant that the model considers gas flow both horizontally in the bulk matrix as well as gas flow vertically within the fractures as driven by pressure responses due to varying surface pressure.

In this section, an analytical outline of the double-porosity model is presented as a foundation for the numerical treatment that it will receive in the next chapter. Beyond facilitating an understanding of the numerical approach, this analytical theory also provides an upper bound estimate of the amount of the outflow possible with barometric pumping as the driving force. A large amount of the following is derived from the work of Nilson *et al.* (1991).

2.4.1 Overview of the model

Figure 2.12 depicts the scenario as well as the major parameters that influence the double-porosity model. The model considers homogeneous slabs of bulk matrix media, porosity ϕ_m and permeability k_m, embedded with vertical fractures of width δ_f and separated by an average distance δ_m. The contaminating gas is assumed to be distributed uniformly throughout the matrix medium below the interface line. Above the

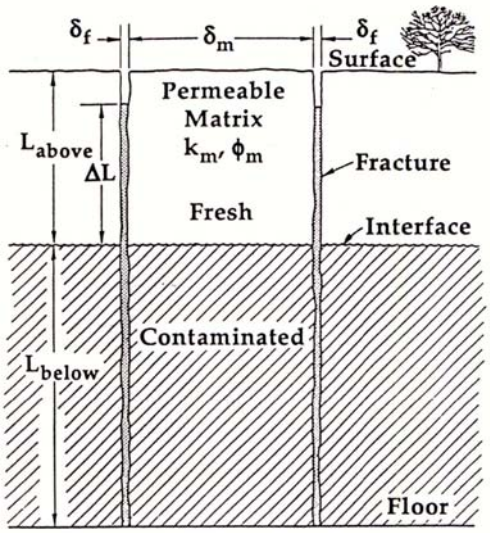

Figure 2.12 Schematic of the double-porosity model, from Nilson & Lie (1990).

contaminated zone lies an assumedly partially-saturated fresh air buffer zone; saturation effects in this model are presumed to be accounted for in the values of ϕ_m and k_m. Unlike the model presented in Section 2.3.3, seepage from the fractures into this buffer region is assumed with the effect being that gas moving upwards along a fracture gets filtered, thus trapping rising contaminant.

The first objective in this model is to modify Equation (2.11) to determine the pressure response of this modified matrix plus fracture system, where before only the matrix was considered. From this, a *breathing efficiency* is derived to describe the amount of gas that "breathes" in and out of the system during a single barometric cycle. Next, the actual contaminant transport within the combined fracture-matrix system is analytically determined based on the harmonically varying flow of fluid induced by the calculated pressure response. As contaminant rises (and falls) within the fractures, seepage into the buffer region results in a generally upward migration of the contaminant front with each cycle. From this a *diffusion-exchange efficiency* is derived to quantify the

fraction of gas that flows out. After a number of barometric cycles, a quasi-steady state is established in which the maximum contaminant outflow per cycle is estimated by the overall transport efficiency, a combination of the breathing efficiency and the diffusion-exchange efficiency.

2.4.2 Pressure response of the fracture-matrix system

Pressure within the fracture and matrix individually follow diffusive equations like Equation (2.9). Because there is an exchange between the two, an additional interaction term must be included. Defining the *x*-direction as decreasing upward along a fracture and the *y*-direction as horizontal into the matrix, the flow of gas within the system is governed by two coupled partial differential equations

$$\begin{aligned} \frac{\partial p}{\partial t} &= \alpha_f \frac{\partial^2 p}{\partial x^2} + \frac{2\phi_m \alpha_m}{\delta_f} \frac{\partial p}{\partial y} \qquad \text{Fracture} \\ \frac{\partial p}{\partial t} &= \alpha_m \frac{\partial^2 p}{\partial y^2} \qquad\qquad\qquad\quad \text{Matrix} \end{aligned} \quad . \tag{2.14}$$

Parameters α_f and α_m are termed pneumatic diffusivities and relate the speed of pressure waves along the fracture (laminar flow[9]) and within the porous matrix ("Darcian" flow[10]) respectively, defined

$$\alpha_f = \frac{\left(\delta_f\right)^2}{12} \frac{p_0}{\mu} \qquad \text{and} \qquad \alpha_m = \frac{k_m p_0}{\mu \phi_m} . \tag{2.15}$$

For a sinusoidal variation in barometric pressure at the surface, an exact solution to Equation (2.14) can be found through separation of variables to be the real part of

$$\frac{p - p_0}{\Delta p} = \frac{\cosh \lambda_{fm} \sqrt{i} \left(1 - \frac{x}{L}\right)}{\cosh \lambda_{fm} \sqrt{i}} \frac{\cosh \lambda_m \sqrt{i} \left(1 - \frac{2y}{\delta_m}\right)}{\cosh \lambda_m \sqrt{i}} e^{i\omega t} \tag{2.16}$$

---

[9] Laminar flow can be thought of as smooth flow without obstruction.
[10] Just refers to flow through a porous medium following Darcy's laws.

where $\sqrt{i} = (1+i)/\sqrt{2}$ (Nilson *et al.*, 1991). A derivation of this solution is also included in Appendix C.1 concerning pressure response verification of the UTEX model. The parameters λ_m, λ_f, and λ_{fm} are so-called Fourier numbers defined according to

$$\lambda_m = \frac{\delta_m}{2}\sqrt{\frac{\omega}{\alpha_m}} \qquad \text{and} \qquad \lambda_f = L\sqrt{\frac{\omega}{\alpha_f}} \tag{2.17}$$

$$\lambda_{fm} = \lambda_f \left(1 + \frac{\phi_m \delta_m}{\delta_f} \frac{\tanh \lambda_m \sqrt{i}}{\lambda_m \sqrt{i}}\right)^{1/2} \tag{2.18}$$

where L is the total depth from the surface to the impermeable floor.

If the velocity u within the fracture at the surface is given by

$$u = -\frac{(\delta_f)^2}{12\mu}\frac{\partial p}{\partial x} = \frac{(\delta_f)^2}{12\mu}\frac{\Delta p}{L}\lambda_{fm}\sqrt{i}\tanh\left(\lambda_{fm}\sqrt{i}\right)e^{i\omega t} \tag{2.19}$$

then the outflow volume of gas that leaves and then reenters the system at the surface each cycle can be calculated from

$$\Delta V = \int_0^{T/2} u\,dt = \frac{\Delta p}{p_0} L\delta_f \left|\frac{\lambda_{fm}^2}{\lambda_f^2}\frac{\tanh \lambda_{fm}\sqrt{i}}{\lambda_{fm}\sqrt{i}}\right|. \tag{2.20}$$

This result, ΔV, represents the *actual* volumetric outflow in a given cycle. A theoretical *maximum* volumetric outflow is obtained if the pressure response, instead of given by Equation (2.16), is assumed everywhere to closely follow the barometric variations at the surface. In this upper bound case

$$\Delta V_{\max} = \frac{\Delta p}{p_0} V_0 = \frac{\Delta p}{p_0} L\left(\delta_f + \phi_m \delta_m\right). \tag{2.21}$$

From Eqs. (2.20) and (2.21), the breathing efficiency is defined as the ratio of the actual versus the maximum volumetric outflow per cycle

$$\eta_B = \frac{\Delta V}{\Delta V_{\max}} = \frac{\delta_f}{\delta_f + \phi_m \delta_m}\left|\frac{\lambda_{fm}^2}{\lambda_f^2}\frac{\tanh \lambda_{fm}\sqrt{i}}{\lambda_{fm}\sqrt{i}}\right|. \tag{2.22}$$

Figure 2.13 shows values of the breathing efficiency η_B versus the fracture spacing δ_m for several values of $\alpha_{fm} \equiv L^2\omega/\lambda_{fm}^2$. Note that a sharp knee occurs in each

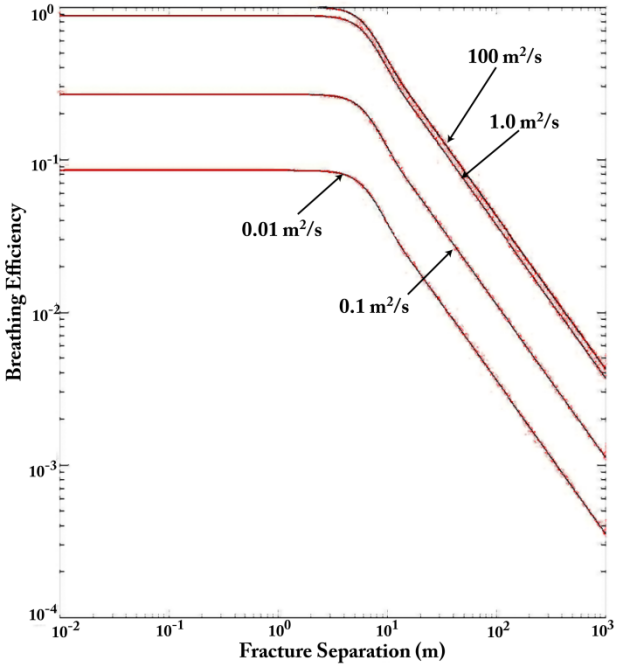

Figure 2.13 Breathing efficiency versus fracture spacing for several values of α_{fm}.

case at around δ_m = 10 m, corresponding roughly to half the *penetration depth* of each pressure wave. For spacing greater than the penetration depth, the efficiency falls off quickly because the inner regions within the matrix slabs are not being reached.

2.4.3 Diffusion exchange efficiency

Having derived the efficiency with which barometric pumping leads to the outflow of gas from the system during each cycle, consider now the actual transport of a small quantity of contaminant gas up through a fracture. As contaminant rises (or falls) within the fracture, diffusion drives contaminant through the permeable fracture walls and into the fresh air-filled regions within the buffer region of the matrix. This creates a filtering effect, and ultimately slows down the initial rise of contaminant within the

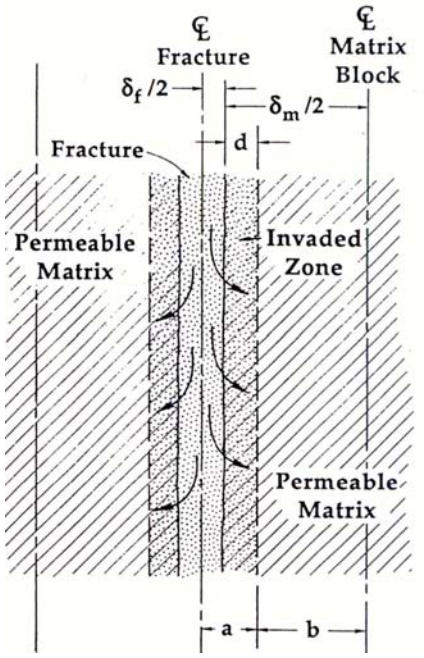

Figure 2.14 Illustration of diffusion exchange between fracture and matrix, from Nilson *et al.* (1991).

fractures as the concentration gradient extends upward. Figure 2.14 depicts a fracture embedded within a permeable matrix, as well as the diffusion effects.

The diffusion exchange model of transport depicted in Figure 2.14 is governed by another pair of differential equations not too different from those in the previous section

$$\begin{aligned} \phi_c \frac{\partial C}{\partial t} + u\frac{\partial C}{\partial x} &= \phi_w \frac{D}{a}\frac{\partial C}{\partial y} && \text{Fracture} \\ \phi_w \frac{\partial C}{\partial t} &= \phi_w D \frac{\partial^2 C}{\partial y^2} && \text{Matrix} \end{aligned} \quad . \tag{2.23}$$

The first equation governs advection along the fracture (left side of the equation) as well as diffusion into the matrix (inhomogeneous term on the right). The porosities ϕ_c and ϕ_w describe the porous material filling the channel of half-width a and the wall of thickness b respectively. The depth to which diffusion occurs in the matrix is given by d. Because

the channel consists of both fracture and matrix material, the channel porosity is taken as a volume-weighted average

$$\phi_c = \frac{\phi_m d + (\delta_f/2)\phi_f}{d + \delta_f/2}.$$

The wall porosity ϕ_w is simply the matrix porosity ϕ_m. The second equation in Equation (2.23) describes simple diffusion within the matrix. Note that the diffusivity here, *D,* is assumed to be the *effective* diffusivity (Equation (2.3) given that diffusion is taking place within a porous medium.

The solution to the coupled differential equations in Equation (2.23) is far from trivial. If the simplifying assumption that the longitudinal velocity (along the fracture) is harmonic, $u = \mathrm{Re}(u_0 \exp(i\omega t))$ and no bulk motion occurs in the transverse direction, then the problem becomes analogous to the heat transfer problem investigated by Chatwin (1975) and Kurzweg (1985). Rather than look for a general solution, consider a particular solution of the form

$$C = \gamma\left(x + bg\left(y^*\right)e^{i\omega t}\right) \tag{2.24}$$

wherein $y^* \equiv y/b$, and $\gamma \equiv dC/dx$ represents the gradient of the time mean concentration along the fracture. If the gradient along the fracture is assumed to be constant, i.e. $\gamma = C_B / L$ where C_B is the time-averaged concentration at the bottom, then upon substituting Equation (2.24) back into the matrix portion of Equation (2.23) the following ordinary differential equation for $g(y^*)$ is found

$$g'' - i\frac{b^2\omega}{D}g = 0. \tag{2.25}$$

This has the solution

$$g\left(y^*\right) = A\cosh\left(\sqrt{i}W\left(1 - y^*\right)\right) \tag{2.26}$$

where $W = b\sqrt{\omega / D}$ is known as the Womersley number. Lastly, substitution of Equations (2.24) and (2.26) into the fracture portion of Equation (2.23) and solving for *A* yields

$$g = \frac{iu_0}{b\omega\phi_c}\left(\frac{W\sqrt{i}}{W\sqrt{i} + \beta\tanh W\sqrt{i}}\right)\frac{\cosh W\sqrt{i}\left(1-y^*\right)}{\cosh W\sqrt{i}} \tag{2.27}$$

where $\beta = b\phi_w / a\phi_c$ is simply the ratio of wall volume to channel volume. With *g* now determined, plugging Equation (2.27) back into Equation (2.24) gives the final expression for the concentration along the fracture at a given time.

The diffusion-exchange efficiency is found by determining the ratio of actual mass outflow in one cycle to the maximum possible outflow. Recall that the velocity of gas was assumed to be harmonic along the fracture, $u = \mathrm{Re}(u_0 \exp(i\omega t))$. Using this, the *actual* mass of contaminant exiting the system in one cycle (period *T*) is given by the time-integral of the flux of contaminant passing through the upper surface at $x = 0$.

$$\begin{aligned}\Delta M &= -\int_0^T \mathrm{Re}(u)\,\mathrm{Re}(C)dt \\ &= -\frac{\gamma u_0^2 T^2}{4\pi\phi_C}\mathrm{Re}\left(\frac{iW\sqrt{i}}{W\sqrt{i} + \beta\tanh W\sqrt{i}}\right).\end{aligned} \tag{2.28}$$

The *maximum* outflow is given by the time-averaged concentration C_B multiplied by the gross outflow per cycle (i.e. no diffusion into the matrix) given by

$$\Delta V = -\int_{T/2}^{T}\mathrm{Re}(u)dt = \frac{u_0 T}{\pi} \tag{2.29}$$

so that

$$\begin{aligned}\eta_D &\equiv \frac{\Delta M}{C_B \Delta V} \\ &= -\frac{\pi}{4}\mathrm{Re}\left(\frac{iW\sqrt{i}}{W\sqrt{i} + \beta\tanh W\sqrt{i}}\right).\end{aligned} \tag{2.30}$$

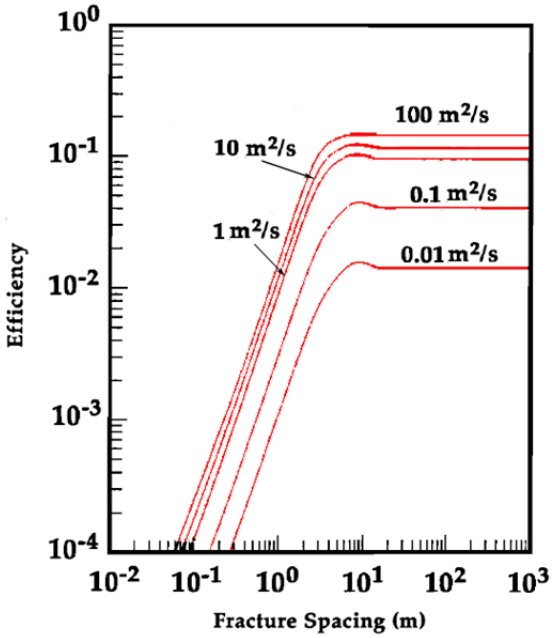

Figure 2.15 Diffusion-exchange efficiency versus fracture spacing for several values of α_{fm}

Figure 2.15 shows a graph of the diffusion-exchange efficiency versus fracture spacing for various values of the pneumatic diffusivity, α_{fm}. Similar to the case of the breathing efficiency, beyond a fracture spacing of 10 m there is no added benefit to the diffusion-exchange efficiency because the pressure wave can only penetrate so far into the matrix.

With both the breathing efficiency η_B and the diffusion-exchange efficiency η_D defined in Equations (2.22) and (2.30), the overall transport efficiency is just

$$\eta = \eta_B \eta_D$$

$$= \left(\frac{\Delta V}{\Delta V_{\max}} \right) \left(\frac{\Delta M}{C_B \Delta V} \right) = \frac{\Delta M}{C_B \Delta V_{\max}} \tag{2.31}$$

Figure 2.16 shows graphs of the overall efficiency versus fracture spacing for several values of α_{fm} using a xenon-approximate value of $D = 3\text{E-}6\ \text{m}^2/\text{s}$. As depicted in the figure, for high pneumatic diffusivities, a maximum overall efficiency of 10% is

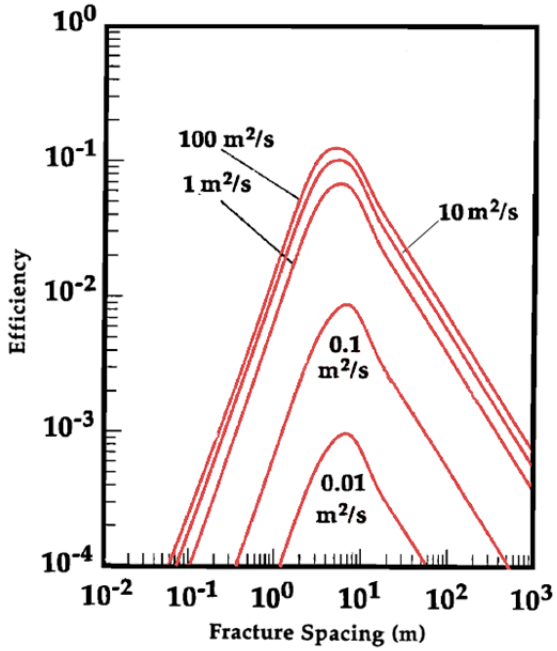

Figure 2.16 Overall efficiency versus fracture spacing for several values of α_{fm}.

theoretically possible. If the latter part of Equation (2.31) is rearranged and the approximation that the initial mass of contaminant is $M_0 = C_B V_0 / 2$ then the fraction of contaminant exiting per cycle can be roughly estimated

$$\frac{\Delta M}{M_0} = 2\eta \frac{\Delta p}{p_0}. \tag{2.32}$$

Taking a maximum overall efficiency of 10% as well as a maximum pressure variation of the order 10%, then Equation (2.32) suggests a fractional outflow of about 1% per barometric cycle is theoretically possible after substantial buildup of the concentration front.

Clearly, as a rigorous mathematical evaluation of a real scenario, Equation (2.32) and perhaps even the idea of an overall efficiency are lacking. However, as a back-of-the-envelope approximation they serve a great deal to suggest an upper bound theoretical limit for the effectiveness of barometric pumping as a mechanism for subsurface

transport. Additionally, within the analytical framework presented here, the governing equations for a numerical vertical transport model have been laid out.

Chapter 3. UTEX model

In the preceding chapter, the governing equations for isothermal gas transport in the double-porosity model have largely been laid out. Though perhaps implied previously but not exactly stated explicitly, the applicability of the double-porosity model is founded on five broad assumptions regarding the system of study (Tang *et al.*, 1981):

1. Fracture width is assumed to be much less than the length of the fracture, $\delta_f \ll L$.
2. Complete mixing across the fracture width is assumed.
3. The matrix permeability, $k_m << 1$.
4. Fracture transport is assumed to be much faster than matrix transport.
5. Isothermal transport is assumed; heat transfer could also apply

These assumptions combined facilitate the simplification of the model as locally 1D, in that, the two-dimensional system reduces to two coupled, orthogonal 1D systems: vertical transport in the fracture and horizontal transport in the adjacent matrix.

A flow diagram of the major subroutines within the UTEX code is shown in Figure 3.1. An outline for the numerical processes is as follows. At the beginning of a given time step, the pressure response throughout the system due to variation of the surface pressure is calculated. From that, resulting fluid velocities can be estimated. Next, the concentrations of contaminant within the system can be determined through the coupled tracer transport equations, which assume diffusion and advection along the fracture, orthogonal transfer of mass between the fracture and surrounding matrix blocks, and finally diffusion and advection within the adjacent horizontal matrix blocks. Radioactive decay and source ingrowth will as well be accounted for throughout the

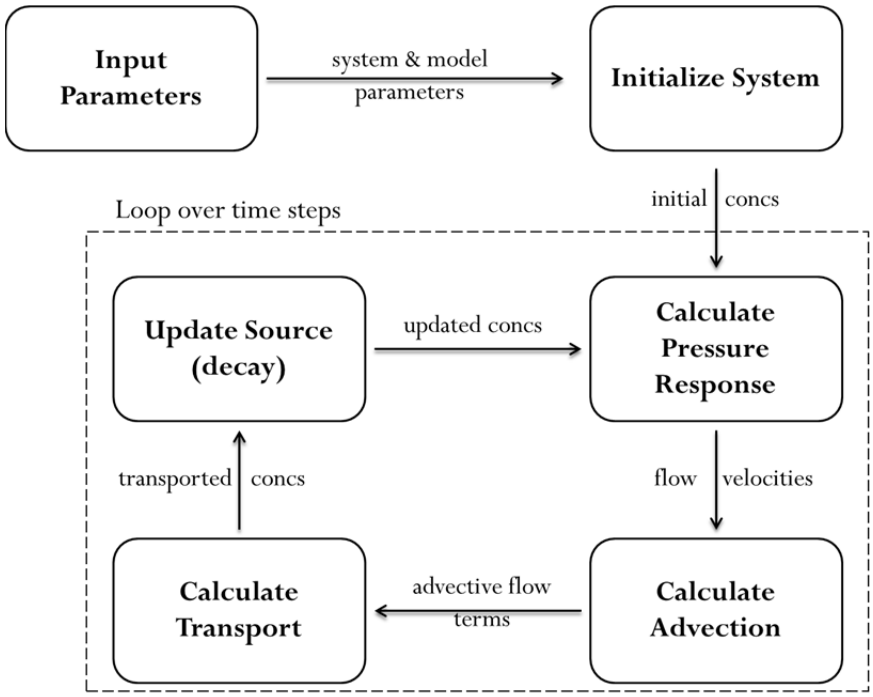

Figure 3.1 Flow diagram of the modularized UTEX code.

system. Note that because this work is concerned primarily with the transport of the noble gas xenon, sorption effects are not considered in the model.

Lastly, the introduction of numerical approximation schemes for differential operators in advective transport equations can lead to effects of so-called numerical diffusion. These effects are due largely from the repetitive switching of the periodic "upwind direction" in the calculation. These errors are most dangerous as they accumulate over many cycles. To combat the potential erroneous effects of numerical diffusion, the filtering remedy and methodology (FRAM) originally suggested in a study by Chapman (1981) and extended in Chapman and Waisman (1985) is to be employed.

3.1 UTEX SYSTEM DEFINITION

An illustration of the system as it is modeled is given in Figure 3.2. All parameter definitions as utilized in the previous chapter are reused here. Specifically, fractures are assumed to have an average width δ_f and have an air-filled porosity of ϕ_f. Fractures are separated by matrix slabs of thickness δ_m, and are characterized by an air-filled porosity ϕ_m and permeability k_m. Given the symmetry of the system, only one *half-slab* of matrix and fracture is modeled at a time. An $N \times M$ computational mesh is utilized wherein the positive *y*-direction is downwards along the fracture with $i \in [1, N]$ while the positive *x*-direction stretches into the matrix with $j \in [1, M]$.

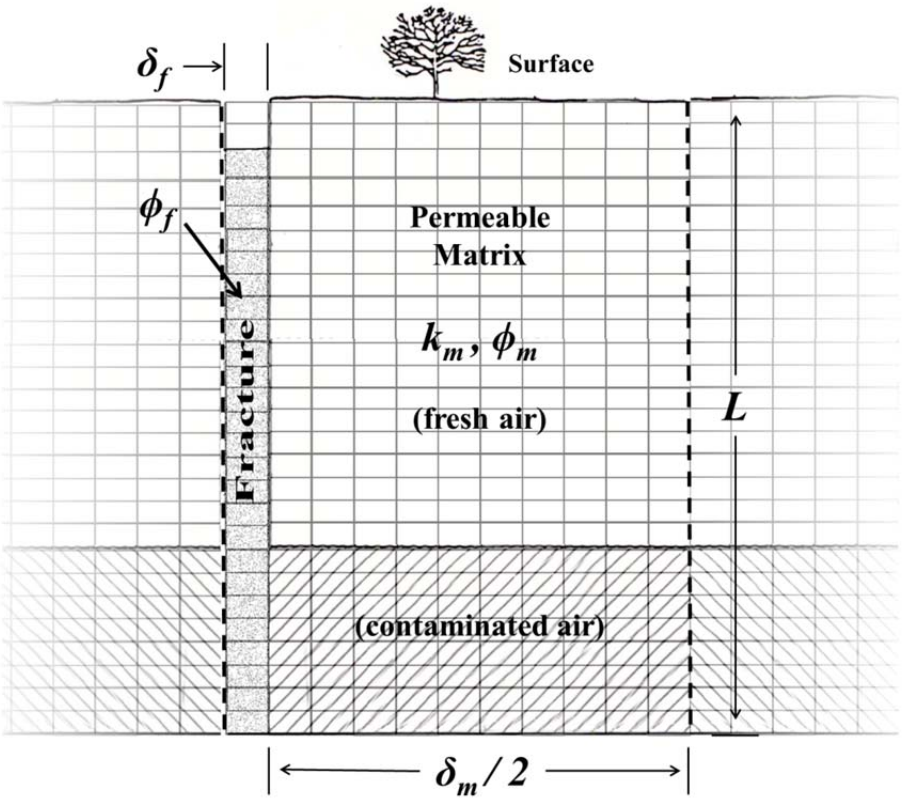

Figure 3.2 Illustration of the double porosity and discretized system model, with relevant system parameters noted. The dashed lines identify the unit cell concept within the larger extended system.

Throughout this chapter, subscripts i and j will refer to y and x cell indices respectively, while superscripts n will denote time steps. Cell widths as illustrated in Figure 3.2 will be defined by Δx and Δy and time step duration will be denoted Δt.

3.2 GOVERNING EQUATIONS

3.2.1 Pressure response

Transport in the UTEX model is assumed to take place by both gas diffusion and bulk advective flow. The latter is driven by pressure gradients that arise in the system due to the variation of atmospheric pressure at the top of the system (surface). Specification of the surface pressure as a function of time is thus a necessary input to the model and UTEX allows for a completely general specification of the surface pressure as a function of time. Linear interpolation is used to estimate the surface pressure in cases where the simulation time steps are shorter than the pressure history resolution. When the pressure at the top of the system changes in time, the resultant change in pressure throughout the rest of the system is neither homogeneous nor instantaneous. This *pressure response*, assuming the double-porosity system model, is indicative of the isothermal flow of an ideal gas and is governed by the coupled pore-fluid diffusion equations:

$$\frac{\partial p(x,y)}{\partial t} = \frac{\partial}{\partial x}\left(\alpha_m \frac{\partial p(x,y)}{\partial x}\right) \tag{3.1}$$

$$\frac{\partial p(x,y)}{\partial t} = \frac{\partial}{\partial y}\left(\alpha_f \frac{\partial p(x,y)}{\partial y}\right) - \underbrace{\frac{\Gamma}{A}\frac{\phi_m}{\phi_f}\int_0^{\delta_m/2} \frac{\partial p(x,y)}{\partial t}\,dx}_{\text{Fracture}-\text{Matrix Interaction Term}} \tag{3.2}$$

wherein A is defined as the cross-sectional area of the fracture and Γ is the fracture-matrix contact area per unit length, which can be assumed for simplicity to satisfy $\Gamma = A$. Equation (3.1) applies horizontally along a row of bulk matrix medium and Equation

(3.2) applies vertically within the fracture column. The pore-fluid diffusivities within the fracture and matrix respectively, α_f and α_m are given by

$$\alpha_f = \frac{(\delta_f)^2}{12}\frac{p_0}{\mu\varphi_f} \quad \text{and} \quad \alpha_f = \frac{k_m p_0}{\mu\varphi_m} \tag{3.3}$$

where again ϕ_f and ϕ_m are the fracture and bulk matrix media porosities respectively, k_m is the bulk permeability, μ is the dynamic viscosity of air, and δ_m is the average separation of fractures.

To facilitate the simplification of Equations (3.1) and (3.2), the diffusivities of Equation (3.3) are treated as constants by taking $p(x,y) \approx p_0$, the average pressure in the system, in the numerators, which is justified because even large variations in atmospheric pressure constitute only small fractional changes from mean pressures. Note that for non-homogeneous geologic models in which layers are present, Equation (3.3) could not be treated as constants because the porosities and bulk permeability would then be functions of depth within the system, however, such a change would not alter the method of solution, only the resulting coefficients that go into the calculation. On the system mesh defined in Figure 3.2, Equations (3.1) - (3.3) define the first coupled system of equations that must be solved by the UTEX model.

3.2.2 Mass transport

The coupled equations describing mass transport in the system are very similar to those describing the pressure response, except with the addition of a few terms. First, an additional term to account for advection resulting from the variation in pressure response throughout the system is needed. Second, a spatially-dependent source term is needed to account for a generalized source. Lastly, radioactive decay of transported nuclides can be implicitly accounted for in the mass balance with the decay constant λ. Thus the position

dependent concentration of the i^{th} radioxenon isotope is determined by solution of the following coupled system of equations:

$$\phi_m \frac{\partial C(x,y)_i}{\partial t} + \frac{\partial}{\partial x}\left(C(x,y)_i v(x,y)\right) = \frac{\partial}{\partial x}\left(\phi_m D_i \frac{\partial C(x,y)_i}{\partial x}\right) - \phi_m \lambda_i C(x,y)_i + s(x,y)_i \tag{3.4}$$

$$\begin{aligned}\phi_f \frac{\partial C(x,y)_i}{\partial t} + \frac{\partial}{\partial y}\left(C(x,y)_i u(y)\right) = \frac{\partial}{\partial y}\left(\phi_f D_i \frac{\partial C(x,y)_i}{\partial y}\right) - \phi_f \lambda_i C(x,y)_i + s(x,y)_i \\ - \int_0^{\delta_m/2} \phi_m \frac{\partial C(x,y)_i}{\partial t}\, dx\end{aligned} \tag{3.5}$$

Equation (3.4) describes the horizontal transport of gas in the bulk matrix medium at a given height *y* corresponding to a horizontal row in Figure 3.2, and Equation (3.5) describes the vertical transport along the fracture column where again *x = 0*. These equations take into account diffusion and advection as well as the radioactive decay of the isotopes and a general time-dependent source term *s(x,y)* (Ci/cm^{2}s). The diffusion coefficients D_i(cm^2/s) appearing in Equations (3.4) and (3.5) are tortuosity-weighted. The flow velocities *u(y)* and *v(x,y)* (cm/s) are determined by the differential pressures that arise in the system due to variations in atmospheric pressure according to

$$u = \frac{\left(\delta_f\right)^2}{12\mu}\frac{\partial p}{\partial y} \qquad \text{and} \qquad v = -\frac{k_m}{\mu}\frac{\partial p}{\partial x}. \tag{3.6}$$

3.2.3 Discretization scheme

To be clear, for each horizontal row of Figure 3.2 whose depth is defined by a constant *y* there is an associated Equation (3.1) and (3.4) for the pressure response and gas transport respectively in that row during each time step. There is also an Equation (3.2) and (3.5) for the pressure response and gas transport along the single vertical fracture; these are coupled to the systems of equations describing the horizontal bulk matrix rows through the "fracture-matrix interaction" integrals appearing in those equations.

Pressure Response

Solution of pressure response and mass transport equations for each time step can be made by Gaussian elimination with periodic boundary conditions at the interior of the matrix and a closed bottom boundary. To account for time (and other first) derivatives, a first-order backwards difference approach is employed, meaning that

$$\frac{\partial p}{\partial t} \longrightarrow \frac{p_{ij}^{n+1} - p_{ij}^{n}}{\Delta t} \tag{3.7}$$

and second-order diffusive operators are estimated by second-order centered differencing, for example

$$\frac{\partial^2 p}{\partial x^2} \longrightarrow \frac{p_{i-1j}^{n} - 2p_{ij}^{n} + 2p_{i+1j}^{n}}{\Delta x^2}. \tag{3.8}$$

Of the two governing equations for the pressure response, Equation (3.1) can be represented in a fully implicit discretized form. Application of the differencing schemes above yields

$$\frac{p_{ij}^{n+1} - p_{ij}^{n}}{\Delta t} = \frac{\alpha_m}{\Delta x^2}\left(p_{ij-1}^{n+1} - 2p_{ij}^{n+1} + p_{ij+1}^{n+1}\right). \tag{3.9}$$

Equation (3.9) can then be rearranged to reveal the following tridiagonal system of equations

$$a_j p_{ij-1}^{n+1} + b_j p_{ij}^{n+1} + c_j p_{ij+1}^{n+1} = f_{ij} \tag{3.10}$$

for any horizontal line of fixed *i* where

$$\begin{aligned} a_j &= -\alpha_m \Delta t / \Delta x^2 \\ b_j &= 1 + 2\alpha_m \Delta t / \Delta x^2 \\ c_j &= a_j \\ f_{ij} &= p_{ij}^{n} \end{aligned} \tag{3.11}$$

The *i* and *j* subscripts appearing here denote the vertical and horizontal mesh indices respectively while the *n* and *n+1* superscripts denote the previous and current time steps respectively.

Equation (3.2) for the pressure response down the vertical fracture simplifies similarly except there is an additional interaction integral term to discretize, which for now will just be denoted I_i :

$$A_i p_{i-11}^{n+1} + B_i p_{i1}^{n+1} + C_i p_{i+11}^{n+1} + I_i = F_{i1} \tag{3.12}$$

$$A_i = -\alpha_f \frac{\Delta t}{\Delta y^2}$$

$$B_i = 1 + 2\alpha_f \frac{\Delta t}{\Delta y^2} \tag{3.13}$$

$$C_i = A_i$$

$$F_{i1} = p_{i1}^n$$

Equations (3.10) and (3.12), aside from the interaction term in the latter, represent familiar systems of tri-diagonal equations, for which a number of solution schemes exist. With the pressure response throughout the system determined, the resulting flow velocities can be determined as follows

$$\begin{aligned} u_i^{n+1} &= \frac{\left(\delta_f\right)^2}{12\mu} \frac{p_{i+11}^{n+1} - p_{i-11}^{n+1}}{2\Delta y} && i \in [2, N-1] \\ v_{ij}^{n+1} &= -\frac{k_m}{\mu} \frac{p_{ij+1}^{n+1} - p_{ij-1}^{n+1}}{2\Delta x} && i, j \in [2, N-1] \times [2, M-1] \end{aligned} \tag{3.14}$$

Gas Transport

The discretized equations for mass transport within the UTEX are entirely analogous to those of the pressure response with one important exception. Equations (3.4) and (3.5) include an additional advection term that must be handled somewhat carefully

due to the numerical schemes being considered. A straightforward discretization of these two terms using the scheme of (3.7) is not difficult, but due to the random and rapid periodic nature of the driving surface pressure, care must be taken in how the advection terms are calculated. These concerns are addressed in the mesh reduction and benchmarking portion of this chapter. The approach adopted in the early UTEX model followed that suggested in Nilson and Lie (1990) based on the FRAM filtering scheme of Milt Chapman (1981). An overview of how this scheme was previously applied is detailed in the Appendix B.

Discretization of the transport equations (3.4) and (3.5) is now outlined (J.D. Lowrey & Osborne, 2011). These equations are rewritten below for easy reference. Along the matrix:

$$\phi_m \frac{\partial C}{\partial t} = -\frac{\partial}{\partial x}(Cv) + \frac{\partial}{\partial x}\left(\phi_m D_m \frac{\partial C}{\partial x}\right) - \phi_m \lambda C$$

and down the fracture:

$$\phi_f \frac{\partial C}{\partial t} = -\frac{\partial}{\partial y}(Cu) - \int \phi_m \frac{\partial C}{\partial t} dx + \frac{\partial}{\partial y}\left(\phi_f D_f \frac{\partial C}{\partial y}\right) - \phi_f \lambda C$$

Making substitutions for discretization, along the matrix this becomes

$$\phi_m \frac{C_{ij} - C_{ij}^n}{\Delta t} = \phi_m D_m \frac{C_{ij+1} - 2C_{ij} + C_{ij-1}}{\Delta x^2} - v \frac{C_{ij+1} - C_{ij-1}}{2\Delta x} - C_{ij} \frac{v_{ij+1} - v_{ij-1}}{2\Delta x} - \phi_m \lambda C_{ij}$$

and down the fracture

$$\phi_f \frac{C_{ij} - C_{ij}^n}{\Delta t} = \phi_f D_f \frac{C_{i+1j} - 2C_{ij} + C_{i-1j}}{\Delta y^2} - u_{ij} \frac{C_{i+1j} - C_{i-1j}}{2\Delta y} - C_{ij} \frac{u_{i+1} - u_{i-1}}{2\Delta y}$$
$$- \phi_f \lambda C_{ij} - \phi_m \sum \frac{C_{ij} - C_{ij}^n}{\Delta t} \Delta x$$

Matrix equations

Since the matrix equation is simpler as it does not include an interaction term, it is considered first:

$$C_{ij} - C_{ij}^n = \left\{C_{ij+1} - 2C_{ij} + C_{ij-1}\right\}\frac{D_m \Delta t}{\Delta x^2} - \left\{C_{ij+1} - C_{ij-1}\right\}\frac{v\Delta t}{\phi_m 2\Delta x} - C_{ij}\left(v_{ij+1} - v_{ij-1}\right)\frac{\Delta t}{\phi_m 2\Delta x}$$
$$- \lambda C_{ij}\Delta t$$
$$C_{ij+1}\left\{\frac{v\Delta t}{\phi_m 2\Delta x} - \frac{D_m \Delta t}{\Delta x^2}\right\} + C_{ij}\left\{1 + 2D_m\frac{\Delta t}{\Delta x^2} + \left(v_{ij+1} - v_{ij-1}\right)\frac{\Delta t}{\phi_m 2\Delta x} + \lambda\Delta t\right\}$$
$$+ C_{ij-1}\left\{-\frac{v\Delta t}{\phi_m 2\Delta x} - \frac{D_m \Delta t}{\Delta x^2}\right\} = C_{ij}^n$$

This gives the tridiagonal matrix coefficients:

$$E = \frac{v\Delta t}{\phi_m 2\Delta x} - \frac{D_m \Delta t}{\Delta x^2}$$
$$B_{ij} = 1 + 2D_m\frac{\Delta t}{\Delta x^2} + \left(v_{ij+1} - v_{ij-1}\right)\frac{\Delta t}{\phi_m 2\Delta x} + \lambda\Delta t \qquad (3.15)$$
$$A = -\frac{v\Delta t}{\phi_m 2\Delta x} - \frac{D_m \Delta t}{\Delta x^2}$$

Fracture equations

The situation down the fracture is analogous to the matrix but with the addition of the fracture-matrix interaction term, I_i

$$C_{i1} - C_{i1}^n = \left\{C_{i+1,1} - 2C_{i1} + C_{i-1,1}\right\}\frac{D_f \Delta t}{\Delta y^2} - \left\{C_{i+1,1} - C_{i-1,1}\right\}\frac{u\Delta t}{2\phi_f \Delta y}$$
$$- C_{i1}\left(u_{i+1} - u_{i-1}\right)\frac{\Delta t}{2\phi_f \Delta y} - \lambda C_{i1}\Delta t - \Delta t\Delta x\frac{\phi_m}{\phi_f}\sum_j \frac{C_{ij} - C_{ij}^n}{\Delta t}$$

$$C_{i+1,1}\left\{\frac{u\Delta t}{2\phi_f \Delta y} - \frac{D_f \Delta t}{\Delta y^2}\right\} + C_{i1}\left\{1 + 2\frac{D_f \Delta t}{\Delta y^2} + \left(u_{i+1} - u_{i-1}\right)\frac{\Delta t}{2\phi_f \Delta y} + \lambda\Delta t\right\}$$
$$+ C_{i-1,1j}\left\{-\frac{u\Delta t}{2\phi_f \Delta y} - \frac{D_f \Delta t}{\Delta y^2}\right\} + I_i = C_{i1}^n$$

So the coefficients for the fracture are:

$$
\begin{aligned}
c_i &= \left\{ \frac{u_{ij}\Delta t}{2\phi_f \Delta y} - \frac{D_f \Delta t}{\Delta y^2} \right\} \\
b_i &= \left\{ 1 + 2\frac{D_f \Delta t}{\Delta y^2} + \left(u_{i+1} - u_{i-1}\right)\frac{\Delta t}{2\phi_f \Delta y} + \lambda \Delta t \right\} \\
a_i &= \left\{ -\frac{u_{ij}\Delta t}{2\phi_f \Delta y} - \frac{D_f \Delta t}{\Delta y^2} \right\}
\end{aligned}
\tag{3.16}
$$

Special attention must be paid to the fracture concentrations C(1,1), C(2,1) and C(3,1) because of the boundary. In these cases, advection is neglected. Hence:

$$
\begin{aligned}
c_{[1:3]} &= -\frac{D_f \Delta t}{\Delta y^2} \\
b_{[1:3]} &= 1 + 2\frac{D_f \Delta t}{\Delta y^2} + \lambda \Delta t \\
a_{[1:3]} &= -\frac{D_f \Delta t}{\Delta y^2}
\end{aligned}
\tag{3.17}
$$

and similarly for the bottom of the fracture.

After substitution of matrix concentration equation, the fracture-matrix interaction term can be written:

$$
\begin{aligned}
I_i &= \Delta t \Delta x \frac{\phi_m}{\phi_f} \sum_{j=2} \left[\frac{D_m}{\Delta x^2}\left\{C_{ij+1} - 2C_{ij} + C_{ij-1}\right\} - \frac{u_{ij}}{\phi_m 2\Delta x}\left\{C_{ij+1} - C_{ij-1}\right\} \right. \\
&\qquad \left. - C_{ij}\frac{\left(u_{ij+1} - u_{ij-1}\right)}{\phi_m 2\Delta x} - \lambda C_{ij} \right] \\
I_i &= \Delta t \Delta x \frac{\phi_m}{\phi_f} \sum_{j=2} \left[C_{ij-1}\left\{ \frac{D_m}{\Delta x^2} + \frac{u_{ij}}{\phi_m 2\Delta x} \right\} + C_{ij}\left\{ -\frac{\left(u_{ij+1} - u_{ij-1}\right)}{\phi_m 2\Delta x} - \lambda - \frac{2D_m}{\Delta x^2} \right\} \right. \\
&\qquad \left. + C_{ij+1}\left\{ \frac{D_m}{\Delta x^2} - \frac{u_{ij}}{\phi_m 2\Delta x} \right\} \right]
\end{aligned}
\tag{3.18}
$$

The above equations still include an implicit term accounting for radioactive decay. In the final UTEX model, radioactive decay and source ingrowth are handled explicitly at the end of each time step as depicted in Figure 3.1 and thus is not included from this point forward in the mass balance equations.

3.3 SOLUTION SCHEMES

Equations (3.9) - (3.18) effectively define the pressure response and gas transport within the UTEX modeled system. Initially the UTEX model employed a solution scheme that followed that suggested in Nilson and Lie (1990) known as the Thomas Algorithm (Lowrey, 2011). During the course of code development and benchmarking three different numerical solution methods for solving the above systems of equations were considered and compared: Thomas algorithm (TA) solution, simultaneous matrix (SM) solution, and Newton's method (NM) solution.

The three numerical solution methods detailed in the following sections were applied to both the pressure response and gas transport systems of equation. While these two sets of equations represent separate physical phenomena, they have already been shown to be discretized such that they are mathematically of the same form, differing only in the coefficients and along boundaries. For purposes of brevity and to avoid unneeded redundancy, the focus of the solution comparisons of this section is on solutions to the pressure response. Solutions of the transport equations follow the same procedures but with modified coefficients.

3.3.1 Thomas Algorithm (TA)

The Thomas Algorithm, or Tri-Diagonal Matrix Algorithm, is a simplified Gaussian elimination approach that makes use of successive forward and then backward sweeps through the system to determine a unique solution from the boundary conditions. In its application to the UTEX model systems of equations, it represents an arguably less-sophisticated approach than the next two methods to follow, but is straightforward to implement and has previously been used with the double porosity geological model (Nilson & Lie, 1990).

The Thomas Algorithm applied to (3.10) for the horizontal rows offers a recursive solution

$$p_{ij}^{n+1} = e_{ij}^{n+1} p_{ij-1}^{n+1} + d_{ij}^{n+1} \tag{3.19}$$

with modified coefficients given by

$$\begin{aligned} e_{ij}^{n+1} &= -\frac{a_j}{b_j + c_j e_{ij+1}^{n+1}} \\ d_{ij}^{n+1} &= \frac{f_{ij} - c_j d_{ij+1}^{n+1}}{b_j + c_j e_{ij+1}^{n+1}} \end{aligned} \tag{3.20}$$

subject to the inner boundary condition $e_{iM}^{n+1} = 1$ and $d_{iM}^{n+1} = 0$ where $j = M$ is the innermost matrix point. This requires knowledge of the pressure in the adjacent fracture (the other boundary condition), p_{i1}. To facilitate coupling to the fracture, it is convenient to write each p_{ij} in terms of the adjacent fracture value p_{i1} so that for a fixed row i the pressure anywhere in the matrix row can be written

$$p_{ij}^{n+1} = g_{ij}^{n+1} p_{i1}^{n+1} + h_{ij}^{n+1} \tag{3.21}$$

where again the coefficients are given recursively as

$$\begin{aligned} g_{ij}^{n+1} &= g_{ij-1}^{n+1} e_{ij}^{n+1} \\ h_{ij}^{n+1} &= h_{ij-1}^{n+1} e_{ij}^{n+1} + d_{ij}^{n+1} \end{aligned} \tag{3.22}$$

with $g_{i1}^{n+1} = 1$ and $h_{i1}^{n+1} = 0$. Equations (3.19) - (3.22) together form a recursive solution to Equation (3.10) for the pressure in the rows, provided a solution to fracture pressures can be found.

Solution for the fracture pressure response, Equation (3.12) is set up in nearly the exact same way, except that the additional interaction term that provides fracture-matrix coupling must be dealt with. In fact, Equations (3.21) and (3.20) allow this to be done easily, starting with the discretized form of the interaction integral appearing in Equation (3.2):

$$\phi_m \sum_{j=1}^{M} \frac{p_{ij}^{n+1} - p_{ij}^{n}}{\Delta t} \Delta x = \phi_m \frac{\Delta x}{\Delta t} \sum_{j=1}^{M} \left[\left(g_{ij}^{n+1} p_{i1}^{n+1} + h_{ij}^{n+1} \right) - \left(g_{ij}^{n} p_{i1}^{n} + h_{ij}^{n} \right) \right]$$
$$= \left(\phi_m \frac{\Delta x}{\Delta t} \sum_{j=1}^{M} g_{ij}^{n+1} \right) p_{i1}^{n+1} + \phi_m \frac{\Delta x}{\Delta t} \sum_{j=1}^{M} \left(h_{ij}^{n+1} - h_{ij}^{n} \right) - \left(\phi_m \frac{\Delta x}{\Delta t} \sum_{j=1}^{M} g_{ij}^{n} \right) p_{i1}^{n} \tag{3.23}$$

What is important to note in Equation (3.23) is that only one term multiplies a p_{i1}^{n+1} term - the remaining terms are all *known* values. As such, Equations (3.10) and (3.12) become

$$A_i p_{i-11}^{n+1} + B_i p_{i1}^{n+1} + C_i p_{i+11}^{n+1} = F_{i1} \tag{3.24}$$

with

$$A_i = -\alpha_f \frac{\Delta t}{\Delta y^2}$$

$$B_i = 1 + 2\alpha_f \frac{\Delta t}{\Delta y^2} + \frac{\phi_m}{\phi_f} \Delta x \sum_{j=1}^{M} g_{ij}^{n+1} \tag{3.25}$$

$$C_i = A_i$$

$$F_{i1} = p_{i1}^{n} + p_{i1}^{n} \frac{\phi_m}{\phi_f} \Delta x \sum_{j=1}^{M} g_{ij}^{n} + \frac{\phi_m}{\phi_f} \Delta x \sum_{j=1}^{M} \left(h_{ij}^{n} - h_{ij}^{n+1} \right)$$

Solution to the fracture pressure is then set up exactly like was done for the matrix rows. All that is needed is the top boundary value which corresponds to the new $t = n+1$ surface pressure. Once the fracture pressures are solved, those pressures provide the boundary values for the matrix row pressures. A summary of the solution scheme is thus:

For each time step, the following routine is executed

1. For each *i* (horizontal line into matrix):
   Sweep from *j* = M to 1 and calculate e_{ij} and d_{ij}^{n+1} using Equation (3.20).
   Sweep from *j* = 1 to *M* and calculate g_{ij}^{n+1} and h_{ij}^{n+1} using Equation (3.22).
2. For each *j* = 1 (along fracture):
   Sweep from *i* = *N* to 1 and calculate e_{i1} and d_{i1}^{n+1} using Equation (3.20).
   Sweep from *i* = 1 to N and calculate g_{i1}^{n+1} and h_{i1}^{n+1} using Equation (3.22).

Sweep from i = 1 to N and calculate p_{i1}^{n+1} using Equation (3.21).

3. For each i (horizontal line into matrix):
   Sweep from j = 1 to M and calculate p_{ij}^{n+1} using Equation (3.21).

3.3.2 Simultaneous Matrix (SM)

The objective of the simultaneous matrix solution approach is to formulate Equations (3.10) and (3.12) such that they can be written as a single, (very) large matrix equation, $\mathbf{A}P = b$ to be solved by modern sparse matrix solution routines. This formulation can be achieved by expanding out the sum that defines the fracture-matrix interaction term, I_i, in Equation (3.12) and *vectorizing* the matrix of pressures p_{ij} so that

$$P = [(p_{2,1}, p_{2,2}, ..., p_{2,M}), (p_{3,1}, p_{3,2}, ..., p_{3,M}), ..., (p_{N,1}, p_{N,2}, ..., p_{N,M})]$$

where the system is assumed to be N rows deep and M columns across.

Making use of Equation (3.1) and discretizing the second order derivative, the interaction term for a row i can be written

$$I_i = D\sum_{j=2}\left(p_{i,j-1} - 2p_{i,j} + p_{i,j+1}\right) \tag{3.26}$$

where the superscripts $n+1$ have been left off for clarity and

$$D_i = \alpha_m \frac{\phi_m \Delta t}{\phi_f \Delta x^2} \tag{3.27}$$

Plugging Equation (3.26) into Equation (3.12), simplifying and grouping terms leads to an expression for fracture pressures given by

$$A_i p_{i-1,1} + (B_i + D_i) p_{i,1} + C_i p_{i+1,1} - D_i p_{i,2} - D_i p_{i,M-1} + D_i p_{i,M} = p_{i,1}^n \tag{3.28}$$

where Equations (3.10) - (3.11) still apply within the matrix rows.

Figure 3.3 shows an example matrix construction given a system that is 5 rows deep with a 6th virtual row for the boundary condition and likewise 5 columns wide with

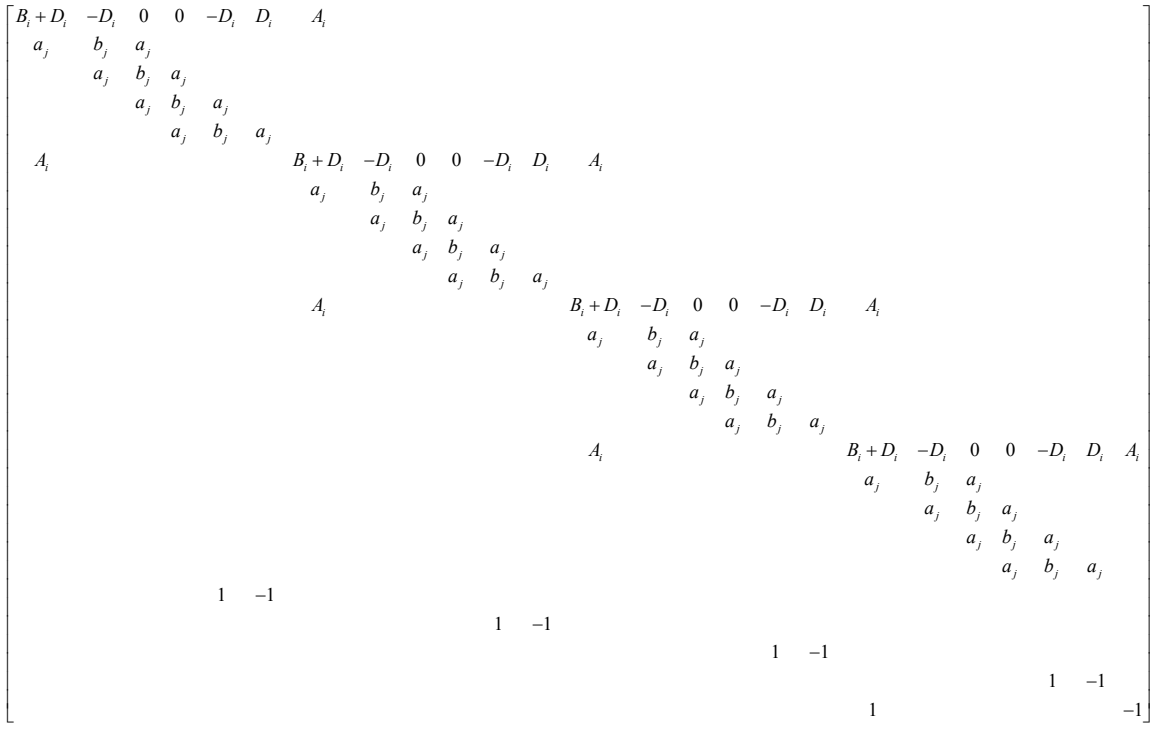

Figure 3.3 Example simultaneous matrix representation for 5x5 system.

a 6th virtual one. The right-hand constant side for this example would be

$$b = [p^n_{2,1} - Ap^{n+1}_{1,1}, p^n_{2,2}, p^n_{2,3}, p^n_{2,4}, p^n_{2,5}, p^n_{3,1}, p^n_{3,2}, p^n_{3,3}, p^n_{3,4}, p^n_{3,5}, \ldots$$
$$p^n_{4,1}, p^n_{4,2}, p^n_{4,3}, p^n_{4,4}, p^n_{4,5}, p^n_{5,1}, p^n_{5,2}, p^n_{5,3}, p^n_{5,4}, p^n_{5,5}, 0, 0, 0, 0, 0]$$

Then, as stated before, the system solution for $t = n+1$ would be given by solution for P to the matrix equation $\boldsymbol{A}P = b$.

3.3.3 Newton's Method (NM)

As evidenced in the previous two solution schemes, the only really complicating factor in solving the pressure response (and transport) equations for the double porosity model in UTEX is the fracture-matrix interaction term I_i of Equation (3.12) which couples the otherwise separate vertical and horizontal pathways. The first two solution schemes have striven to simultaneously solve for the fracture column and matrix rows;

this last Newton's Method scheme iterates over the matrix and fracture solutions separately during each time step until the system converges to the unique solution.

Much of the formalism needed to apply Newton's Method has already been laid out, but for conciseness and ease of reference it is summarized here again in a slightly different form. The discretized pressure equations for the matrix rows and fracture column are reproduced below:

$$a_j p_{ij-1} + b_j p_{ij} + a_j p_{ij+1} - p_{ij}^n = 0 \tag{3.29}$$

$$A_i p_{i-11} + B_i p_{i1} + A_i p_{i+11} + I_i - p_{i1}^n = g_i \tag{3.30}$$

where the coefficients appearing here are

$$\begin{aligned} a_j &= -\alpha_m \Delta t / \Delta x^2 \qquad & A_i &= -\alpha_f \Delta t / \Delta y^2 \\ b_j &= 1 + 2\alpha_m \Delta t / \Delta x^2 \qquad & B_i &= 1 + 2\alpha_f \Delta t / \Delta y^2 \\ I_i &= \alpha_m \frac{\phi_m \Delta t}{\phi_f \Delta x^2} \sum_{j=2} \left(p_{i,j-1} - 2p_{i,j} + p_{i,j+1} \right) \end{aligned} \tag{3.31}$$

Again, the $n+1$ superscripts have been dropped and all terms have been moved to the left-hand side of the equations with the exception of a new term g_i introduced in Equation (3.30). The idea is that $G = (g_1, g_2, \ldots g_i, \ldots, g_N)$ is a vector of solutions to the set of simultaneous equations, and in order to satisfy the true pressure equation for the fracture, all entries of G have to be zero.

Newton's Method obtains an iterative solution for the fracture pressure, denoted by the vector p, by computing

$$p^{k+1} = p^k - J^{-1} G(p^k) \tag{3.32}$$

where k here refers to the index of Newton iterations (not time steps), and J refers to the Jacobian matrix, which is computed by taking the first derivative of the solution vector G with respect to the fracture pressure vector p and is defined

$$J = J(p) = \frac{dG}{dp} = \begin{bmatrix} \frac{\partial g_2}{\partial p_2} & \frac{\partial g_2}{\partial p_3} & \cdots & \frac{\partial g_2}{\partial p_{N-1}} \\ \frac{\partial g_3}{\partial p_2} & \frac{\partial g_3}{\partial p_3} & \cdots & \frac{\partial g_3}{\partial p_{N-1}} \\ \vdots & \vdots & \vdots & \vdots \\ \frac{\partial g_{N-1}}{\partial p_2} & \frac{\partial g_{N-1}}{\partial p_3} & \cdots & \frac{\partial g_{N-1}}{\partial p_{N-1}} \end{bmatrix}.$$

In practice, however, J is computed by slightly perturbing the fracture pressures by Δp, calculating the resulting solution vector G(p + Δp) from Equation (3.30), and then finally

$$J \approx \frac{\Delta G}{\Delta p} = \frac{G(p) - G(p + \Delta p)}{\Delta p}. \tag{3.33}$$

The implementation of the Newton's Method scheme then goes as follows:

1. Compute matrix pressures $p_{ij}^{k=0}(t + \Delta t)$ using Equation (3.29) and the fracture pressure vector $p(t)$ as the boundary condition (BC).
2. Compute the interaction term $I_i^{k=0}(t + \Delta t)$ from Equation (3.31) using these $p_{ij}^{k=0}(t + \Delta t)$.
3. Compute the fracture pressures $p_i^{k=0}(t + \Delta t)$ from Equation (3.30) using the $I_i^{k=0}(t + \Delta t)$ and $G(p^0)=0$
4. Given a convergence threshold ε, while $p_i^{k+1} - p_i^k > \varepsilon$ perform Newton's Method:
   a. Perturb the fracture pressures: $p_i^k{}' = p_i^k + \Delta p$
   b. Compute perturbed matrix pressures $p_{ij}^k{}'$ using Equation (3.29) and $p_i^k{}'$ as the BC
   c. Compute perturbed interaction term $I_i^k{}'$ from Equation (3.31) using the $p_{ij}^k{}'$
   d. Compute a perturbed solution vector $G(p^k + \Delta p)$ from Equation (3.30) using $p_i^k{}' = p^k + \Delta p$ and $I_i^k{}'$

e. Compute J from Equation (3.33) using $G(p^k + \Delta p)$ and $G(p^k)$

f. Compute the new p^{k+1} from Equation (3.32)

5. When the fracture pressure has converged, the interaction term and matrix pressures will also have converged. The system has then moved forward to $t + \Delta t$ and the solution is repeated for the next time step.

3.4 UTEX BENCHMARKING

3.4.1 Analytical solution comparisons

For the sake of comparison with the numerical calculation conducted in the UTEX model, the pressure response in the system can be computed analytically if one chooses a simple analytic function to represent the surface pressure variations, such as

$$p(0,0;t) = p_0 + \Delta p \cos(\omega t). \tag{3.34}$$

With Equation (3.34) for the driving surface pressure, standard separation of variables can be applied to Equations (3.1) - (3.2) in order to find a closed-form solution for the pressure everywhere in the system (Nilson *et al.*, 1991). This is the same result as Equations (2.16) - (2.18), a derivation of which is shown in Appendix C.1.

The vertical transport code calculates and utilizes pressure information as it deviates from the average surface pressure; i.e. $p(x,y;t) - p_{0.}$ Thus an analytical comparison to the numerical estimation of pressure response within the system is easily carried out with Equation (2.16) multiplied by the amplitude of the surface pressure variations Δp_0.

Table 3.1 Summary of physical system parameters used in conducting numerical vs. analytical pressure response comparison.

Parameter	Assumed Value	Parameter	Assumed Value
porosity (matrix)	$\phi_m =$ 0.1	fracture width	$\delta_f =$ 0.001m
porosity (fracture)	$\phi_f =$ 0.95	matrix slab width	$\delta_m =$ 1m
permeability (matrix)	$k_m =$ 10^{-15} m^2	mean surface pressure	$p_0 =$ 10^5Pa
tortuosity	$\tau =$ 10	max pressure variation	$\Delta p =$ $5p_0/30$
dynamic viscosity (air)	$\mu =$ 2×10^{-5} Pa·s	period of oscillation	$T =$ 8 days
		total system depth	$L =$ 500m

The numerical versus analytical comparisons conducted here make use of the physical system parameters listed in Table 3.1. The transport code requires specification of the number of vertical and horizontal mesh points, *N* and *M*, as well as the length of time step, Δt. From these, the time and position values needed for Equation (2.16) are easily derived, and Equation (2.16) is easily implemented within the code to make a side-by-side calculation of the analytical pressure response with the numerical approximation.

As a base for comparison, a system scenario defined by ($N\times M$) = (200×7) was utilized[11]. The pressure response at each time step is tracked explicitly at every mesh point within the model, and since Equation (2.16) can be used at any given (*x,y;t*), a comparison of the numerical scheme with the analytical solution can be carried out in many ways. A strict way of doing so is to consider a specific point within the system and track the evolution of the numerical versus analytical pressure response at that point.

[11] This is to say, 200 vertical mesh points by 7 horizontal.

At the top of the system, mesh point (1,1), there is no "response" to be calculated – the pressure here is merely the harmonically varying surface pressure. Figure 3.4 (on the next page) indeed shows that both numerical and analytical solutions overlap exactly, as they should. As a first critical point for testing, Figure 3.5 shows the same plot as Figure 3.4 but for the mesh point (199,1) located at the bottom of the fracture. Again, the numerical calculation almost exactly models the analytical solution with maximum deviations on the order of 10 Pa, which represents about 0.01% of the mean barometric pressure at the surface.

Of greater interest is a point deep within the matrix slab; Figure 3.6 shows the pressure response for the mesh point (199, 6), which can be considered to be at the bottom of the system. The numerical estimation of the pressure response is again very close to that of analytical solution, but there is now some noticeable deviation between the two. Figure 3.7 shows a "close-up" of the rising edge to illustrate the deviation in greater detail, which presents itself as if the numerical solution has the same shape and amplitude but slightly lags behind the analytical solution in phase

The modeling of the fracture-matrix interaction term is of central concern. As demonstrated above, the pressure response within the fracture as estimated numerically is practically identical to the analytical solution. This is not really all that surprising, sense the physics of the pressure response within the fracture is rather simple. However, as is also demonstrated above, considering points beyond the fracture within the matrix slab introduces some small disagreement between the numerical and analytical solutions, so a natural question to consider is how does the numerical model hold up to increasing widths of matrix slabs, δ_m?

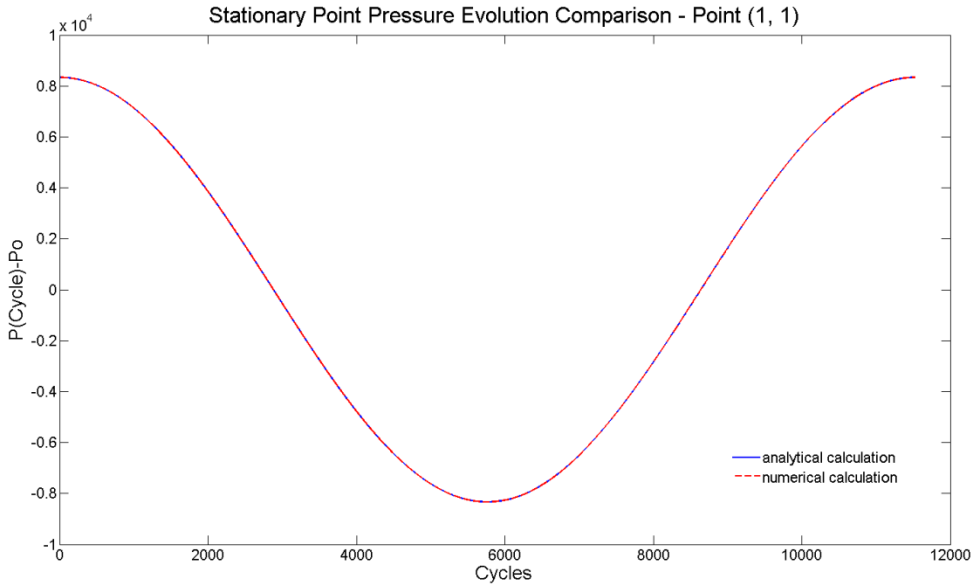

Figure 3.4 Pressure response tracking at (1,1) in 200x7 mesh model.

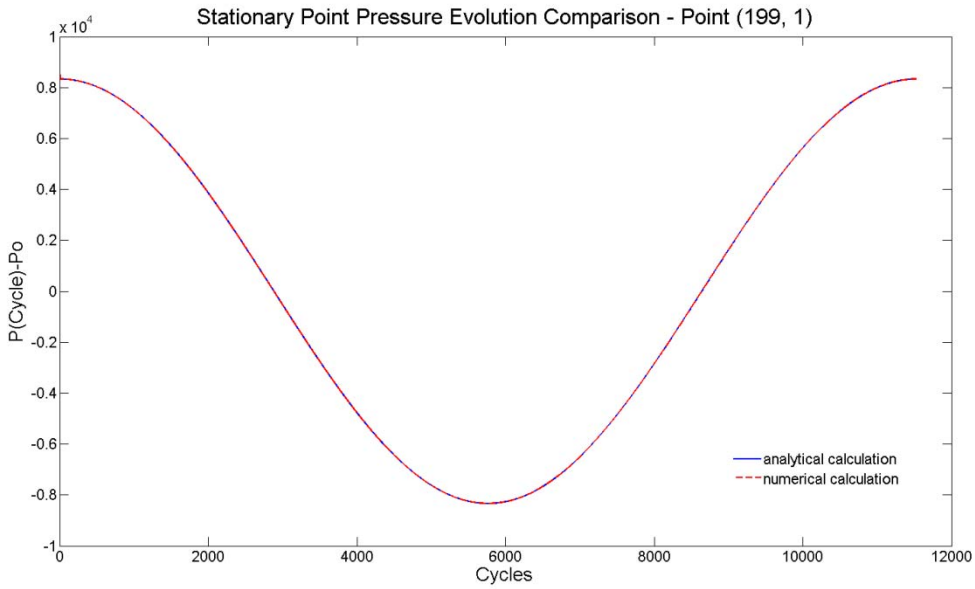

Figure 3.5 Pressure response tracking at (199,1) in 200x7 mesh model.

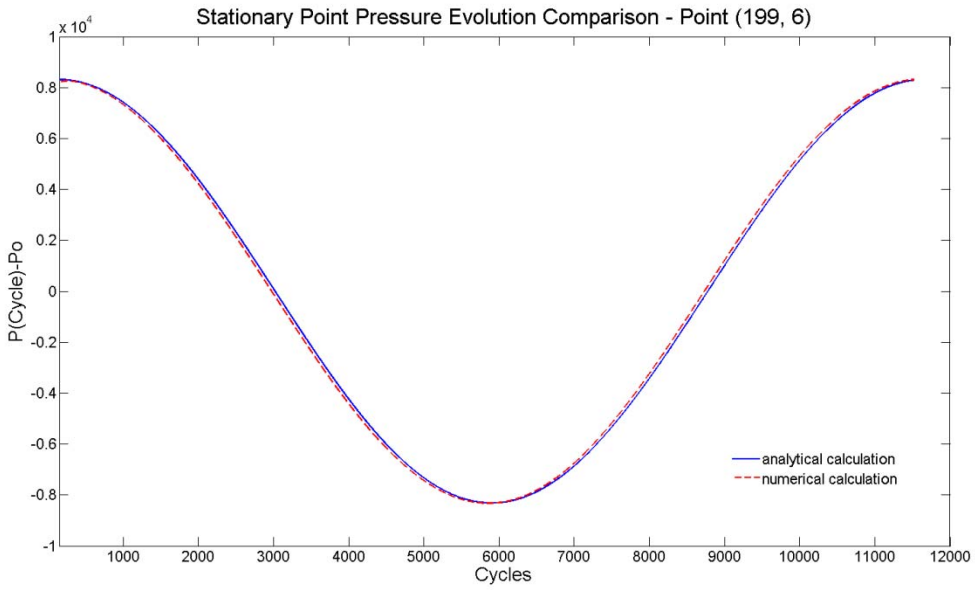

Figure 3.6 Pressure response tracking at (199,6) in 200x7 mesh model.

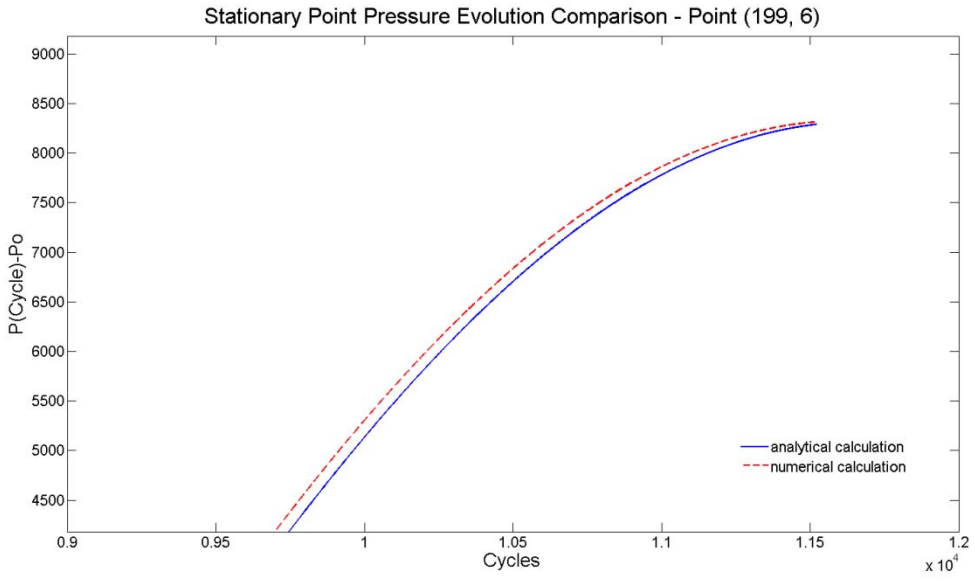

Figure 3.7 Close-up of the deviation in pressure response at (199,6) in 200x7 mesh model.

Figure 3.8 shows a plot of the pressure response with the exact same system and model configuration as the plot in Figure 3.6 except that now $\delta_m = 10$ m instead of 1 m, thus the point (199, 6) corresponds to a point about ten times deeper within the matrix. As compared with Figure 3.6, the response of Figure 3.8 is very "delayed" and much more suppressed, which is exactly what is expected because there exists a limited diffusion depth beyond which pressure variations from the fracture simply cannot penetrate further into the matrix slab. This depth for the given system parameters is about 10 m, thus at depths of $\delta_m = 10$ m and greater the pressure response should fall of quickly. More to the point, however, is that this greater depth results in a significantly greater deviation of the numerical result from the analytical pressure response solution.

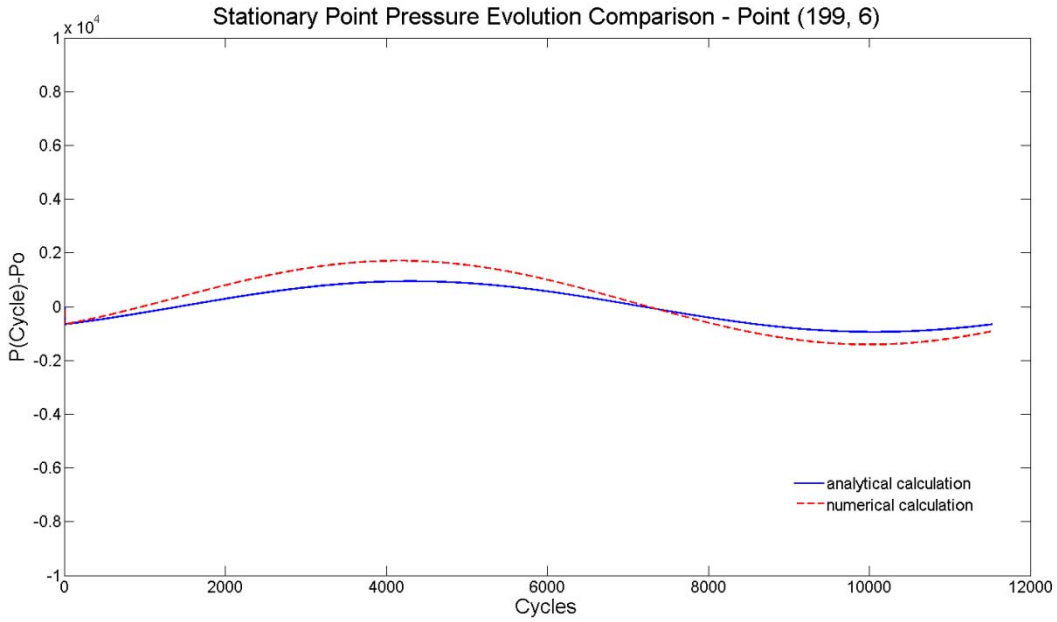

Figure 3.8 Pressure response tracking at (199,6) in 200x7 mesh model, now using $\delta_m = 10$m slab-width.

The increased "error" depicted in Figure 3.8 as compared to Figure 3.6 is due to numerical diffusion. By increasing $\delta_m = 10$ m from 1 m, the horizontal mesh spacing has effectively been made coarser and the diffusive transport of the pressure waves is overestimated by the numerical scheme. Consider lastly Figure 3.9, which now models the $\delta_m = 10$ m using a horizontal mesh spacing ten times smaller than that of Figure 3.8, i.e. M = 70 instead of 7. The result is that the numerical pressure response calculation now much more closely follows the analytical solution. This leads now to the mesh reduction study conducted to determine an optimal mesh on which to run UTEX simulations.

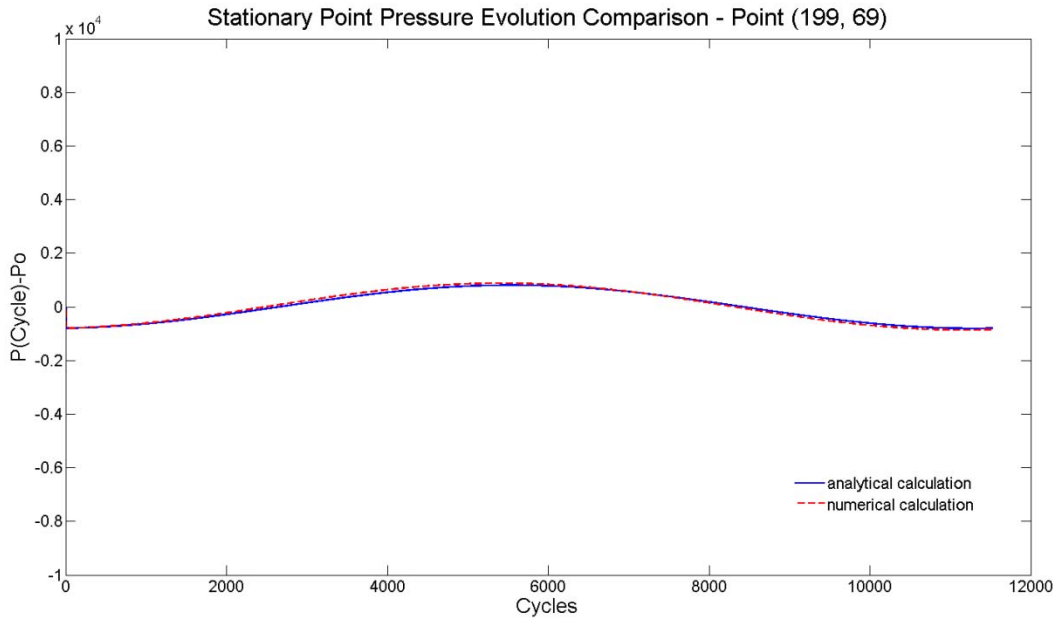

Figure 3.9 Pressure response tracking at (199,69) in 200x70 mesh model, using $\delta_m =$ 10m slab-width.

3.4.2 Mesh reduction study

A number of analyses were conducted to assess the effect of mesh reduction on the squared standard errors resulting from various numerical versus analytical calculations. These included studies of the above pressure response, some of the results of which are presented here, as well as other comparisons of simple diffusion and advection transport scenarios, such as those presented Appendix C.2 and C.3.

In Figure 3.10, the effect of varying the length of the time step in the numerical simulation of the pressure response is summarized; the driving surface pressure is again described by Equation (3.34) and the analytical solution is the same as before in Equations (2.16) - (2.18). Length of the time step is the mesh parameter with the most direct effect on the total simulation time, and the $\Delta t = 60$ s that is used in the larger sensitivity study was selected because, as shown in Figure 3.10, a factor of ten further decrease (and factor of ten longer simulation time) resulted in only a fractional improvement in the deviation.

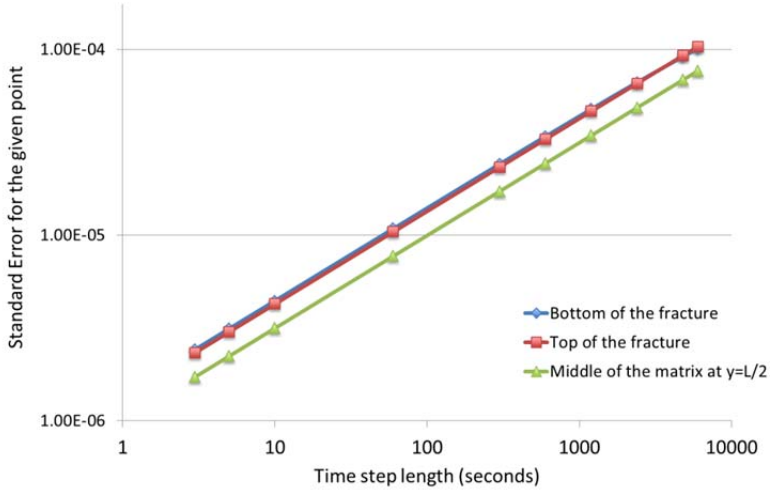

Figure 3.10 Error in the numerical pressure as a function of Δt. The deviations of the numerical pressure calculation from the analytical one are plotted at three different points in the system, using a 100 x 200 mesh, on a log-log scale.

Figure 3.11 and Figure 3.12 show similar results of mesh reduction for vertical and horizontal mesh spacing respectively, using the time step Δt = 60 s. In Figure 3.11 the average error along the fracture improves by an amount of order 1E-8 as the number of vertical mesh points is increased from 100 to 1000. As shown in Figure 3.12, the error along a row of matrix exhibits a greater dependency on the number of horizontal mesh points than the fracture errors do on the number of vertical mesh points. A mesh size of 100×200 vertical and horizontal mesh points was chosen to optimize numerical deviation from analytical as well as keep simulation times reasonable; this choice is assumed much of the remainder of this work.

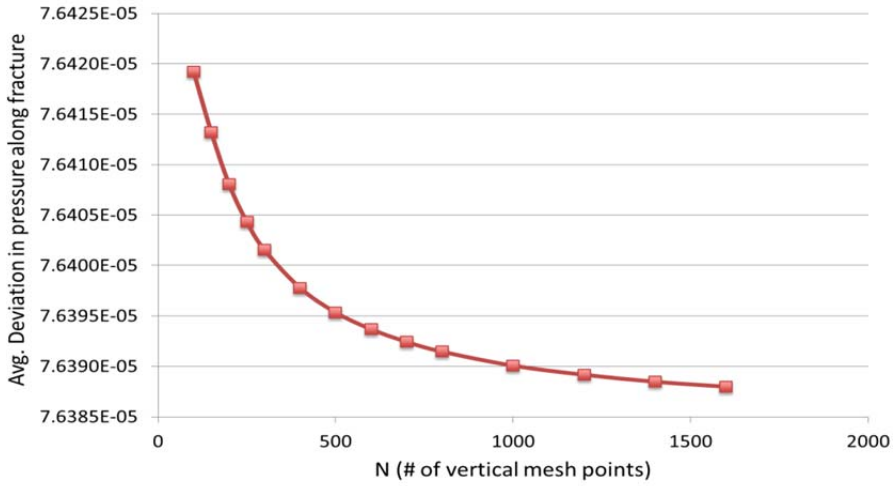

Figure 3.11 Error in the numerical pressure as a function of number of vertical mesh points. The average deviations along the fracture of the numerical pressure calculation from the analytical one are plotted versus N.

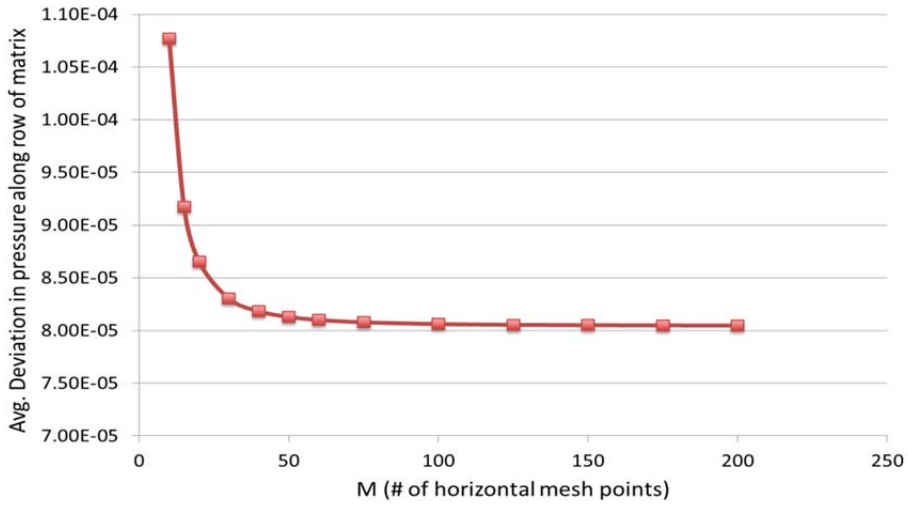

Figure 3.12 Error in the numerical pressure as a function of number of horizontal mesh points. The average deviations along a row of matrix (at $y = L/2$) of the numerical pressure calculation from the analytical one are plotted versus M.

3.4.3 Alternate solution method comparison

Comparison of the initial UTEX Thomas Algorithm numerical estimate with the analytic solution to the pressure response for the simple harmonically varying surface pressure of the previous section led to the choosing of an optimal system mesh on which to run the UTEX model. This mesh was then utilized to compare the Thomas Algorithm (TA) scheme to the two additional solution methods based on a simultaneous matrix (SM) representation of the system of equations and a Newton's Method (NM) iterative method. Results presented here were obtained using a pressure history compiled from 1-hour interval true barometric data at Mercury, NV over a period of 70 days and linearly interpolated to obtain pressures at smaller resolution to match the 60-second time steps.

This same pressure history was also utilized in subsequent UTEX sensitivity studies, which are discussed in detail in the next chapter. All three numerical solution methods detailed above were implemented into the UTEX MATLAB® code for calculation of both the system pressure response and the simulated gas transport at each time step. Again for brevity's sake, illustration of the comparisons of this section is on solutions to the pressure response and analogous results for transport are summarized.

In Figure 3.13 is shown an example plot of the pressures calculated down the fracture as a function of depth for each of the three solution methods after 100 iterations of the code.[12] The three solution curves, on this scale are indistinguishable; in fact, the solutions are in exact agreement to nine significant digits. To facilitate visualizing the deviation in calculated pressures between the methods, Figure 3.14 shows the same pressures after subtracting out the first eight significant digits of the solutions at each point. What is immediately evident on this closer look is that the Newton's Method and Simultaneous Matrix solutions tend to match very closely while the Thomas Algorithm calculations can deviate slightly from the other two. This is even more obvious in Figure-5, which shows the absolute pressure deviation of each method from the mean of the three solutions at each mesh point down the fracture. Again, the largest deviations are in the Thomas Algorithm solution while the deviations from the other two are smaller and match closely.

[12] The pressures in Pascal are with respect to a roughly mean atmospheric pressure of 10^5 Pa.

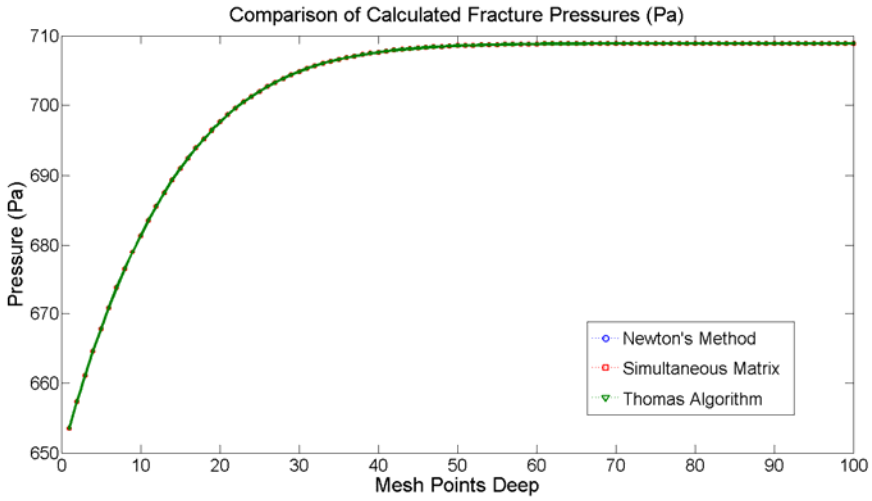

Figure 3.13 Comparison of the calculated fracture pressures as a function of depth after 100 time steps for each of the three numerical methods; on this plot scale the curves are indistinguishable from one another. The mesh spacing corresponds to a physical depth of 4.5 m.

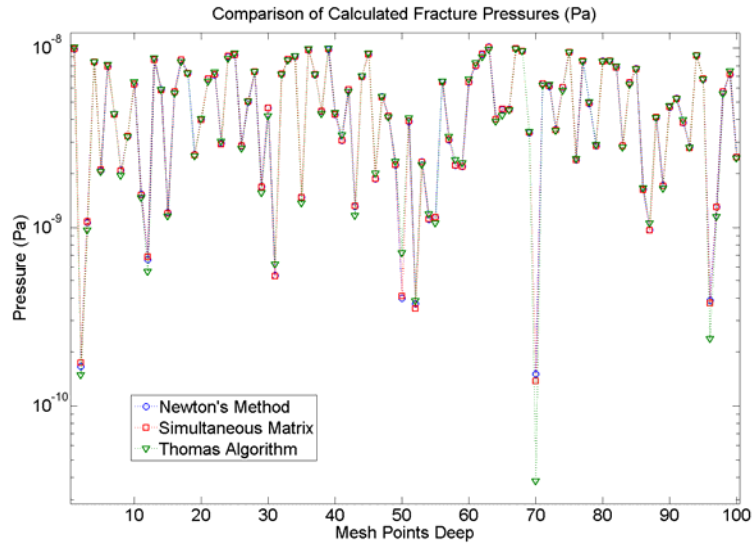

Figure 3.14 Comparison of the calculated fracture pressures as a function of depth after 100 time steps for each of the three numerical methods with the agreeing 8 significant digits subtracted out.

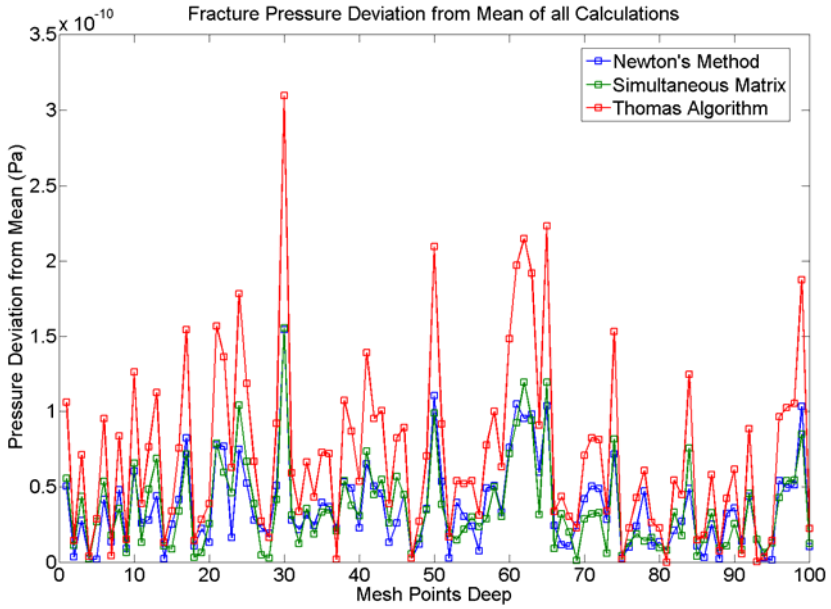

Figure 3.15 Fracture pressure deviations from the mean of all three calculations as a function of depth after 100 time steps for each of the three numerical methods.

The nature of these deviations can almost certainly be attributed to an accumulation of round-off error in the calculation of these solutions using double-precision floating point numbers for which the best accuracy in MATLAB is 2.2204E-016. Each of the three solution implementations, though starting from same system of equations to be solved at each time step, proceeds to solution by different sets of floating point operations. As a result, due to the inherent limitation of machine precision, it is expected that each solution method should incur an error associated with repeated round-off or truncation in these operations; the resulting error is often described as round-off noise and the stochastic nature of this noise is clear in the pressure deviations shown in Figures 3-7 (Widrow & Kollár, 2008).

In Figure 3.16, absolute deviations between the three different pairings of the three solution methods are plotted as a function of depth down the fracture. Again, the

smallest deviations and thus strongest correlations are given predominantly by the deviation between the Newton's Method (NM) and Simultaneous Matrix (SM) methods suggesting that they agree the strongest. Correlating the Thomas Algorithm (TA) method with either of the other two results in a deviation that is on-average an order of magnitude higher (these two curves overlap in Figure 3.16 and Figure 3.17). A likely explanation for this is that the TA implementation entails a large number of explicit point by point computations in the forward and backward sweeps over which truncation error can accumulate, whereas the NM and SM methods rely much more on built-in MATLAB functions to solve the system (in particular the '\' or slash operator). Additionally, in Figure 3.17, the means of the three correlations of Figure 3.16 are plotted as a function of time steps to show that these deviations remain fairly stable as the UTEX simulations proceed.

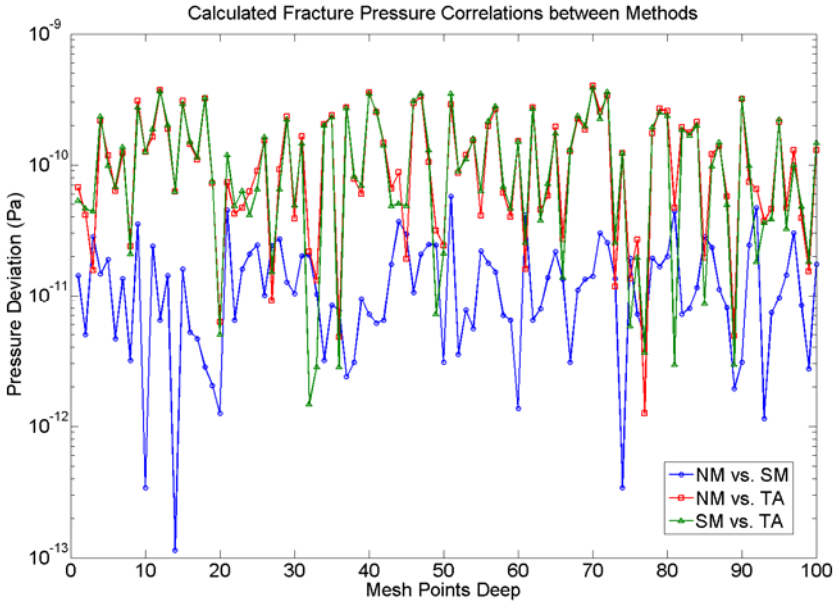

Figure 3.16 Fracture pressure deviations among the three numerical methods as a function of depth down the fracture after 100 time steps of simulation.

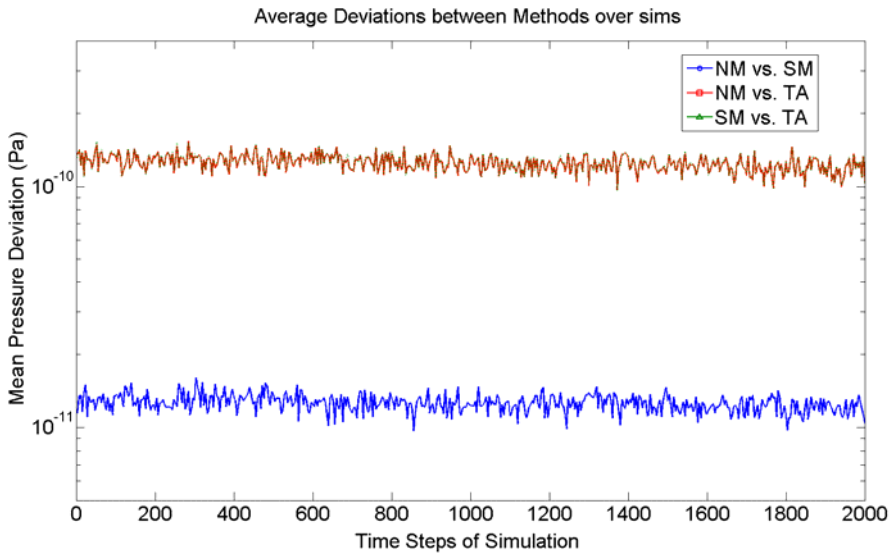

Figure 3.17 The average pressure deviations along the whole fracture length (i.e. mean of the curves in Figure 3.16) as a function of time step of simulation. Note that the (higher) NM vs. TA and SM vs. TA very closely overlap.

These observations for the pressure response calculations down the fracture apply equally to the pressure elsewhere in the system as well as for the solutions to the gas transport component of the UTEX model. Table 3.2 summarizes the mean cross-deviations in pressure and concentration between the three different solution methods after 2000 iterations of the code. Note that the magnitude of concentrations being considered are three orders of magnitude smaller than the pressure values, but what is important to notice in Table 3.2 is that deviation trends for the concentration are the same as for the pressure calculations - the Newton's Method and Simultaneous Matrix solutions are closer by about of factor of 10 than they are to the Thomas Algorithm, and in all cases the deviations only occur beyond the ninth significant digit.

Table 3.2 Summary of solution method comparisons for the pressure response and gas transport in UTEX calculated as deviations among the pairs of methods at different points within the system after 2000 iterations of the code.

	NM vs. SM	**NM vs. TA**	**SM vs. TA**
	Mean Pressure deviations (Pa)		
m=1 (fracture)	0.08466e-10	0.84563e-10	0.84995e-10
m = 100 (midpoint)	0.01103e-09	0.11104e-09	0.11152e-09
m = 200 (endpoint)	0.01023e-09	0.10220e-09	0.10272e-09
	Mean Concentration deviations (Ci/m^3)		
m=1 (fracture)	0.10328e-13	0.96524e-13	0.99814e-13
m = 100 (midpoint)	0.03468e-12	0.29417e-12	0.29228e-12
m = 200 (endpoint)	0.03321e-12	0.29154e-12	0.28841e-12

Lastly, the relative computation time for the three solution methods to simulate 2000 iterations varies as follows, the Thomas Algorithm proved the fastest in this test at just less than 10 minutes, Newton's Method solution at 14 minutes and the Simultaneous Matrix solution at 19 minutes. The bulk of the calculation time in the latter two consists of converting to and manipulation of very large sparse matrices such as that shown in Figure 3.3.

3.5 CONCLUSIONS

A big advantage of streamlining and modularizing the early UTEX code was that it facilitated a piece-by-piece examination of the numerical implementation for testing purposes. A number of mesh reduction studies were undertaken to evaluate the precision of the numerical calculations with respect to choices in mesh size. The most important of these studies was a comparison of the modeled pressure response to an analytical solution

for a simple harmonically varying surface pressure. This was used to benchmark the numerically calculated pressure response in UTEX as the mesh spacing was varied. Results of this and similar studies led to an eventual choosing of an optimal system discretization of $N \times M = 100 \times 200$, that is 100 mesh points vertically and 200 horizontally.

A number of studies were also undertaken to benchmark the transport results of UTEX to verify that the numerical code was actually calculating what it was supposed to be calculating. Analytical solutions for gas transport in the system as a whole are intractable. To make analytical solutions possible, the different transport mechanisms were examined individually. By turning off the pressure variations (or forcing flow velocities to be zero) and setting decay constants to zero, it is possible to reduce the transport equations to simple one-dimensional diffusion equations that have analytical solutions. The same can be done in the UTEX model to facilitate an evaluation of the numerical accuracy in the diffusion transport calculations. Similarly, diffusion can be turned off and the flow velocities forced to remain constant to again obtain a tractable set of transport equations for comparison of advective transport. Numerical accuracies for these cases compared to analytical solutions were all of the order 0.01% or smaller, but in general these accuracies are dependent on the specified values for the geologic input parameters, particularly the size of the mesh spacings and time step. This is related to the concept of the Courant number, which places a confidence bound on mesh spacing for a given length of time step and flow velocity.

The most basic conclusion that can be drawn from the numerical solution scheme study presented in this chapter is that the Thomas Algorithm, Simultaneous Matrix, and Newton's Method solution implementations within the UTEX code all yield solutions to the system physics that agree to better than nine significant digits. This lends a very

strong confidence that within the context of the mathematical equations formulated to represent the system, precise solutions can be obtained on the chosen system mesh with any of the three methods. The very small disparity between the solution methods is very likely due to the limitations of machine precision and the resulting accumulation of truncation error, which is manifested in a round-off noise associated with the very least significant digits.

Aside from simple considerations of computation time, there are other practical differences in the three implementations. The Thomas Algorithm, while slightly faster than Newton's Method in the cases considered, is seemingly most susceptible to round-off error as well as the most difficult method of the three to adapt to other systems. For instance, a natural progression in UTEX capability is to consider systems of arbitrary width with multiple systems of fracture and bulk matrix medium. Whereas the Thomas Algorithm and Simultaneous Matrix solution methods would be altered significantly and become extremely memory intensive as the system grew larger, the Newton's Method implementation is almost naturally portable to larger, more complex systems. For this reason alone, as well as the observation that all three methods yield confident solutions, the Newton's Method approach was chosen for continued UTEX development and optimization, applications of which will be demonstrated in subsequent chapters.

Chapter 4. Initial UTEX Transport and Source Studies

Early development of the Underground Transport of Environmental Xenon (UTEX) model began as a Master's project, the goal of which was to establish the possibility that subsurface movement could alter the isotopics of radioxenon gas as it might emanate from an underground nuclear explosion (Lowrey, 2011). As such, the modeling capabilities of UTEX have evolved substantially, and largely speaking, the goal of this Ph.D. work was to develop, demonstrate, and explore these various modeling capabilities. In this chapter, the earlier results of modeling with UTEX are presented, which lays the foundation for exploration of more specific aspects of the code input and applications to OSI scenarios in the chapters that follow.

4.1 SMOOTH PRESSURE TRANSPORT IN EARLY UTEX

4.1.1 Non-decay source

The general physical system considered in early transport work with UTEX consists of an assumed system depth of L = 500 m, an initial contaminant distribution that begins at a depth of L_0 = 300 m and continues to the bottom of the system (therefore there is an initial fresh-air buffer zone extending down 200 m from the surface). As an initial effort to reproduce a transport scenario considered in Nilson *et al.* (1991), in the base case of the early study the fracture width is taken to be δ_f = 1 mm and the fracture separation δ_m = 1 m. The porosities of the fracture and bulk matrix are respectively ϕ_f = 1 and ϕ_m = 0.1 and the matrix permeability is assumed to be $k_m = 10^{-15}$ m^2.

For the purpose of simplifying the transport in the system and isolating individual parameters and their effect on the results, a simple sinusoidal variation in surface pressure

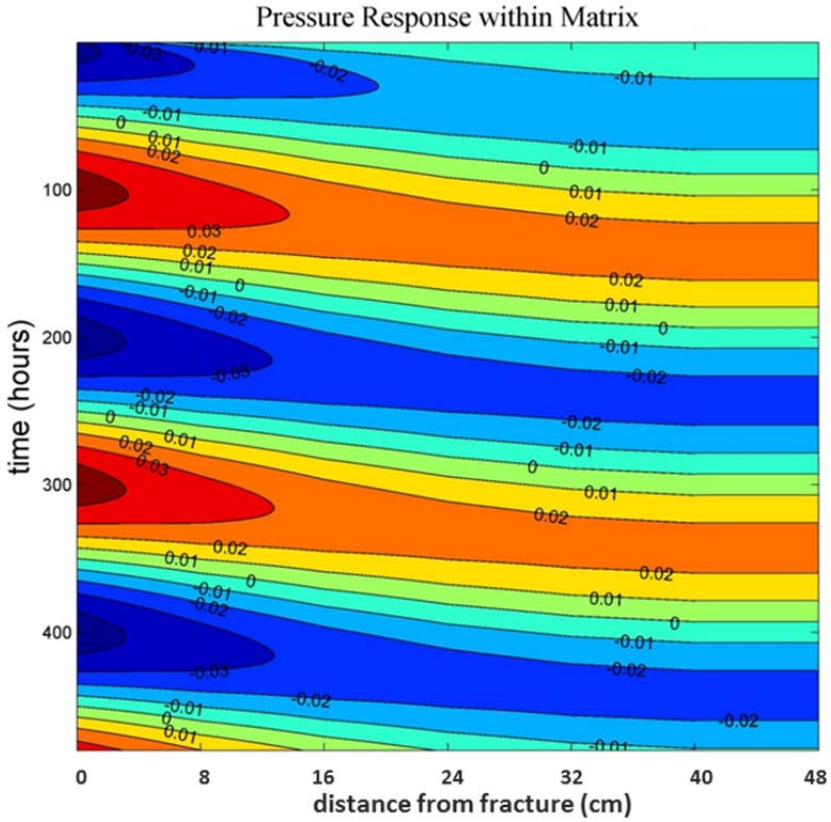

Figure 4.1 Pressure response across a horizontal slice of the matrix over two periods of barometric oscillations at depth x = 400 m. Note that time evolves downwards in the plot.

is assumed with a period of 200 hours and starting with an amplitude of $2/30p_0$ where p_0 is the mean pressure in the system. Figure 4.1 shows a plot of the pressure response (as a fractional deviation from p_0) in the system for a single horizontal row in the bulk matrix medium. As time progresses downwards, the surface pressure varies harmonically; at points in the matrix nearest the fracture, the propagated pressure response is felt quickly. Deeper in the matrix, however, the pressure fluctuations occurring at the surface are attenuated and propagate much less rapidly.

Initially, transport of a stable xenon gas over 100 days was simulated using this smooth pressure function to drive advective flow in the system. The resulting instantaneous and cumulative gas outflows (as a fraction of the total initial inventory) are shown in Figure 4.2. In the early time regime over the first three months or so, the gas outflow is largely suppressed as the amplitude of the surface pressure fluctuations are not enough to immediately draw out gas. However, due to fracture-matrix diffusion of gas moving along the fracture, the concentration gradient extends upward, so that at later times the various pumping cycles begin to pull ever more gas to the surface. Eventually a so-called *quasi-steady* state is achieved during which the amount of subsurface contaminant brought to the surface each cycle remains fairly constant. This observation is very much consistent with the conclusion of Nilson *et al.* (1991). Since there is no additional source of contaminant in this example, eventually outflows decrease and the cumulative outflow line of Figure 4.2 approaches 1 asymptotically.

4.1.2 General radioactive decay source

With the addition of radioactive decay to the vertical transport code, contaminant removal from the simulated system no longer occurs just due to the physical transport mechanisms being modeled. In earlier environmental transport modeling codes, it was not uncommon to estimate the subsurface movement of a radioactive contaminant by first simulating the transport of a non-decaying contaminant, and then applying a radioactive decay correction to the resultant concentration. For the case of modeling an underground, time-dependent source, this approach is somewhat unsatisfactory, unless the transport is simulated from start to finish by considering different sources at discrete times, and then summing the transport from all sources at the end. Obviously this would be an efficient approach.

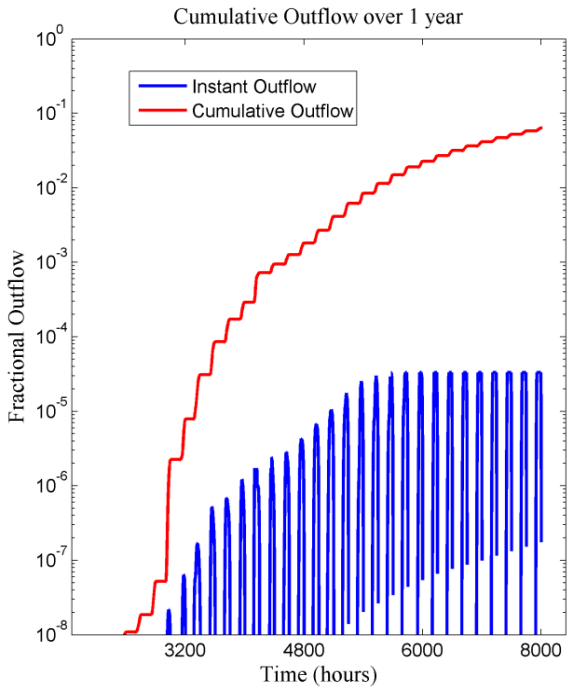

Figure 4.2 Cumulative fractional outflow of non-decaying gas overlaid with the instantaneous fractional outflow over a roughly 1-year period in early simulations with UTEX.

Including the effects of radioactive decay in the transport model can be implemented in multiple ways; broadly speaking, however, there are two options. First, the decay can be instituted directly within the mass conservation equations for transport. In this manner, the decay factor occurs as a component of the inhomogeneous coefficient F, which incorporates all of the past system knowledge, and the radioactive decay is therefore handled implicitly as part of the transport solution. In a second approach, the radioactive decay can be applied at the beginning (or end) of each time iteration in the simulation to explicitly decay the point-by-point concentrations of the previous system state by one time step Δt. For small enough time steps, these two options were found to converge to the same results, as they obviously should. Of the two methods, the first is

obviously more elegant; however, the second offers the capability to explicitly track the amount of decay, an advantage that also facilitates modeling the movement of the source itself in the case of ^{133m}Xe and ^{131m}Xe.

As a first example application of the UTEX code to the problem of modeling the transport of the various UNE noble gases, the HEU source term results of Table 2.4-2.6 were used to determine an estimated activity outflow for ^{131m}Xe, ^{133m}Xe, ^{133}Xe, ^{135}Xe, and ^{37}Ar. As before, the modeled system is taken to consist of a total depth of L = 500 m below the surface, with an initial source term distributed over L_0 = 300 m, leaving 200 m of fresh-air buffer above the initial contaminant front. The following physical parameters were again utilized: the fracture width and separation is taken to be δ_f = 1 mm and δ_m = 1m respectively; values of ϕ_f = 1 and ϕ_m = 0.1 for the fracture and matrix porosities were assumed, and the matrix permeability was $k_m = 10^{-15}$ m^2. The barometric pressure at the surface was taken to vary harmonically with period T = 200 hours and amplitude $\Delta p = 2/30 p_0$ about the mean static pressure $p_0 = 10^5$ Pa. The dynamic viscosity of air was taken to be $\mu = 2 \times 10^{-5}$ Pa·s. The resulting outflow is summarized in Figure 4.3.

The effect of the barometric pumping driving force is clearly evident in Figure 4.3, as the outflows exhibit the characteristic step feature seen without radioactive decay in Figure 4.2. The difference in this example is that now the transporting gas isotopes are subject to radioactive decay as well as ingrowth from a time-dependent source term. In this case, even with source terms that continue adding new concentrations to the system for the first few weeks, all four radioxenon isotope outflows have effectively ceased by 50 days simulated transport. The leakage of ^{135}Xe, despite a total initial inventory of over 10^6 Ci, barely reaches an estimated cumulative outflow of 10^{-20} mBq/m^3 by 20 days before stopping. This is of course due mostly to the post-UNE radioxenon source term (Figure 2.8), in which ^{135}Xe very quickly reaches a maximum within the first day and

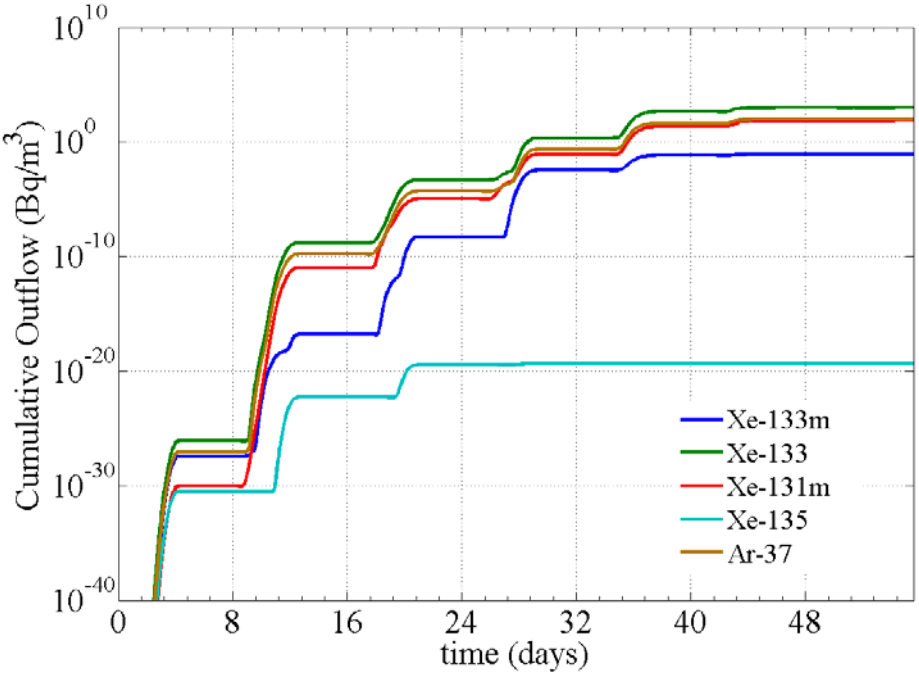

Figure 4.3 Estimated outflow of radioxenon and soil-activated argon from simple UNE transport scenario with smoothly varying atmospheric pressure.

then rapidly decays with a 9.1 hour half-life. Because of the nature of barometric pumping, ^{135}Xe is just too short-lived in the simulations to undergo any substantial build-up. Both ^{131m}Xe and ^{133}Xe have significantly longer half-lives, and therefore represent much more likely candidates for subsurface leakage, as depicted in Figure 4.3.

In the case of ^{131m}Xe with a half-life of nearly 12 days, the initial post-UNE concentration builds up relatively slowly, coming to a maximum more than 10 days later; however, its longer lifetime eventually facilitates a greater movement of the gas towards the surface. For ^{133}Xe, the inventory maximum occurs very quickly by comparison, however at three orders of magnitude higher concentration, enough of the gas remains at later times to allow for substantial barometric pumping upwards to the surface. Also as seen in Figure 4.3, ^{37}Ar is simulated to leak from the system in appreciable amounts. Although the activated soil concentration of argon is only of the order 10^3 Ci and does

not have an additional source component in time, its 35 day half-life is long enough that its vertical migration in the system is not greatly inhibited by radioactive decay.

4.1.3 Initial sensitivity study of radionuclide outflow

Table 4.1 summarizes a cursory sensitivity study that was conducted on the major physical parameters of the UTEX model input using the system configuration outlined above as a base case and varying parameters from there. The results presented in the table are plotted in the figures of the following pages for all isotopes except ^{135}Xe; this radioisotope was not included in the graphical results simply because the resulting outflows were typically 15 orders of magnitude smaller than the other four, variations of which could not be depicted on the same scale as the other three.

The first set of data considers variations of the fracture separation, δ_m, the results of which are plotted in the top portion of Figure 4.4. The effect of the fracture separation is complicated component of the barometric pumping process. On the one hand, smaller separations mean that trace gas within the matrix has less far to travel horizontally during barometric lows to enter the fracture. On the other hand, however, smaller separations mean that the trace gas migrating upwards along the fracture diffuses less into the buffer regions of the matrix. This is a *very* critical feature of the double-porosity model because if gas does not seep into the higher matrix levels, then the concentration gradient does not stretch upwards and no "ratcheting" effect ensues. The effect of radioactive decay complicates this balance even further because it places a time restriction on how long the contaminant has to migrate upwards and establish quasi-equilibrium.

Table 4.1 Summary of sensitivity study on cumulative post-UNE radionuclide release for simple underground transport with smooth atmospheric pressure function. The shaded rows are for the initial system configuration that was used to produce Figure 4.3. Parameters are varied around these values.

Physical Parameters					**Cumulative Outflow at 55 days (Bq/m^3)**				
δ_m (m)	δ_f (m)	$\Delta p/p_0$	ϕ_m	ϕ_f	^{133m}Xe	^{133}Xe	^{131m}Xe	^{135}Xe	^{37}Ar
Fracture separation sensitivity									
0.1	0.001	2/30	0.1	1	3.651E-04	1.007E+00	3.425E-02	3.185E-13	9.224E-02
0.25	0.001	2/30	0.1	1	1.536E-02	4.518E+01	3.552E+00	5.851E-13	4.459E+00
0.5	0.001	2/30	0.1	1	2.726E-05	2.269E+02	2.439E+01	4.847E-19	2.246E+01
1	0.001	2/30	0.1	1	8.608E-02	1.022E+03	8.147E+01	4.753E-20	1.033E+02
2	0.001	2/30	0.1	1	1.536E-02	9.857E+02	8.553E+01	5.853E-24	9.719E+01
5	0.001	2/30	0.1	1	6.557E-04	1.728E+01	8.023E-02	2.509E-26	1.671E+00
10	0.001	2/30	0.1	1	2.563E-03	9.215E+01	2.901E+00	1.344E-24	8.432E+00
Fracture width sensitivity									
1	0.00005	2/30	0.1	1	3.507E-02	7.394E+02	7.379E+01	0.000E+00	6.662E+01
1	0.0001	2/30	0.1	1	9.782E-02	9.209E+02	6.378E+01	6.076E-21	8.647E+01
1	0.0005	2/30	0.1	1	5.924E-02	1.184E+03	7.915E+01	1.198E-20	1.127E+02
1	0.001	2/30	0.1	1	8.608E-02	1.022E+03	8.147E+01	4.753E-20	1.033E+02
1	0.002	2/30	0.1	1	9.203E-02	1.023E+03	8.267E+01	5.645E-20	1.008E+02
1	0.005	2/30	0.1	1	9.070E-02	1.124E+03	7.827E+01	6.359E-20	1.013E+02
1	0.01	2/30	0.1	1	8.202E-02	1.071E+03	7.732E+01	5.134E-20	1.037E+02
1	0.05	2/30	0.1	1	8.030E-02	1.025E+03	8.341E+01	1.483E-20	9.246E+01
Pressure variation sensitivity									
1	0.001	5/90	0.1	1	1.009E-03	2.307E+02	4.492E+01	1.712E-29	2.291E+01
1	0.001	2/30	0.1	1	8.608E-02	1.022E+03	8.147E+01	4.753E-20	1.033E+02
1	0.001	7/90	0.1	1	5.820E-01	2.660E+03	9.990E+01	7.236E-16	2.599E+02
1	0.001	8/90	0.1	1	2.084E+00	4.694E+03	1.638E+02	1.623E-13	4.624E+02
Bulk matrix porosity sensitivity									
1	0.001	2/30	0.01	1	2.276E-01	1.586E+03	1.105E+02	8.761E-18	1.446E+02
1	0.001	2/30	0.05	1	1.567E-01	1.258E+03	1.002E+02	1.589E-19	1.249E+02
1	0.001	2/30	0.08	1	1.104E-01	1.101E+03	9.544E+01	5.922E-23	1.009E+02
1	0.001	2/30	0.1	1	8.608E-02	1.022E+03	8.147E+01	4.753E-20	1.033E+02
1	0.001	2/30	0.2	1	6.195E-03	5.978E+02	6.294E+01	7.169E-32	5.392E+01
1	0.001	2/30	0.3	1	1.012E-03	1.922E+02	8.438E+00	1.881E-34	1.757E+01
1	0.001	2/30	0.5	1	9.151E-09	2.055E-05	1.513E-08	1.960E-38	2.026E-06
Fracture porosity sensitivity									
1	0.001	2/30	0.1	0.5	3.323E-25	1.123E-20	1.665E-18	1.484E-53	1.122E-21
1	0.001	2/30	0.1	0.7	1.037E-05	8.090E-01	1.899E-03	1.024E-41	7.435E-02
1	0.001	2/30	0.1	0.9	6.296E-03	4.551E+02	5.489E+01	1.373E-27	4.396E+01
1	0.001	2/30	0.1	1	8.608E-02	1.022E+03	8.147E+01	4.753E-20	1.033E+02

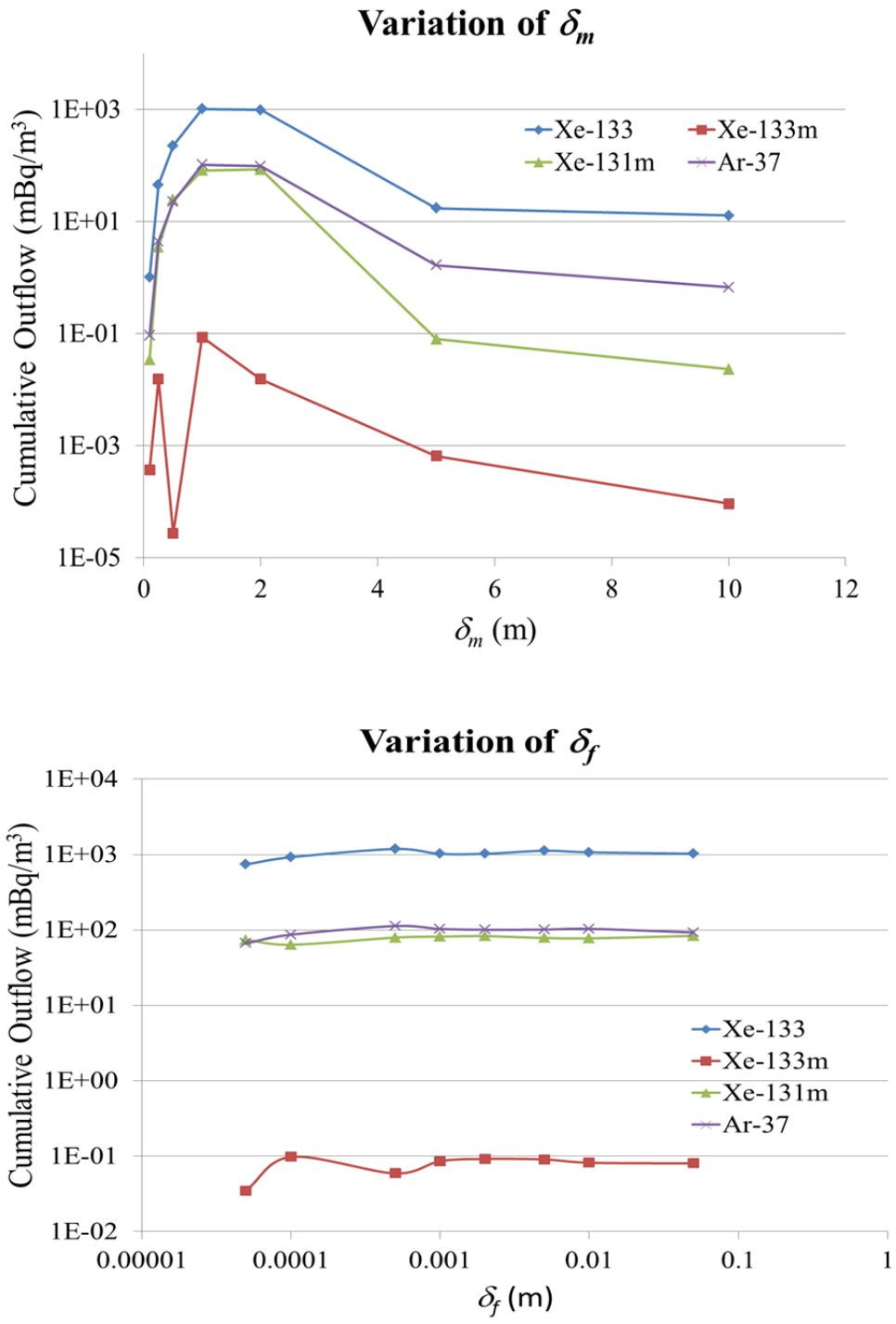

Figure 4.4 Plot of simulated 55 day radionuclide outflows for various values of the fracture separation and width parameters δ_m and δ_f respectively and other input values held constant.

With regard to the results in Figure 4.4, fracture separations below 1 m lead to a decrease in the outflow at 55 days, attributable to the lack of effective seepage distance in the buffer regions. At *very* small fracture separations on a scale similar to the fracture width (1 mm here), the numerical solution begins to break down as huge velocity gradients surpass the capability of the FRAM scheme to eliminate spurious oscillations. At slightly larger values than 1 m, the effects of radioactive decay begin to outweigh the benefit of fracture-matrix diffusion, as gas that migrates deeper into the bulk medium will be more likely to decay before being drawn back out. Beyond roughly 5 m, effect of further decreasing the fracture separation is diminished because will only penetrate so far into the matrix before it can no longer be expected to contribute to surface outflow at later times.

In contrast, variation of fracture width, δ_f, which is depicted in the lower plot of Figure 4.4, exhibits much less effect on the resulting outflow of all three radioxenon isotopes. This is somewhat expected because even though a larger width can cause faster vertical flow along the fracture, these effects will be countered by a subsequent decrease in the rate of fracture-matrix diffusion, which tends to lessen the overall outflow. In effect, movement of gas upwards along the fracture, at least in the simulation set considered here, is not the limiting factor in the effectiveness of barometric pumping. Increasing fracture width so large that diffusive mixing through the fracture volume cannot be assumed would effectively reduce diffusion-exchange of gas with the surrounding bulk medium, and therefore inhibit the effects of barometric pumping. This case, however, was not considered here. At very small fracture widths, the volume of gas migrating along the fracture will eventually grow small that surface transport cannot occur. The beginning of this is apparent in the leftmost data points of Figure 4.4.

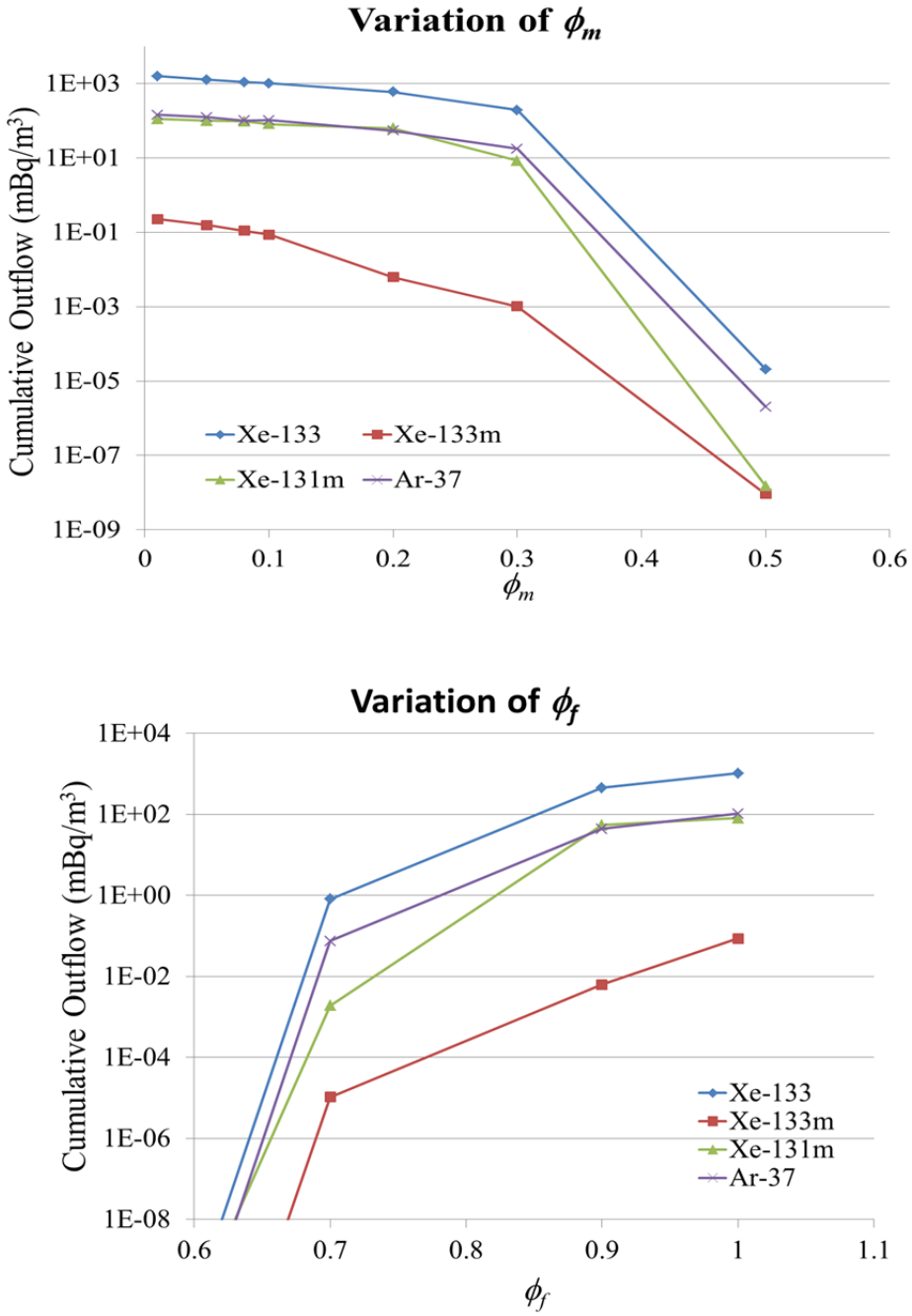

Figure 4.5 Plot of simulated 55 day radionuclide outflows for various values of the bulk matrix and fracture porosity and other input values held constant.

The effect of varying the matrix porosity ϕ_m is shown at the top of Figure 4.5 and shows a relatively easy to explain correlation. The net effect of increasing the matrix porosity is that pressure waves extend increasingly far into the matrix, and subsequently horizontal advection essentially washes out the fracture-matrix seepage mechanism required for the barometric "ratcheting" effect. Beyond porosities of 0.3 to 0.5, gas that manages to migrate into the bulk medium is easily removed on subsequent pressure highs, so that gas essentially move in and right back out down the fracture. This enhanced breathability prevents substantial buildup of concentration in the higher system region, thus inhibiting overall outflow at later times. Decreasing the fracture porosity ϕ_f below 1.0 has an equally decided effect on the overall outflow, as shown in the lower plot of Figure 4.5. The net result of a lower porosity in the fracture is that a smaller volume of gas is available for both upward transport toward the surface as well as fracture-matrix diffusion exchange. Additionally, the lower porosity increases the speed with which fracture pressures are equalized, resulting in a diminished flow velocity in response to pressure lows at the surface.

Figure 4.6 shows the results of varying the amplitude of the pressure variations. Given that the entire model is based on transport driven by pressure gradients, increasing the strength of the variations has the obvious effect of drawing out more of the contaminant. Of all the parameters of variation considered in the sensitivity study, variation of the pressure amplitude seems to have the most direct, and profound, effect on the resulting isotopic ratio of cumulative radioxenon and argon outflow. This is explored in more detail in the next section, in which a true atmospheric pressure history is used to drive the system in place of the smooth sinusoidal one considered here.

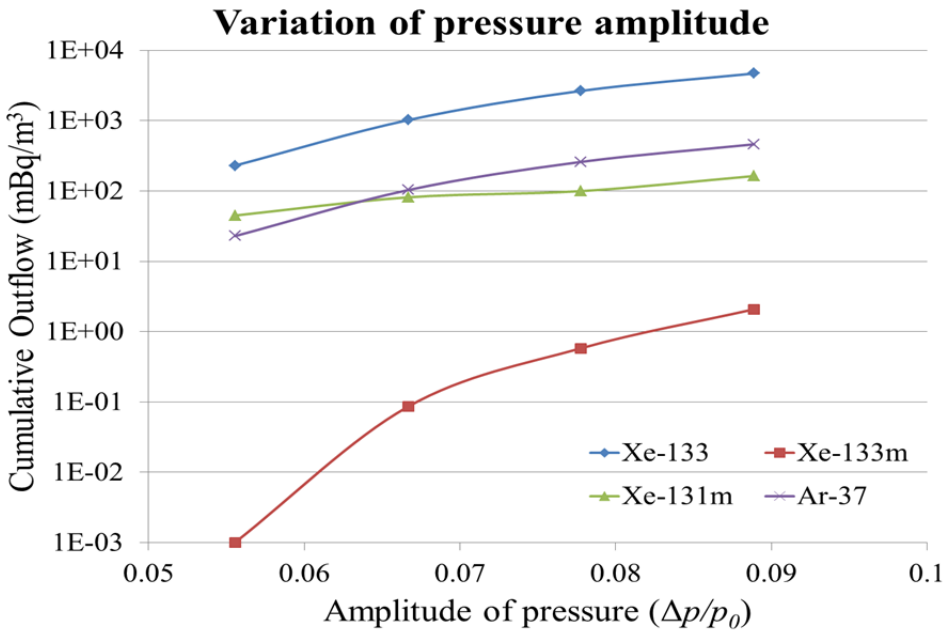

Figure 4.6 Plot of simulated 55 day radionuclide outflows for various values of the atmospheric pressure amplitude and other input values held constant.

4.2 UTEX MODELED XENON ISOTOPIC SENSITIVITY STUDY

Much of the initial transport simulations with the earliest version of the UTEX model presented in the previous section was conducted largely as part of a Master's project found in Lowrey (2011). Following this work, the transport code underwent significant rewrite, modularization and general efficiency improvement as well as verification to bring it more in line with its current state and capabilities. As the focus of UTEX modeling has always been on an examination of the potential for geologic transport to alter isotopic ratios of hypothetical UNE noble gas, the first task considered by the revamped model was a large scale sensitivity study to look at how varying the major geologic input parameters can result in fluctuations in the isotopics of radioxenon.

4.2.1 Simulation input

One of the improvements to UTEX that was made in the vetting phase of work was the ability to incorporate an arbitrary, user-supplied atmospheric pressure history to drive the advective transport within the system. In considering this transition and the potential transport effects that can result, a couple of points should be made about the assumption of a simple harmonic pressure variation. First, the nature of pressure-dependent bulk transport of gas in the subsurface (advection) is due to the existence of pressure gradients that develop in the system pressure response. The smooth variation of a sinusoidal atmospheric pressure approximation induces a similarly smooth response in the geological system, as can be seen in Figure 4.1, where pressure gradients arise as a result of the attenuated and time lagged response at different points in the system. A true atmospheric pressure history is not typically smooth even during periods of relatively stable pressure. This difference is certain to induce larger gradients in the system. Second, the amplitude of the simulated sinusoidal pressure variations corresponds to very large fluctuations in pressure that would be representative of unusual events such as large thunderstorms, etc. Together, these two points make the results presented in 4.1.3 perhaps representative of the conceptual effects of changing atmospheric pressures, but not directly indicative of real world scenarios.

The atmospheric pressure history adopted as input for UTEX simulations of UNE gas transport is shown in Figure 4.7. This pressure history was compiled from 1-hour resolution atmospheric data at Mercury, NV was linearly-interpolated within UTEX preprocessing to provide pressure data at arbitrary time step resolution. Also shown for comparison is an example smooth sinusoidal pressure history as might have been assumed in simulations of the previous section. The mean static pressure line in the figure corresponds to the mean of the “real pressure” date. Clearly the real pressure example is

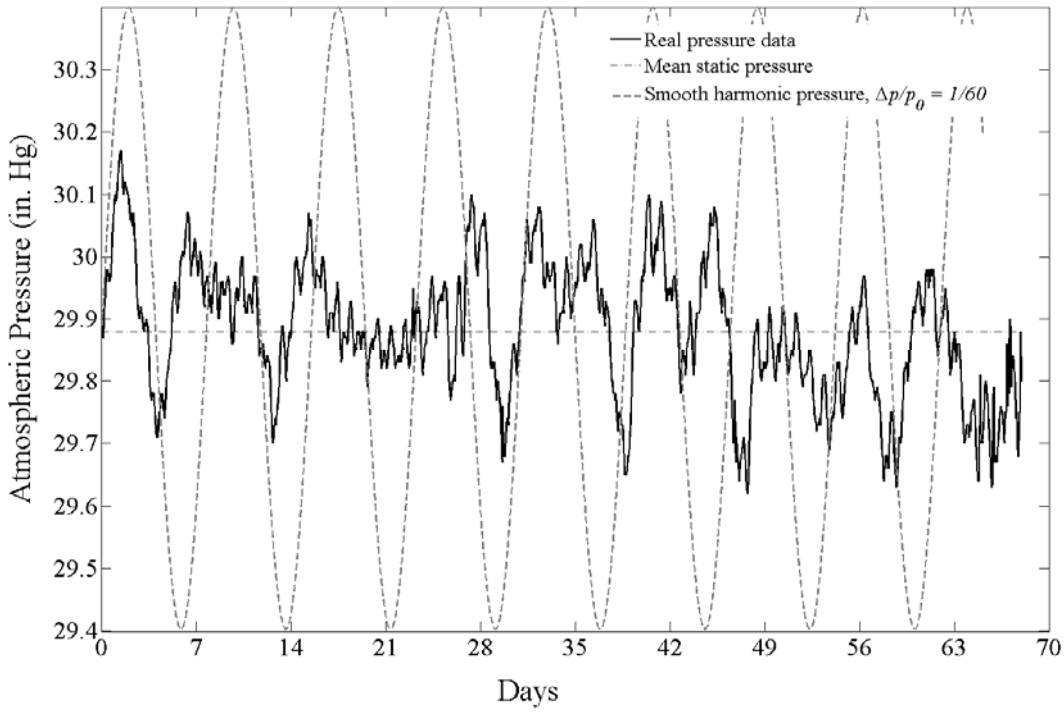

Figure 4.7 Plot of the atmospheric pressure history compiled from real data at Mercury, NV utilized as input for present and subsequent UTEX simulations presented in this work. For comparison, overlaid is a smooth, sinusoidal-varying pressure history like that used in previous simulations.

far from smooth; the largest fluctuations appearing in Figure 4.7 are of the order 1-2% and occur over several days while smaller variations of a fraction of a percent can occur hourly. The effect of real barometric fluctuations on driving transport in a fractured system is much more complicated and as well be shown, more interesting with regard to effects on UNE gas isotopics.

Given the variability of geologies worldwide, selection of appropriate geologic test cases is somewhat arbitrary and difficult to define. However, since a great deal of work has been done to characterize the geology of the Nevada Test site (NTS) and it is obviously relevant to the present topic, available NTS data was used to make a general characterization of potential UNE testing environments (DeNovio *et al.*, 2005; McCord,

2007). Ranges for the major physical parameters that serve as input into the UTEX model are summarized in the first data column of Table 4.2. The second column denotes the chosen parameter values utilized within the UTEX sensitivity study that follows.

Table 4.2 Generalized geologic parameter ranges from the Nevada Test site considered for the geologic parameter sensitivity study of UTEX simulated transport of UNE noble gas (DeNovio *et al.*, 2005; McCord, 2007).

	NTS Geological Range	**Parameter Space**
Detonation Depth (m)	450-600	[450, 525, 600]
Matrix Porosity	0.01-0.05 and 0.35-0.45	[0.01,0.05,0.1,0.3,0.37,0.45]
Matrix Permeability (m^{-2})	1E-17 to 1E-15	[1E-17, 1E-16, 1E-15]
Fracture Spacing (m)	1.0-15.0	[1.0,2.5,5.0,10,15]
Fracture Width (mm)	0.005-1.5	[0.01, 0.1, 1.0]

4.2.2 HEU source transport results

The atmospheric pressure history and parameter space shown in Figure 4.7 and Table 4.2 respectively were used to simulate transport in UTEX of the source term defined by fast pulse reactor fissioning of highly enriched uranium (Tables 2.4-2.6). This calculated source term was initially distributed in a "halo region" of thickness 200 m located at a system depth corresponding to the "detonation depth" parameter of Table 4.2. Simulations with UTEX explicitly tracked the radioxenon concentrations at each point in the spatial mesh and quantities which reached the upper boundary of the system were assumed to escape the medium and diffuse into the atmosphere. These simulated outflows, no longer subject to isotopic fractionation in the geologic medium, were "collected" and used to evaluate the evolution of radioxenon ratios that comprise the hypothetical event's "signature."

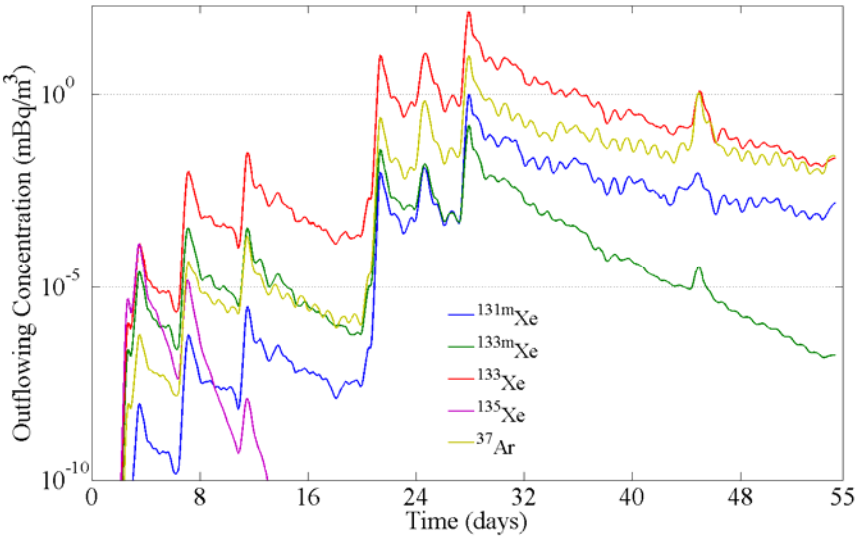

Figure 4.8 Simulated outflow curves over 55 days for four radioxenon isotopes as well as ^{37}Ar for one set of values in the sensitivity study parameter space. Note that ^{37}Ar, with a much longer half-life than the longest-lived xenon isotope, typically falls much slower between release spikes.

Figure 4.8 shows an example simulated radioxenon and ^{37}Ar release history resulting from UTEX simulation of transport over 55 days with one set of values from the parameter space defined in Table 4.2. The effects extended pressure lows in ratcheting up the radionuclide concentration are obvious in the plot. All the radioxenon isotopes (except short-lived ^{135}Xe) reach a maximum removal concentration following pressure lows between 20 and 30 days. ^{37}Ar, which is not continuously produced from parent decay, builds up much more efficiently than the shorter-lived radioxenon isotopes. Past 30 days, the concentration of ^{37}Ar releases falls more slowly than xenon. Simulated maximum concentrations of ^{37}Ar leakage are an order of magnitude smaller than ^{133}Xe but an order of magnitude higher than the ^{131m}Xe peak. This release estimate is consistent with Haas *et al.* (2010) and Carrigan & Sun (2012).

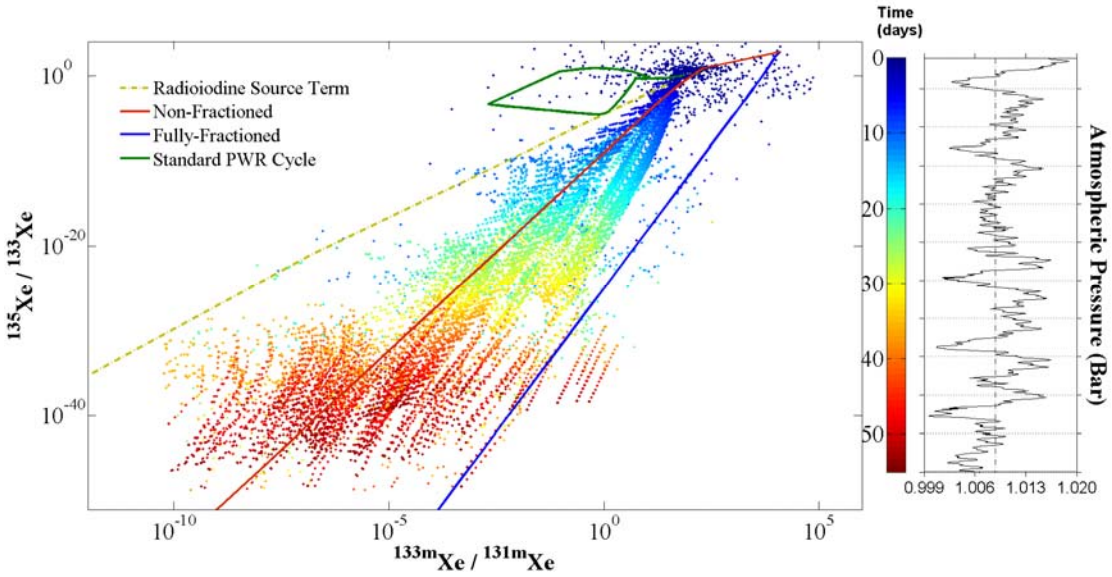

Figure 4.9 Multi-isotopic ratio correlation (MIRC) plot with 1-day sampled simulation data from an HUE source term transport sensitivity study. Data points are color-coded according to the number of days post-detonation the sample was removed from the system.

A total of 990 simulations covering various permutations of the values in the parameter space defined in Table 4.2 were conducted. Transport was modeled over 55 days and the resulting 1-day sampled radioxenon leakage ratios for the four isotopes of greatest concern are plotted on a multi-isotopic ratio correlation plot, as shown in Figure 4.9. For reference, the associated atmospheric pressure history is plotted on a horizontal axis to correspond roughly to the progression of time in the MIRC plot. While the variation of ratios seen in this plot as well as their relation to bounding cases will be discussed further in Section 4.3, some immediate points can be made about the results presented in this plot.

- All of the simulations of the sensitivity study were run from the same initial source term. Thus, if the transport processes had no effect on the isotopics, one would expect

the simulated curves to follow a single line of decay on the MIRC plot. Clearly this is not the case.

- While a large portion of the data points fall within the non-fractioned and fully-fractioned[13] decay "bounds" (note, many such cases overlap in the plot and appear as single points), roughly 15% of the estimated outflow points fall outside the bounded area traditionally associated with a nuclear explosion signature.
- The proposed addition of a new "iodine source term" bounding line catches the majority of points outside traditional bounds. This is further discussed in the following section.

The results of this sensitivity study for an HEU fast pulse fission burnup source term has been published in Lowrey *et al.*, (2013). It is important at this point to comment that isotopic ratios of xenon resulting from numerically simulated transport are easy to calculate regardless of the order of magnitude of the actual concentrations being considered. In other words, many of the simulated ratios appearing in Figure 4.9 certainly correspond to "non-detectable" points in the sense that ^{133m}Xe and ^{135}Xe can have concentrations simulated to be orders of magnitude smaller than detection limits. Additional MIRC plots of the simulated radioxenon releases are shown in Appendix D.

4.2.3 Pu source parallel study

Parallel to the HEU source term used in the above sensitivity study, a Pu source term simple faster reactor burn was also calculated, results of which were also given in Table 2.4-2.5 Mostly for the sake of completeness and to further demonstrate the potential ambiguity that underground transport processes can induce in possible UNE

[13] The “non-fractioned” decay case corresponds to xenon ingrowth from iodine and precursors continuously building into the inventory while “fully-fractioned” assumes a removal of xenon precursors from the picture so that xenon inventories are determined only according to xenon decay rates.

explosion signatures, a large portion of the HEU sensitivity study was repeated with the slightly different Pu fast pulse fission source term. Generally speaking, transport effects on isotopic variations should affect xenon gas coming from a plutonium source the same way as from an HEU source - the net result of the transport is essentially the smearing of the xenon signatures.

For the case of plutonium, an additional consideration was made for the possible xenon contribution from the spontaneous fission of ^{240}Pu in the leftover debris. An estimate of such a source was made by simply assuming no burnup of the initial ^{240}Pu. The half-life of the nuclide is 6564 years and has spontaneous fission branching ratio of 5.7E-6%. The result is a relatively constant radioxenon production source from spontaneous fission that is many orders of magnitude smaller than the initial post-UNE amount and only slightly higher than the general range of radioxenon background levels, which are discussed in-depth in a later chapter on soil-gas background. This spontaneous fission was added to the UNE-produced iodine source term.

Results of the parallel Pu sensitivity study, which covered half the number of simulations depicted in Figure 4.9 are shown in Figure 4.10. Clearly, the nature of transport effects are essentially the same - transport processes can alter the UNE source signature from that which would be expected if xenon isotopic were only being determined by radioactive decay. The addition of spontaneous fission to the source creates even further ambiguity in the original source signature behind Figure 4.10; the later time swings in pressure clearly visible in Figure 4.9 still appear in Figure 4.10, but the additional spread in the data points make it apparent. This only further emphasizes the main point that subsurface transport processes have the potential to smear underground radioxenon signatures beyond the bounded areas traditionally associated with underground nuclear explosions.

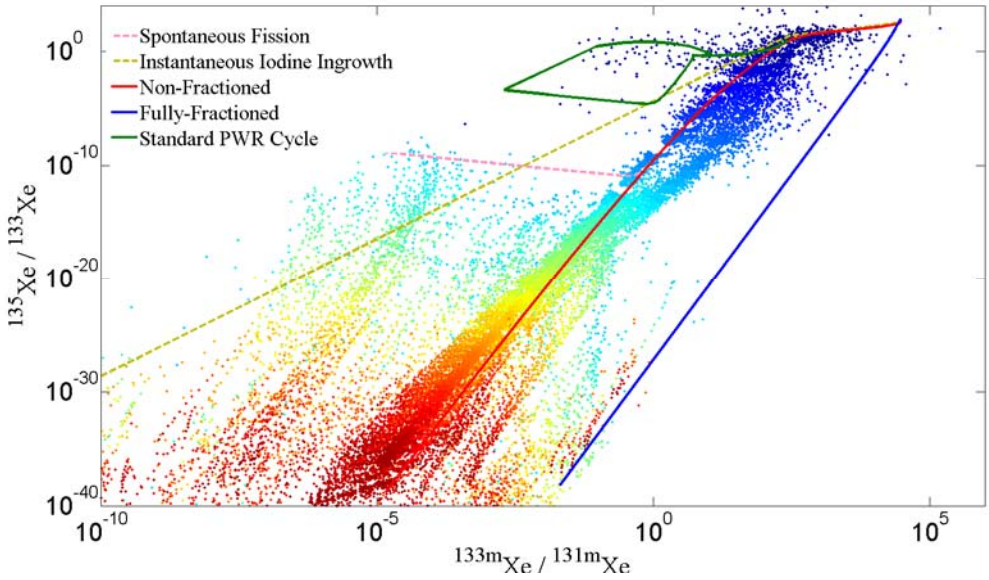

Figure 4.10 Multi-isotopic ratio correlation (MIRC) plot with 1-day sampled simulation data from Pu source term transport sensitivity study. Data points are color-coded according to the number of days post-detonation the sample was removed from the system, as in Figure 4.9.

4.3 ISOTOPIC RATIOS DISCUSSION

Looking at the very busy plots of Figure 4.9 and Figure 4.10, it is clear that the influence of subsurface transport on radioxenon signatures is complex and not entirely transparent. In this section, the mechanisms that determine the various bounding cases and induce the isotopic fluctuations seen in Figure 4.9 are discussed. Largely speaking, the wide range in isotopic ratios can be explained by the source mixing that results from variations in transport rates and to a much lesser extent the differential transport of the various xenon isotopes.

4.3.1 Bounding cases

The isotopic signal seen above ground is the result of xenon that was produced directly by the fission event and a time dependent source term that results from the decay of iodine precursors. Traditional underground nuclear explosion signatures are typically assumed to fall somewhere between non-fractioned and fully-fractioned decay bounds. The former refers to a decay case in which xenon ingrowth from iodine and precursors factors into the inventory while the latter assumes a removal of xenon precursors from the picture so that xenon quantities are determined only according to xenon decay rates. The most notable difference between "new" and "old" xenon in these respective cases is ^{135}Xe - in the non-fractioned decay scenario, the much shorter-lived ^{135}Xe is more noticeably propped up through parent nuclide decay than the other isotopes. In simple, continuous transport scenarios without changes in flow direction, a discrete sample of radioxenon from a UNE source, once removed from iodine, will decay according to the fully-fractioned case. Including more realistic transport perturbations potentially induces more interesting signature changes.

Low atmospheric pressure spikes can have a significant effect by quickly drawing gas to the surface and partially depleting the xenon inventory in parts of the underground environment. The ratios of radioxenon isotopes emitted above ground *after* such low pressure periods in the short term would then be more heavily influenced by xenon coming from radioiodine decay in those regions. This xenon removal scenario is illustrated in Figure 4.11. An analytical examination of this effect and how it leads to a new iodine ingrowth boundary line is presented in Figure 4.12:

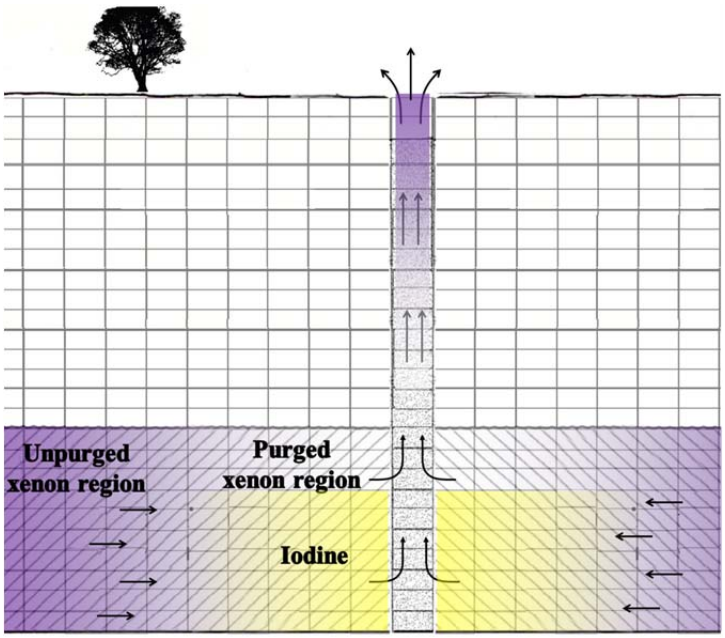

Figure 4.11 Illustration of localized subsurface radioxenon depletion that can potentially result in a xenon isotopic signature dominated by iodine ingrowth.

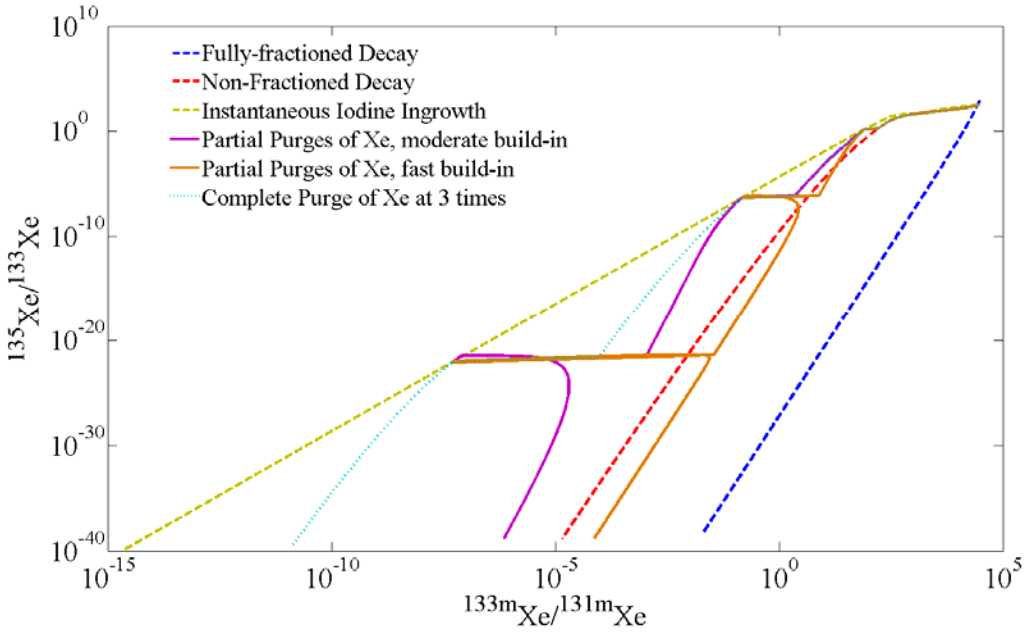

Figure 4.12 Analytical consideration of the effects of temporary xenon depletion on resulting radioxenon signatures for three cases of iodine and non-purged xenon ingrowth from HEU source term.

- The yellow dashed line corresponds to radioxenon ratios that result from instantaneous ingrowth of xenon from iodine.
- The light blue decay curve corresponds to a situation in which 100% xenon inventory is purged at three different times in the transport, and xenon builds back in after those times. Note that immediately after purging, the xenon ratios lie on the dashed yellow iodine line.
- The purple and orange paths represent cases where xenon is purged "locally" near a fracture, and is subsequently replaced by both iodine ingrowth as well as movement of "unpurged" xenon gas in the surrounding media, as illustrated by Figure 4.11. What results is a *spike* in the signature towards the dashed yellow iodine line followed by a movement of the decay lines back towards the more traditional UNE signature area.

Figure 4.9 shows several instances of this xenon depletion effect (most notably beginning around day 38) where the simulated xenon ratios are pushed toward the signal that would come solely from decay of radioiodine precursors (indicated by the dashed yellow line). In situations such as these, monitoring of down-wind air samples (which would detect the purged xenon) and on-site sampling (which would detect xenon from recently decayed iodine) could produce very different signals. With respect to simulated transport in general, after 10 days post-detonation, none of the simulated data coincide with the radioxenon signal from a commercial light water reactor. So even though the proposed iodine boundary has implications for the usefulness of proposed discrimination lines, it would still be easy to rule out power reactor sources for the situations simulated during an on-site inspection if all four radioxenon isotopes of interest are measured.

Xenon ratios that fall to the left and right of the iodine and fully-fractioned lines can be explained in terms of differential transport. Decreasing atmospheric pressure will increase the rate of xenon movement into fractures as well as its upward advection within them. The individual xenon isotopes can be thought of as comprising separate, overlapping plumes. The rate at which isotopes diffuse through the bulk geology is inversely proportional the square root of their mass (Bird *et al.*, 2006). As a result, lighter xenon isotopes will travel faster than do the heavier ones. While the difference in diffusion rates is small, in certain conditions it can cause the leading edge of the isotope plumes to reach the surface at slightly different times. Because isotope concentrations can vary by orders of magnitude across a plum's leading edge, this can significantly skew the isotope ratios, pushing the $^{133m}Xe/^{131m}Xe$ and $^{135}Xe/^{133}Xe$ signals to the left of the iodine line. Increases in pressure would correspondingly force gases back down the fractures. Rapid fluctuations in atmospheric pressure can then set up a situation where lighter isotopes are preferentially depleted from the geology, which would push the $^{133m}Xe/^{131m}Xe$ and $^{135}Xe/^{133}Xe$ signals to the right of the fully-fractioned lined. In both cases the effect would be most pronounced during the first few days after a detonation, when the location of an underground plume's leading edge is most important, which is what is seen in Figure 4.9.

4.3.2 Parameter sensitivity

An evaluation of the modeled HEU source radioxenon isotopic ratios sensitivity on geologic parameter values was made in Lowrey *et al.*, (2012) . To evaluate the effect of varying each individual geologic parameter on the resulting fractionation in the HEU source sensitivity study, the isotopic ratios $^{133m}Xe/^{131m}Xe$ and $^{135}Xe/^{133}Xe$ were tabulated at regular intervals for each value of the parameters in question while holding all of the

others constant. A pseudo *variance* factor was then calculated for each set of data describing the (log) average spread in simulated ratios that resulted from considering the variation of only one parameter while holding all others fixed. This deviation from the log average ratio was calculated for each one-minute time step and then averaged over the full 55-day simulation time for each of the simulations conducted in the geologic sensitivity study. This allowed for a large-scale survey of the variability in isotopic ratios resulting from 990 parameter permutations and the determination of their degrees of inter-dependency.

An example dependency comparison is provided in Figure 4.13 and Figure 4.14 to illustrate the variance concept described above. Figure 4.13 shows the simulated 55-day radioxenon ratios plot for three different values of the total depth parameter, L, while holding all other values fixed. In this case, the effect of varying the total system depth was very small, as almost no variation in xenon ratios is seen in Figure 4.13; the calculated variance in the radioxenon ratios in this case was 0.0039. Figure 4.14 shows the effect of varying the bulk matrix porosity, ϕ_m, while holding all other parameters fixed. Isotope fluctuations in Figure 4.14 are clearly evident, and it can be concluded that the porosity is having a considerable effect on the radioxenon ratios that leak from the system following transport. The variance for the scenario in Figure 4.14 is 2.2162, much higher than that of the ratios plotted in Figure 4.13. These illustrations mark only two cases where a single parameter is varied while others are held constant. Additionally, the same can be done by varying multiple parameters to gain insight into correlation of parameters.

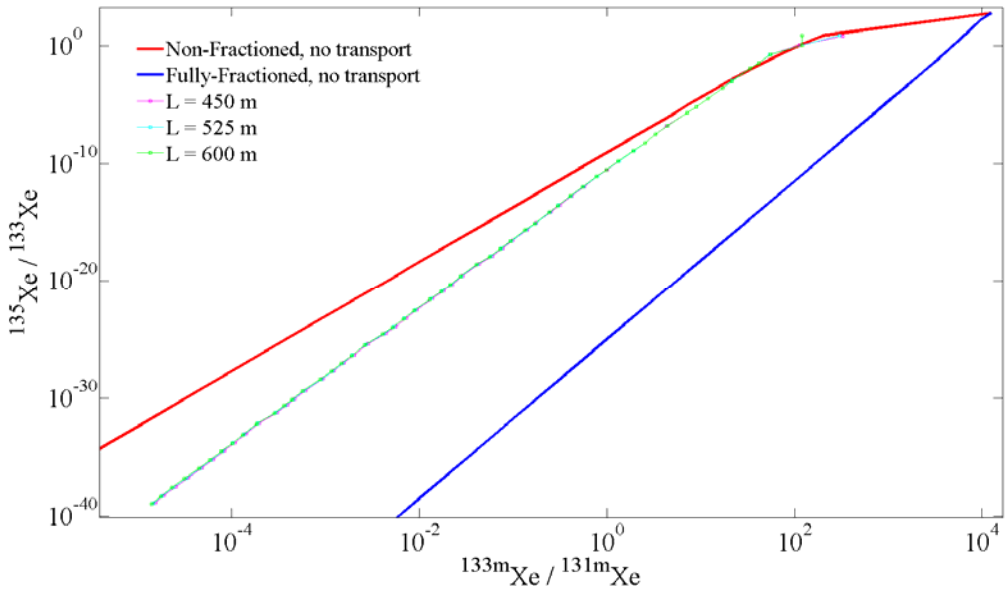

Figure 4.13 Very small radioxenon fractionation dependence on total system depth, L. Other parameters are held fixed. This set of data had a small variance of 0.0039.

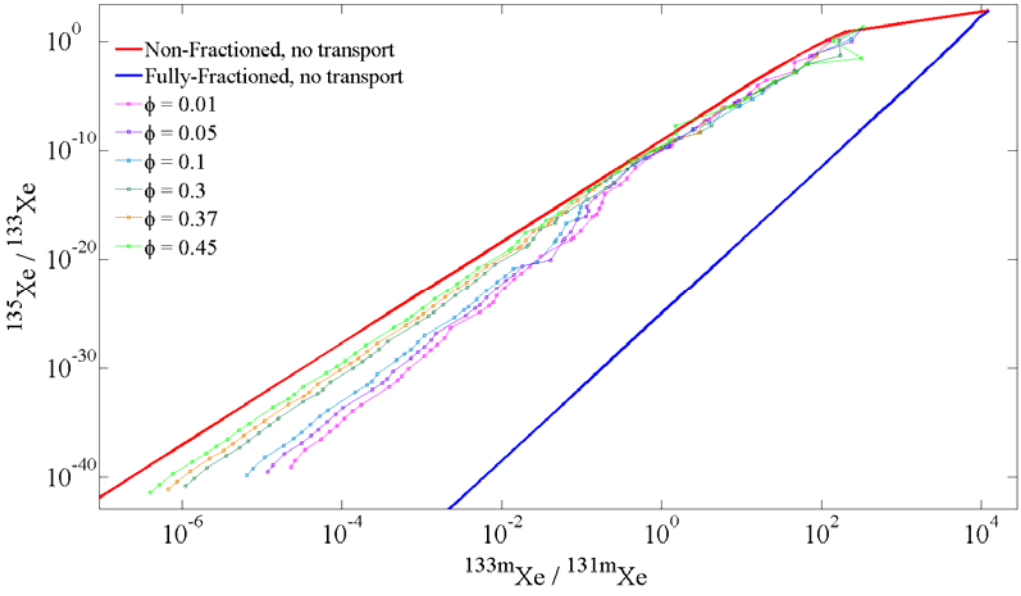

Figure 4.14 Significant radioxenon fractionation dependence on bulk matrix porosity, ϕ_m. Other parameters are held fixed. This set of data had a much larger variance of 2.2162 as compared to that of Figure-2

The results of the variance factor calculations for all 990 simulations run for this study are summarized in Table 4.3. The mean variance column of Table 4.3 lists the log average spread in radioxenon ratios on a four isotope MIRC plot like Figure 4.13 and Figure 4.14 that results from considering all cases where four of the input parameters are held fixed while one is varied over its parameter space. By this definition, a parameter that has no effect on the resulting isotopic ratios of radioxenon leakage would have a corresponding mean variance of zero. From these results, the parameters δ_f, δ_m, ϕ_m, and k_m all show significant effect on the radioxenon ratios; for a given set of fixed values, varying the lower system depth, L, shows a much smaller effect on the variability of ratios.

A few physical insights can be easily drawn from these results. For instance, the fracture in these simulations is taken to be a very narrow *open* channel, so pressure variations at the top of the system propagate down more rapidly than they do laterally from the fracture to the deeper parts of the less porous matrix medium. As a result, ratio variability is more sensitive to the lateral fracture spacing δ_m than the system depth L. Also, varying the matrix porosity over nearly two orders of magnitude has a substantial effect on radioxenon ratios – as the bulk matrix is essentially opened up, transport everywhere in the system becomes more homogeneous and differential transport rates less important. The result is a less fractionated radioxenon signature, Figure 4.14. Variation of the permeability, k_m, has a similar effect.

Table 4.3 Concise summary of results for the variance of radioxenon ratios for different geological parameters.

	mean variance	**p-values** *on correlation of column variance with row parameter*				
		L	δ_f	δ_m	ϕ_m	k_m
L	0.0535	-	0.523	**0.091**	**0.006**	**0.003**
δ_f	0.4124	0.311	-	0.415	0.891	0.341
δ_m	1.6313	**0.039**	0.497	-	**<0.001**	**0.049**
ϕ_m	0.5223	**0.009**	0.599	**<0.001**	-	**0.032**
k_m	0.8247	**0.005**	0.672	**0.052**	**0.021**	-

The mean variance summarization of the 990 simulation sensitivity study in column 2 of Table 4.3 allows for a coarse generalization of isotopic variability. However, it also oversimplifies the nature of the transport mechanics by ignoring the fact that some parameters are more likely to be important in certain scenarios while maybe not so much in others. To begin to gain insight into the inter-dependency of the different parameters and how they can influence the resulting radioxenon ratios, the variances calculated for each test parameter were analyzed for correlation with the other parameters. These results are summarized as p-values in Table 4.3 for the likelihood that the observed mean deviation could be expected if the two parameters were indeed uncorrelated (the null hypothesis for a χ^2 test). The bolded p-values in the table are "statistically significant" and correspond to those column parameters that apparently affect the amount of ratio variability caused by changing the value of the row parameter.

For example, Figure 4.15 shows the averaged fractionation variance of the parameter δ_m for the six different fixed values of matrix porosity ϕ_m. This particular choice appears to have a very strong correlation and accordingly had a p-value in Table 4.3 of <0.001. It is important at this point to note that the strength of the correlation implied by the p-values does not necessarily reflect the size of the mean variance of that

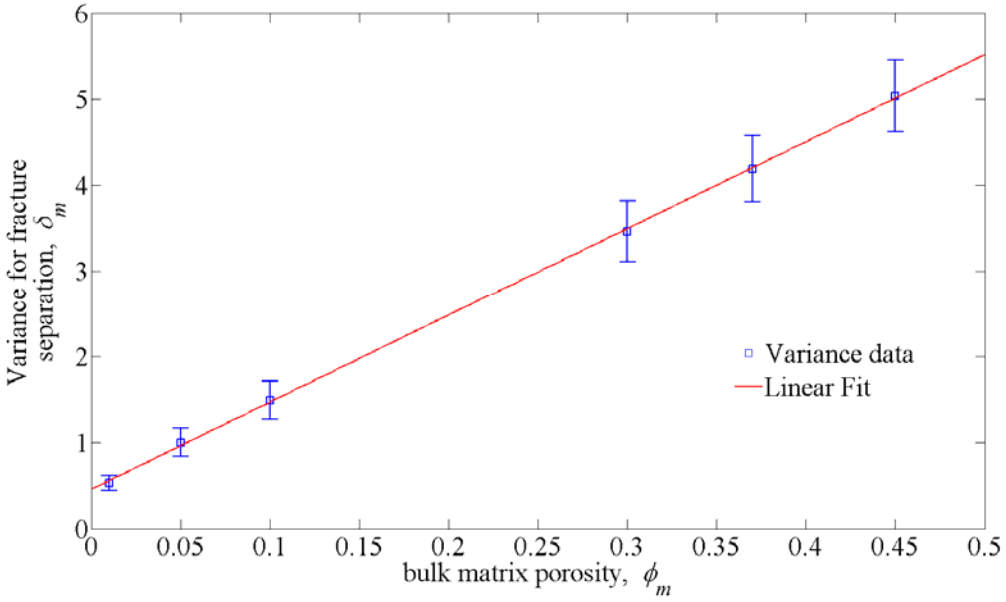

Figure 4.15 Averaged ratio variance of the parameter δ_m for the six different fixed values of matrix porosity ϕ_m suggesting a very strong correlation. The "error bars" represent standard error in the calculation of the means.

parameter in column 2 of Table 4.3. This is most relevant for the case of the system floor parameter L - while the variability of the radioxenon ratios with changing L appears to be correlated with the variability of several other parameters, the *size* of the variance is nevertheless small. Within this sensitivity study, varying the depth L of the emplaced halo contaminant has the least effect on the resulting isotopic ratios of xenon leaking from the surface. In the case of the fracture width δ_f, while its value apparently does influence ratios, this variation is not strongly correlated with values of the other parameters.

4.4 SAMPLING CONSIDERATION

In the preceding results, the UTEX model simulates the *act of sampling* in the simplest, most non-invasive way. Gas is allowed to transport to the top of the system where upon it is "sampled" by being tabulated and removed from the system at each time step – material that reaches the top is therefore assumed to escape into the atmosphere and is lost from the system. These releases from the system are summed in discrete time bins to simulate a sample over that time. In reality, soil-gas sampling can be conducted in different ways, some quite intrusive to the point that the method of collection could even alter the resulting fractionation. This specific scenario is considered in Chapter 7 dedicated to on-site inspection modeling. In this section, a quick examination is made of the additional fluctuation in isotopic ratios that can result by considering the continued decay of gas even as it is being sampled. Also, results of a smaller study similar to that presented in 4.3.2 is presented to look at the variation of radioxenon isotopic ratios with the position of the sampling point near the top of the UTEX modeled system.

4.4.1 Sample decay correction

For initial simplification and flexibility, radioactive gas outflows in the early UTEX simulation results were essentially frozen in time upon removal from the system. As a result, the effects of further decay and temporal mixing were ignored. Intuitively, the error introduced by not simulating sample decay should increase as sampling times increase and radioisotope half-lives decrease. To obtain detectable amounts of radioxenon, typical high-volume air sampling times are in the range of 12 to 24 hours (Carrigan & Sun, 2011).

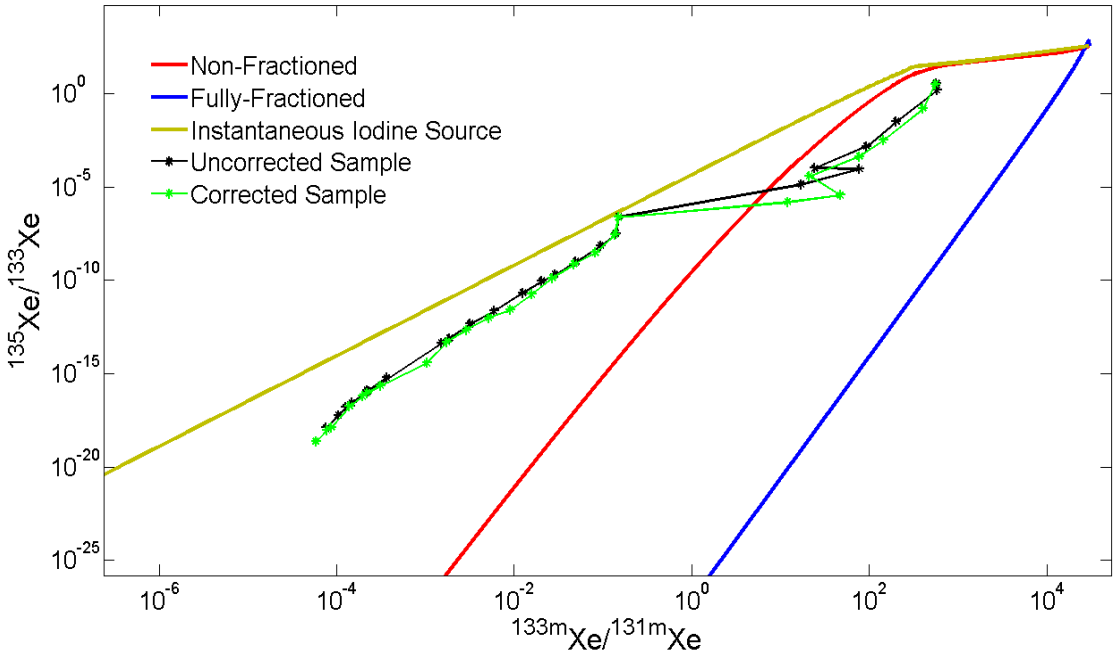

Figure 4.16 An example of before and after sample decay correction for a single instance of UTEX transport within the larger geologic parameter sensitivity study. Most importantly is that the non-corrected curve overestimates short-lived ^{135}Xe in the sample.

Correcting for the continued decay of sampled radioxenon is easily fixed in a post-simulation process and for the most part was found to not significantly affect the simulated radioxenon isotopics. The results of the original HEU source subsurface transport sensitivity study presented above and appearing in Lowrey *et al.*, (2012) and Lowrey *et al.*, (2013) were re-analyzed correcting for sample decay, and showed no significant difference. Of the radioxenon isotopes simulated in UTEX transport, only ^{135}Xe with a 9-hour half-life undergoes substantial decay within a 1-day sampling window. On the four-isotope log-log MIRC plots largely considered in this chapter, the partial decay of sampled ^{135}Xe will have the effect of slightly shifting ratio curves down the y-axis. Figure 4.16 shows an example of this correction and its effect on the ratio curve, which basically adjusts the previously overestimated ^{135}Xe. The degree of this

overestimate in the xenon leakage estimates is dependent on the timing of the largest outflows in the simulated sample - if a large outflow occurred early in the sampling window, the decay of the sample is more noticeable than if that spike occurred near the end of the time window.

4.4.2 Sample position sensitivity

Lastly, the variability of the radioxenon ratios as a function of sampling depth and between-fracture position was examined. The ratios were calculated as a function of time at depths between 0 m to 27 m as well as located at points corresponding to $0.25\delta_m$, $0.50\delta_m$ and $0.75\delta_m$ within the bulk matrix medium, where δ_m is the fracture spacing[14]. The dependency on depth and position for a given set of geologic parameters was also evaluated.

A plot of the results of the fractionation variances for sampling the radioxenon ratios at different depths below the surface and positions within the bulk matrix medium is given in Figure 4.17. Two things are immediately evident from this plot. First, perhaps surprisingly, the inter-fracture sampling position dependence of the ratios is greater than the sampling depth dependence. Second, *both* dependencies are apparently very small - compared to the geological parameter sensitivities considered in the previous section, sampling depth and position have only a minute effect on altering the sampled ratios of radioxenon. Figure-7 shows multi isotopic ratio correlation plots for typical fractionation due to varying the position and depth of sampling over the ranges considered in this study.

---

[14] Since UTEX actually models $\delta_m/2$ width slabs of bulk matrix material, the position points are really fractions of $\delta_m/2$.

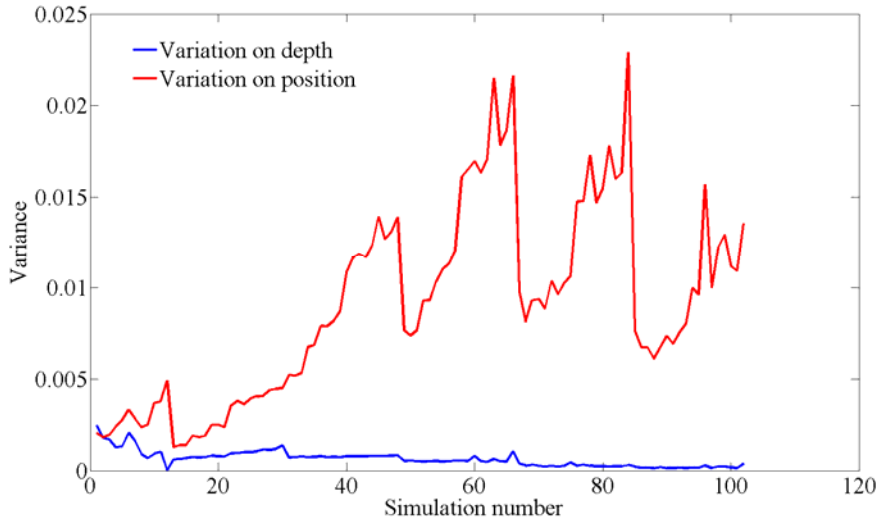

Figure 4.17 Plot of the radioxenon ratio variances resulting from considering samples at points corresponding to different sampling depths and lateral positions within the bulk matrix material for 102-simulation set of geologic parameters.

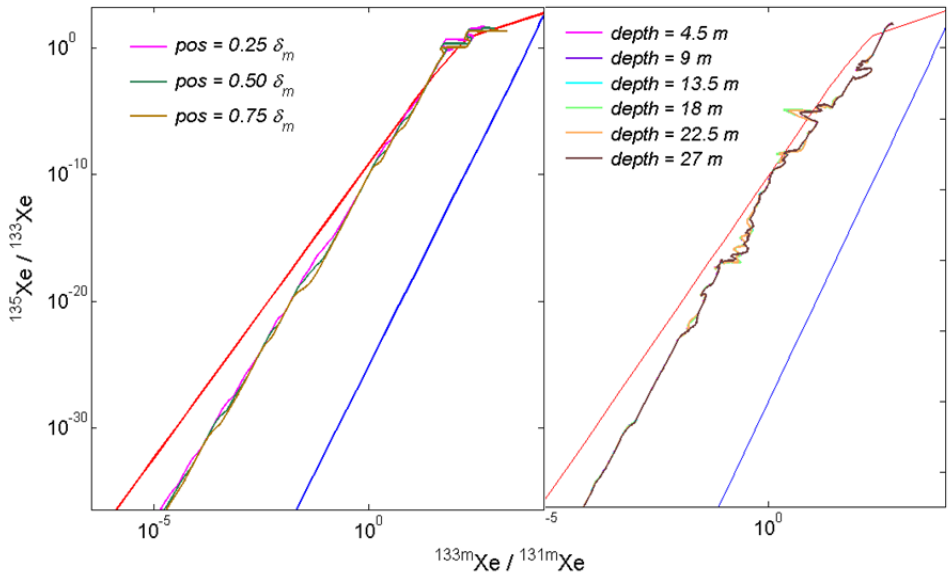

Figure 4.18 Examples of the small fractionation changes resulting from simulating sampling of radioxenon ratios at different lateral positions within the matrix and at different depths below the surface. Note the scales are smaller than previous multi isotopic ratio correlation plots so that the smaller differences are visible

4.5 CONCLUSION

It is clear from the UTEX simulations of the sensitivity studies presented here that geological transport of xenon gas can significantly affect the isotopic ratios that are used to determine whether or not a clandestine nuclear test has taken place. While much of the simulation data fall within the traditionally expected bounds for an underground nuclear explosion, there are many instances in which radioxenon isotope ratios have been simulated to fall well outside of the standard domain. Verification of an underground nuclear explosion test under the CTBT can only be done through the detection of anthropogenic isotopes. The present work has shown that the effect that geological transport has on radioxenon isotope ratios should be considered when using these data to determine whether or not a test has taken place. It remains very important that all but a small fraction of the simulated radioxenon isotope ratios fall between the bounds resulting purely from decay of radioiodine and radioxenon produced only in the fission event. The variability of radioxenon ratios that sit between the proposed radioiodine and the non-fractioned signature bounds should be considered carefully when evaluating data and assigning possible source of emanation.

With respect to the effect of geologic transport on radioxenon isotopics, several broad conclusions can be drawn from the results presented here. First and foremost is that radioxenon fractionation due to geologic transport is a complicated phenomenon. Of the physical parameters considered in this study, it is evident that the presumed fracture width, average fracture separation, bulk matrix porosities and permeabilities all can have very strong effects on the radioxenon isotopic ratios that transport through the system, while the total assumed system depth within the parameter space considered appears to have a lesser generalized effect. This complex influence is especially evident from the p-

values of Table 4.3, which suggest that many of the xenon ratio changes due to one variable are correlated to changes in other variables as well.

The effect of varying the sampling depth down to 27 m and the position within the bulk matrix medium are less compelling, but perhaps not that surprising. The total system depth was varied from 450 m to 600 m, and the variable sampling depth went down to only 27 m – a small fraction of the total depth. The small changes in sampling depths represent only a fraction of the total system depth and that such small changes would have only a minor effect on the observed ratios makes intuitive sense. The effect of altering the sampling position between fractures is harder to examine because the fracture separation distance was a major parameter being varied in this study. Generally, points farther from the fracture exhibit a more suppressed response to pressure variations at the surface. An in-depth study modeling a more realistic sampling scenario in which a bore hole is made in the medium and a pump is used to collect samples is made in Chapter 7.

Chapter 5. Geologic Considerations

Beyond characterization of the physical parameters of an assumed homogenous environment, few assumptions have been made thus far in UTEX modeling about the geology in which a radionuclide source is emplaced. The benefit of previously assuming very simplistic system geology with homogeneous physical characteristics is that it more easily allows for an examination of the sensitivity of radionuclide transport to the various parameters that define the system. As has already been demonstrated, even with a homogeneous geologic model, isolating and understanding the sensitivities of individual parameters is a difficult enough task. Including multiple geologic layers compounds this complexity, but the reality is that true geologies are stratified and inhomogeneous. The capability to model such in UTEX is thus an important step forward. Additionally, the actual effect an underground nuclear explosion (UNE) has on the surrounding geology can substantially affect the distribution of radionuclides within the medium. An examination of this is also made and integrated into the UTEX modeling capabilities.

5.1 Overview of UNE impact in geology

The true relevance of the UTEX model is in considering the transport of well-contained, deep underground nuclear explosions. "Well-contained" in this context refers to the absence of significant venting of radionuclide gas and particulates from the ground, even though it may be possible for some surface effects of the UNE to be noticeable. This does not preclude the model's relevance to situations in which an immediate radionuclide venting, potentially large enough to be noticed in stations of the International Monitoring System (IMS), occurs and is followed by a collapse of rock that subsequently creates a contained underground environment. The point is that the barometric pumping of

subsurface gas through micro-fracture networks in a geologic system, as modeled in UTEX, works to bring UNE evidence to the surface on a timescale of weeks; if quicker transport pathways are available, the delayed effects of barometric pumping might be suppressed or otherwise trumped.

The most immediate effect of a nuclear explosion in the deep underground is the creation of an immensely hot and high-pressure bubble of gas that rapidly expands from the explosion point. Subsequently, a massive shock wave forms that propagates in all directions, crushing or fracturing the rock it traverses. Within the first second following detonation, the pressure of the gas bubble forms an explosion cavity lined by molten rock. In the time that follows, the extreme temperatures and pressures begin to dissipate. The molten rock within the cavity cools and solidifies at the bottom of the cavity (Glasstone & Dolan, 1977). As the pressure decreases in the cavity, the rock overburden can collapse the cavity roof. Further fractured rock above that can likewise crumble, leaving what is referred to as a "chimney" of broken rock or rubble. Assuming the surface is not breached by the progression of falling chimney collapse, an empty void space is left at the top of the chimney whose volume is of the same order as the initial cavity (multiplied by porosity of the filling rubble) (Sweeney, 1999). An illustration of these concepts is shown in Figure 5.1 (Glasstone & Dolan, 1977).

The net geologic effect of a deep UNE is the massive fracturing of the surrounding medium. The scale of this impact is, of course, dependent on the size of the detonation, but according to Glasstone and Dolan (1977) the height of the rubble chimney as well as the radius of crushed and fractured rock can extend more than a hundred meters for small 1 kton-scale UNEs. Even if the rubble chimney fails to extend all the way to the surface and the UNE is technically well-contained, new transport pathways

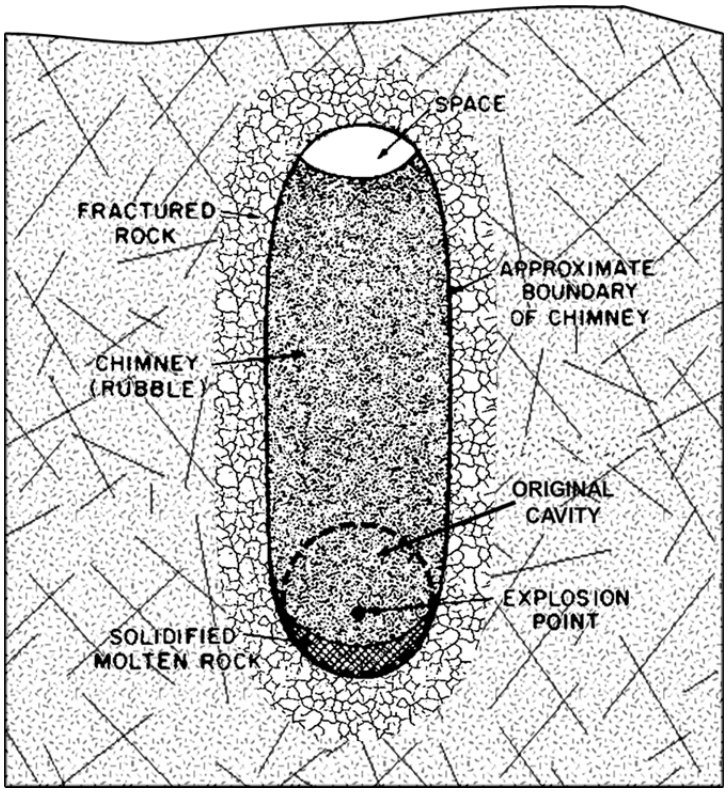

Figure 5.1 Conceptual illustration of the geologic impact of a UNE, adapted from Figure 2.103 of Glasstone & Dolan (1977).

through the fractured rock are created, thus enhancing the likelihood of eventual gas leakage by barometric pumping.

In addition to the geological effects, the high pressure in the early cavity can inject UNE gases directly into the surrounding crushed and fractured regions. Within a period of hours to the first day or two, this cavity over-pressurization dissipates, but Carrigan & Sun have conducted studies indicating that the large thermal gradients resulting from the UNE may have not. In this case, they predict that subsurface convection could still actively draw gas towards the surface through the newly fractured network, and ultimately enhance the likelihood of noble gas detection at the surface

(Carrigan & Sun, 2011). Driven by the initial cavity pressure and thermal convection, within the first day (or more) following a UNE event a contaminant halo will have formed in the fractured rock area around the original cavity. The exact settling of the cavity, chimney, and surrounding fractured rock will all affect the distribution of radionuclide-containing gas in the halo. Thus even in the case of a well-contained UNE, it may be possible for the early noble gas halo to extend upwards hundreds of meters from the cavity with "detectable" amounts of ^{133}Xe and ^{37}Ar driven to the surface even within the first couple of days, though too small to be eventually detected by IMS stations after atmospheric dilution.

5.2 GEOLOGICAL TEST CASE SCENARIO

In the UTEX model, the true complexity of a physical geology is boiled down to specification of just a handful of parameters at each location in a simulation grid. To this point, the "geologies" considered in simulation studies have been largely homogeneous throughout. That is to say, a single set of physical parameters applied to each point in the simulated bulk matrix as a whole. The benefit in this assumption is not really mathematical, for in a finite element model point-by-point specification of different parameters does not really add significant complexity to the numerical solution of the transport. Assuming a homogeneous geology throughout facilitates an examination of the sensitivity of gas transport to the various parameters that define that geology. In reality, true physical geologies are comprised of layered geological zones that facilitate or inhibit gas transport in a more complex way.

5.2.1 Geology types

One limitation of the UTEX model is its assumption that vertical transport of gas takes place in vertically-running fractures embedded within the medium. Within this framework, however, it is possible to define numerous horizontal zones that can correspond to stratification of various geologies. The task thus comes to characterizing these various geologic zones in terms of the major parameters utilized by the UTEX model to estimate gas transport in the system. While this is not difficult to do, a large number of permutations of various geology types stratified in different ways exist in nature, so choosing representative examples for exploration is necessary unless a specific site scenario is being considered.

Within the dual porosity geologic framework of the UTEX model, characterization of the fracture network in terms of average width and separation essentially defines the system scale and paths of transport within. The actual transport and exchange of mass between fractures and adjacent bulk media is determined by the porosities and permeabilities of the simulated geology. These two properties affect transport in different ways and are not always correlated. Porosity refers to the open pore space of a rock in which a fluid or gas can be held, and therefore determines the mass of gas that can occupy the volume. Permeability is basically a measure of the resistance to flow of a fluid through rock, or more accurately, how easily a fluid flows through. (Bear, *et al.*, 1993)

Table 5.1 and Table 5.2 demonstrate the ranges of possible values of porosity and permeability for various bulk geologies. An examination of the two tables will show that there are many examples in natural geology of high porosity but low permeability rock, and vice versa. Figure 5.2 illustrates the relationship between porosity and permeability for various example configurations of grains and pores. For a given

porosity, a higher permeability implies that a larger mass of fluid or gas can flow due to an existing pressure gradient. For rocks of different porosities, a higher permeability in a lower porosity rock can result in less overall mass transport. Soil and sand mixtures are generally of high permeability, but finer varieties exhibit low porosity due to the closeness of grain compaction. Both limestone and sandstone rocks generally have a higher porosity, but can have vastly varying permeability.

Table 5.1 Porosity ranges for a variety of common bulk geologies, adopted from Freeze and Cherry (1977); Hebel (2010).

rock type	density (g/cm3)	porosity (%)
granite	2.75	0-5 - 1-5
granodiorite	2.76	0.5 . 1.5
gneiss	2.75	0.5 . 1.5
syenite	2.79	0.5 . 1.5
pegmatite	2.75	0.5 . 1.5
gabbro	3.01	0.1 . 0.2
basalt	3.01	0.1 . 1.0
quartzite	2.7	0.1 . 0.5
sandstone	2.32	5 - 25
marl	2.1	< 10
tuff	1.8	1 - 53
limestone	2.3	5 - 20
soil, granite	1.7	< 40
soil, lime	1.6	< 40
soil, clay	1.8	< 40
soil, sand	1.6	< 40
soil, volcanic	1.8	< 40
monazite sand	3	< 40

Table 5.2 Permeability ranges for a variety of common bulk geologies. a - unfractured rock; b - fractured rock; adopted from Bear (1972); Bruce (1980); Wang & Narasimhan (1986).

	Permeability Range (m^2)						
Rock Type	10^{-20}	10^{-18}	10^{-16}	10^{-14}	10^{-12}	10^{-10}	10^{-8}
Unconsolidated							
Gravel							
Clean sand							
Silty sand							
Silt							
Clay							
Shale							
Consolidated							
Igneous & metamorphic[a]							
Nonwelded tuff							
Welded tuff							
Sandstone							
Limestone							
Igneous & metamorphic[b]							
Basalt							

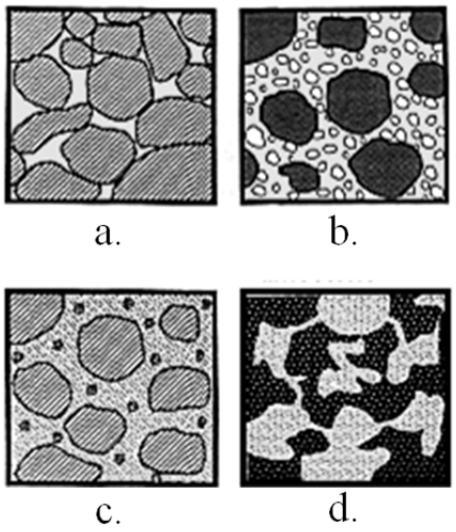

Figure 5.2 Examples of grain-pore configurations in rock demonstrating varying relationship between porosity and permeability. a. low porosity and permeability; b. & c. high porosities and varying degrees of permeability; d. high porosity and low permeability, (McNeill, 1980).

In addition to the inherent differences in porosity and permeability among the major rock and soil types, these properties are also affected by the specific environment of the rock. Compaction, saturation, and clay composition all affect the properties of specific rock formations. For instance, looking at Figure 5.2, examples a) and c) could represent sandstone rock under different degrees of compaction. In a) the grains are tightly packed together, minimizing both pore space and pore connectedness whereas in c) grains are packed more loosely resulting in more connected pore space. Similarly, comparing b) and c) shows a roughly equal compaction of primary grains, but varying amounts of clay content that affects the pore space volume and less so the connectedness. In both of these comparisons, the major rock composition and grain size are the same, and the ability of compaction and clay content to greatly affect rock porosity and permeability are illustrated.

5.2.2 Test Case

Geologic stratigraphy

While there are numerous rock and soil types with characteristics that are influenced by a variety of factors, with respect to UTEX modeling of a test case everything about the geologies can be defined through simple specification of porosity and permeability throughout the system. The choice of a test case geological scenario is somewhat arbitrary, but given that the goal is to simulate possible UNE scenarios, a fair representative geology can be taken from the general region of the Nevada Test Site. Figure 5.3 shows a cross section illustration of the major stratigraphy of the Yucca Flats area at the Nevada Test Site, which is composed primarily of stacked tuff regions. Tuff refers generally to consolidated rock consisting largely of ash and other volcanic debris and is an extremely common, as well as diverse, rock type. On top of the tuff zones sits

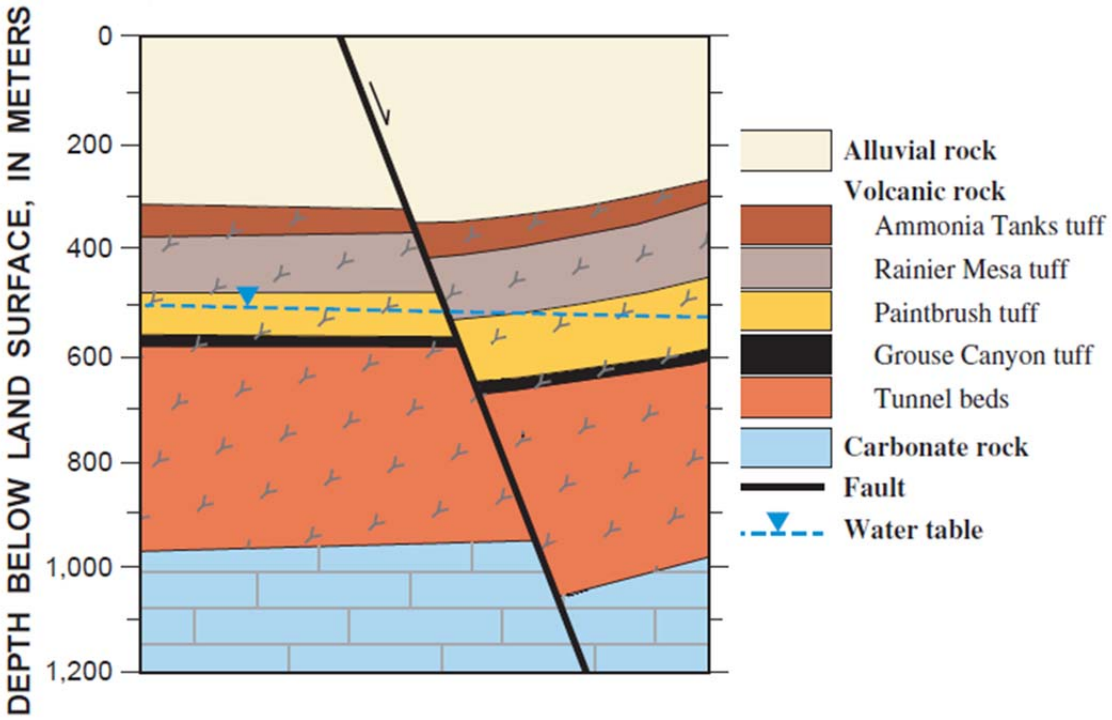

Figure 5.3 General hydraulic stratigraphy cross section of the Yucca Flats area of the Nevada Test Site, adopted from Halford *et al.* (2005)

200-300 m of alluvium, (Halford, *et al.*, 2005; Sinnock, 1982). This cross section model is the one adapted here for UTEX consideration.

An estimate of the porosity and permeability values corresponding to each of the formations depicted in Figure 5.3 based on a compilation of estimates is listed In Table 5.3, (Flint, 1998; Winograd & Thordarson, 1975; Wohletz, *et al.*, 1999). This particular geology cross section is representative of a more general scenario in which the primary bedrock of a region is overlain by an alluvium cover. Alluvium refers to loose, unconsolidated sediment that has been eroded and redeposited by water, typically of a non-exact source such as a flood plain. Alluvium is composed of a variety of fine silt and

clay particles as well as courser sand and gravel, and as shown in Table 5.3 often has a substantially higher permeability than the bedrock that it often covers (Miall, 1990). The various tuffs comprising the Yucca Flats area are attributable to volcanic activity during different epochs in the geological timeline.

Table 5.3 Estimated porosity and permeability values for the representative geologic stratigraphy in Figure 5.3, compiled from estimates in Flint (1998); Winograd & Thordarson (1975); Wohletz *et al.* (1999).

Formation	**Porosity, ϕ**	**Permeability k_m (m^2)**
Alluvial rock	0.20	1E-11
Ammonia Tanks tuff	0.40	1E-13
Rainier Mesa tuff	0.46	1E-14
Paintbrush tuff	0.40	1E-14
Grouse Canyon tuff	0.41	1E-14
Tunnel beds	0.35	1E-14
Carbonate rock	0.35	1E-13

Cavity and surrounding area

As outlined at the beginning of this chapter, a deep UNE event itself greatly impacts the geological environment, at least locally. A further examination of the effects of a heterogeneous geology on the subsurface transport of UNE radionuclide gas should also make some kind of account for the induced cavity and surrounding rubblized zone. Quantifying such effects on the geology in a generalized, hypothetical UNE scenario is very difficult. The size of the resulting initial post-UNE cavity is very much a function of depth of burial and the characteristics of the surrounding rock environment, as well as the yield size of the explosion. On top of that, the pattern and scale of rubblization

surrounding the cavity are affected by the same parameters, as well as additional variability due to height of the resulting chimney and degree of cavity roof collapse.

For moderately deep, contained UNEs, Glasstone & Dolan (1977) give an estimate for the resulting cavity radius of the order 10 m for a 1 kton detonation. Since the real object of the present work is to demonstrate the capability to model cavity and similar effects and gain insight into their influence on radionuclide gas transport, an order of magnitude estimate of the cavity size is more than sufficient for general purposes. The nature of the rock surrounding the cavity is highly variable. Due to the very high pressure of the event, the shock-induced rubblization, and the large overburden, the porosity and permeability of the rock surrounding the cavity is expected to decrease significantly. Estimates of the cavity and surround region porosity and permeability in the simulated post-UNE system are therefore highly variable and subject to a large number of influencing factors. For the purpose of general illustration, values adopted here for the cavity porosity and permeability are $\phi = 0.40$ and $k_m = 1\text{E-}13\ \text{m}^2$ respectively, and for the surrounding disturbed zone: $\phi = 0.04$ and $k_m = 1\text{E-}19\ \text{m}^2$ with a total diameter of 100 m (Garber, 1971; Wohletz *et al.*, 1999). An extended vertical chimney is not assumed, even though incorporation of one in the model would be straightforward.

5.3 SIMULATED TEST CASE

Figure 5.4 and Figure 5.5 show the assumed porosity and permeably profiles of the UNE test case input for UTEX modeling. The geological strata in these figures depict a simplified conceptualization of that shown in Figure 5.3 down to a water table of an approximate depth of 400 m, which marks the lower boundary in the simulated geological model. Included rock formations in the test case model consist of 150 m thick

alluvium followed by three tuff zones of thicknesses between 50 and 100 m. Embedded within the tuff bedrock at a depth of 300 m is the center of the assumed cavity with a "radius" of 10 m extending in the vertical direction. Likewise, a rubblized region extends 50 m out from the center of the cavity.

Obviously the scales of the horizontal and vertical axes of Figure 5.4 and Figure 5.5 are different by two orders of magnitude. Recall that UTEX considers transport in dual porosity vertical slabs, or half-slab unit cells, that include a single vertical fracture and half of the bulk medium separating adjacent fractures, $\delta_m / 2$. Mass exchange between adjacent unit cells occurs at shared boundaries, so that in theory UTEX can simulate transport in a system of arbitrary vertical and horizontal extent within the unit cell framework. In practice, however, this method of *piecing together* unit cell-simulated transport quickly gets computationally expensive. For this reason, the modeled system width in the present test case is 10 m, representing six adjacent unit cells in which transport is simulated across $\delta_m / 2 = 3.3$ m. This representation, as seen in the porosity and permeability figures, reduces the simulated cavity and rubblized zone widths (in the horizontal direction) to roughly 3 m. While such an ellipsoid is of course not directly representative of a spherical cavity, it still allows for the effects of vertical transport and lateral spread of gas to be studied within a more modest computational setting.

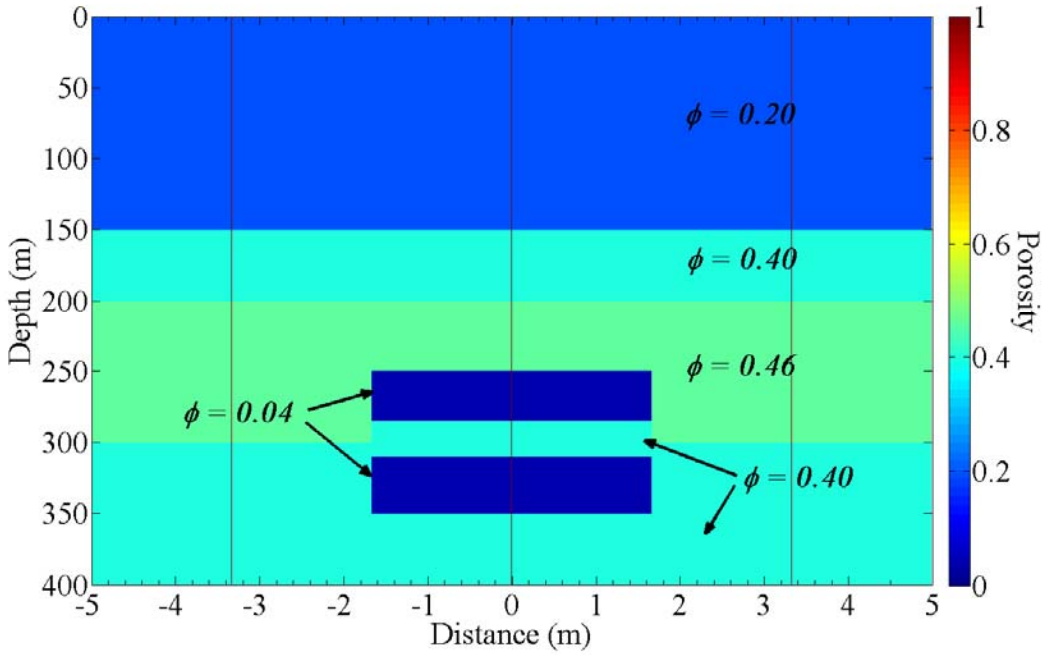

Figure 5.4 UNE geological test case simulated porosities within the UTEX model input.

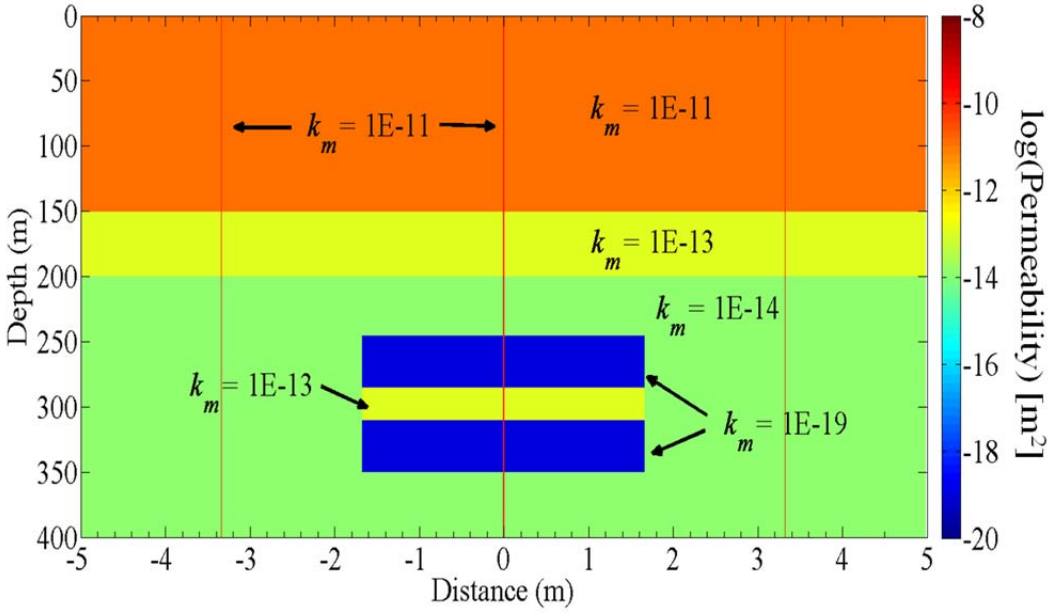

Figure 5.5 UNE geological test case simulated permeabilities within the UTEX model input.

Simulated transport for the test case illustration was conducted over 55 days. The assumed average fracture width and separation were taken to be 1 mm and 3.3 m respectively. Snapshots of the ^{133}Xe concentration profiles within the simulated system are shown in Figure 5.6 and Figure 5.7 to depict the transport of UNE gas within the UTEX model. The following points can be made regarding the transport of UNE gas as simulated and depicted in these snapshots.

- The initialized system begins with a uniformly distributed concentration of ^{133}Xe throughout the estimated cavity volume, which has a total thickness of 100 m (in the vertical direction). This uniform concentration includes the cavity region.
- At 1 Day, ^{133}Xe concentration is already seen beginning to move upwards through the middle fracture. Lateral migration into the surrounding bulk medium is also seen. The distribution of the iodine and iodine precursors were assumed, somewhat arbitrarily to be 75% in the cavity and 25% in the halo – the higher concentration ingrowth of ^{133}Xe in the cavity region is visible.
- At 2 Days, the effect of the various geological zones are evident in the vertical progression of gas up the middle fracture - the higher permeability regions inhibit the quick movement of trapped gas back out of the bulk medium, resulting in an apparent "pooling" at the boundaries. Also evident are the differential migration rates between the two tuff zones of very slightly different porosities whose boundary is located at 300 m depth (refer back to Figure 5.4).
- Between 5 and 15 days, lateral gas migration reaches adjacent fractures and begins vertical transport there. Note at 10 days the apparent evacuation of the fracture.
- Jumping ahead to 40 and 50 days, the total ^{133}Xe inventory has reduced substantially (note the change in colorbar scale). The vertical concentration profile is more uniform and the contaminant front has effectively reached the surface.

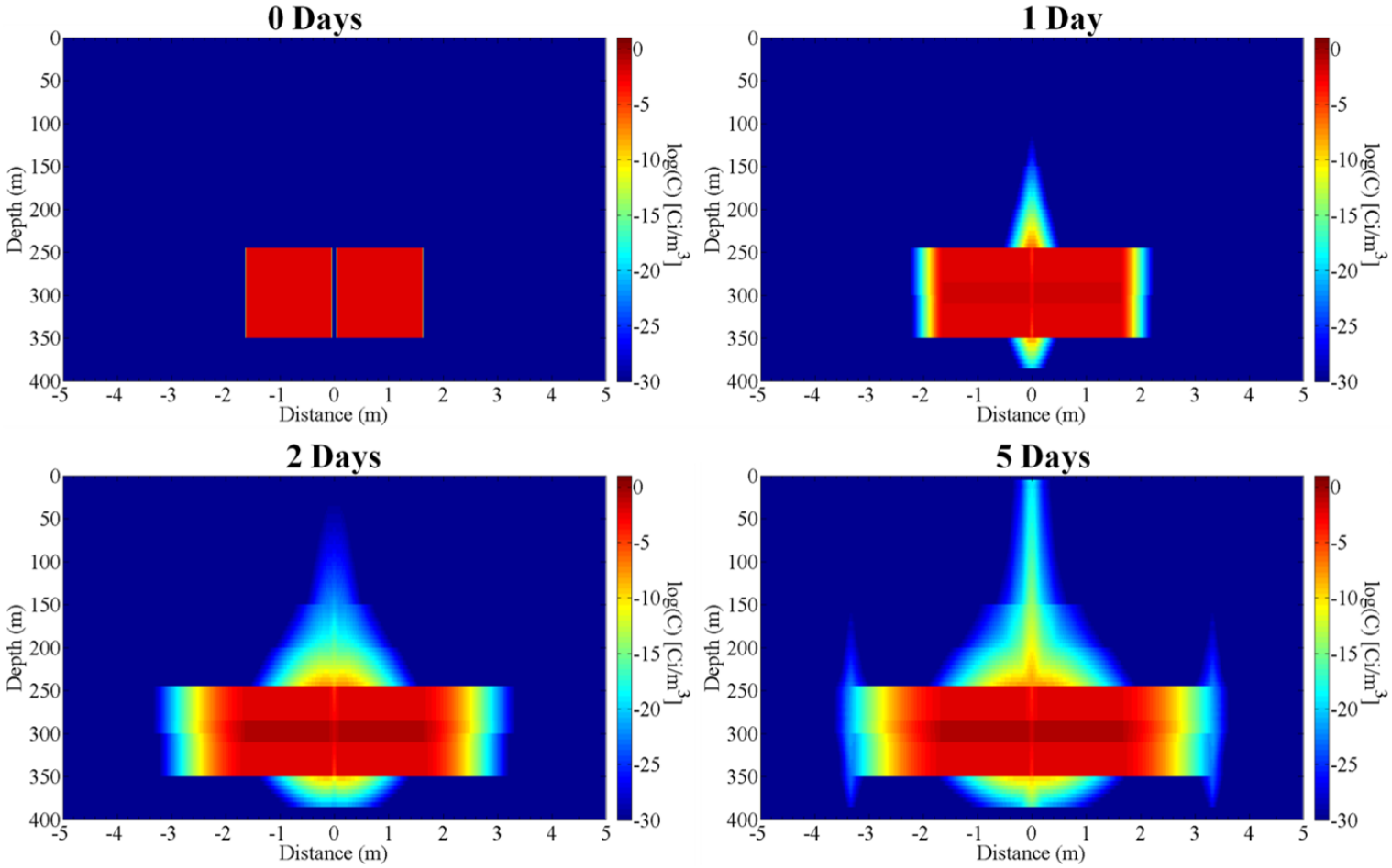

Figure 5.6 133Xe concentration profile snapshots for test case results at various times during simulation over the first 5 days.

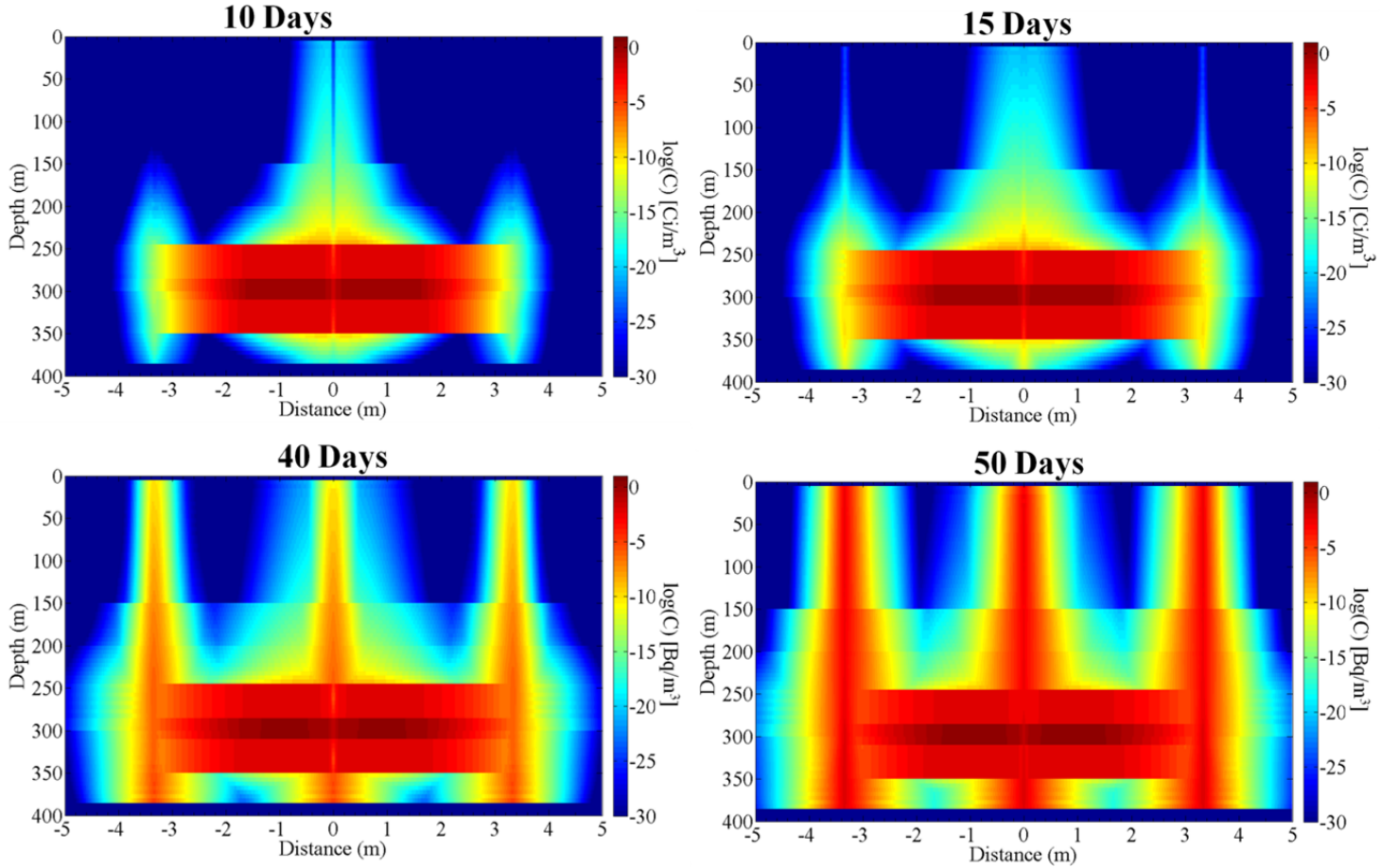

Figure 5.7 ^{133}Xe concentration profile snapshots for test case results at various times during simulation from 10 to 50 days; note the change in color bar scale from Ci to Bq at 40 and 50 days..

5.4 TRANSPORT EFFECTS

5.4.1 Geological effects

The effects of the stratified geological zones in the illustrative test case depicted in Figure 5.6 and Figure 5.7 are largely as expected. In the lower cavity region, smaller porosity and permeability mediums inhibit the advective flow of contaminant gas, essentially *attenuating* the effects of rapid atmospheric pressure fluctuations deeper within the system. In the higher regions where vertical transport brings contaminant gas toward the surface, ^{133}Xe migrating into the adjacent bulk mediums is more effectively trapped in the tuff regions than in the more porous and permeable alluvium zone. Over time and after numerous oscillations in the pressure, the concentration of ^{133}Xe builds up along the fractures in the upper zones where it eventually spreads into the bulk matrix. By 40 days simulation time, movement of gas within the fractures up towards the surface is very efficient as the vertical concentration profile is nearly constant; in effect, the contaminant front has risen close to the top of the system.

Qualitatively, the most prominent effect of the heterogeneous geology on the vertical gas transport simulated in UTEX is in the obvious stratification of the contaminant front that is depicted in simulation snapshots of Figure 5.6 and Figure 5.7. To better examine the influence of the various simulated geological strata on the transport, simulation studies similar to the test case presented in Section 5.3 were made by removing various modeled features and comparing the resulting transport. Results of these simulations are presented in Figure 5.8, which plots the estimated ^{133}Xe concentration at the top of the center fracture during the 55-day simulation time. Four cases were modeled; the first was the test case from above in which the full cavity/halo region and three tuff layers overlain by an alluvium zone are modeled. Simulations then

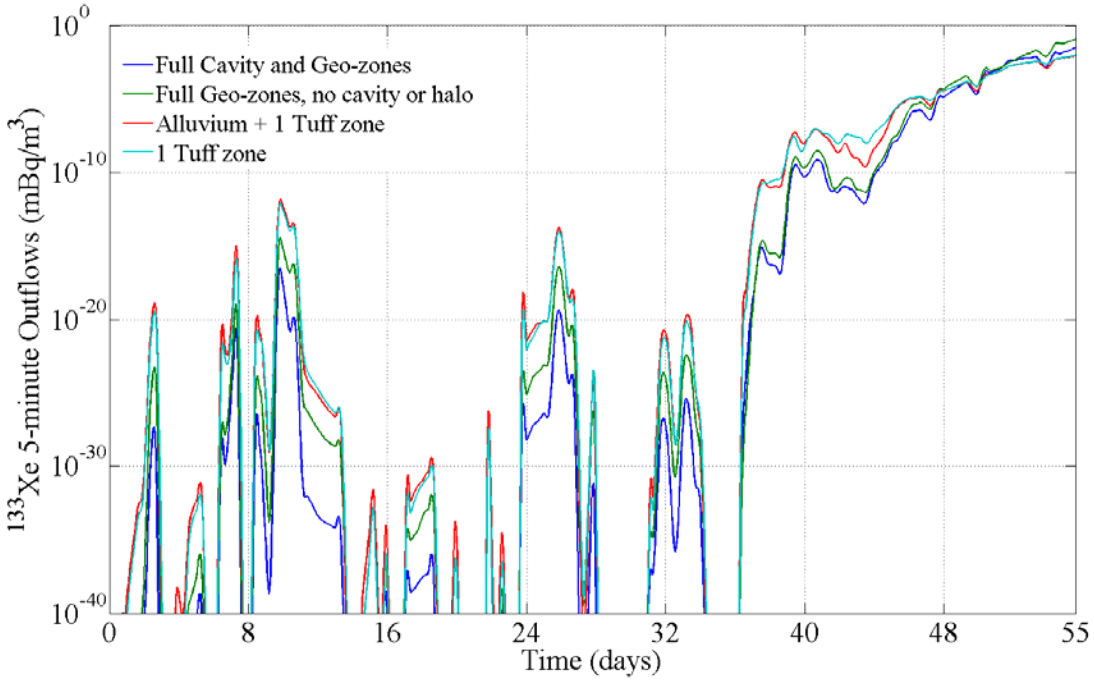

Figure 5.8 ^{133}Xe instantaneous surface level outflows for different configurations of the UTEX system geology for simulations carried out over 55 days of subsurface transport.

considered removal of the modeled cavity/halo region in the immediate vicinity of the assumed UNE event; i.e., as if the event had no effect on the geology. The last two cases simulated considered the transport through just one tuff and an alluvium region as well as one tuff region only.

The blue curve of Figure 5.8 represents the base case of this study in which the conceptual stratification of the geology is modeled, and in most instances of ^{133}Xe reaching the top of the fracture simulated the lowest concentrations. The effects of neglecting the cavity and halo geologies shown by the green line are not entirely straightforward. In the early to middle portion of the simulated time frame, the clear effect exhibited in Figure 5.8 is a marked increase in UNE gas concentration at the top of the middle fracture. The major difference in this case is the removal of the non-porous

and impermeable halo region where a smaller fraction of the radioxenon ingrowth from iodine is assumed to occur from to the initial distribution of UNE gas outside the cavity. This ^{133}Xe contribution from this region is expected to now be much greater because: a) the porosity of the halo region is now much higher and so can contain a much larger volume of gas, and b) the permeability is considerably higher as well which facilitates a more rapid movement of the gas out of the region. The net effect is seen in the figure – in the time frame where gas reaching the top of the fracture largely emanates from the UNE source region, the concentration is higher than in the base case. This difference is less pronounced at later times, however, where the effects of barometric pumping have built up the contaminant front, and the gas reaching the top of the fracture is not necessarily primarily composed of gas directly from the lower regions of the system.

The third case is represented by the red line of Figure 5.8 and models just the alluvium region and a single tuff region defined by $\phi = 0.40$ and k_m = 1E-13 m^2. Fracture concentrations at the top of the system are, somewhat unsurprisingly, higher than in the previous cases at almost all times, since the lower porosity and permeability tuff regions have been removed. The effect of the barometric pumping still exists, and at the later times the effects of the altered geology are less pronounced. In fact, at roughly 50 days the concentrations simulated in the single tuff model are slightly suppressed, which could be attributable to slightly more open tuff region, implying a more efficient removal of gas at earlier times can potentially inhibit the overall build-up of the concentration front at later times. Interestingly, in the last case, where the alluvium region is removed and the one tuff region is assumed throughout, the resulting fracture concentrations are hardly affected until the later parts of the simulated time. Again, the removal of the slightly lower porosity and more permeable alluvium region could enhance the barometric

pumping within the system at shallower depths, though this effect is less prominent than in the difference between the previous cases.

5.4.2 Cavity and halo effects

UNE cavity and halo dimensions are difficult to predict in a general sense because they are sensitive to a large number of factors that interact in a complex way. The size of the UNE, the depth of burial, and the nature of the emplaced bedrock will all affect the resulting post-detonation environment (Glasstone & Dolan, 1977). No attempt is really made in the present work to correlate these factors for a specific set of geological and explosion parameters; instead, for the benefit of maintaining generality, the order of magnitude estimates of Section 5.3 were adopted. Since the size of the cavity and disturbed rock halo zone are certainly important variables in characterizing a potential UNE event, UTEX was used to simulate the resulting gas transport resulting from scenarios which spanned a small range of cavity and halo sizes.

Top of the fracture ^{133}Xe concentrations simulated for these few cases are shown in Figure 5.9. The first three curves in the figure plot concentrations resulting from various assumed diameters or thicknesses of the modeled cavity with porosity and permeability as described already. These curves vary only slightly throughout the simulation time, and largely speaking the apparent cavity size effect grows smaller as simulation time progresses. Around 10 days' time, the residual ^{133}Xe following a sizable pressure low is noticeably higher for larger cavity thicknesses. This observation is likely attributable to the larger fraction of xenon gas that emanates in the higher porosity and permeable cavity region versus the surrounding halo. Once again, the differences between the cases are less pronounced at later times, likely owing to the fact that on the total vertical system scale of 400 m, changes in the cavity size of the order 10 m does not

greatly influence the bulk migration of the xenon contaminant front due to barometric pumping.

The last curve of Figure 5.9 (green line) shows the concentration result for the case of halo region that is twice the thickness of the previous cases. A couple of interesting points regarding the observed effects can be made. First, the distribution of noble gas source is now substantially larger, and even though the modeled halo is not as comparatively favorable to rapid transport as the cavity is, some fraction of the xenon source is now substantially closer to the surface. In the figure, an earlier ^{133}Xe outflow peak occurs at roughly 1 day simulation time, certainly the result of the direct UNE-produced xenon in the upper regions of the halo. At medium times, the effect of the extended halo seems to be to inhibit some of the ^{133}Xe outflow at the top of the fracture, since movement of gas out of the region in response to pressure fluctuation is slower. At later times, however, as the overall distribution of xenon builds up vertically in the system, the extended halo region is more quickly saturated than the previous tuff regions and thus better facilitates the effects of barometric pumping in this time frame. By 35-40 days simulation time, the resulting concentration front is ahead of the previous, smaller halo cases. At the latest times, all the cases converge and no effect of the extended halo is observable.

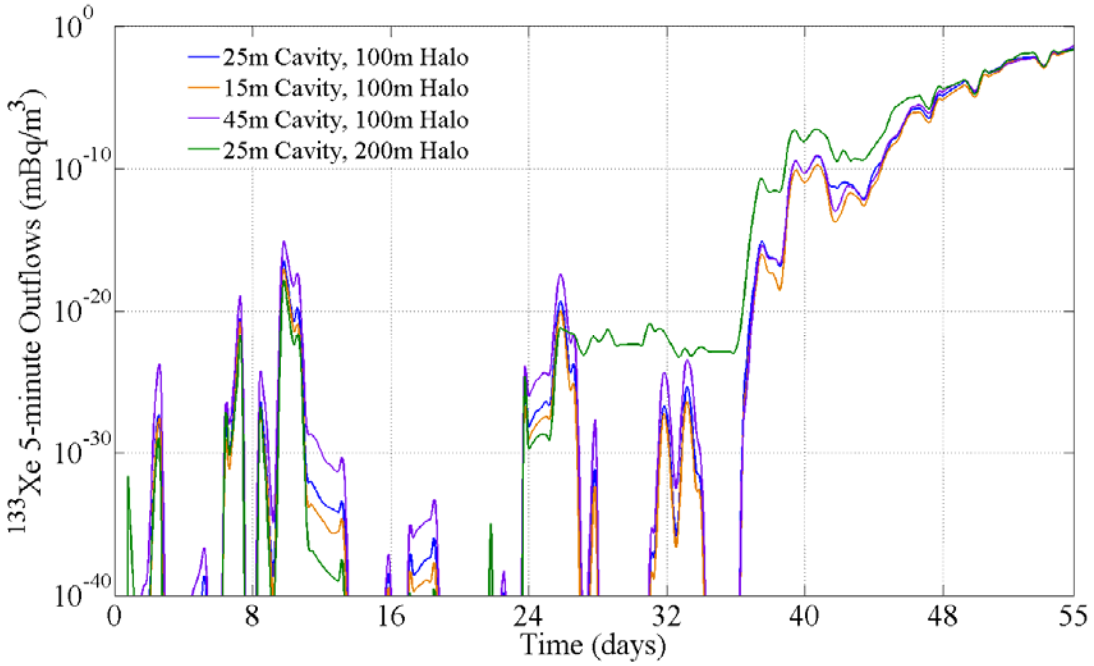

Figure 5.9 ^{133}Xe instantaneous surface level outflows for the full cavity/halo and geological zone test case model simulations carried out over 55 days of subsurface transport with different cavity and halo thicknesses assumed. Stated dimensions refer to the simulated total thickness.

5.4.3 Cavity overpressurization effects

Additionally, UTEX simulations were conducted using the test case scenario but assuming a variable initial pressurization of the cavity region to consider the potential effects of the post-event high pressure state of the system. The results for four overpressurization scenarios are shown in Figure 5.10; note that the cavity pressure is initialized to the indicated overpressures and then allowed to evolve according to the calculated system pressure response rather than artificially held fixed for any length of time. The effects of the overpressure are more or less clear. With no overpressurization (i.e., the base case), the first *spike* in the fracture concentration as indicated by the blue

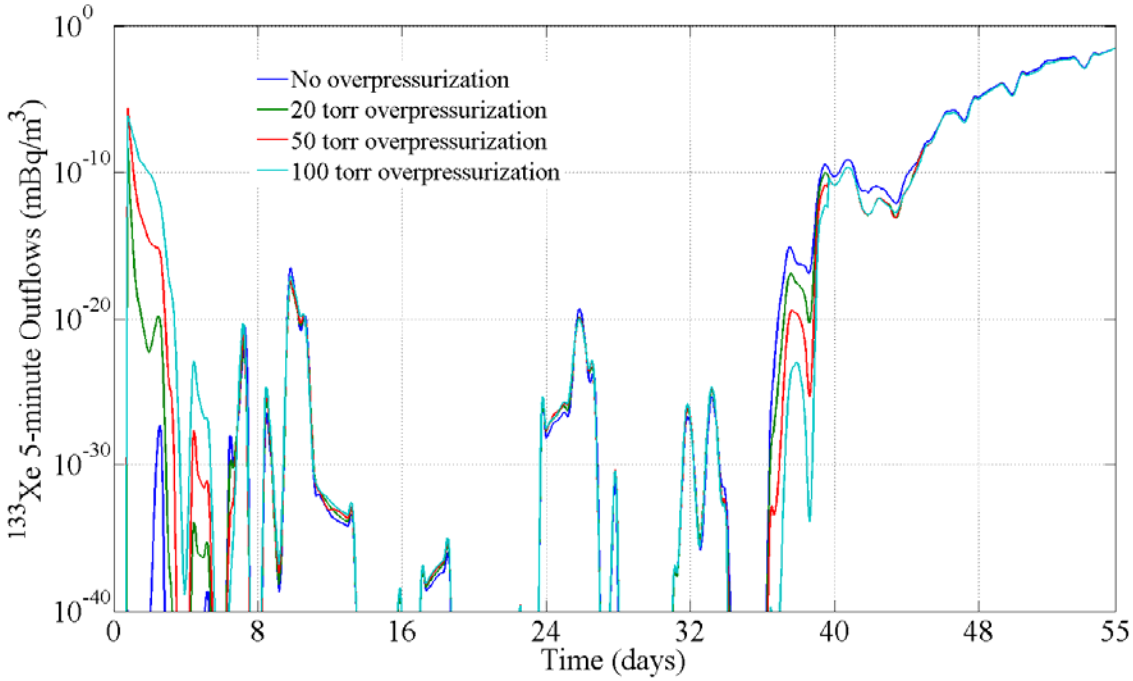

Figure 5.10 ^{133}Xe instantaneous surface level outflows for the full cavity/halo and geological zone test case model simulations carried out over 55 days of subsurface transport with different initial cavity overpressurizations assumed.

line in the figure occurs between 3 and 4 days simulation time. In all three cases of an initial overpressurization of the cavity region, the fracture concentration quickly spikes at around 1 day and continues for a period of time that depends on the size of the pressure. For the largest overpressurization considered, roughly 13% of atmospheric pressure, the initial ^{133}Xe push continues for more than three days. The fact that all three overpressurization cases result in an initial ^{133}Xe spike of roughly equal maximum concentration suggests that the bulk of this outflow is due to an evacuation of the cavity regions nearest to the open fracture. The larger initial pressures then impose a more sustained flow towards the surface as the equalization time is longer.

By 8 days simulation time the effects of cavity overpressurization are much less noticeable. A large part of this is the dissipation of the high pressure within the rest of the system, but the influence of the atmospheric pressure, at least in the UTEX model, are important too. The high number of periods of extended atmospheric pressure lows in the early simulation time frame facilitates an equalization of the cavity pressure that might otherwise persist longer. The differing effects are also evident at around 35-40 days simulation time where the contaminant front is quickly building up in the higher regions of the system. Here, however, the trend is reversed – the overpressurized cases exhibit temporarily lower fracture concentrations, likely due to the substantially greater earlier time evacuation of UNE gas from the lower regions. Still, by and large, the overpressurization of the cavity in the UTEX simulations has a small effect on the long term release of UNE gas due to barometric pumping.

Finally, Figure 5.11 shows a four isotope MIRC plot for five of the UTEX simulated scenarios presented in this chapter for illustration of resulting variability in the radioxenon isotopics. The points on the plot represent xenon *collection* in the modeled system over 12 hours with decay corrected in the cumulative sampling windows. The most interesting features of the decay in this plot are:

- At roughly day 2, the full-model, 100 torr overpressurized case (dashed magenta line) exhibits a sizable fluctuation, attributable to the rapid movement of the initial cavity xenon gas towards the surface.
- At roughly day 14, an additional fluctuation in the ratios is present in all of the simulated cases following a sizeable pressure low and movement of gas to the top of the fracture. The size of this fluctuation is nearly equal for both the initially pressurized and unpressurized full-model cases (note that the lines overlap in the figure), but with further simplification of the geology (removing cavity, halo,

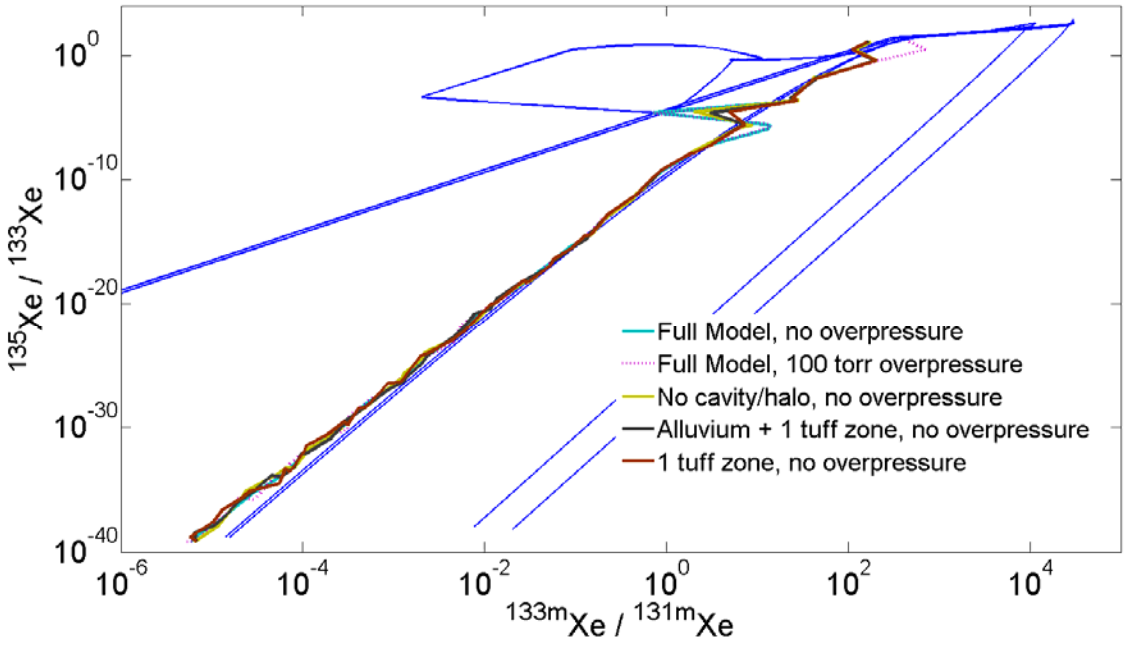

Figure 5.11 Four xenon isotope MIRC plot comparing the various geological and overpressurization cases presented in this work. Note that the first two curves (aqua and dashed magenta lines) overlap in the largest spike; in the earliest time spike, the 100 torr case does not overlap any other lines.

alluvium, etc.) the amplitude decreases. The implication of this is similar to previous conclusions – the less permeable, lower porosity regions of the simulated geology inhibit the rapid flow of gas due to pressure fluctuations. As the system is opened up and homogenized in the various test cases, the effects of source mixing are reduced as gas is less likely to be trapped in the bulk medium.

- The radioxenon ratios at later times tend to fluctuate little between the cases and are more less representative of the non-fractioned decay case.

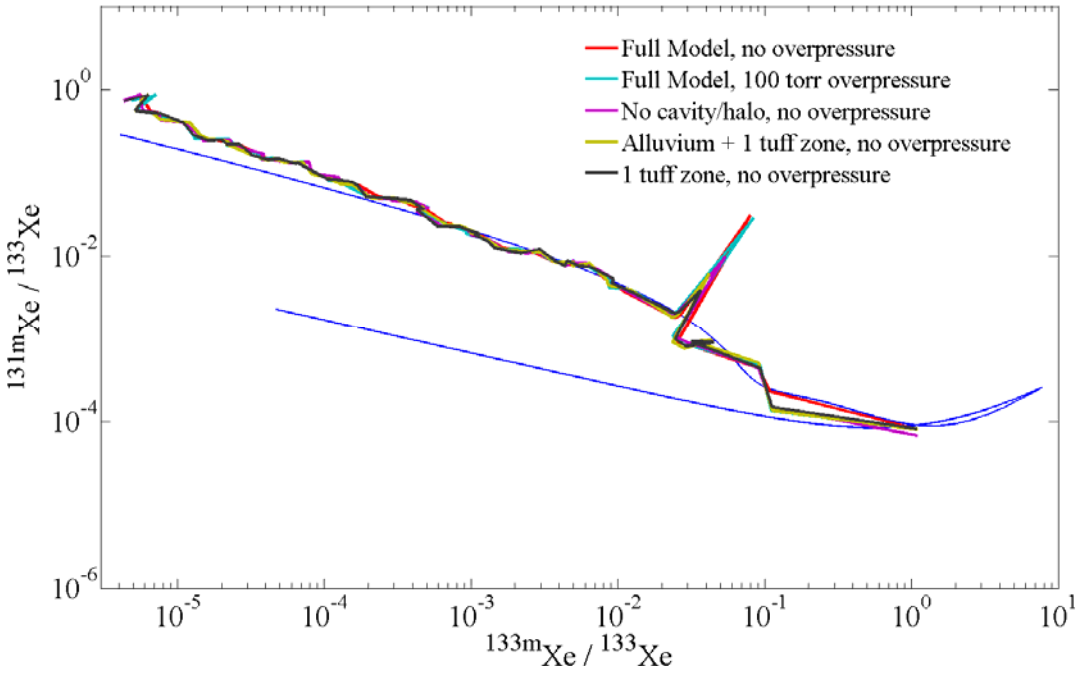

Figure 5.12 Two ratio, three xenon isotope MIRC plot comparing the various geological and overpressurization cases presented in this work.

Figure 5.12 shows the same results but on a three isotope MIRC plot that does not include ^{135}Xe. The same effects and trends are evident – the overpressurization case shifts the isotopics slightly in the early time, but has no real noticeable effect at later times. The largest isotopic fluctuation in the various simulations is reduced as the overall system is effectively homogenized and opened up.

5.5 Conclusions

Within the dual porosity framework of the UTEX model, the capability to simulate conceptually realistic heterogeneous geologic scenarios has been demonstrated in this chapter for a somewhat generic test case. Many of the simulated UNE gas transport effects from considering geologies with multiple rock formations presented in

this chapter are more or less intuitive. The introduction of highly impermeable and low porosity zones in the modeled system results in an attenuation of the bulk air flow in those regions, which depending on the situation, can either enhance or inhibit vertical gas migration from a deep UNE source. Generally speaking, movement of radioactive gas from a deep underground source operates on two substantially different timescales. In the short term, higher porosity and more permeable mediums allow for a more rapid and efficient movement of noble gas in response to barometric fluctuations at the surface. However, with regard to gas invading the upper levels of the bulk matrix medium, this more open geology is less effective at trapping gas in those higher regions. The result of this difference is that on longer time scales, effects of barometric pumping are subdued in the more open geologies, as the UNE gas front is not as effectively built up towards the surface.

Similarly, it has been demonstrated that in some respects the potential variability of the geology can have a significantly greater impact on UNE gas seepage closer to the source than near the surface. As seen in Figure 5.8, the substantial effect of replacing the higher permeability (but slightly lower porosity) alluvium layer with tuff in the top 150 m of the system was substantially less pronounced than changes made to the lower tuff regions. This is not altogether surprising considering that the gas being considered for transport here is radioactive so that its eventual transport to the surface is an inherent race against time. The faster the UNE noble gas can escape the lower regions, the much higher probability that it can leak from the system on subsequent swings in the atmospheric pressure.

This trend is likely especially true of the geologic conditions in the immediate vicinity of UNE cavity. How the cavity fills in and how the surrounding environment fractures and gets compacted due will have a large influence on how quickly noble gas

can move upwards in system. Additionally, the actual distribution of radioxenon, iodine, and radioargon gas in the early halo zone is certainly of importance as well, and is likely a good subject for further investigation in this area. However, as shown in Figure 5.8 as well, the effects of the variability in the geology are less pronounced in the long term process of barometric pumping, at least in an order of magnitude sense. This is largely attributable to the dominance of fracture transport in the dual porosity model, something that is not completely emphasized in this study and should be incorporated into future development considerations.

A cursory examination of the effects of the highly overpressurized post-UNE cavity state has also been made. UTEX simulations of these cases indicate that the overpressurization does indeed lead to a substantial increase in the movement of UNE gas to the to the shallow depths in the short term time frame, but within a week's simulation time these induced outflows have largely subsided. An additional, less critical effect of the overpressurization may occur at later simulation times when the cumulative effects of barometric pumping result in a rise of the contaminant front into the higher system regions. At this point, the concentration levels of the overpressurized cases lagged behind somewhat, likely due to the earlier outflow of gas from the lower regions. These effects, however, only appeared temporarily in the simulations and largely speaking the effects of overpressurizing the UNE cavity were minimal on the long term migration of radioxenon due to barometric pumping.

Lastly, the isotopics of the resulting radioxenon outflows at the top of the simulated system were considered. The overpressurized cavity case was found to exhibit a substantial fluctuation at the very early times, corresponding to a removal of gas directly from the cavity environment that was void of iodine ingrowth. This fluctuation was short-lived, and beyond the first couple of days the xenon isotopics did not seem to

be affected by the initial pressure in the cavity. In looking at the various cases where more impermeable and less porous tuff regions were considered, the simulated effect of removing such zones from the modeled geology were to reduce the magnitude of isotopic fluctuations. In essence, regions within the geology that inhibit rapid movement of gas in response to atmospheric pressure fluctuations are also more likely to induce isotopic fluctuations through the trapping of upward-moving noble gas. By homogenizing the geology and essentially opening the system up to greater freedom of movement, the radioxenon ratios are less disturbed by movement through the geology. These effects, especially with regard to modeling of the cavity environment as well as the pulverized and fractured region surrounding, are very likely candidates for additional future study with the UTEX model.

Chapter 6. Radionuclide Soil-Gas Background

Ideally, measured soil-gas concentrations of radionuclides used as evidence of underground nuclear explosions would be entirely anthropogenic in origin. While the bulk of the current work is aimed at the examination of radionuclide signatures for the purpose of distinguishing among various anthropogenic sources, some attention to naturally-occurring radionuclides is necessary for the context of an OSI. Broadly speaking, radionuclides within soil-gas can originate from three potential sources:

- Underground anthropogenic sources
- Atmospheric sources - anthropogenic and natural
- Natural soil-gas background

Both atmospheric infiltration and natural soil background levels of radionuclides have the potential to contribute to measured soil-gas samples, thus an understanding of their origin and distribution throughout the subsurface environment is important to isolating radionuclide signatures that might emanate from an underground nuclear detonation.

Characterization of global natural soil-gas backgrounds has become a larger priority in recent years as radionuclide detection sensitivities continue to improve and the need to distinguish between low concentration sources increases. Current radioxenon detection limits for field and laboratory SAUNA systems are approaching 2 mBq/m^3 and 0.2 mBq/m^3 respectively (Haas *et al.*, 2010). On the radioargon side of things, the reported detection limits of the Chinese MARDS system is 25 mBq/m^3 (Xiang *et al.*, 2008) and a new laboratory ultra-low-background proportional counter developed at Pacific Northwest National Laboratory (PNNL) is 1.2 mBq/m^3 (Aalseth *et al.*, 2013); additionally, PNNL scientists have placed lower limits on ^{37}Ar field and laboratory systems at ~20 mBq/m^3 and ~0.02 mBq/m^3 respectively (Haas *et al.*, 2010). These

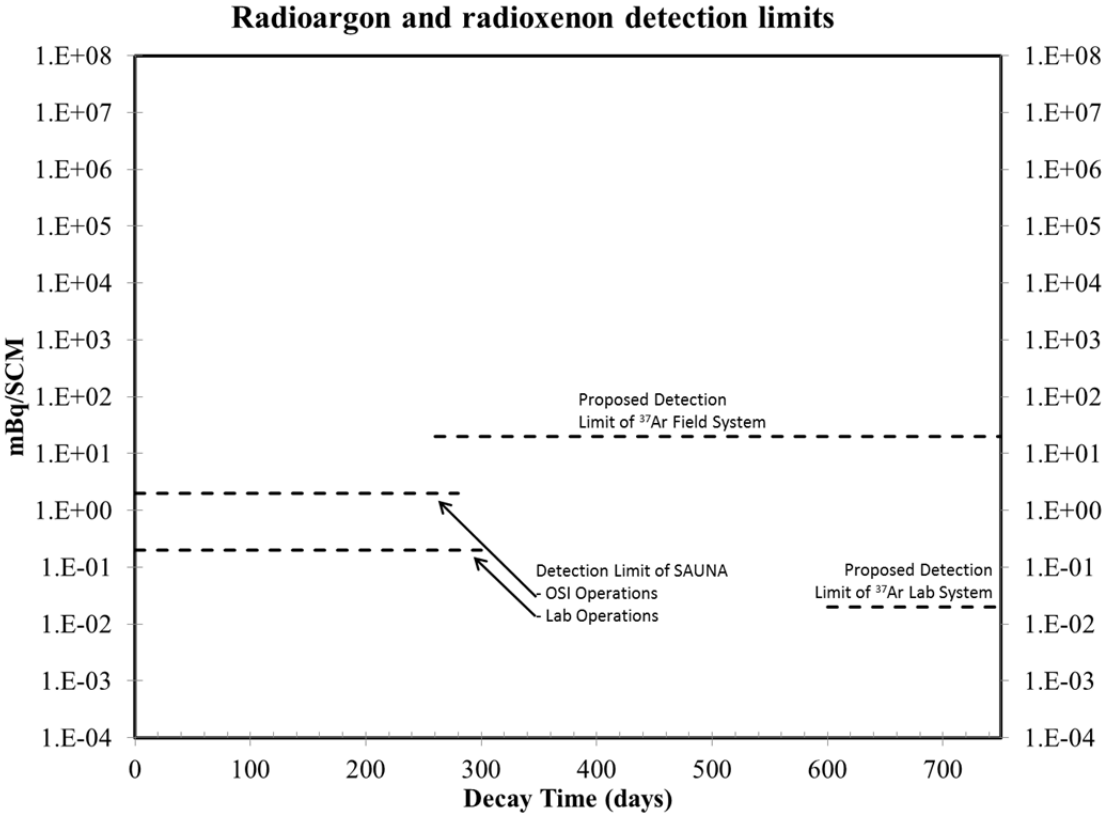

Figure 6.1 Radioargon and radioxenon detection limits on empty decay plot; adapted from Haas *et al.* (2010).

various detection limits are shown in Figure 6.1 on an empty radioactive decay plot for comparison and to illustrate the range of radioxenon and radioargon detection capabilities.

The goal of the work presented in this chapter was to establish representative natural soil-gas background source profiles of xenon and argon to be used in the UTEX model to examine how gaseous diffusion and barometric fluctuation-driven advection can affect equilibrium concentrations. A cursory examination of the processes relevant to radioxenon and argon soil-gas background production is made based on previous work is made. Current literature on the subject typically provides order of magnitude ranges on

background equilibrium concentrations based on radioactive decay and an approximation of gas emanation from rock space into porous air space. The radionuclide source production rates that are needed as an input to run UTEX simulations could be obtainable from these equilibrium estimates, but only if the details of the assumed geologic porosity and emanation coefficient and the estimates as a function of depth are provided in the literature. Furthermore, the use of cumulative xenon yields to produce most literature estimates is not entirely conducive to integration into the UTEX model, as is explained near the end of this chapter.

6.1 OVERVIEW OF CONTRIBUTIONS TO SOIL-GAS BACKGROUND

Radioactive nuclides naturally present in the ground exist in concentrations that are determined predominantly by the following factors:

- Source – the rate of radionuclide production in the ground, as determined by the natural distribution of elements and neutron fluxes.
- Decay – the rate of radionuclide loss through radioactive decay, along with production rate determines the radioactive equilibrium concentrations within the soil-gas background.
- Emanation – the process of radionuclides that are produced within a rock matrix moving into the air-filled pore space within the bulk rock volume where it can be transported, collected, and/or measured.
- Transport – the movement of gas in a porous medium by diffusion or bulk advection will influence the equilibrium concentrations.

While a large number of processes are capable of producing radioxenon, it is predominantly a product of fission reactions. As such, the background concentration of

radioxenon within a specific geology is greatly dependent on the natural distribution of fissionable isotopes, most notably uranium (comprised of ^{238}U and a small fraction of ^{235}U) and thorium (mostly ^{232}Th) in the ground. Furthermore, fission of these isotopes can occur both spontaneously in a small fraction of radioactive decays as well as induced by neutrons. An estimation of the background neutron flux is therefore required for the consideration of both neutron-induced fission reactions as well as the multitude of other xenon yielding processes. With respect to radioargon, neutron flux estimation is also important for an examination of ^{37}Ar in natural background because of its genesis by ^{40}Ca neutron activation and much smaller contribution from activation of naturally-present ^{36}Ar in soil-gas air.

The bulk of this chapter is dedicated to establishing an estimate of radionuclide production rates in different depths of a variety of geology types. To accomplish this, a survey is made of the possible neutron and more generalized-particle reactions that can produce radioxenon and radioargon, which are qualitatively evaluated for relevance to soil-gas backgrounds based on natural elemental compositions and length of half-lives. The neutron flux attributable to cosmic ray sources and natural subsurface fission reactions is also considered, though quickly, to estimate neutron-induced reaction rates. These collectively provide an approximation to the natural radionuclide source term used as input for the UTEX model to consider the effects of transport on the background distribution.

6.2 COSMIC RAY BACKGROUND

Cosmic radiation refers generally to the wide array of solar and extra-solar particles, typically of very high energy, that impact Earth's atmosphere. The term "cosmic

ray" is somewhat of an historical misnomer, as it was originally believed to be largely made up of electromagnetic radiation. In fact, today gamma rays or X-rays are regarded separately from cosmic particle radiation, which is comprised of protons (86%), α-particles (11%), nuclei of heavier elements up to uranium (1%), and free electrons (2%) (Perkins, 2003). With elemental compositions similar to stars, recent research has concluded that cosmic rays largely originate from stellar supernovae (Ackermann *et al.*, 2013).

Primary cosmic ray particles, upon entry into Earth's atmosphere, induce massive showers of secondary particles through collision with heavy air that is termed cosmic ray spallation. An illustration of this process is shown in Figure 6.2; secondary particles produced in the initial primary particle collision are a variety of pions (π^+, π^-, π^0), kaons, neutrons, as well as smaller fragmented nuclei (not shown in the figure). The charged pions have a proper lifetime of only 26 ns and a mean free path on the order 55 m for 1 GeV energies before undergoing decay by[15]: $\pi^+ \rightarrow \mu^+ + \nu_\mu$ and $\pi^- \rightarrow \mu^- + \overline{\nu}_\mu$. These daughter muons subsequently undergo decay themselves with a proper lifetime of 2200 ns: $\mu^+ \rightarrow \beta^+ + \nu_e + \overline{\nu}_\mu$ and $\mu^- \rightarrow \beta^- + \overline{\nu}_e + \nu_\mu$. The longer muon lifetime means that a significantly greater percentage of muons than pions reach the Earth's surface - the mean free path of a 1 GeV muon is about 7 km as compared to 55 m for a charged pion. At energies of around 3 GeV, muons produced in the atmosphere have a substantial chance of reaching the surface (Perkins, 2003).

---

[15] Assuming an example pion energy E_π = 1 GeV, $m_\pi c^2$ = 0.139 GeV, then $\gamma = E_\pi / m_\pi c^2$ and the mean free path given a proper lifetime τ is $\lambda = \gamma c \tau$ = 55 m (Perkins, 2003).

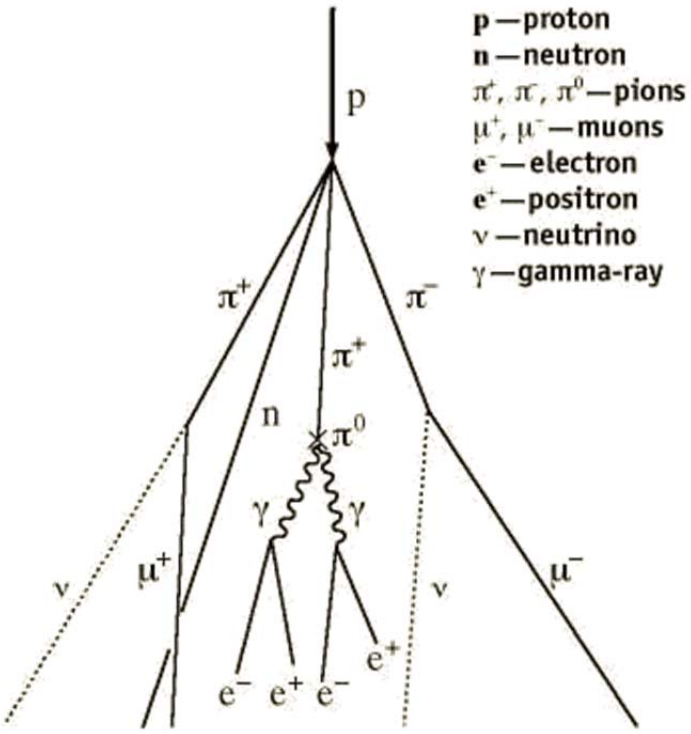

Figure 6.2 Cosmic ray spallation illustration with primary particle (proton) inducing a cascade of secondary particles (pions and neutrons as well as fragmented smaller nuclei not shown in the illustration) that induce further interactions (LANL, 2011).

A number of factors contribute to the flux of cosmic ray particles entering the upper atmosphere, including the solar wind and magnetic field of the Earth, both of which generally serve to deflect particles and reduce the cosmic ray flux, especially at energies <1 GeV. The solar wind, however, is not constant and can result in variation of the cosmic ray flux on the order of 50%. Also, the Earth's magnetic field strength is generally dependent on latitude and longitude, and thus also factors into the variability of the cosmic ray background flux. Cosmic ray originating neutrons, protons, α-particles, muons, and neutrinos all have at least some small potential to induce radionuclide-generating reactions in the subsurface environment, though most of these are likely to

contribute negligibly to the soil-gas radionuclide background. Many of these subsurface reaction mechanisms are mentioned in Section 6.4.2 and their likelihood of background contribution at least qualitatively discussed.

6.3 DEFINITION OF SOIL-GAS BACKGROUND SOURCES

The cosmic ray background flux of high-energy particles is largely attenuated by the atmosphere, thus limiting their contribution to the radioxenon and radioargon soil-gas background. Concentrations of these gases are thus predominantly determined by rates of spontaneous fission as well as neutron-induced reactions (both fission and non-fission). It turns out that the greatest contribution of the cosmic ray background to soil-gas radionuclide levels is in the neutron flux within the subsurface environment, particularly in the upper few meters. Beyond the shallow depths, in-situ fission neutrons largely determine the neutron flux. A characterization of the neutron flux that drives neutron-induced reactions is thus an important component to establishing an estimate of the radionuclide natural soil-gas source term.

6.3.1 Spontaneous fission

An estimation of the radionuclide background due to spontaneous fission is straightforward compared to that resulting from neutron interactions because the former is dependent only on the assumed natural concentrations of fissionable nuclei. Spontaneous fission occurs with a small probability along with other types of decay of very heavy nuclei, particularly those having atomic masses greater than 92 amu. The fraction of decays that occur by spontaneous fission rather than α-decay is termed the spontaneous fission branching ratio, I^{sf}. This branching ratio typically increases with the

atomic mass of the nuclei, but is very small in naturally occurring isotopes of uranium, thorium, and even plutonium.

Given an atomic density N_i of an isotope i, a volume V, and a decay constant λ_i, the activity of the nuclide can be expressed

$$A_i = \lambda_i N_i V .$$

Since the branching ratio Γ^{sf} is the fraction of total decays that occur by spontaneous fission, the spontaneous fission *rate* of the nuclide i is just

$$R_i = A_i \Gamma_i^{sf} . \tag{6.1}$$

If the associated yield of a particular isotope j from the reaction of nuclide i is Y_j^i, then the rate of production of that nuclide due to spontaneous fission of i can be expressed

$$P_j^{i,sf} = R_i Y_j^i = A_i \Gamma_i^{sf} Y_j^i . \tag{6.2}$$

6.3.2 Particle-induced reactions

For the case of radioxenon production in soil-gas background, the most relevant particle-induced reactions are neutron induced reactions, particularly fission of ^{235}U, ^{238}U, and ^{232}Th. Besides fission, a number of other neutron and more general particle interactions in natural geology can produce radioxenon. In Hebel (2010), many non-fission xenon-producing reactions were evaluated for their potential to contribute to soil-gas background levels; most of these were largely expected to contribute negligibly to the Xe background in comparison. While a survey characterizing these possible Xe-generating interactions is made here, in quantifying the expected radioxenon background, attention is confined to neutron-induced fission genesis. Similarly, the focus of ^{37}Ar production is on the neutron activation of ^{40}Ca as well as possible muon interaction with potassium.

Neutron interactions

Like spontaneous fission, conceptually the task of quantifying neutron-induced reaction rates and subsequent radionuclide yield is straightforward. Neutron-induced reaction rates are dependent on the atomic density N_i of the target nuclei i, the cross section for the generalized (n,X) reaction, σ_i^X, and the flux of neutrons ϕ. For the case of a monoenergetic neutron flux $\phi(E_k)$ of energy E_k, the reaction rate is simply

$$R_i^X(E_k) = \phi(E_k)\sigma_i^X(E_k)N_iV\,.$$

such that the rate of production of radionuclide j with a yield $Y_j^{i,X}$ due to the i (n,X) j reaction is given by

$$P_j^{i,X}(E_k) = \phi(E_k)\sigma_i^X(E_k)N_iVY_j^{i,X}(E_k)\,. \tag{6.3}$$

However, Equation (6.3) is only correct when assuming a flux of neutrons of a single energy. In the more general case that $\phi = \phi(E)$, both the reaction cross section and yield become a function of the incoming neutron energy, and thus the reaction and radionuclide production rates become dependent on the neutron flux energy distribution. The need to characterize the natural neutron flux background significantly complicates the estimation of the neutron-induced reaction rates. Given an estimate of the neutron flux $\phi(E)$, the energy-integrated equivalent of Equation (6.3) is

$$P_j^{i,X} = N_iV\int_E \phi(E)\sigma_i^X(E)Y_j^{i,X}(E)dE\,. \tag{6.4}$$

An examination of the soil background neutron flux needed for utilization of Equation (6.4) is made in Section 6.5.

Table 6.1 Xenon-and argon-producing neutron reactions of potential relevance to the natural soil- gas radioxenon background. Relevant xenon reactions adapted from Hebel (2010); argon reactions compiled from online endf tables by Chadwick *et al.* (2011). *These are argon-producing reactions not expected to be relevant due to low natural elemental composition.

Xenon-131m	**Xenon-133m**	**Xenon-133**	**Xenon-135**	**Argon-37**
$^{235}U(n,f)^{131m}Xe$	$^{235}U(n,f)^{133m}Xe$	$^{235}U(n,f)^{133}Xe$	$^{235}U(n,f)^{135}Xe$	$^{39}K(n,2n+p)^{37}Ar$
$^{238}U(n,f)^{131m}Xe$	$^{238}U(n,f)^{133m}Xe$	$^{238}U(n,f)^{133}Xe$	$^{238}U(n,f)^{135}Xe$	$^{40}Ca(n,\alpha)^{37}Ar$
$^{232}Th(n,f)^{131m}Xe$	$^{232}Th(n,f)^{133m}Xe$	$^{232}Th(n,f)^{133}Xe$	$^{232}Th(n,f)^{135}Xe$	
$^{130}Te(n,\gamma)^{131}Te$		$^{132}Xe(n,\gamma)^{133}Xe$	$^{134}Xe(n,\gamma)^{135}Xe$	*other less-relevant:
$^{132}Xe(n,2p)^{131}Te$		$^{133}Cs(n,p)^{133}Xe$	$^{135}Cs(n,p)^{135}Xe$	$^{36}Ar(n,\gamma)^{37}Ar$
$^{132}Xe(n,d)^{131}I$		$^{134}Ba(n,2p)^{133}Xe$	$^{136}Ba(n,2p)^{135}Xe$	$^{38}Ar(n,2n)^{37}Ar$
$^{132}Xe(n,n+p)^{131}I$		$^{134}Xe(n,2n)^{133}Xe$	$^{136}Xe(n,2n)^{135}Xe$	$^{39}Ar(2,3n)^{37}Ar$
$^{133}Cs(n,^3He)^{131}I$		$^{134}Xe(n,2p)^{133}Te$	$^{136}Xe(n,2p)^{135}Te$	$^{41}Ca(n,n+\alpha)^{37}Ar$
$^{134}Xe(n,\alpha)^{131}Te$		$^{134}Xe(n,d)^{133}I$	$^{136}Xe(n,d)^{135}I$	
$^{134}Xe(n,n+t)^{131}I$		$^{134}Xe(n,n+p)^{133}I$	$^{136}Xe(n,n+p)^{135}I$	
$^{135}Cs(n,n+\alpha)^{131}I$		$^{135}Ba(n,^3He)^{133}Xe$	$^{137}Ba(n,^3He)^{135}Xe$	
		$^{135}Cs(n,^3He)^{133}I$	$^{138}Ba(n,\alpha)^{135}Xe$	
		$^{135}Cs(n,n+d)^{133}Xe$		
		$^{135}Cs(n,t)^{133}Xe$		
		$^{136}Ba(n,\alpha)^{133}Xe$		
		$^{136}Xe(n,4n)^{133}Xe$		
		$^{136}Xe(n,\alpha)^{133}Te$		
		$^{137}Ba(n,n+\alpha)^{133}Xe$		

The first four columns of Table 6.1 list a multitude of radioxenon-producing neutron interactions that can potentially contribute to the soil-gas background, adapted from Hebel (2010). These processes are deemed relevant based on an evaluation of target half-lives being long enough to undergo interaction as well as products consisting of either xenon or direct parent nuclides. Under these criteria, for example, radioactive xenon isotopes themselves are excluded as potential targets for neutron interaction since their short half-lives would result in interaction rates orders of magnitude lower than other relevant reactions. The last column of Table 6.1 lists the two primary neutron interactions capable of producing ^{37}Ar obtained from the ENDF online database search tool (Chadwick *et al.*, 2011); also shown are other argon-producing reactions that are less relevant because of the low or non-existent natural abundance of the target nuclei in geologies (Chang, 2000).

Proton interactions

Protons comprise roughly 86% of the cosmic ray primary particle flux entering the top of Earth's atmosphere. Even though such protons have very high-energy (see Figure 6.3), only a fraction could be expected to reach sea-level and have a direct impact on radionuclide production underground. Attenuation of the flux or intensity, $I(E,x)$, of nucleons passing through a medium can be approximated by

$$I(E,x) \approx I(E,0)e^{-x/\Lambda} \tag{6.5}$$

where $I(E,0)$ is the initial intensity, x is depth traversed, and Λ is attenuation length. For protons in the atmosphere, $\Lambda \approx 123$ g cm^{-2}; Figure 6.4 shows an estimate of the energy-integrated vertical fluxes of various cosmic ray nucleons versus depth of atmosphere. For the $p + n$ curve, the initial proton fraction is about 0.9 whereas the fraction sea level is stated as about 0.66 (Groom & Particle Data Group, 2000). The proton flux above 1 GeV

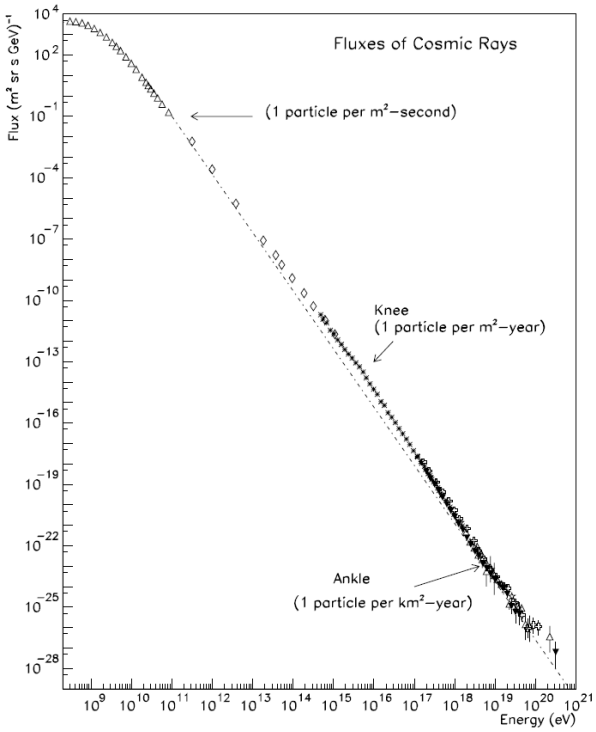

Figure 6.3 Cosmic ray all-particle flux spectrum, (Swordy, 2001).

thus drops by about four orders of magnitude to around $1\ m^{-2}s^{-1}sr^{-1}$ or about $0.001\ cm^{-2}\ s^{-1}$.

Free protons that manage to reach the underground environment would have an extremely short lifetime - even high-energy protons would quickly downscatter in energy. Proton-induced interactions typically will occur by elastic scattering; some (*p,X*) interactions are possible, most notably with lead, bismuth, nickel, iron and some lighter metals, but these are generally high-energy reactions and genesis of radioxenon by such reactions is not possible. Similarly, while ^{37}Ar and ^{40}Ca (and other relevant isotopes) are possible yields from some proton reactions (like $^{56}Fe(p,X)$ for example), the high energy

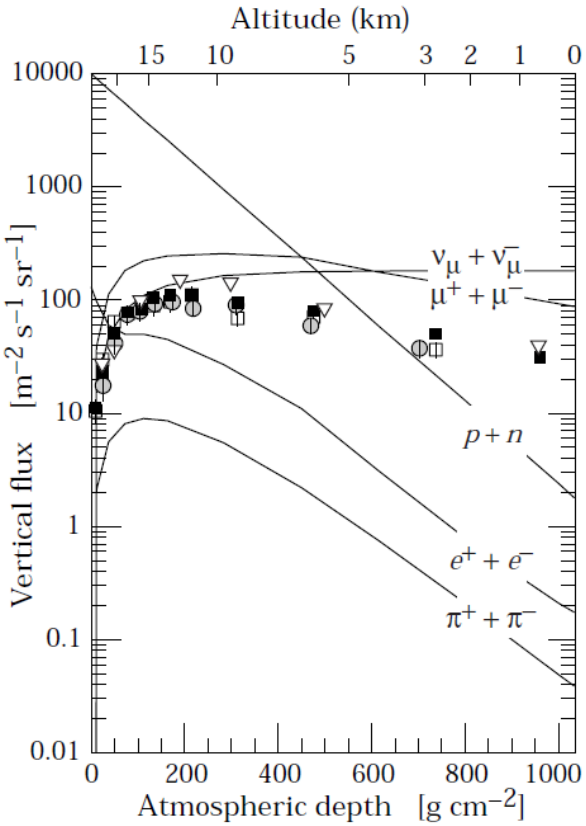

Figure 6.4 Estimated vertical fluxes of cosmic rays in the atmosphere having energy E > 1 GeV (Groom & Particle Data Group, 2000).

dependence and low yield numbers for such reactions make them negligible contributions to radioargon background levels (Chadwick *et al.*, 2011).

Muon interactions

Muons are generated through the decay of charged pions and kaons, which are secondary cosmic ray particles (see Figure 6.2). As described in Section 6.2, their 2.2 μs proper lifetime means that muons have a substantial chance of reaching ground level before decay and therefore should be considered for their potential to produce radioxenon and radioargon. The most relevant interaction is muon capture by protons in the

subsurface environment; this interaction can be summarized $p + \mu^- \rightarrow n + \nu_\mu$ and can yield radionuclide products according to:

$$\begin{aligned} \mu^- + (Z, A) &\rightarrow (Z-1, A)^* + \nu_\mu \\ (Z-1, A)^* &\rightarrow (Z-1, A-X) + X \cdot n \end{aligned} \tag{6.6}$$

where X = 0, 1, 2, ... is the number of free neutrons that determines the product nucleus. The potential contribution of such muon interactions to the radioxenon background has been considered previously by Hebel (2010) using a production rate expression developed by (Charalambus, 1971), which is also adopted here.

Given a parent nuclide of (*Z,A*), the rate of production of isotope $(Z-1, A-X)$ is approximated by

$$P_i^\mu = I_{\mu^-}(x) \cdot f_c \cdot f_d \cdot f_r \,. \tag{6.7}$$

The factors appearing in Equation (6.7) are as follows[16]:

- $I_{\mu^-}(x)$ is the estimated number of negative muons stopped per unit mass per time as a function of depth (see Figure 6.5).
- f_c is the fraction of muons reaching the 1s muonic level of the target element and therefore capable of being captured. This can be approximated using the Fermi-Teller "Z-Law," which has $(f_c)_i = a_i Z_i / \sum_N a_n Z_n$ where a_i and Z_i are the abundances and charge of each isotope in the medium (Hebel, 2010).
- f_d is the actual fraction of available muons that are captured before muon decay (see Figure 6.6.
- f_r is the probability of the excited (*Z - 1,A*)* nucleus yielding the desired (*Z - 1,A - X*) nucleus (see Table 6.2).

---

[16] The equation as it appears in Charalambus (1971) includes an additional factor $\kappa < 1$ that accounts for variability of the muon intensity based on elevation and latitude. As done in Hebel (2010), this term is assumed for generality and simplicity to be equal to 1.

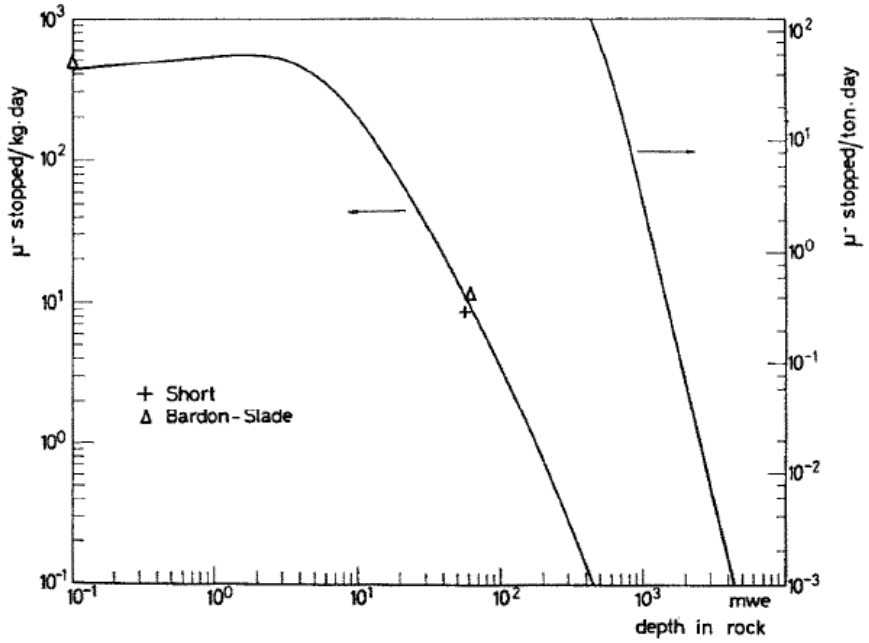

Figure 6.5 Stopping rate of negative muons as a function of depth, (Charalambus, 1971).

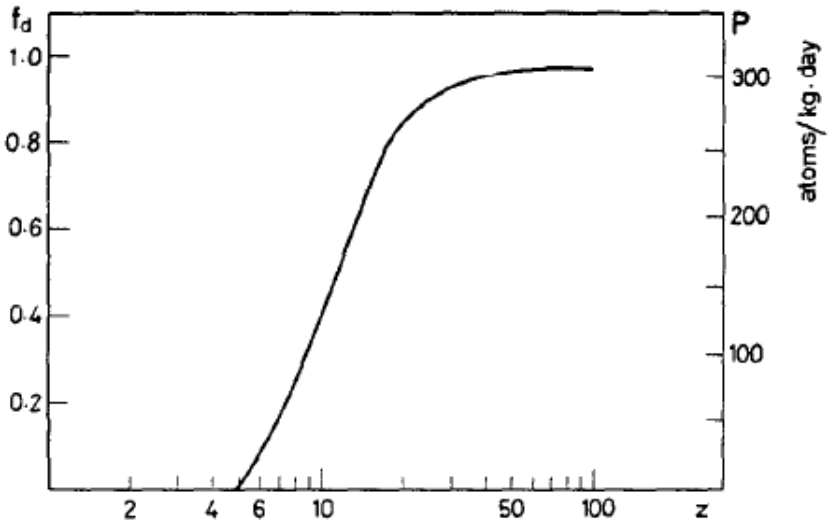

Figure 6.6 Fraction of negative muons captured by the nucleus from the 1s muonic atom level as function of the atomic number (left scale), (Charalambus, 1971).

Table 6.2 Proposed neutron emission probabilities for use in Equation (6.7), (Charalambus, 1971).

Neutrons emitted	0	1	2	3	4
f_r	0.10<	0.60-0.70	0.15-0.20	0.05	0.02

One of the conclusions of the background analysis in Hebel (2010) is that the muon contribution to radioxenon soil-gas background levels is negligible (< 1%) compared to spontaneous fission levels. A similar analysis utilizing Equation (6.7) is utilized in subsequent sections to reproduce and extend Hebel's analysis to include ^{37}Ar production from potassium.

6.4 CHARACTERIZATION OF THE NEUTRON FLUX

A quantification of the subsurface neutron flux depth and energy profiles presents the greatest challenge in estimating soil-gas radionuclide background source terms. Developing a neutron flux profile from the ground up is a sizable task that extends well beyond the transport-centric scope of this work, but an estimate is still needed to determine background radionuclide production estimates. Fortunately, a sizable body of literature already exists on the subject, and is leaned upon in this section.

6.4.1 Neutron sources

Generally, the total underground neutron flux is the product of neutrons from a number of different sources that can be categorized as either lithogenic or cosmogenic in origin, which distinguishes those neutrons as emanating from sources either within the

lithosphere or incoming cosmic rays. Lithogenic sources are comprised mainly of neutrons created in fission processes as well as (α,n) reactions. Cosmogenic sources include secondary neutrons from cosmic ray spallation as well as muon-induced reactions. While lithogenic neutrons are largely independent of subsurface depth and mostly a function of elemental composition, the cosmogenic flux is an atmospheric source and therefore attenuated as neutrons pass through the geologic medium. These sources are discussed briefly here and literature estimates of their contributions are used to compile a neutron flux depth profile for various geologies for use in establishing neutron-induced radionuclide production source terms. Figure 6.7 shows the major contributions to the underground neutron flux as a function of depth and is the model on which the flux profile adopted in this section is based (Fabryka-Martin, 1988).

Fission neutron source

Fission neutrons come from both spontaneous and neutron-induced fission of natural uranium and thorium in the ground and have a neutron yield of roughly $Y_n^f \approx 2\frac{1}{fission}$. An estimate of the neutron production due to spontaneous fission is therefore a straightforward application of Equation (6.2), as the fission rate is dependent only on the isotopic composition of the medium. As illustrated in Figure 6.7, for a homogeneous elemental composition, the contribution of spontaneous fission neutrons is constant with depth and therefore relatively more important to the neutron flux profile at larger depths.

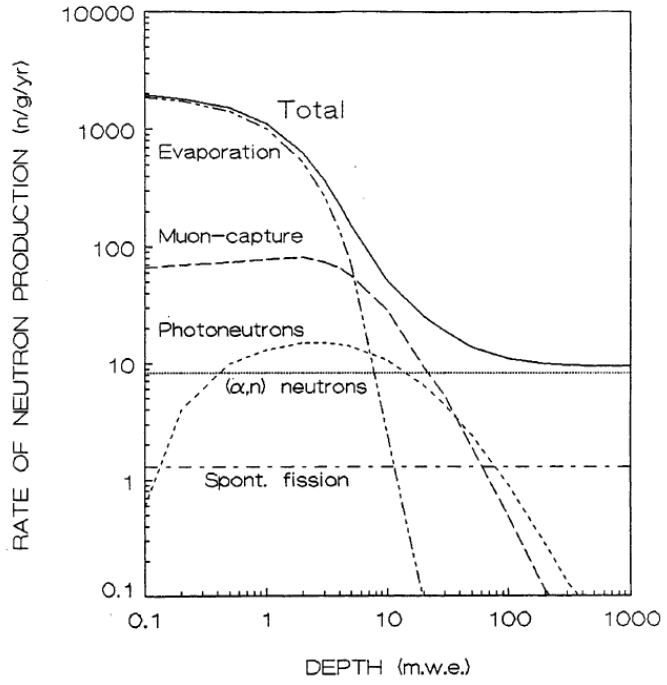

Figure 6.7 Neutron production profiled as a function of meters of water equivalent (mwe) depth for a high-Calcium granite geology; taken from Figure 2.13 of Fabryka-Martin (1988).

Production of neutrons by neutron-induced fission is itself a function of the neutron flux, with a production rate generalized in Equation (6.4). The resulting additional contribution to the neutron flux can be arrived at iteratively by first assuming a neutron distribution derived only from flux-independent processes and then correcting based on production through n-induced reactions. Figure 6.8 shows the neutron fission cross sections for the natural uranium and thorium isotopes found in earth. It can be shown using this cross section information and Equation (6.3) that the total neutron flux necessary for the n-induced fission contribution to be on par with that of spontaneous fission is of the order 10^7 cm^{-2} yr^{-1}, which it turns out is two orders of magnitude larger than the largest neutron fluxes that could be expected in shallow ground. Even with such

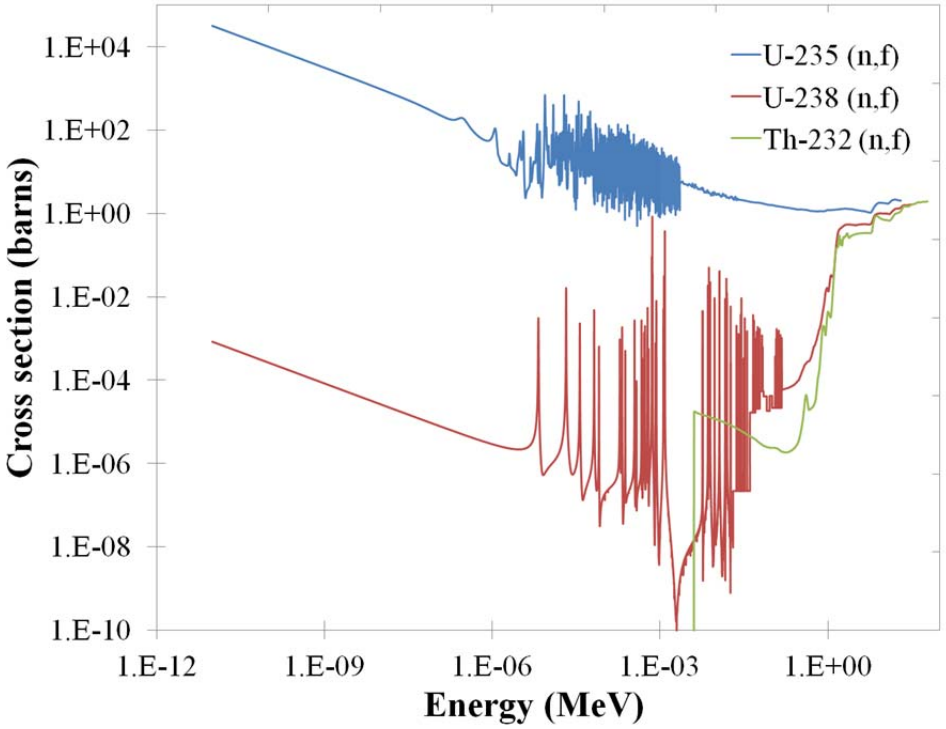

Figure 6.8 Neutron fission cross sections for ^{235}U, ^{238}U, and ^{232}Th (Chadwick *et al.*, 2011).

unrealistically high fluxes, by comparison with other sources in Figure 6.7, this contribution would still be negligible.

(α,n) neutron source

Alpha particles can emanate from a number of sources in the subsurface environment, but are predominantly created through the decay of nuclides of the uranium and thorium decay series' with energies between 4.0 and 8.8 MeV (Hebel, 2010). As seen in Figure 6.7, like spontaneous fission the (*α,n*) production rate is relatively constant throughout a homogenous underground medium. Cross sections for (*α,n*) reactions underground are high since alpha particles interact strongly with the light nuclei that comprise the bulk of the geologic composition.

Fabryka-Martin (1988) utilizes a method from Feige, *et al.*, (1968) to estimate the (α,n) neutron production rate based on a homogenous distribution of all elements within the geology. Is has been noted that these estimates, which are adapted here as well, should serve as an upper bound estimate. The primary reason for this is that the main alpha emitters are generally found in uranite (UO_2) and thorium oxide (ThO_2) mineral phases respectively rather than distributed homogeneously within natural geology (Martel, *et al.*, 1990). With grain sizes ordering on several hundred μm, many alpha particles created within such minerals are trapped within since the 15-45 μm alpha particle mean free path is comparatively small. The result is that alphas created within oxide minerals lead to fewer neutron spallation interactions compared to if they were produced in a truly homogeneous environment (Hebel, 2010).

Cosmic ray spallation source

As seen in Figure 6.7, lithogenic fission and (α,n) sources dominate the neutron production at depths of 10-20 mwe. In the very first few meters of ground, neutrons emanating as secondary cosmic ray particles from atmospheric interactions dominate. As described in Section 6.2, quantification of the cosmic ray neutron flux reaching Earth's surface is very complex, as its variability is influenced by geospatial location as well as solar activity.

Given that a neutron flux of $\phi(0)$ reaches the surface-atmosphere interface, the flux can be expected to fall off exponentially. This attenuation as a function of depth, z [g cm^{-2}] can be approximated just as in Equation (6.5)

$$\phi(z) = \phi(0)\exp\left(\frac{-z}{\Lambda}\right) \tag{6.8}$$

where Λ is an attenuation length dependent on the bulk geology density (Riedmann & Purtschert, 2011). Typical values of Λ for neutrons in soil/rock media are of the order

100-150 g cm^{-2}; a value of Λ = 148 g cm^{-2} is utilized in Riedmann & Purtschert (2011) for the evaluation of the cosmic ray neutron attenuation in "average dry terrestrial" soil. Fabryka-Martin (1988) utilizes a similar exponential function to determine the attenuation curves in various geologies, one of which is shown as the "Evaporation" of cosmic ray neutrons curve in Figure 6.7, which is an estimate of neutron production from evaporation and spallation sources of cosmic ray particles.

Cosmic ray muon source

As detailed in Section 6.3.2, the length of the muon lifetime allows for cosmic ray muons to induce reactions in the subsurface environment. While such interactions when considered for the production of individual isotopes might be of minor importance, muon reactions as a whole can contribute substantially to the neutronics within the first 10 m of ground. The generalized muon-induced reaction (μ^-,X·n) of consideration can yield up to $X = 4$ neutrons with substantial probability, according to Table 6.2 (Charalambus, 1971). The neutron production from cosmic ray muons can be estimated through application of Equation (6.7) with the addition of a neutron yield factor, $Y_n^{\mu,X} = X$ and summing over all elements and X values. Assuming a homogeneous distribution of elements throughout, the only factor appearing in Equation (6.7) that is dependent on depth is the estimate of the negative muon stopping rate, $I_{\mu^-}(x)$. As a result, the shape of the "muon-capture" curve in Figure 6.7 from Fabryka-Martin (1988) is determined by the depth-dependence of $I_{\mu^-}(x)$ in Figure 6.5. The maximum muon stopping rate occurs at a depth between 1-2 mwe and has associated with it a neutron production rate on the order of 100 *neutrons/g·y* depending on the muon intensity, $I_{\mu^-}(0)$, at the surface-atmosphere interface.

6.4.2 Neutron flux estimate

Elemental compositions for seven generalized geologies commonly found in the environment and utilized in the radionuclide background work here are presented in Table E.1 of Appendix E; some of their respective physical properties are listed in Table E.2. Neutron production rates as a function of depth calculated based on the various mechanisms in Section 6.4.1 were made by Fabryka-Martin (1988); these results are tabulated in Table E.3 and plotted in Figure 6.9. The individual components of the total neutron source are evident when compared with Figure 6.7. At shallow depths down to

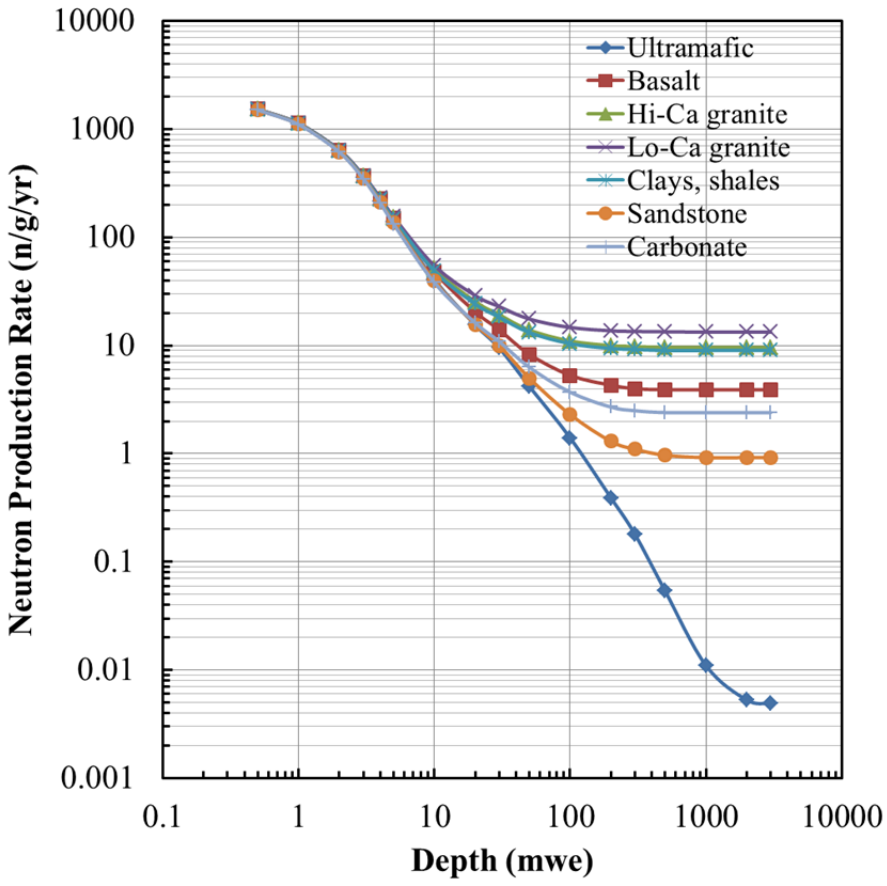

Figure 6.9 Total neutron production rates as a function of depth for the seven geology types utilized in neutron flux profiling, as calculated in Fabryka-Martin (1988).

10 m, cosmogenic neutron sources dominate and the total neutron production rate in this region does not vary greatly among the different geological compositions. For deeper depths, the estimated contribution of spontaneous fission and (α,n) reactions become more important – the "deep lithospheric" neutron production values level off, and are determined mainly by the concentration of uranium and thorium in the various geologies. The ultramafic rock composition of U and Th is roughly three orders of magnitude lower than the other geologies, which accounts for its deep lithospheric neutron production value falling much lower than the rest.

Neutron thermalization

Evaluation of the neutron flux from estimates of the neutron production profile requires an assessment of neutron thermalization from fast energies. This slowing-down occurs primarily by elastic scattering of neutrons with oxygen, hydrogen, and silicon within the medium. Energy loss through elastic scattering is a function of an energy transition probability whose density is typically described in terms of a quantity called lethargy, $u = \ln(E_0/E)$, where E_0 is an arbitrary energy used for scaling, nominally the highest available system energy. The average *lethargy* increase per elastic collision can be written

$$\overline{\Delta u} \equiv \xi = \int_{\alpha E}^{E} \ln\left(\frac{E_0}{E}\right) P(E \rightarrow E')dE'$$

where α is defined $\alpha = \left[(A-1)/(A+1)\right]^2$ and αE is the minimum energy of a scattered neutron from a target of atomic mass A. For hydrogen (A = 1), this energy loss term is 1.00; for scattering from heavier nuclei, this average can be approximated by Equation (6.9) (Lamarsh, 2002).

$$\xi_i = \frac{2}{A_i + \frac{2}{3}} \tag{6.9}$$

Neutron capture before thermalization must also be taken into account, the probability of which is quantified for particular elements by a dilute resonance integral, I_i, which has the units of a cross section [cm^2]. The total effective resonance integral, I_e [$cm^2\ g^{-1}$] for a bulk rock medium is then

$$I_e = \sum_i N_i I_i \tag{6.10}$$

where N_i is the atom density of component i in [atoms/g]. Evaluation of Equations (6.9) and (6.10) for the rock compositions listed in appendix Table E.1 have been made in Fabryka-Martin (1988).

The probability of neutron thermalization, or resonance escape, can be expressed

$$p(E_{th}) = \exp\left(-I_e / \sum_i \xi_i N_i \sigma_{s,i} \right) \tag{6.11}$$

where $\sigma_{s,i}$ is the scattering cross section of neutrons from atoms of element i (Glasstone & Edlund, 1952).

Thermal and epithermal neutron flux

Neutrons that reach thermal energies can be expected to be quickly absorbed in the bulk rock matrix. Similar to Equation (6.10) for the resonance capture of neutrons, the total effective (macroscopic) absorption cross section for thermal energies can be expressed

$$\Sigma_a = \sum_i N_i \sigma_{a,i} \tag{6.12}$$

where $\sigma_{a,i}$ is the microscopic absorption cross section [cm^2] of neutrons for element i. Values for thermal macroscopic absorption cross sections range from 0.011 $cm^2\ g^{-1}$ to 0.0042 $cm^2\ g^{-1}$ for water saturated carbonate and clay/shales respectively.

Given the neutron production profiles, P_n, in Table E.3, the effective resonance integral of Equation (6.10), the resonance escape probability of Equation (6.11), and the

total thermal macroscopic absorption cross section of neutrons of Equation (6.12), the total neutron flux can be conveniently divided into thermal and epi-thermal components

$$\phi_n = \phi_n(E_{th}) + \phi_n(> E_{th})$$

with

$$\phi_n(E_{th}) = \frac{p(E_{th})P_n}{\Sigma_a} \quad \text{and} \quad \phi_n(> E_{th}) = (1 - p(E_{th}))\frac{P_n}{I_e}. \tag{6.13}$$

Values for the thermal and epithermal neutron fluxes calculated with Equation (6.13) as a function of depth are presented in Table E.6 of Appendix E. Two sets of these flux profiles for hi-Ca granite and clay/shale geologies are plotted in Figure 6.10 for illustration.

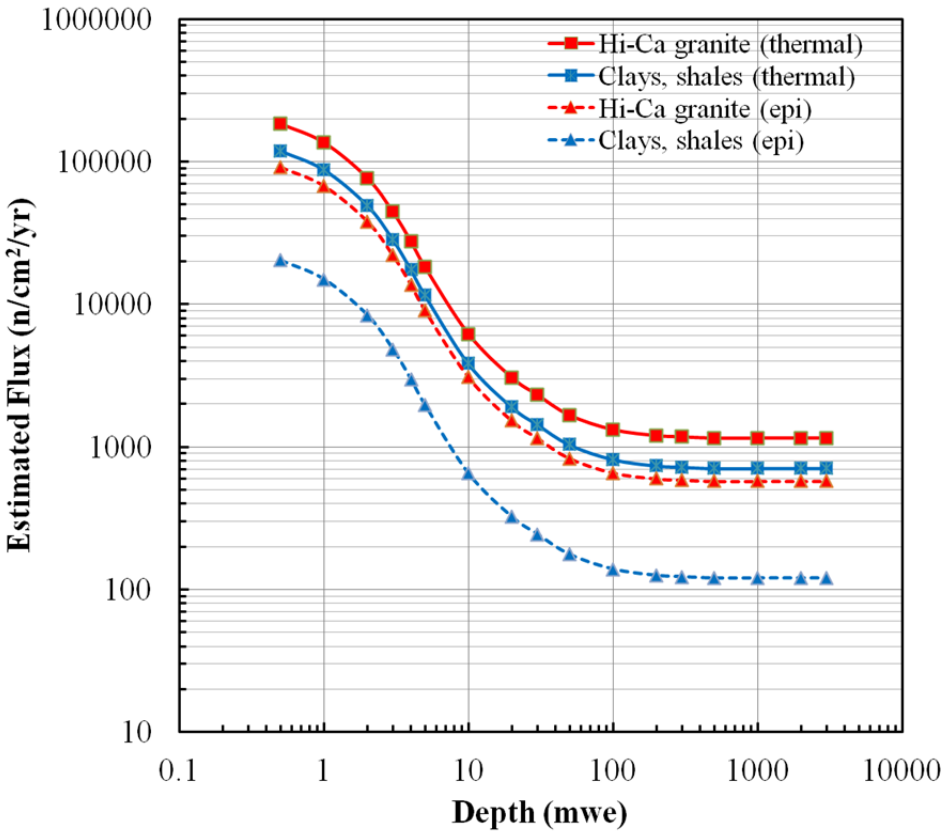

Figure 6.10 Estimated thermal and epithermal neutron flux depth profile from the values in Table E.6 for two of the geologic compositions considered in this work.

Neutron spectrum assumption

The division of the neutron flux into thermal (E_{th}) and epithermal ($>E_{th}$) components is one of the most simplistic assumptions; for reactions that heavily favor thermal neutrons this is indeed a fair approximation. A more generalized utilization of Equation (6.4) for the evaluation of neutron-induced reaction rates beyond the thermal regime requires some additional assumption be made for the treatment of the epithermal region of neutrons. This can be approached by adopting an assumed neutron spectral shape, which can be scaled so that the total integrated flux is equal to values estimated by Equation (6.13).

In Figure 6.11 is presented one assumption of the neutron spectrum compiled by Hebel (2010) based on flux measurements made by Chazal *et al.* (1998) at the Laboratoire Souterrain de Modane very deep underground. A particular feature of this assumption is the 2.4 MeV peak due to ^{238}U spontaneous fission neutrons which is more appropriate to the deep underground case where fission neutrons are more likely to dominate the neutron flux. The results presented in the present work are based on the Modane spectrum assumption in Figure 6.11, though other shapes were considered as well that model a flatter fast neutron spectrum without the 2.4 MeV peak. In particular, the "Stripa granite" assumption adopted in Hebel (2010) based on measurements in Stripa, Sweden were used as well and yielded results that differed little from the Modane spectrum (Andrews, *et al.*, 1986). The general shape of the neutron spectrum does not greatly alter calculated estimates, which are generally more dependent on the magnitude of thermal flux. The major point of difference between a 200 m spectrum and a 1-5 m spectrum is the 2.4 MeV fission neutron peak, but this difference is not large enough to

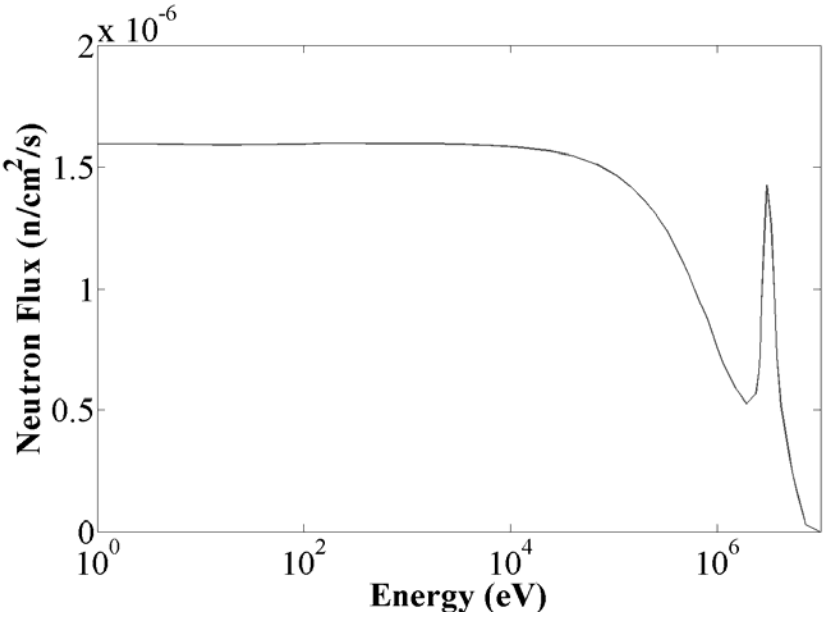

Figure 6.11 Neutron spectrum estimate made by Hebel (2010) based on deep underground neutron flux measurements taken at Modane by Chazal *et al.* (1998).

even greatly affect estimates of ^{232}Th fission (Figure 6.8) and ^{40}Ca activation (Figure 6.13), cross-sections for both of which favor fast neutron reactions.

6.5 RESULTS OF BACKGROUND CALCULATIONS

6.5.1 Radioxenon background

Radioxenon natural background production was quantified for the seven geologies whose compositions are listed in Table E.1, based on both spontaneous fission and neutron-induced fission of natural uranium and thorium. These elemental compositions, along with natural isotopic abundances and the bulk geological densities of Table E.2, were used to estimate the atomic densities of U and Th within the various

geology types, shown in Table 6.3. From these densities and the estimated subsurface neutron flux of the previous section, the spontaneous and neutron-induced fission production rates of xenon were calculated using Equations (6.2) and (6.4) respectively with cumulative fission yields acquired from England & Rider (1995) and Koning & Rochman (2011).

Table 6.3 Uranium and thorium percent natural isotopic abundances and atom densities as determined from the elemental compositions of Table E.1 and bulk densities of Table E.2.

			N (atoms/cm^3)						
Element	A	Natural %	ultramafic	basalt	hi-Ca granite	low-Ca granite	clay/shale	sandstone	carbona
Th	232	100	2.91E+13	2.91E+16	5.96E+16	1.19E+17	6.85E+16	1.01E+16	1.19E+
U	234	0.006	3.96E+08	3.96E+11	1.15E+12	1.15E+12	1.09E+12	1.46E+11	8.41E+
	235	0.720	5.17E+10	5.17E+13	1.49E+14	1.49E+14	1.42E+14	1.91E+13	1.10E+
	238	99.28	7.03E+12	7.03E+15	2.03E+16	2.03E+16	1.93E+16	2.60E+15	1.49E+

Spontaneous fission production rates, P_i^{sf}, of radioxenon as well as radioactive decay equilibrium concentrations are given in Table F.1 of Appendix F. Radioactive equilibrium concentrations, for any production mechanism, are calculated according to

$$\frac{dN_i}{dt} = P_i - \lambda_i N_i = 0$$

$$A_i^{eq} = P_i \tag{6.14}$$

Calculated neutron-induced fission production rates of radioxenon for select depths of geology are given in Table F.2 of Appendix F.

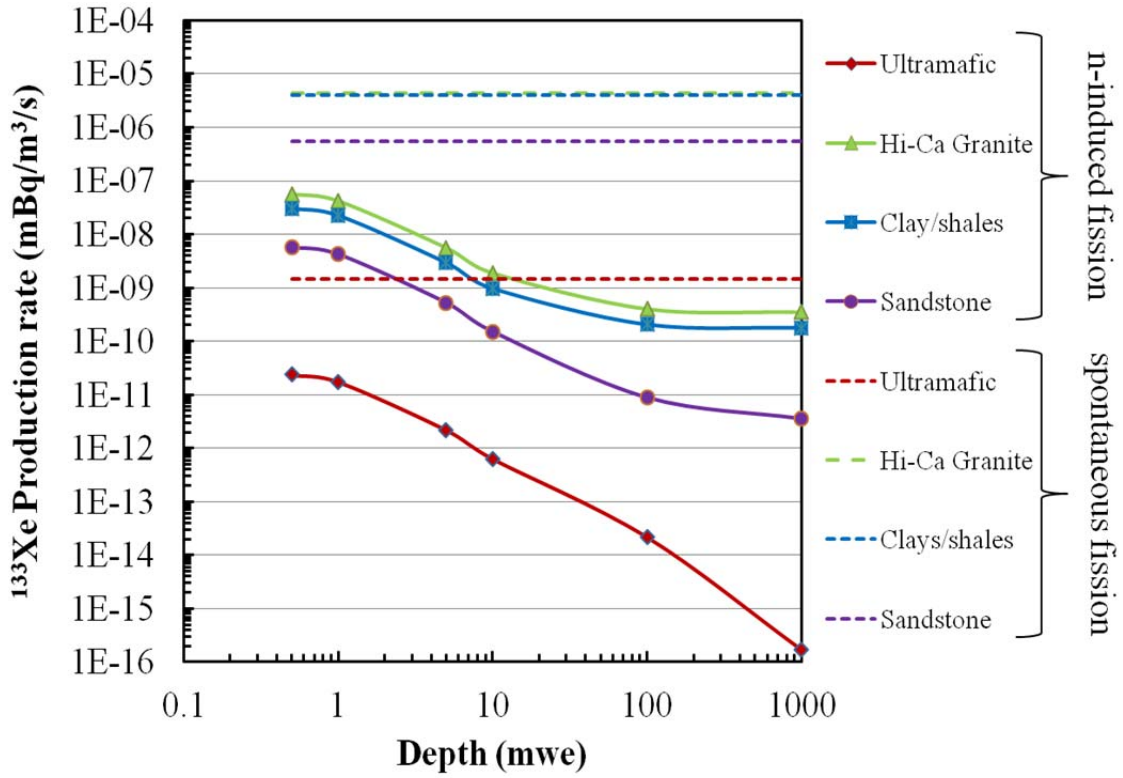

Figure 6.12 Estimated spontaneous and neutron-induced fission production rates (in mBq/m^3/s) of ^{133}Xe for four specific geological compositions to a depth of 1000 mwe.

Figure 6.12 shows a plot of the neutron-induced and spontaneous fission production rates of ^{133}Xe for four of the seven geologic compositions considered in this work. In the very shallow, first 1-5 m of bulk medium where the cosmic ray neutron flux is highest, the neutron-induced fission contribution to the ^{133}Xe background is roughly two orders of magnitude smaller than the spontaneous fission contribution. Estimates from Table F.1 and Table F.2 for the other radioxenon species indicate that the same holds true. At larger depths, especially below 10 m, the spontaneous fission contribution is greater by closer to four orders of magnitude, as the cosmic ray neutron flux is almost entirely attenuated and the neutronics driven by fission and (α,n) neutrons (Figure 6.7).

6.5.2 Radioargon background

^{40}Ca(n,α)^{37}Ar *interactions*

Figure 6.13 shows the cross section for neutron activation of ^{40}Ca, which is regarded as the most direct and relevant production path for ^{37}Ar in the environment (Egnatuk *et al.*, 2012; Riedmann & Purtschert, 2011). The ^{40}Ca target atom densities determined from the elemental compositions of Table E.1 and bulk densities of Table E.2 are given in Table 6.4. These target densities and the approximated neutron flux from Section 6.4.2 were used in an evaluation of Equation (6.4) to obtain the calculated values for the ^{37}Ar production rates and radioactive equilibrium concentrations resulting from neutron activation of ^{40}Ca given in Table F.4. Figure 6.14 plots the ^{37}Ar concentration curves versus depth along with the proposed 20 mBq/m^3 field system detection limit for comparison.

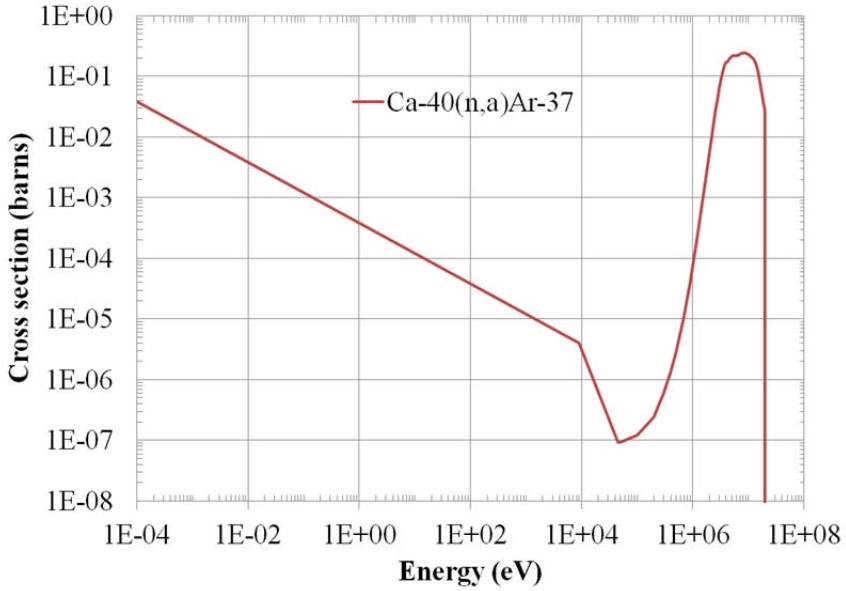

Figure 6.13 Neutron activation cross section of ^{40}Ca for the reaction ^{40}Ca(n,α)^{37}Ar, from data found at Chadwick *et al.* (2011).

Table 6.4 Potassium and calcium percent natural isotopic abundances and atom densities as determined from the elemental compositions of Table E.1 and bulk densities of Table E.2.

Element	A	Nat %	N (atoms/cm^3) ultramafic	basalt	hi-Ca granite	low-Ca granite	clay/shale	sandstone	carbonate
K	39	93.26	1.61E+18	3.35E+20	9.80E+20	1.63E+21	7.88E+20	3.54E+20	1.05E+20
	40	0.012	1.97E+14	4.09E+16	1.20E+17	2.00E+17	9.64E+16	4.33E+16	1.28E+16
	41	6.730	1.11E+17	2.30E+19	6.73E+19	1.12E+20	5.41E+19	2.43E+19	7.21E+18
Ca	40	96.94	1.02E+21	3.11E+21	9.97E+20	2.01E+20	8.86E+20	1.31E+21	1.19E+22
	42	0.647	6.49E+18	1.97E+19	6.34E+18	1.28E+18	5.63E+18	8.34E+18	7.57E+19
	43	0.135	1.32E+18	4.02E+18	1.29E+18	2.60E+17	1.15E+18	1.70E+18	1.54E+19
	44	2.086	2.00E+19	6.08E+19	1.95E+19	3.93E+18	1.73E+19	2.57E+19	2.33E+20
	46	0.004	3.67E+16	1.11E+17	3.58E+16	7.21E+15	3.18E+16	4.71E+16	4.27E+17
	48	0.187	1.64E+18	4.99E+18	1.60E+18	3.23E+17	1.42E+18	2.11E+18	1.91E+19

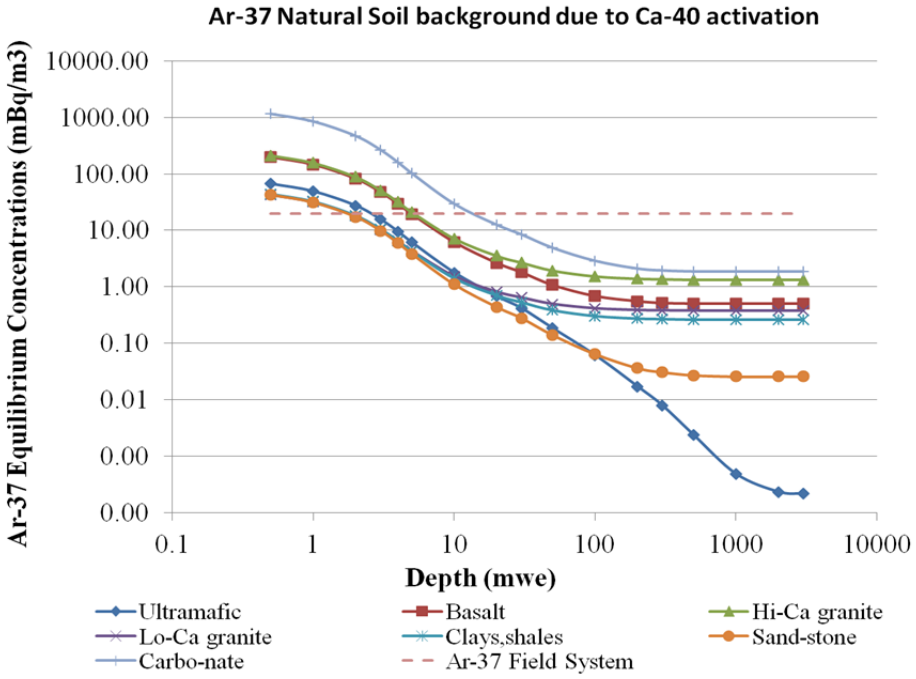

Figure 6.14 Estimated ^{37}Ar equilibrium concentrations resulting from ^{40}Ca neutron activation in the subsurface and the 20 mBq/m^3 proposed detection limit.

K(μ,X·n) reactions

As introduced in Section 6.3.2, another potential avenue for ^{37}Ar production in the environment is through the muon interaction in Equation (6.6), which can be summarized as: $^{37+X}\mathrm{K}(\mu,X\cdot n)^{37}\mathrm{Ar}$ where X is the number of free neutrons that result from the compound reaction. Table 6.5 lists the possible potassium isotopes with corresponding X free neutrons that can yield ^{37}Ar through muon interaction. Of the possible candidates for interaction, ^{37}K and ^{38}K are not expected to be present naturally in the geologies, as shown in Table 6.4 and so are excluded from consideration.

An estimate of the ^{37}Ar production rate is made using Equation (6.7), with muon stopping rate versus depth obtained from Figure 6.5 and values for f_d and f_r estimated from Figure 6.6 and Table 6.2 respectively. The fraction of muons, f_c reaching the 1s muonic level of potassium is approximated using the Fermi-Teller "Z-Law," which has $\left(f_c\right)_i = a_i Z_i / \sum_N a_n Z_n$ where a_i and Z_i are the abundances and charge of each isotope in the various media (i.e. from Table E.1) (Hebel, 2010).

Table 6.5 Possible values for X free neutrons in the muon interaction with potassium that yield ^{37}Ar. ^{37}K and ^{38}K are not expected to contribute due to low abundance. Estimated values for f_d and f_r from Figure 6.6 and Table 6.2 respectively.

$^{37+X}\mathrm{K}(\mu,X\cdot n)^{37}\mathrm{Ar}$ reaction possibilities

A	X	f_d	f_r
37	0	-	-
38	1	-	-
39	2	0.8	0.15
40	3	0.8	0.05
41	4	0.8	0.02

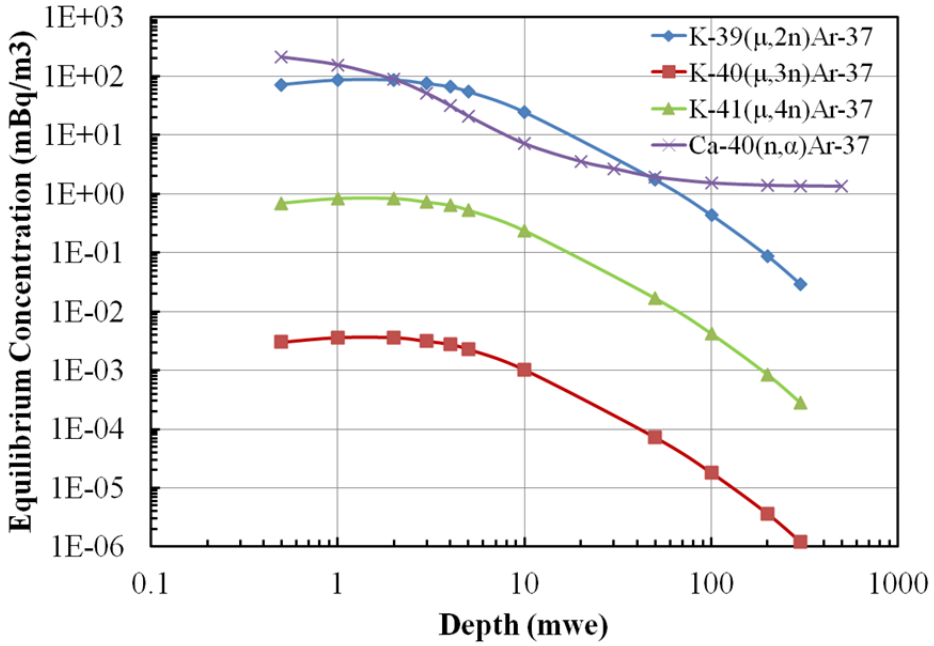

Figure 6.15 Estimated ^{37}Ar equilibrium concentration profiles resulting from various K(μ,X·n) reactions compared to ^{40}Ca neutron activation for the Hi-Ca granite geological composition.

Results of these calculations for ^{37}Ar equilibrium concentrations are listed in Table F.5. An estimate of the total ^{37}Ar soil-gas background concentration obtained from addition of ^{40}Ca activation and potassium-muon interactions is given in Table F.6. Figure 6.15 shows a plot of the various contributions to the ^{37}Ar radioactive equilibrium concentrations for the case of hi-Ca granite. As in all of the geologies, the greatest muon-interaction contribution comes with ^{39}K by roughly two orders of magnitude. In this particular case, the muon contribution appears to be potentially comparable to the ^{40}Ca(n,α)^{37}Ar within the first 10 m of depth. It must be stated, however, that the ^{37}Ar production by muon interaction calculated here should be regarded as a maximum potential contribution. What is not considered in Equation (6.7) is a true assessment of the scaled muon intensity; this equation as it appears in Charalambus (1971) includes an

additional factor $\kappa < 1$ that accounts for variability of the muon intensity based on elevation and latitude. The maximum value $\kappa = 1$ is assumed here for generality, so the results presented here are also a maximum estimate.

6.6 MODELING OF BACKGROUND

The entirety of this chapter has been dedicated to establishing natural background radioxenon and radioargon production rates as a function of depth in various geologies. To this point, no mention has been made of transport - the "equilibrium" values discussed thus far and listed in the tables of the Appendix are radioactive equilibrium values as determined through the balancing of nuclide production versus decay rates in Equation (6.14). This equilibrium state implicitly assumes a closed system - that there are no loss terms due to removal of gas from the system, which is not what would be expected in a true physical system.

The greatest attention is typically paid to soil-gas backgrounds in the first few meters of ground where simple analytical diffusion and advection approximations should provide decent approximation. For the case of ^{37}Ar in particular, such approximations have been well-supported by experimental data (Riedmann & Purtschert, 2011). The aim in this chapter was to establish a similar radionuclide background capability within the UTEX model, where transport is simulated to arbitrary depths along fracture networks.

6.6.1 Radionuclide emanation

Soil-gas radionuclides are produced within the mineral or grain structure of the bulk geologic medium, rather than in the air-filled porous volume. The physical parameter porosity, ϕ (not a flux), refers to the ratio of porous volume to the total bulk volume of a medium, which includes both porous and non-porous volumes. Before

transport of radionuclide gas can be simulated, the fraction of produced gas that *emanates* from the mineral structure of the rock medium into the air-filled volume must be taken into account. Unfortunately, despite decades of research especially with respect to radon, gas emanation is not a very well understood phenomenon.

Emanation of gas is generally defined in terms of an *emanation coefficient*, ε, that describes the ratio of air concentration of gas (C_{air}) to the maximum possible concentration within the mineral structure (C_{rock}) (Riedmann & Purtschert, 2011), from which

$$C_{air} = \varepsilon \frac{1-\phi}{\phi} C_{rock} . \tag{6.15}$$

Table 6.6 lists ranges of values for the C_{air}/C_{rock} ratio for a span of values on the porosities and emanation coefficients. Table 6.7 is adapted from Hebel (2010) and gives an overview of the porosity and emanation coefficient values possible for various rock types as well as their rough elemental equivalent to the geologies defined in Table E.1.

Looking at Table 6.6 and Table 6.7, the ratio C_{air}/C_{rock} spans a range from $\varepsilon = 0.01$ to roughly $\varepsilon = 50$, which is nearly four order of magnitude. Furthermore, within a given rock type such as granite, the same ratio estimate can easily vary by nearly two orders of magnitude; this variation is even greater for less well-defined soil types whose porosities are not easily determined. For this reason, radionuclide gas emanation is not greatly explored in this work and is regarded, in the present work at least, as a means for bounding maximum soil-gas concentrations.

Table 6.6 Ranges of values for the ratio C_{air}/C_{rock} in Equation (6.15).

		$\varepsilon(1-\phi)/\phi$ for the following column ε								
ϕ	$(1-\phi)/\phi$	0.01	0.02	0.03	0.05	0.1	0.2	0.3	0.4	0.5
0.01	99.0	0.99	1.98	2.97	4.95	9.90	19.80	29.70	39.60	49.50
0.05	19.0	0.19	0.38	0.57	0.95	1.90	3.80	5.70	7.60	9.50
0.1	9.0	0.09	0.18	0.27	0.45	0.90	1.80	2.70	3.60	4.50
0.2	4.0	0.04	0.08	0.12	0.20	0.40	0.80	1.20	1.60	2.00
0.3	2.3	0.02	0.05	0.07	0.12	0.23	0.47	0.70	0.93	1.17
0.4	1.5	0.02	0.03	0.05	0.08	0.15	0.30	0.45	0.60	0.75
0.5	1.0	0.01	0.02	0.03	0.05	0.10	0.20	0.30	0.40	0.50

Table 6.7 Ranges of porosities and emanation coefficients for various rock types as well as their approximate elemental equivalence to geologic compositions of Table E.1; adapted from Table 4.2 of Hebel (2010).

rock type	ε (%)	density (g/cm3)	porosity (%)	Elemental Equivalent
granite	6.8 - 32.7	2.75	0-5 - 1-5	hi-Ca granite
granodiorite	16.9 - 40.0	2.76	0.5 . 1.5	low-Ca granite
gneiss	1.0 - 14.4	2.75	0.5 . 1.5	hi-Ca granite
syenite	9.3	2.79	0.5 . 1.5	low-Ca granite
pegmatite	4.3	2.75	0.5 . 1.5	hi-Ca granite
gabbro	3.6	3.01	0.1 . 0.2	basalt
basalt	2.5	3.01	0.1 . 1.0	basalt
quartzite	5.3	2.7	0.1 . 0.5	sandstones
sandstone	5.2	2.32	5 - 25	sandstones
marl	2.6	2.1	< 10	carbonate / sandstones
tuff	1.7	1.8	1 - 53	basalt
limestone	1.6	2.3	5 - 20	carbonate
soil, granite	46	1.7	< 40	hi-Ca granite
soil, lime	33	1.6	< 40	carbonate
soil, clay	30	1.8	< 40	clays
soil, sand	9	1.6	< 40	sandstones
soil, volcanic	49	1.8	< 40	basalt
monazite sand	9 - 49	3	< 40	-

6.6.2 Radionuclide background modeling

Like many aspects of transport simulation within the UTEX framework, actual analysis of modeled soil-gas background transport is a difficult task due to so many variables affecting the problem. That said, it is not difficult to predict the affect that transport should have on the soil-gas background. In the top few meters of earth, the influence of direct vertical diffusion and advection of gas into the atmosphere has been considered previously (Johnson & Biegalski, 2012; Riedmann & Purtschert, 2011). The result is that the radioactive equilibrium concentrations are reduced due to an additional loss term. As seen in the results from Johnson and Biegalski (2012) in Figure 6.16, the radionuclide concentration falls off near the surface as gas escapes into the atmosphere. What results is likely a flow of soil-gas develops vertically towards the surface that is

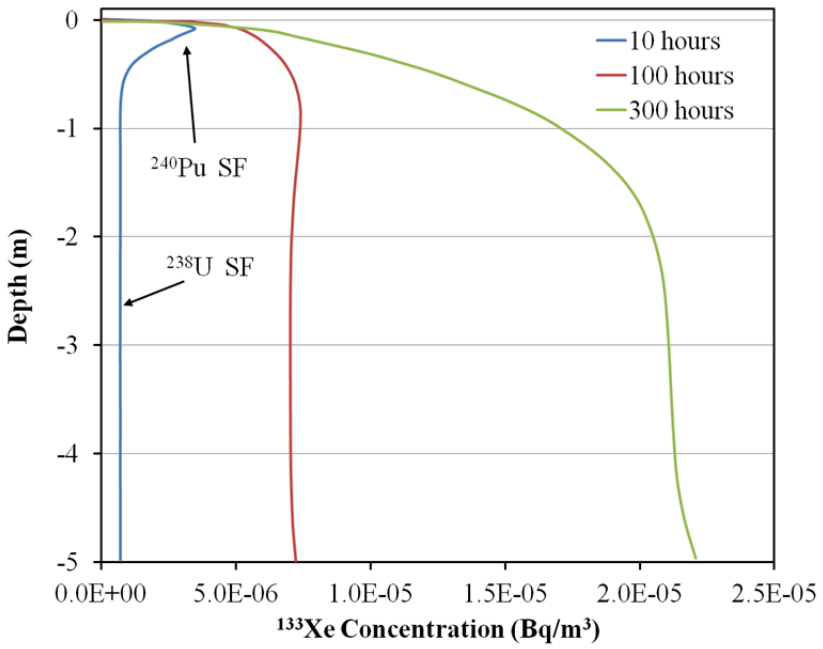

Figure 6.16 Estimated ^{133}Xe soil-gas background concentrations near ^{240}Pu contaminated site resulting from spontaneous fission of ^{240}Pu (near the top) and ^{238}U (distributed throughout) following different times of simulation with diffusion and advection; data from Johnson and Biegalski (2012).

dependent on the physical parameters of the geology as well as the rate of advection due to pressure differentials in the system. At greater depths, these simpler models estimate an asymptotic level of soil-gas backgrounds. Background concentrations near cracks in a fractured medium would be expected to show a similar affect as the concentrations near the surface - a pressure-dependent flow of gas should arise into (or out of) open fractures.

In the present work, the emphasized goal now that a soil-gas background source term has been defined in Section 6.5 is to establish the capability of the UTEX model to integrate it into its more general source term module. One drawback to having simply adopted values for the radionuclide background from the literature is that the focus of such studies is typically on quantifying radioactive equilibrium using *cumulative* yield estimates for radioxenon. The difficulty with this is that the UTEX source term handling includes its own Bateman equation solver, which for the case of radioxenon modeling, requires independent yield data. Essentially, supplying cumulative yield input for ^{133}Xe and ^{135}Xe would substantially overestimate those background concentrations as ^{133m}Xe and ^{135m}Xe decay would be counted twice. While there are workarounds to this, use of independent yields for xenon and cumulative yields for iodine facilitates a smoother integration into the existing UTEX framework.

Figure 6.17 shows simulated soil-gas concentration curves of radioxenon and ^{37}Ar as a function of distance from fractures at a depth of 5 m (roughly 14 mwe) in granite after 14 days. Again, the specific characteristics of the concentration curves near open fractures are dependent on the dynamic system barometrics. As a demonstration of this, Figure 6.18 shows concentration curve calculations from UTEX modeling of ^{37}Ar natural soil-gas background at several time points during the simulation. At time $t = 0$, the system concentrations are set at values that would be expected in a closed geologic system; i.e., with the emanation-adjusted depth-dependent concentrations from Appendix

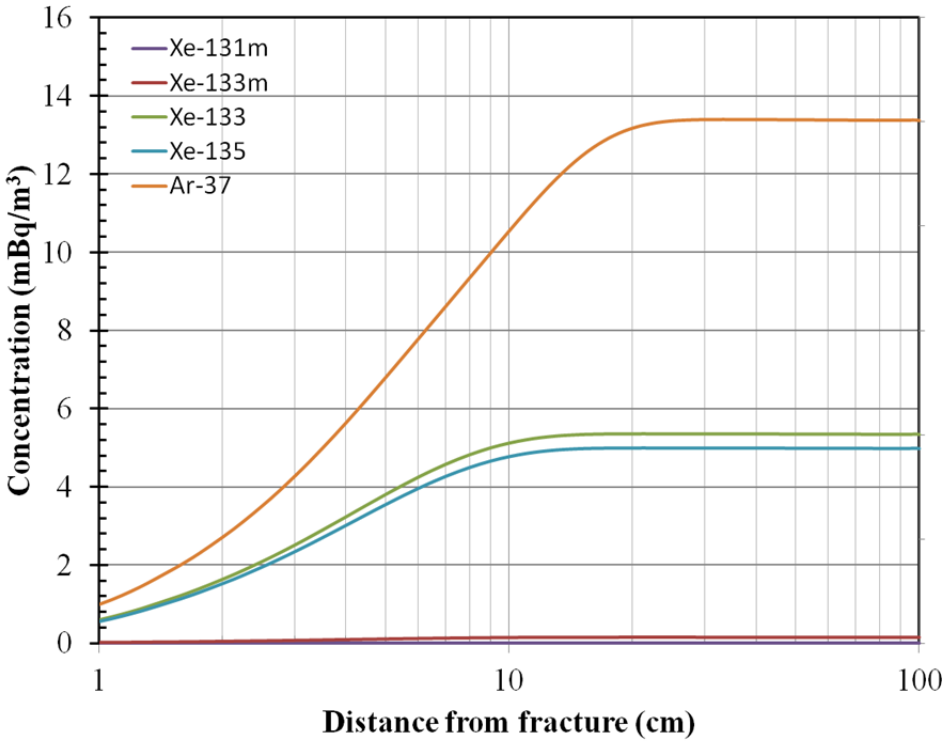

Figure 6.17 Simulated radionuclide background concentrations curves in [mBq/m^3] at 5 m depth granite (about 14 mwe) following 14 days of transport in UTEX.

F distributed throughout the bulk medium (and zero initial concentration in fractures). As time progresses, soil-gas is allowed to flow out of the bulk medium into the fractures.

At certain times of increasing pressure flow into the fracture can be inhibited or in fact reversed, such as the 'Day 12' and 'Day 14' example curves in Figure 6.18. These specific curves correspond to system states flow is directed into the bulk medium, and concentration near open fractures begin to build up. Figure 6.19 shows concentration curves of ^{37}Ar for vertical cuts of the bulk medium at distances of 2 cm and 50 cm from open fractures at different intervals during the same 14 day simulation[17]. As concluded

[17] The vertical resolution of simulations were 4 m granite, or roughly 11 mwe. The first vertical data point, therefore, is significantly below the maximum concentration at shallower depths (<10 mwe).

from Figure 6.18, at only 2 cm from the fracture (top plot of Figure 6.19), the concentration curve is strongly influenced by the exchange of gas with the open fracture - this is particularly evident again at days 12 and 14 where the curves show a rise compared to previous days. Deeper within the bulk medium (bottom plot of Figure 6.19), the influence of fracture-matrix exchange is barely felt, as the curves at different times are hardly distinguishable.

6.6.3 Soil-gas Xe ratios

Lastly, a cursory examination of the radioxenon isotopic ratios was made following UTEX simulated 14-day transport of the soil-gas background source term. In short, the effects of gas transport on the relative isotopics of xenon during test simulations were unnoticeable. Figure 6.20 shows (overlapping) isotopic ratios of radioxenon at a simulated point corresponding to 5 m depth and 2 cm from open fracture for various times through a 14-day simulation. This result is not altogether surprising, however, given that the radioxenon background source production is constant in time and ratios calculated from data in Table B.3 are nearly identical as a function of depth. The result of this is a minimization of the source mixing that characterizes significant fluctuations in the radioxenon isotopics resulting from a deeper, more localized source.

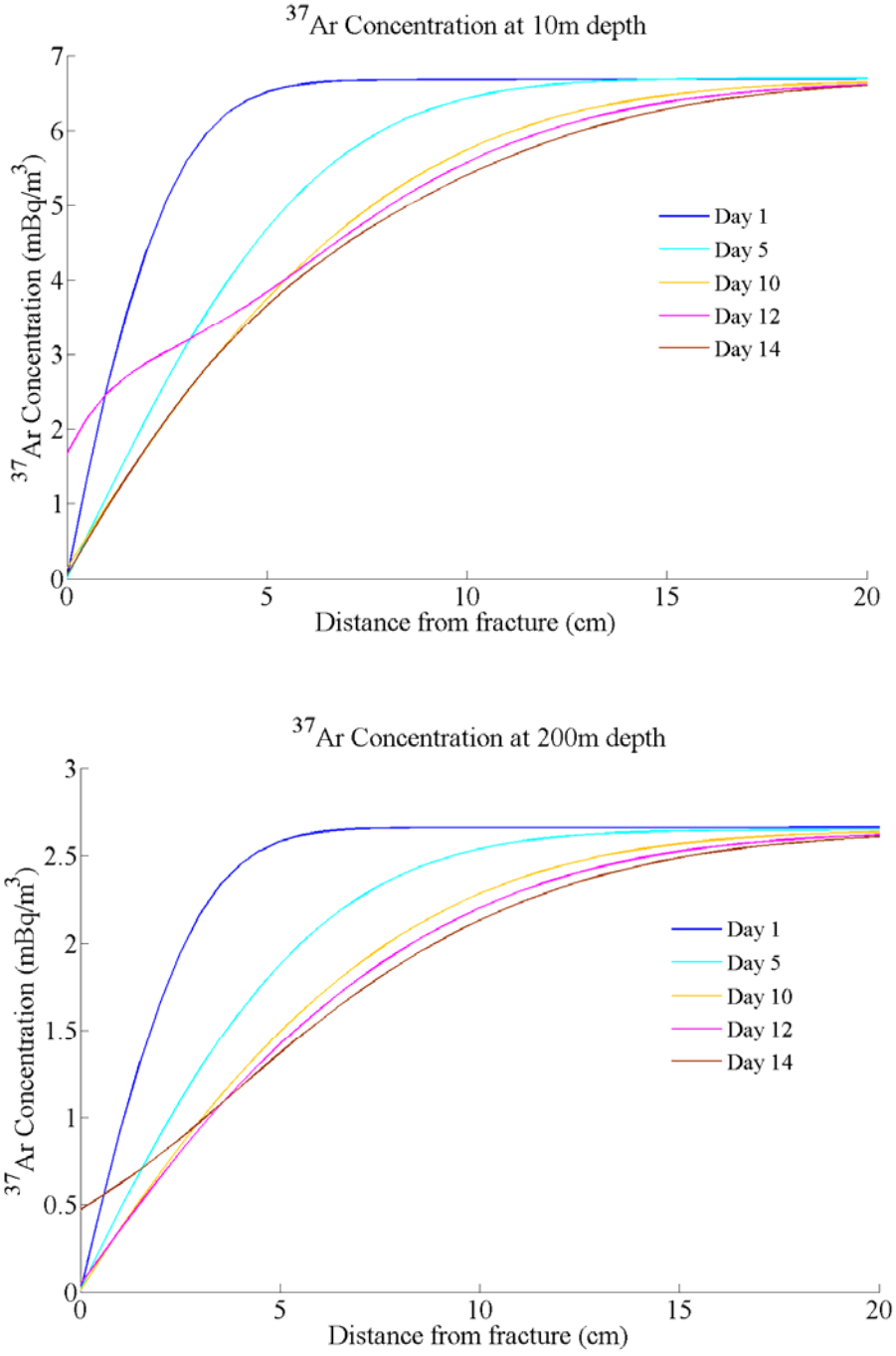

Figure 6.18 Simulated horizontal radionuclide background concentrations curves in [mBq/m^3] at 10 m and 200 m depth granite (about 14 mwe) at different intervals during 14 days of transport in UTEX.

6.7 CONCLUSIONS

In this chapter a characterization and evaluation of the soil-gas radionuclide background has been made. For the case of radioxenon, in the very shallow, first 1-5 m of bulk medium where the cosmic ray neutron flux is highest, the neutron-induced fission contribution to the xenon background is still roughly two orders of magnitude smaller than the spontaneous fission contribution. At larger depths, especially below 10 m, the spontaneous fission contribution is greater by closer to four orders of magnitude, as the cosmic ray neutron flux is almost entirely attenuated and the neutronics driven by fission and (α,n) neutrons. The total xenon background production rates (and equilibrium activities) are given in Appendix Table F.3. For ^{133}Xe, these estimated concentrations (discounting the effects of emanation) in the shallow surface are of the order 0.1-1.0 mBq/m^3. These total estimates are similar to those made by Hebel (2010) for very shallow geologies. The nature of gas emanation in a porous environment was not thoroughly explored in this work, but as suggest by Hebel (2010) and others, emanation marks a great uncertainty within soil-gas background calculations and thus warrants further study.

An estimate of the total ^{37}Ar soil-gas background concentration obtained from addition of ^{40}Ca activation and potassium-muon interactions is given in Table F.6. The greatest muon-interaction contribution comes with ^{39}K by roughly two orders of magnitude. In this particular case, the muon contribution appears to be potentially comparable to the ^{40}Ca$(n,\alpha)^{37}$Ar within the first 10 m of depth, as shown in Figure 6.15. It must be stated, however, that the ^{37}Ar production by muon interaction calculated here should be regarded as a maximum potential contribution. The total estimated ^{37}Ar soil-gas background at shallow depths was found to vary substantially based on the estimated ^{40}Ca and potassium content in the geology, but was of the order 50-200 mBq/m^3. These

maximum estimates are comparable to the measurements made by Reidmann & Purtschert (2011) in the top few meters of soil.

The soil-gas background estimates were integrated into the UTEX model to examine the effect of gas transport on the equilibrium concentrations. As expected, the concentrations varied greatly based on the nature of the barometric pressure as well as depth in the ground and distance from open fractures. Deep within the modeled system, the radioactive decay equilibrium concentrations were affected much less at points closer to the fractures. Lastly, likely due to the proximity and homogeneity of the modeled soil-gas background source, simulation of gas transport within UTEX showed very little impact on the isotopic ratios of xenon.

Chapter 7: On-site Inspection Science

7.1 On-site inspection overview

With respect to the CTBT verification regime, radionuclide detection has an importance in both atmospheric monitoring within the IMS as well as in an OSI. For the most part, the particular relevance of examining noble gas transport mechanics and their effects on isotopic ratios in this work is in the interpretation of trace signatures in soil-gas samples obtained through an on-site inspection. In the search for radionuclide evidence of a potential UNE, the major factors that inhibit gas reaching detectors are geologic containment and radioactive decay. In a technically well-contained UNE event, assuming there is no rapid venting of gas and particulate material, eventual release of gas from the ground can still occur by slow migration through porous and fractured media, driven in large part by the evolution of atmospheric pressure above the contaminated ground (Auer, *et al.*, 1996; Carrigan *et al.*, 1997; Nilson *et al.*, 1991).

Prompting for an OSI might follow a seismic reading or elevated radionuclide gas/particulate atmospheric concentration measurement by stations within the IMS. In such a case, a suspected event's potential location might be estimated through seismic data analysis and atmospheric transport modeling of the radionuclide source. The goal of an on-site inspection, then, would be to obtain localized evidence of a subsurface radionuclide source given pre-determined target area. In particular, soil-gas levels of ^{131m}Xe, ^{133}Xe and ^{37}Ar significantly above subsurface background are widely regarded as extremely strong indicators of a recent UNE (Purtschert *et al.*, 2007; Saey, 2007).

Upon an on-site inspection team's arrival and set up of a base of operations (BoO) in the field, a selection of several dozen target sampling sites in the general region of the

suspected event must be made within the negotiated inspection areas.[18] For each sampling site, a 5-10 m depth borehole, roughly 2" in diameter is made in the ground. A gas sampling tube is placed into the hole, connected to a pump, and the hole is back-filled or packed to isolate the subsurface sampling point from the atmosphere. Soil-gas is pumped from the sampling point at a rate on the order of 1 L/minute and collected and compressed into high-pressure gas bottles. The conceptual design of a subsurface sampling unit is shown in Figure 7.1. Ar and Xe gas may be separated from the various samples at the BoO and then counted on field systems such as the SAUNA or ARIX (radioxenon counting) or the Chinese MARDS (^{37}Ar counting) (Saey, 2007).

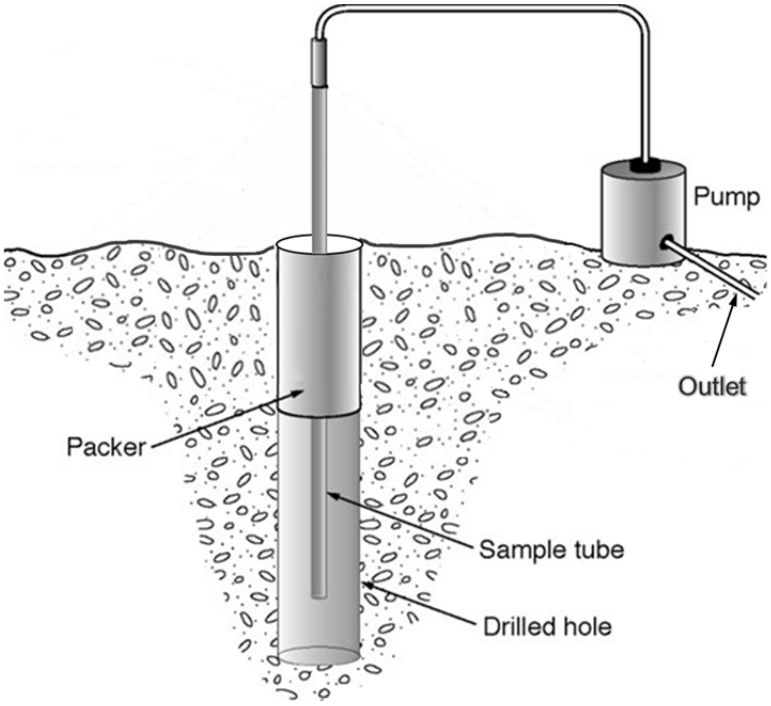

Figure 7.1 On-site inspection soil-gas sampling concept, illustration adapted from Carrigan & Sun (2012).

[18] It is within the power of the Inspected States Party to block access to square restricted areas (RA) 2 km on a side.

Timing of deployment of an OSI team is likely to be critical in the assessment of any suspected UNE event for a number of reasons. Given the time it takes to proceed from an initial IMS measurement trigger to the localization of a possible event area, political considerations and the granting of permission to perform the inspection, and practical allotment of time for deployment of a team and equipment to a potentially remote location, the time window for an on-site inspection deployment likely begins 10-14 days following the suspected UNE. In that time frame, prompt venting and slower emanation of radionuclide gas driven by cavity over-pressurization will most likely have concluded. Carrigan & Sun have conducted studies indicating that while the initial cavity pressure may have equalized in this time period, the large thermal gradients resulting from the UNE may have not. In this case, subsurface convection could still actively draw gas towards the surface through the fractured network, and ultimately enhance the likelihood of noble gas detection at the surface (Carrigan & Sun, 2011).

Driven by the initial cavity pressure and thermal convection, within the days and weeks following a UNE event a contaminant halo will have formed in the fractured rock area around the original cavity as well as perhaps a debris chimney, depending on whether the cavity collapses. The exact settling of the cavity, chimney, and surrounding fractured rock will all affect the distribution of radionuclide-containing gas in the halo. Even in the case of a well-contained UNE, it may be possible for the early noble gas halo to extend upwards hundreds of meters from the cavity with "detectable" amounts of ^{133}Xe and ^{37}Ar driven to the surface even within the first couple of days, though too small to be eventually detected by IMS stations after atmospheric dilution (Carrigan & Sun, 2011). In the time frame of active OSI soil-gas sampling, weeks following a suspected UNE event, noble gas leakage from the ground would be driven more and more by the slower action of barometric pumping.

7.2 ON-SITE INSPECTION CHALLENGES

Despite the supposed proximity of on-site inspection sampling to an estimated UNE event's location, the search for subsurface soil-gas evidence can be like looking for a needle in a haystack. Due to the nature of geologic fracture and fault systems, on-site inspections likely would not serve well in further reducing potential target search areas. Even presuming that a true UNE has occurred and the target area of the event is well-estimated, the success of an on-site inspection effort in obtaining soil-gas radionuclide evidence of such faces a number of challenges. Questions of where, when, and how to conduct soil-gas sampling with the best chance of noble gas detection is of course the subject of much research, including the present work.

7.2.1 Sampling location

Transport of UNE-produced gas to the surface takes place predominantly in vertically-trending fracture networks within the underlying geology. Such vertical transport pathways can be characteristic of the natural geology or created as a result of the extreme pressure and heat from a UNE. Knowledge of the underlying geology in a target search area can therefore be regarded as one of the greatest tools for enhancing the success of on-site inspection efforts. Unfortunately, such knowledge cannot be presumed. The capability of an on-site inspection team to visibly identify fractures in the bedrock is limited by alluvium coverage on the surface and field methods of examining the subsurface structure (e.g. ground penetrating radar) is likely to be of too poor resolution for the identification of small fracture networks.

For barometric pumping to be effective as a means of driving vertical transport of noble gas to the surface, pressure variations in the atmosphere must propagate into the subsurface environment. One effect of an especially thick top alluvium layer could be the effective isolation of the underlying fractured bedrock from surface changes in pressure.

Even if a borehole could be penetrate through the alluvium into the fractured medium below, the inhibited effect of barometric pumping may not be strong enough to induce gas transport into the sample region. The presence of such an alluvium layer presents one of the largest hurdles to OSI success.

7.2.2 Sampling timing

A major conclusion of the 1996 Non-Proliferation Experiment (NPE) and one of the fundamental principles behind the concept of barometric pumping is that vertical transport of gas in a fractured network is driven by atmospheric pressure fluctuations and the largest surface releases are likely to coincide with deep, extended pressure lows (Carrigan *et al.*, 1997; Nilson *et al.*, 1991). Similar to the capability to locate underlying fractured media and transport pathways, targeted sampling during periods of decreasing atmospheric pressure has been proposed as one strategy for maximizing the success potential of soil-gas sampling (Carrigan & Sun, 2011).

So-called barometrically-triggered sampling, however, is not entirely straightforward to implement into a generalized on-site inspection procedure. Of primary difficulty is the fact that soil-gas sampling is in large part limited by flow rate and sampling times of 1-2 -days are likely needed for radioxenon and radioargon analysis. In other words, targeting a specific barometric low covering a sampling period of 1-2 hours is likely to be too low volume for radionuclide analysis. How to integrate targeted sampling windows that span 24 hours or more into regular on-site inspection procedure is one important issue requiring further study.

7.2.3 Sampling practice

Standard OSI practices and procedures remain a work in-progress, but one of the largest questions faced is with regard to the potential for atmospheric infiltration at a

sampling point. This is a potential concern both as a contribution to soil-gas backgrounds as well as direct surface air invasion down a permeable backfilled borehole. Evaluation of the range of the magnitude of such effects is one point of investigation in the following sections. Additionally, one active method for preventing infiltration is to prepare on the surface a plastic tent or tarp above the sampling point to isolate the borehole and immediate sampling area from the atmospheric gas invasion. How effective this practice is at combating infiltration and the degree to which it might inhibit barometric pumping is a matter of ongoing research.

Conceptually, soil-gas sampling at a given location is traditionally conducted with a single sampling tube down a single borehole. It has been proposed that moving from a single sampling point to a distributed sampling strategy with multiple sampling points per location can yield a higher likelihood of detection of soil-gas radionuclides when the underlying fracture network is uncertain (Carrigan & Sun, 2011). The advantage of such a "more is better" approach is intuitively clear, however, the field resources available to a small on-inspection contingency greatly restrict the number of boreholes and sampling sites that can be prepared in short time. Ultimately, the benefit of increasing the number of sampling points per given location would have to be weighed against potentially reducing the number of locations within a larger target area that can be investigated - a more in-depth investigation covering smaller area versus a broader, less thorough one.

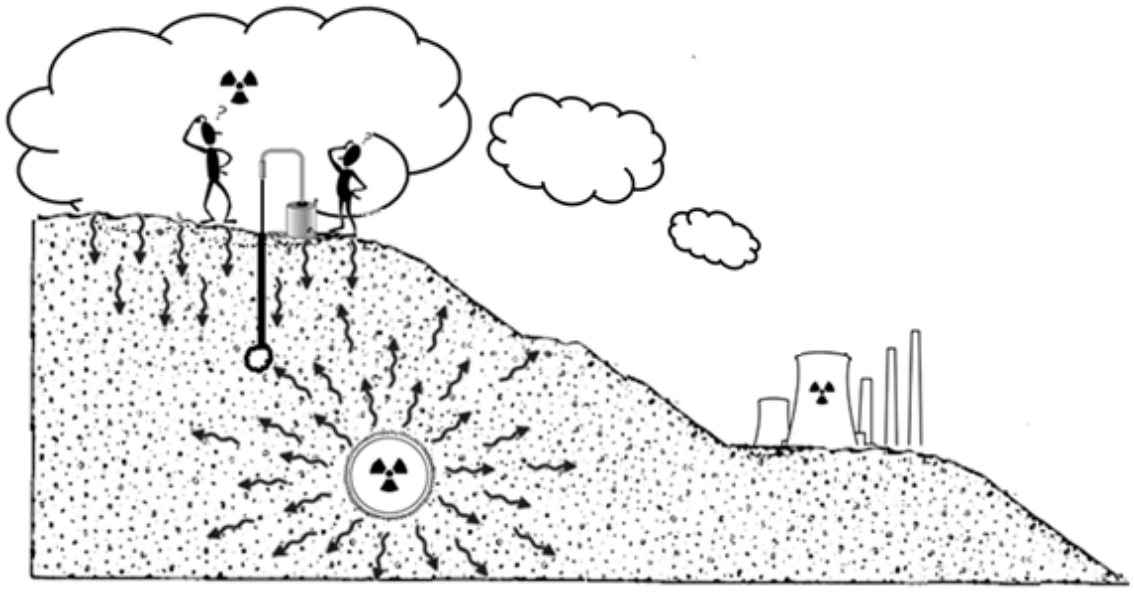

Figure 7.2 Cartoon illustration of the atmospheric infiltration concept where radionuclide-containing air from the atmosphere can be distributed underground, potentially interfering with soil-gas sampling for evidence of a subsurface radionuclide source.

7.3 ATMOSPHERIC INFILTRATION

Susceptibility of an OSI soil-gas sampling effort to infiltration of atmospheric air, and any trace radionuclide concentrations that it might contain, is a matter of critical uncertainty within the current inspection operations strategy. In essence, the problem of atmosphere invasion into the subsurface environment is the reverse of gas being drawn out of the ground through a fractured system. Just as periods of decreasing atmospheric pressure would tend promote gas withdrawal from the ground, an increasing pressure would tend to push atmospheric air into the ground along vertically-trending fractures. This air could then mix with soil-gas.

Atmospheric infiltration is of potential concern in two somewhat distinct ways. The first is in a scenario along the lines described above - the potential mixing of atmospheric gas with soil-gas could in certain circumstances cast a reasonable uncertainty on the exact source of the signature found in a soil-gas sample. For instance, take as a hypothetical situation a case of a suspected UNE in a location that is also not too distant from a commercial nuclear power reactor or medical isotope production facility (see Figure 7.2). If a radionuclide-containing plume is released and carried in the atmosphere over the area of the suspected UNE, what potential fraction of the plume radionuclide concentration can be distributed in the ground due to barometric fluctuations? A second atmospheric infiltration concern in an on-site inspection sampling effort is with regard to the actual in-hole effects of pumping on the underground volume, and will be considered more in Section 7.4 in borehole-specific modeling.

As a first step towards an examination of the possible effects of atmospheric infiltration into the ground, a case study was made of a radioxenon-containing plume above an initially uncontaminated vertical-fracture system, and the resulting subsurface infiltration was simulated for seven days. An estimate of the plume concentrations (Table 7.1) were obtained from data presented in Klingberg *et al.,* (2012) for a an estimated radioxenon release from the Oak Ridge National Laboratory (ORNL) high flux isotope reactor (HFIR) and subsequent atmospheric dilution calculated through NOAA HYSPLIT[19] modeling (see Figure 7.3).

[19] National Oceanic and Atmospheric Administration (NOAA); HYbrid Single-Particle Lagrangian Integrated Trajectory (HYSPLIT), (Draxler & Rolph, 2003).

Table 7.1 Average and maximum radioxenon concentrations in the NOAA Hysplit atmospheric dilution model for ORNL plume release, from Klingberg *et al.* (2012). "Average" values were used in the atmospheric infiltration case study.

	Concentration (Bq/m^3)	
Isotope	Average	Maximum
^{131m}Xe	1.21E-3	3.43E-3
^{133}Xe	8.87E-4	6.21E-3
^{133m}Xe	1.30E-4	3.65E-4
^{135}Xe	2.86E-4	6.82E-4

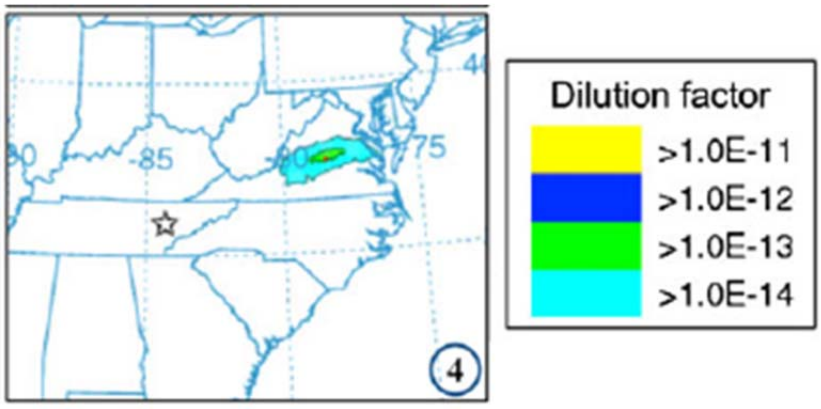

Figure 7.3 Simulated atmospheric dilution of ORNL high flux isotope reactor release, 1-hr integrated following 1 day of transport.

The average plume concentrations from Table 7.1 were utilized as input into UTEX model simulations for the top boundary of the vertical fracture-system. This atmospheric concentration of xenon was held constant for a simulation period covering 7 days of transport, thus this illustrates somewhat of a worst-case scenario in that such plumes are hardly constant in time. Nevertheless, by holding source concentration constant in time, the effects of the barometric driver on the transport are more easily

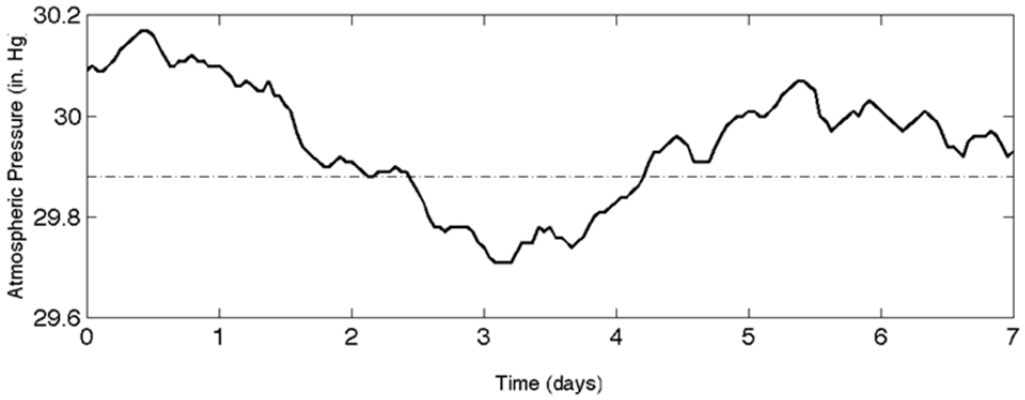

Figure 7.4 Seven day atmospheric pressure history assumed for atmospheric infiltration simulation studies. Note that a decreasing pressure would tend to inhibit infiltration and an increasing pressure (beginning at roughly 3 days) would promote it.

illustrated. The atmospheric pressure used in the simulations is shown in Figure 7.4. Note that the initial decreasing pressure depicted in Figure 7.4 would tend to inhibit infiltration while the increasing pressure beginning at roughly 3 days would promote it. The porosity of the approximated alluvium bulk geology was taken to be 0.2 with a permeability of 10^{-11} to a vertical fracture depth of 250 m. This chosen fracture length is very long, but allows for an examination of the maximum direct vertical infiltration for this pressure scenario. An average fracture width and separation of 1 mm and 5 m were used respectively.

Resulting ^{133}Xe concentrations for infiltration at 1-7 days simulation time are plotted in Figure 7.5 and Figure 7.6 for illustration of the contaminant invasion scenario. Looking also at the pressure history in Figure 7.4, the concentrations appearing in these plots can be regarded as follows:

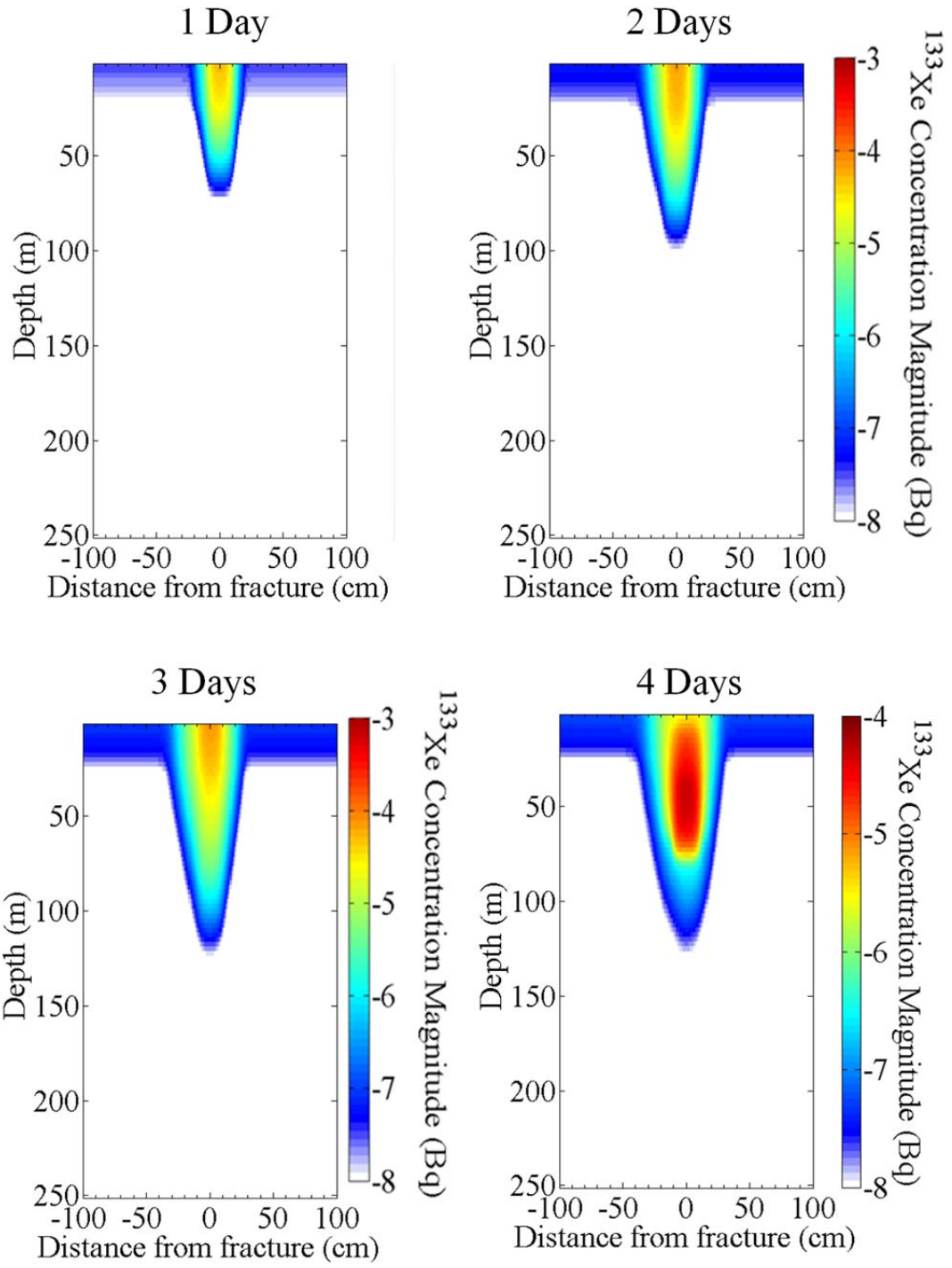

Figure 7.5 UTEX simulated vertical fracture infiltration of ^{133}Xe from a constant 8.87E-4 Bq/m^3 atmospheric source, 1-4 days.

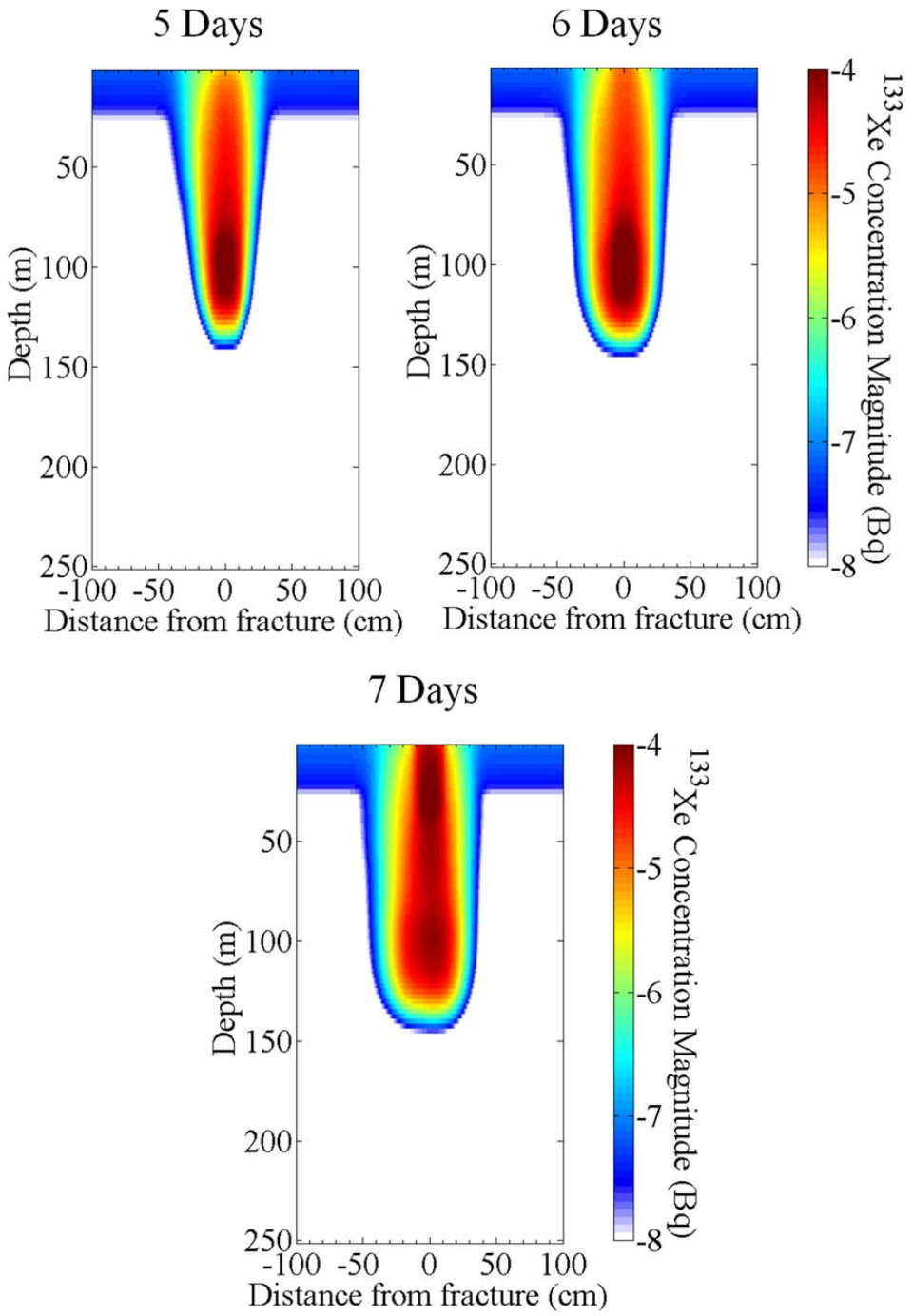

Figure 7.6 UTEX simulated vertical fracture infiltration of ^{133}Xe from a constant 8.87E-4 Bq/m^3 atmospheric source, 5-7 days.

Days 1-3 - The atmospheric pressure during this time is predominantly falling. A small (roughly 0.5%) upward fluctuation in pressure during the first day is responsible for a large part of the initial push of contaminated air down the fracture that is seen in plots of the first 3 days. A small concentration begins to diffuse laterally.

Days 4-5 -. During the fourth day, the atmospheric pressure begins to swing in the other direction and is steadily increasing into the fifth day. This is evident in the Day 4 plot as the first real substantial ^{133}Xe invasion. In the Day 5 plot, the xenon contaminant continues to penetrate down the fracture; the lateral diffusion away from the fracture into the bulk medium is more evident. Also evident, because of the speed of the pressure-induced flow down the fracture, the concentration is higher deeper in the system.

Day 6 - The down-fracture air invasion has already reached its maximum as the atmospheric pressure has peaked and is fluctuating in a slightly downward trend. Lateral diffusion at deeper depths has widened the concentration profile substantially compared to Day 5.

Day 7 - As the pressure is no longer rising sharply and experiences small fluctuations, the concentration down the fracture has equalized somewhat. In fact, a concentration *bubble* near the top can be seen as it rises towards the surface due to the downward trend of the pressure. The lateral diffusion of ^{133}Xe away from the fracture has not increased substantially, especially in the upper parts of the concentration profile; an equilibrium between radioactive decay rate and diffusion is likely near.

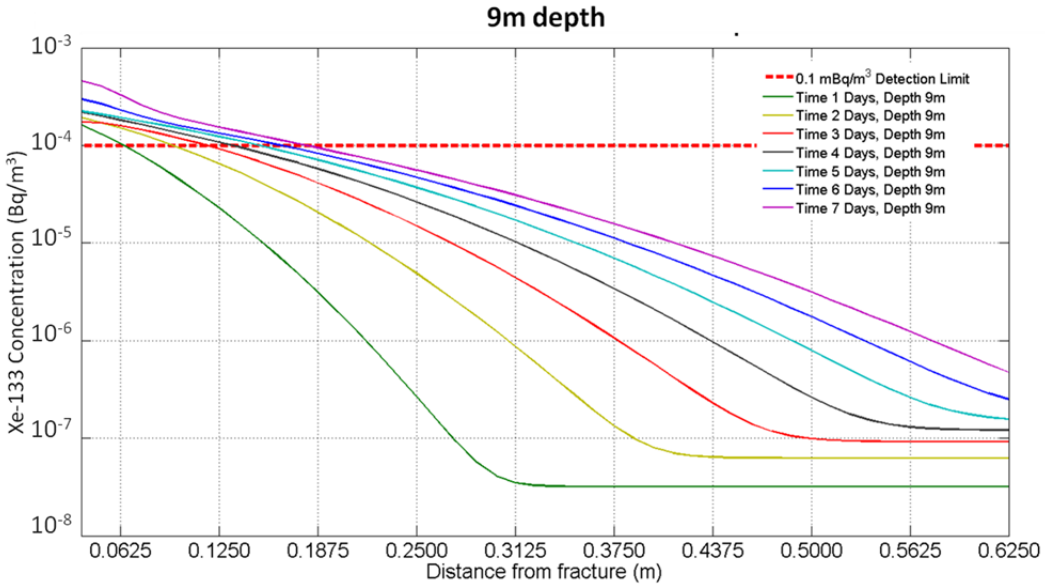

Figure 7.7 ^{133}Xe concentration curves for each of days 1-7 as a function of distance from fracture at a depth of 9 m due to simulated infiltration. The dashed line represents an approximate detection limit.

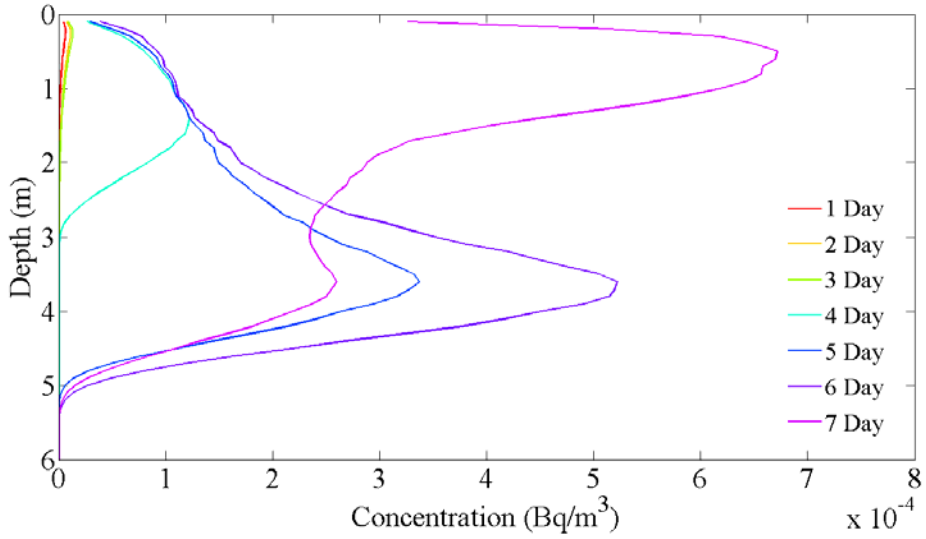

Figure 7.8 The averaged concentration depth profile for the seven days of the ^{133}Xe infiltration simulation obtained by averaging over fracture angles between ±85°.

Figure 7.7 shows the various concentration curves of ^{133}Xe as a function of distance from the fracture at a vertical depth of 9 m for each of the seven days plotted in Figure 7.5 and Figure 7.6. Plots for additional depths are included in Appendix G for further illustration. Many of the same infiltration characteristics are discernible as before. The adjacent fracture concentration does not change significantly in days 1-3, and then shows a marked increase in the following days. At this shallow depth, the rise in the curve further from the fracture slows in time even as the fracture concentration is increasing, which is an indication that further transport deeper into the bulk medium is inhibited by radioactive decay. The flattening of the concentration curves at large distances from the fracture is due to direct vertical diffusion of ^{133}Xe through the bulk medium. This diffusion is of course substantially smaller at greater depths, as seen in the additional plots in Appendix G. Noting that fractures in the ground are unlikely to be strictly vertical, but instead to have a random vertically-trending orientation, Figure 7.8 shows the averaged concentration depth profile of the first 5 m for the seven days of the infiltration simulation obtained by averaging over fracture angles between ±85°.

The plume concentrations adopted in Table 7.1 for this case study are a fair representation of a scenario likely to be of concern for infiltration. The estimated radioxenon concentrations of the plume are just above minimum detectable values, and it is in this regime where potential for an infiltration problem is likely to be difficult to judge. To take the preceding analysis one step further towards evaluating the degree of infiltration that can take place down a vertical fracture, simulations were run using a bulk geologic porosity ranging $\phi = 0.1$ to 0.5. At 9 m depth, the ^{133}Xe above-MDC concentration distance of invasion is shown in Figure 7.9 for different values of the porosity.

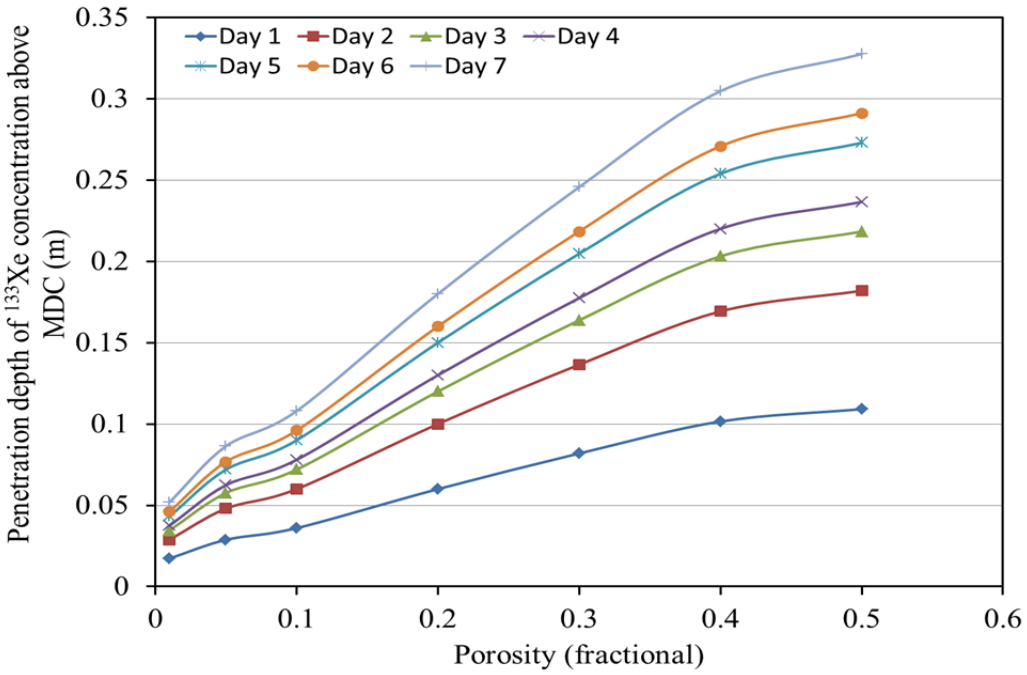

Figure 7.9 Depth of ^{133}Xe bulk matrix penetration at concentration above MDC for Days 1-7 for varying values of the porosity of the medium. Like in Figure 7.7, these values correspond to a depth of 9 m.

7.4 ON-SITE INSPECTION MODELING

While the entirety of the present work on subsurface noble gas source and transport modeling is ultimately in support of on-site inspection science, no real attention has been paid thus far to the actual effect that soil-gas sampling can have on the system it is intended to study. Of very important concern is the degree to which actively drawing air from the subsurface can influence the radionuclide concentrations and isotopics that might (or might not) actually exist there as evidence of a suspected UNE. This section builds on the preceding investigation of generalized atmospheric infiltration towards a more pointed examination of the effects of on-site inspection procedures.

7.4.1 Borehole and pumping

As illustrated in Figure 7.1 and outlined in Section 7.1, soil-gas sampling in an on-site inspection scenario entails the boring of a hole several meters into the ground, emplacing a sample hose into the hole, and pumping on the hole to collect subsurface air. Due to the high-volume requirements for ^{133}Xe (SAUNA) and ^{37}Ar (MARDS) analysis, a typical flow rate induced by soil-gas sampling is of the order 1 L/minute for a sample time of between 12-24 hours (Carrigan & Sun, 2012). This is achieved through a substantial pressure drop in the subsurface environment, which induces a localized gas flow towards the sampling point. Like the atmospheric pressure response effect on generalized underground transport, the scope of the soil-gas sampling effect on the environment is a function of the openness of the geology.

As illustrated in Figure 7.10, one of the most obvious dangers of introducing a sizable pressure sink at shallow depths is the very real potential to induce a flow primarily from the surface, which could greatly undermine a soil-gas sampling effort, intended to collect subsurface gas. Figure 7.11 illustrates the different scales of depth at work in the on-site inspection scenario. The likely soil-gas sampling point (and location of the pressure sink) is only 2-10 m deep in the top part of the geology. The location of a potential UNE could be hundreds of meters deep. Even accounting for the possibility of an extended rubble chimney and gas halo above the initial cavity, the sampling point is much closer to the surface and atmosphere compared to the likely subsurface radionuclide source.

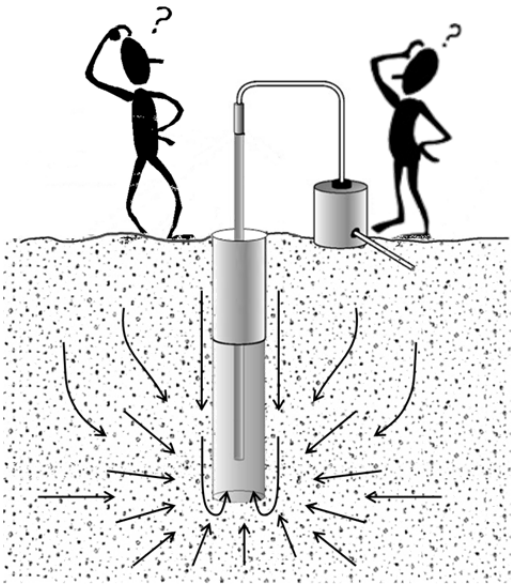

Figure 7.10 Cartoon illustration of the potential for the pressure drop at the point of soil-gas sampling to induce direct air flow from the surface, potentially enhancing the problem of atmospheric infiltration.

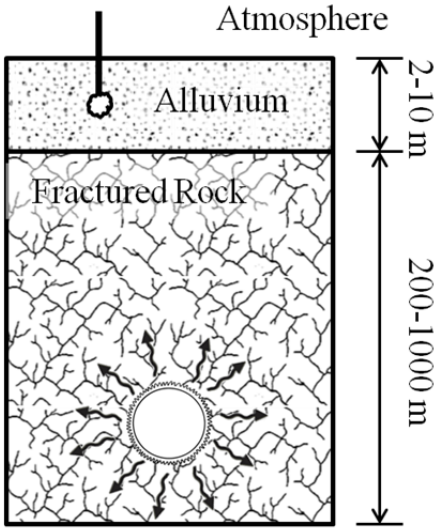

Figure 7.11 Conceptual picture (not to scale) of a likely OSI scenario searching for evidence of a UNE. The soil-gas sampling point is located at shallow depths, perhaps within the first few meters of a thin alluvium layer. The source can be many hundreds of meters deeper than the sampling point. If the alluvium layer pictured here is roughly 1/2" thick on the page, then a scaled fractured rock below it could be of the order 5 pages thick.

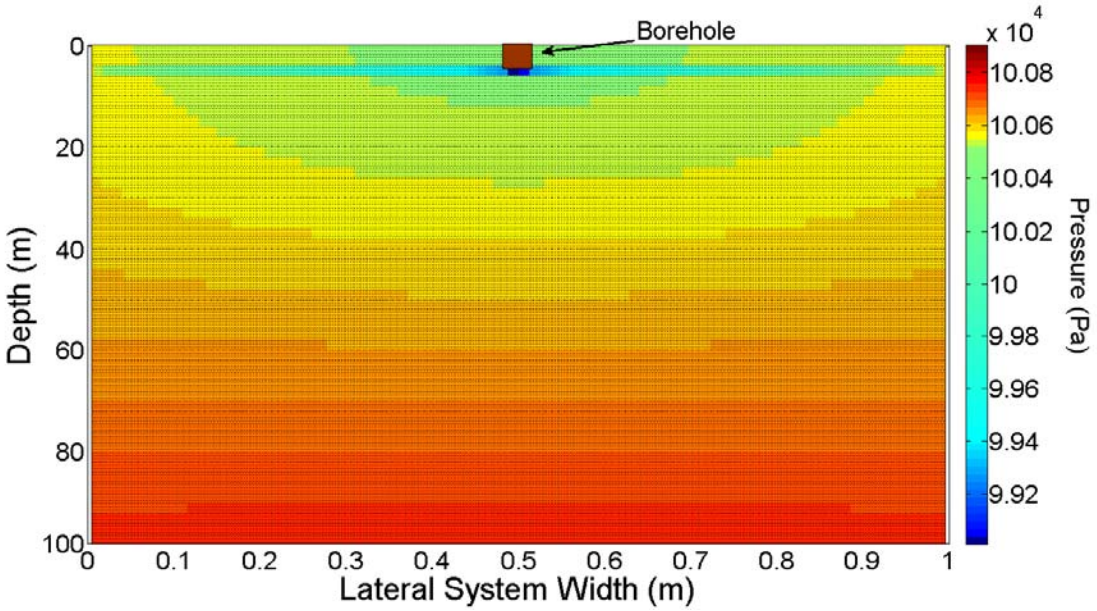

Figure 7.12 Example snapshot of the modeled system pressure state in UTEX simulations where a 100 mbar pressure sink is located at the midpoint between 1 m spaced vertically fractures to represent one instance of soil-gas sampling.

To consider the effect of continuously pumping on the shallow subsurface environment, simulations were run using a pressure sink within the geology, ranging from 10 to 100 mbar in magnitude over a period of 7 days. The assumed geology consisted of a 0.2 porosity medium with 1 mm width fractures and spaced an average of 1 m apart. The real difficulty with modeling this scenario in UTEX is in adapting the simplified double porosity vertical transport code to a generalized physical representation of soil-gas sampling. Consider the situation in Figure 7.12, which shows a snapshot of a UTEX simulation of the pressure response to both atmospheric infiltration and a pressure sink located at the midpoint of two fractures; note the vastly different axis scales. Fractures are located at $x = 0$ and 1 m, down which the changes in the atmospheric pressure propagate. For this given choice of average fracture separation, the position of the sampling point could not be farther from the nearest vertical fracture; the drop in

pressure at this point is felt locally and propagated only a short distance in the bulk medium due to lack of proximity to fractures.

In reality, the sampling point's proximity to the nearest fracture is random, as are the exact number of nearby fractures and their orientation with respect to the vertical and even whether are not they are connected to the surface at all. This challenge is inherent in applying the microscopic modeling perspective within UTEX to a macroscopic, physical situation, and dealing with it represents one of the largest goals for potential future work on UTEX modeling. As a first step forward in that direction, simulations covering a range of fracture locations between points $x = 0$ and 1 m were conducted with the orientation of the fracture varied from near horizontal to vertical. These results were compiled and averaged over possible angle and fracture distribution to obtain a general idea of the potential macroscopic effect of infiltration in a pumping scenario. See Figures G.3 and G.4 for an illustration of the averaging of fractures applied to atmospheric infiltration alone.

In this way, the scenario depicted in Figure 7.12 can be generalized so that fractures are effectively smeared out over possible positions relative to the sampling point and having arbitrary orientation with respect to the vertical. The results of this "smearing" are shown in Figure 7.13 and Figure 7.14 for estimation of atmospheric infiltration alone and atmospheric plus soil-gas sampling-induced infiltration respectively. The additional infiltration effect of the roughly 100 mbar soil-gas sampling pressure sink in Figure 7.14 is clearly outpacing the atmospheric-induced infiltration of Figure 7.13, at least locally within 2-3 m of the sampling point.

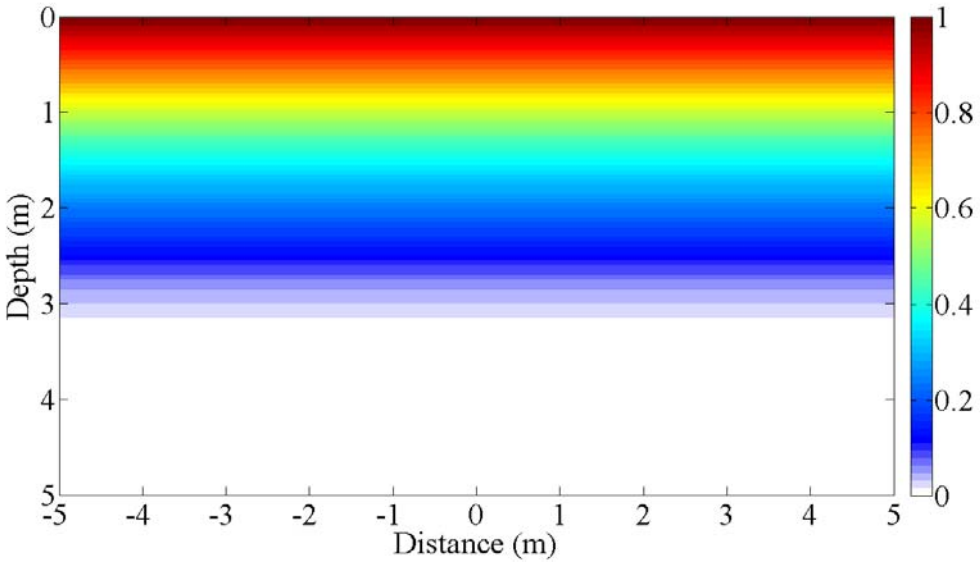

Figure 7.13 Resulting approximation of atmospheric infiltration after 7 days in the top 5 m of the subsurface obtained by smearing fracture position and orientation. The fracture width was 1 mm and average separation was 1 m. Concentrations are normalized to 8.7E-4 Bq/m^3 for generality.

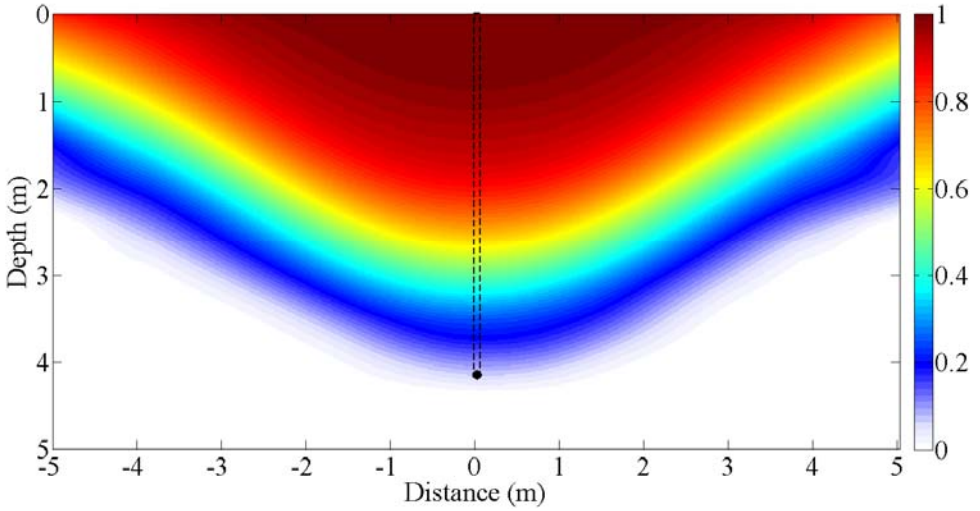

Figure 7.14 Resulting approximation of atmospheric infiltration and 1 L/minute soil gas sampling after 7 days in the top 5 m of the subsurface obtained by smearing fracture position and orientation.

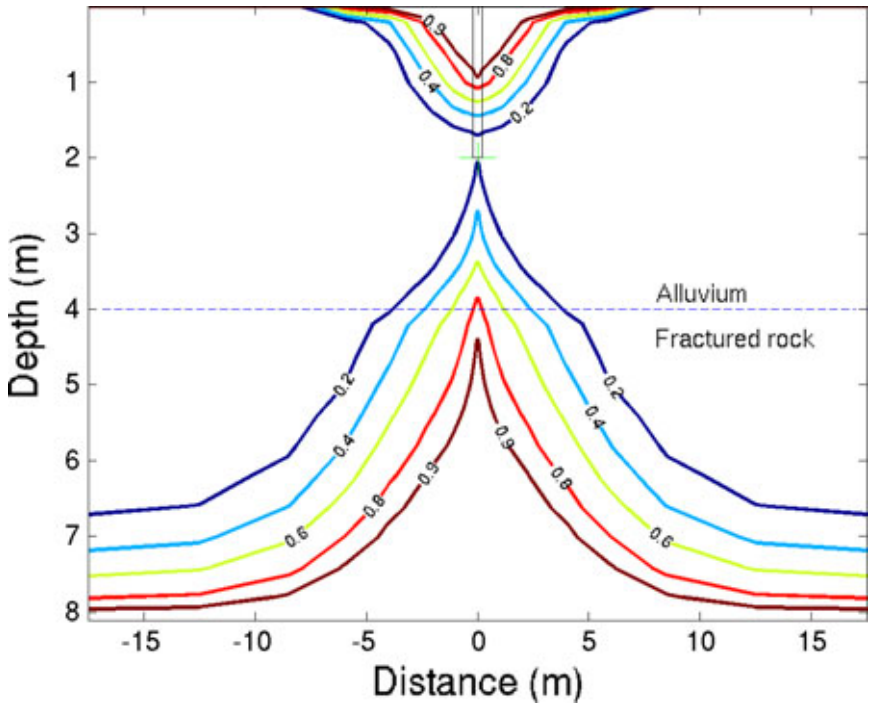

Figure 7.15 Concentration profiles for atmospheric gases drawn downward the sample point and soil gases drawn upward from the fractured rock; from Carrigan & Sun (2012).

Figure 7.15 shows similar results obtained by Carrigan & Sun (2012) for modeling of atmospheric gases drawn downward to the sample point and soil gases drawn upward from the fractured rock. The magnitude of the sampling-induced infiltration effect estimated in Figure 7.14 by the smearing of the surrounding fracture network is in good agreement with the results of Carrigan. Still, use of the "smearing" approximation used in the present work should be regarded as a rough order of magnitude approximation to a true physical scenario. For illustration of the relevant processes the method provides worthy insight while potential future work should focus on refining a better, more accurate, technique.

7.4.2 Atmospheric infiltration and tarping

Atmospheric gas infiltration, due both to natural barometric pumping as well as soil-gas sampling is clearly a realistic concern and has been modeled as such. A widely proposed strategy in the community for combating atmospheric infiltration is to employ the use of a plastic tarp or tent to cover the on-site inspection sampling area, thereby locally isolating the subsurface environment from the atmosphere above it. Intuitively, such an approach should work; the question then turns to the amount of surface area coverage necessary to ensure infiltration is minimized below some control measure.

To study the effects of such a tarp and its ability to inhibit infiltration, UTEX simulations were run similar to those described in Section 7.4.1 but with the addition of a closed surface boundary at the top of the system, corresponding to the area of coverage of a tarp. It should be mentioned that the ability of such a tarp or tent to actually isolate the subsurface from changes in barometric pressure is somewhat of an unknown. In theory, a rigid enclosure should effectively eliminate the direct barometric pressure fluctuations felt in the below subsurface environment, and this is assumed in the simulation results that follow, but the accuracy of this is uncertain.

Figure 7.16 shows the estimated atmospheric invasion driven only by barometric pumping for 7 days of simulation time with a 5 m radius tarp covering the surface directly above the sampling point. The effect of the tarp is clear from a comparison with the analogous no-tarp scenario in Figure 7.13. Atmospheric gas invasion is highest at the edges of the tarp. At deeper depths, lateral diffusion and surface-connected fractures oriented so that their tops are outside the tarped area contribute to the averaged estimate of the invasion towards the sample point. Unsurprisingly, the concentration of invading atmospheric gas is lowest at points directly above the sample point, which are farthest from the uncovered surface.

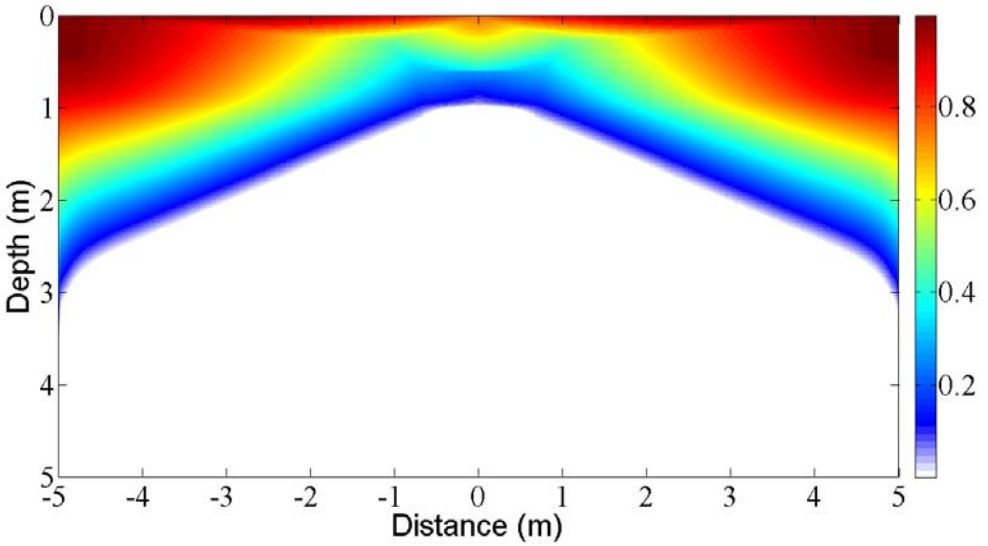

Figure 7.16 Estimated atmospheric invasion due to simulation of 7 days of barometric pumping and no soil-sampling, with 5 m radius tarp coverage at the surface.

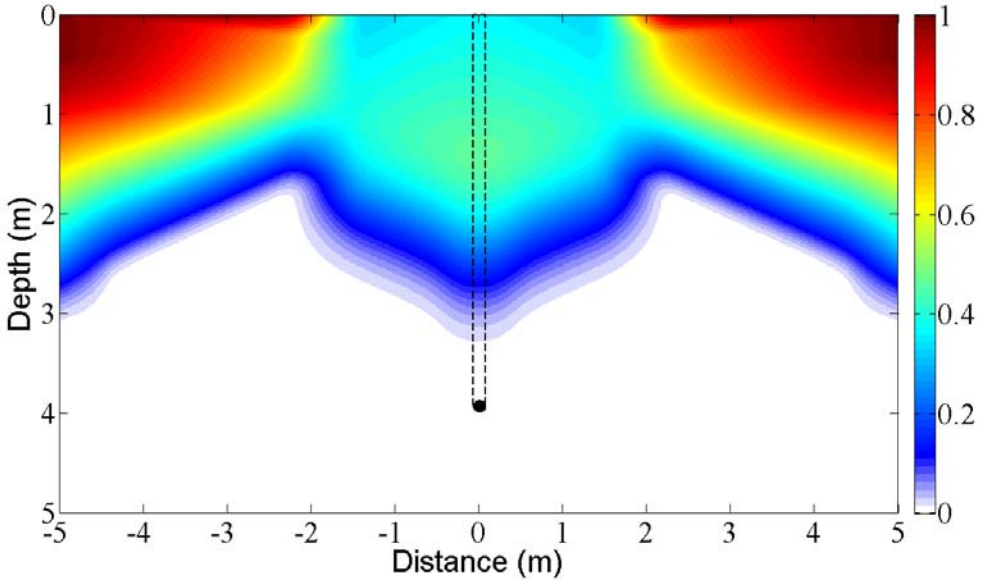

Figure 7.17 Estimated atmospheric invasion due to simulation 7 days of barometric pumping *and* soil-sampling, with 5 m radius tarp coverage at the surface.

Figure 7.17 is analogous to Figure 7.14 with the addition of the 5 m radius tarp inhibiting gas exchange at the surface. Again, the main features exhibited in the plot make intuitive sense - atmospheric pumping infiltration at the edges of the tarp is evident and a comparison with Figure 7.16 shows the net effect of the pressure sink at the sampling point is to further induce flow in this direction. A comparison with the no-tarp invasion scenario in Figure 7.14 makes it clear that the estimated concentration reaching the sampling point is substantially reduced by the addition of the tarp. It should be emphasized at this point that the contaminant transport being simulated here is subject to radioactive decay, and that for a given system pressure response there should exist an equilibrium, of sorts between invasion of gas and its loss through decay.

A somewhat interesting result evident in these simulations that might not be obvious is the effect that the tarped surface can have on slightly promoting pressure gradients in the subsurface. This can be seen in Figure 7.16 where invasion underneath the tarp is higher than would be expected from diffusive mixing of gas alone. Part of this infiltration is a result of a negative pressure gradient that arises in the system by Day 7 of the simulation. Due to the aforementioned assumptions about the tarp inhibiting pressure fluctuations beneath it, the increasing pressure found in Figure 7.4 leading up to Day 7 induces a rise in the system pressure that would be restrained underneath the tarped area. The net effect in this case is that the pressure directly underneath the tarp is lower than the surrounding area.

7.4.3 Radius of influence

That employing a plastic tarp covering above a sampling area simulates a reduction in the potential invasion of atmospheric gas in the sampling region is not surprising. Ideally, anything that *could* be done in field operations to improve confidence

in soil-gas sampling *would* be done. The reality, however, is that on-site inspection teams are limited by both time and resources in the field. Supplies and equipment must be capable of timely transport to potential remote locations with unknown terrain. Upon deployment, an on-site inspection team must work quickly and efficiently to emplace a number of soil-gas sampling stations per day. As a result, any significant alteration to the on-site inspection concept of operations should be evaluated for its feasibility, as well as it should be optimized for generalized implementation. So, if tarping above a sampling area is to be integrated into the OSI standard operations, attention must be paid to evaluation of an optimal area of coverage.

Like many aspects of general subsurface gas transport, a large number of factors are certain to contribute to the capacity for a given soil-gas sampling scenario to induce atmospheric infiltration in the vicinity of the collection point. Simulation results presented in this chapter correspond to just one potential instance of infiltration, and even then, the true nature of the fractured network has been smeared out, essentially neglecting an additional degree of freedom. Still a study was made to evaluate the effects of various geologic parameters on the magnitude of infiltration at a hypothetical subsurface sampling point and is presented here. A recommendation for potential continuing work is also made.

UTEX Estimate

Quantification of the effectiveness of tarping in reducing atmospheric infiltration is not straightforward. A more or less obvious approach is adopted here; a *radius of influence* (ROI) is taken here to correspond to the tarp or tent radius above the sampling point necessary to approximately limit infiltration to less than 1% of atmospheric concentration. Major factors that affect this ROI include, but may not be limited to:

- the flow-rate or assumed induced pressure sink of the sampler

- the depth of the sampling point
- porosity and permeability of the bulk medium
- average fracture separation and orientation
- radioactive decay rate of the isotope in question

Additional factors that surely influence this definition of an ROI but really cannot be quantified in a general sense are the nature of the atmospheric pressure variations as well as the potential for existence of large cracks and fractures that would lead to large scale atmospheric invasion based on a specific path and orientation.

Determination of a handful of estimated ROIs with UTEX was conducted essentially on a trial and error basis; these results are summarized in the plots Figure 7.18 and Figure 7.19. This study was extremely time consuming and computationally expensive, and as such, the span of parameters considered is limited to just large enough to only illustrate some of the initial characteristics of the parameter sensitivity for atmospheric infiltration. In Figure 7.18, simulations covered four values of the porosity of the bulk medium to find that the ROI increases somewhat slowly with increasing porosity. At very low values of the porosity, it would be expected that the tarping necessary to inhibit infiltration would decrease sharply as the porous system space is reduced and flow restricted, and this seems to be the trend in the results.

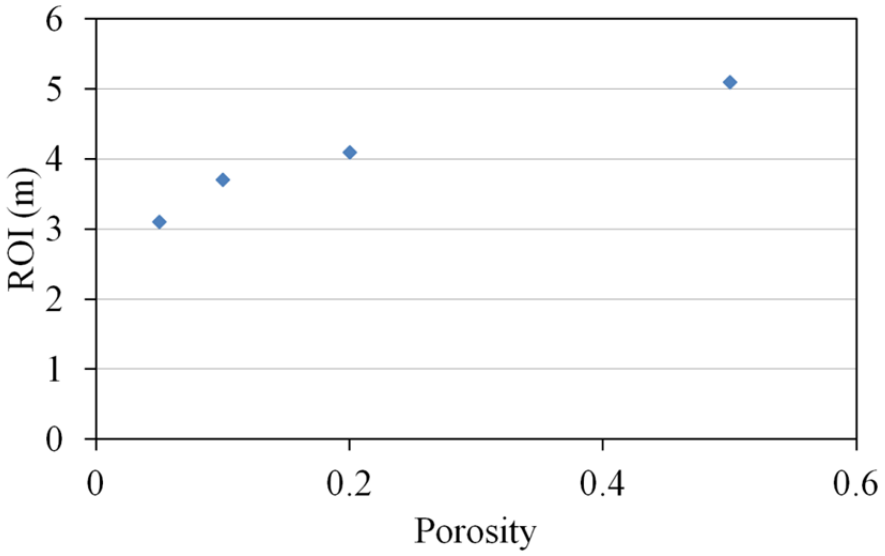

Figure 7.18 Estimated tarp radius needed to reduce atmospheric infiltration to <1% (ROI) as a function of the porosity of the bulk medium in which the sample point is located. Depth and average fracture separation were 4 m and 1 m respectively.

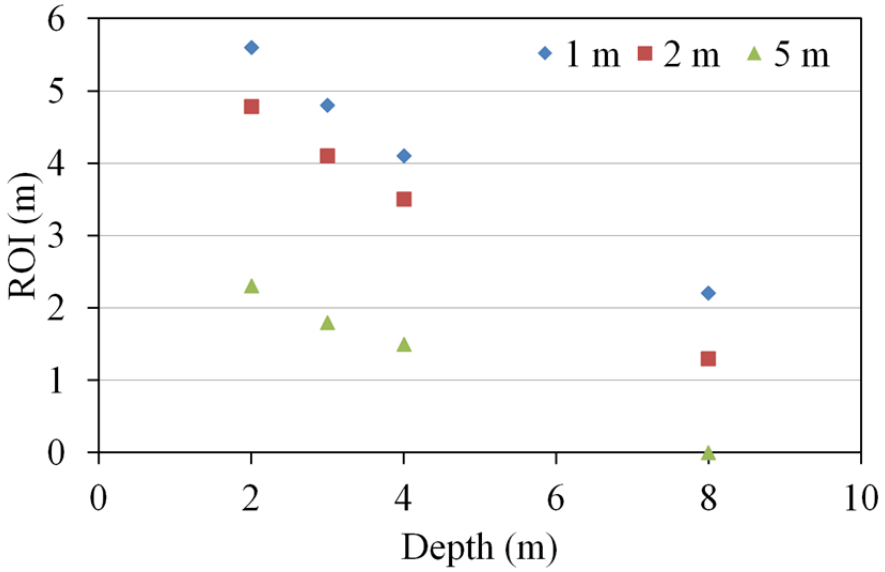

Figure 7.19 Estimated tarp radius needed to reduce atmospheric infiltration to <1% (ROI) as a function of the depth in which the sample point is located for different values of the average fracture spacing. Porosity of the bulk medium was 0.2.

In Figure 7.19, ROIs were estimated as a function of depth for different values of the average fracture separation. Fracture separation is inversely proportional to frequency of fractures - a larger average separation implies a less fractured system, which in turn inhibits the overall rate of transport throughout the system. Thus the correlation of ROI with average fracture separation in the results of Figure 7.19 is not surprising; larger separation necessitates a smaller surface coverage to inhibit infiltration. The dependence of the ROI on depth is also generally shown to follow intuitive expectations - the deeper the sampling point the less likely infiltrating atmospheric gas is to reach the sampling point. At 8 m sampling depth with an average fracture separation of 5 m, simulations estimated that in this scenario atmospheric gas would not reach the sampling point at appreciable concentration even without tarp coverage.

7.5 INFILTRATION INFLUENCE ON ISOTOPICS

The bulk of the effort in quantifying atmospheric infiltration was focused on the single isotope ^{133}Xe. While ^{133}Xe is typically regarded as the most relevant radioxenon isotope of potential for downwind plume contamination, the details of possible various plume isotopic ratios of radioxenon should also be considered. In the example case utilized in this work, four xenon isotopes were assumed to be present in the plume (Table 7.1). To consider the possible isotopic effects of transport from barometric pumping and sampling-induced infiltration, additional simulations were run with all four isotopes present in the system.

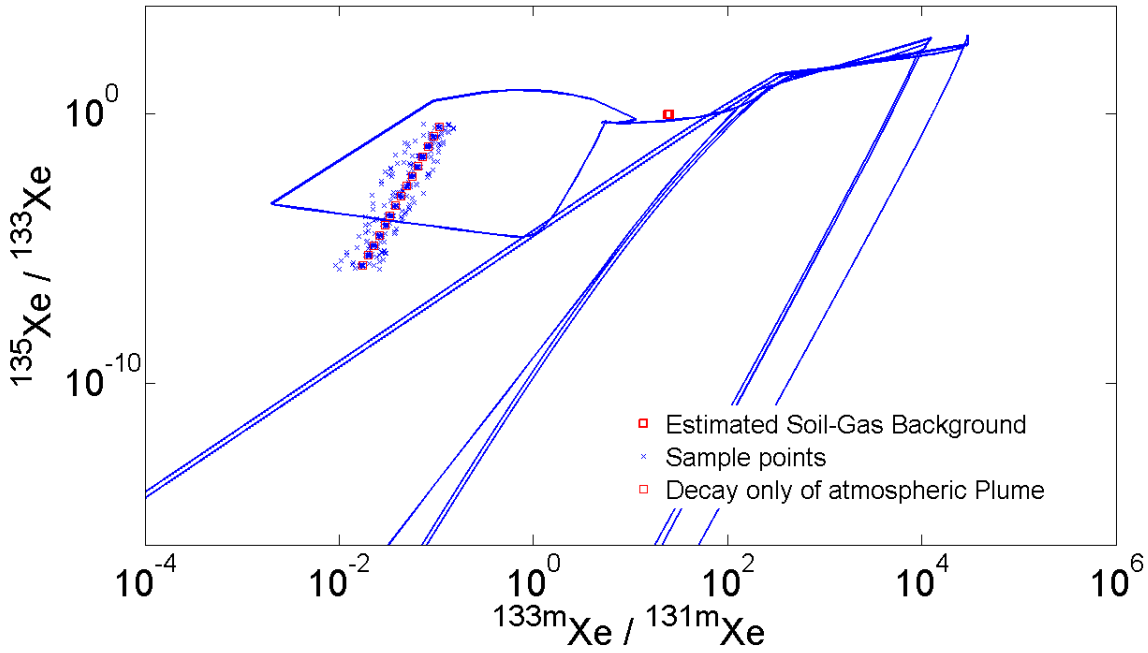

Figure 7.20 Radioxenon isotopic ratios simulated at various points in underground due to infiltration of atmospheric gas emanating from ORNL HFIR. The isotopic signatures deviate little from the decay-only path, suggesting the transport effects on the isotopics are small.

The resulting ratios of radioxenon gas estimated at different locations in the system at various times in the simulation for a small range of values of the porosity and fracture separation are shown in Figure 7.20. The red boxes in the figure represent decay-only evolution of the atmospheric concentration of xenon (the darker red box is the estimate soil-gas background point). By and large, ratios observed in the simulations fell very close to these lines; the majority of deviations from this decay line came at points near the edge of simulated tarp where gas mixing due to quick changes in barometric pressure can have a greater impact. Still, these fluctuations are relatively minor, and overall, the isotopic fluctuations in the near surface due only to transport effects and the sampling-induced pressure sink seem quite small.

This result is, however, only half the story. A major assumption in the preceding simulations was that the atmospheric source of radioxenon was constant in time. Estimated isotopic fluctuations resulting from deeper underground transport of a UNE source were largely the result of mixing of radioxenon source in time. Due to the constant source ratios in time as well as the close proximity of the atmospheric source to the sampling region considered in the infiltration case, this mixing would be much smaller than in the case of an UNE source.

7.6 CONCLUSIONS AND RECOMMENDATIONS

While the predominant focus of this entire work is always concerned with applications to OSI science, the goal of this chapter specifically was to employ the UTEX model in making a cursory examination of the OSI scenario itself, near the sampling point. To this end, the capacity of pressure fluctuations to "imprint" an atmospheric concentration of radioxenon into the sampling region was considered and found to be a realistic possibility. Additionally, the added effect of sampling in the shallow ground was confirmed to enhance the potential infiltration problem. Due to these combined effects, it is not unreasonable to expect that, if left unchecked, invasion of an atmospheric concentration of gas of >10% is possible at depths of up to 5 m or more.

Simulation of infiltration scenarios with the addition of a tarp above the sampling point show that such a practice can indeed be effective at inhibiting direct atmospheric invasion at the sampling point. A radius of influence (ROI) has been used to estimate the area of tarp that would be necessary to limit infiltration to <1% at the sampling point and a short, initial study has been made to estimate this ROI and its dependence on major properties of the geology and depth of sampling. With regard to limitations of this tarp

effectiveness approach, one major point to keep in mind in evaluating infiltration pathways and estimating ROIs is that the modeled ^{133}Xe contaminant is undergoing radioactive decay so that pseudo-equilibrium states arise in the distribution of the gas in the subsurface. ROIs for shorter or longer lived isotopes would therefore be smaller or larger, respectively. Additionally, while the assumed soil-sampling rate can be modeled as constant, the effects of barometric pumping are much more difficult to quantify in a general sense. Simulation results and estimates of ROI dependence on various parameters presented here should be regarded as an approximation of the true physical system in one specific definition of the pressure history. In general, ROIs would be a function of atmospheric pressure as well.

The ROI characterization utilized in this work may not be the best way to quantify the effectiveness of tarping for infiltration reduction. The largest limitation of this approach with UTEX simulations is the inability to incorporate random occurrences that can greatly affect the infiltration scenario, such as barometric fluctuations (discussed above) and specific fracture orientations that together could create "worst case" scenarios for infiltration. Given that knowledge of the underlying fracture system cannot be counted on in an on-site inspection, an evaluation of infiltration possible with and without various size tarping should be made probabilistically. An extension of the UTEX model for potential future work includes incorporating a method of stochastically determining a fracture network within specified average parameters and simulating the resulting transport scenario. In this way, problems such as atmospheric infiltration could be regarded for distinct random scenarios, and probabilities could be associated with the occurrence of certain events such as >1% concentration reaching the sampling point in an OSI.

Chapter 8. Conclusion

The broad objective put forward for this work was to develop and benchmark a complete model for the vertical transport of noble gas from an underground nuclear source to the surface, and then ultimately to apply this model to relevant radionuclide detection scenarios. The predominant focus of such simulations has been concerned with relative transport rates and isotopic ratios. In building the resulting UTEX model from the ground up, establishing a simple fission source term for use at arbitrary times following a hypothetical UNE, verifying and vetting the model, and then examining a number of subsurface gas transport applications, the scope of this work was somewhat ambitious.

8.1 GOALS REVISITED

Quickly revisiting the goal list from the end of Chapter 1, the following summary can be made about work accomplished and demonstrated in this dissertation:

1. Model initial source term – (Chapter 2) Montebruns, in conjunction with MCNP and Origen 2.2, was utilized to create a simple, fast fission model of IAEA significant quantities of HEU and Pu to approximate the source term of a normalized 1 kton, hypothetical underground nuclear explosion. This model included a geologic wrapper around the fissile material to estimate the neutron activation of the surrounding rock environment of a UNE. From this, a simple estimate of the initial radioxenon and ^{37}Ar produced in a generic UNE was established and an estimate of xenon ingrowth from iodine as a function of time four use as an input to the source function of the transport model was facilitated.
2. UTEX transport code development – (Chapter 2 and 3) The Underground Transport of Environmental Xenon (UTEX) model was developed as a Matlab tool for the simulation of simultaneous movement, decay and buildup of various

noble gas isotopes as they might originate from an underground, time-dependent source (similar to a UNE). The model includes general diffusive and advective transport, and is driven by a user-specified atmospheric history, but neglects the effects of adsorption and thermal convective flow.

3. UTEX transport code benchmarking – (Chapter 3) UTEX is a highly modularized, flexible code that facilitates application to generalized sources, geological scenarios, and pressure influences. Much work was done to benchmark the code against analytical solutions for simple case studies to test the veracity of the transport physics being modeled. The code's temporal and spatial meshes were optimized and various numerical solution techniques were explored.
4. General geologic parameter sensitivity – (Chapter 4) UTEX was utilized to consider the ability of geologic transport to affect isotopic ratios in a subsurface nuclear explosion scenario. A large scale sensitivity study was undertaken to look at how varying the major geologic input parameters can result in alterations in the radioxenon signature of outflowing gas. While much of the simulated data was found to fall within the traditionally-assumed non-fractioned and fully-fractioned decay bounds, there were in fact many instances in which radioxenon releases were simulated outside this domain. It is clear from this study that the vertical transport of radioxenon gas from an underground nuclear explosion can significantly affect the isotopic ratios used within the context of the CTBT to determine whether a test has taken place (J. Lowrey *et al.*, 2013).
5. Source term consideration – (Chapter 4) Following the geologic parameter sensitivity study, an evaluation of how fluctuations in radioxenon signatures can arise due to transport was examined. In particular, it was found that ingrowth of radioxenon from iodine potentially marks an additional important bounding case

when considering xenon ratios from a potential UNE. The effects of transport were largely simulated to smear out the un-transported decay signature, potentially adding uncertainty when trying to distinguish a generic UNE source from a peaceful nuclear source.

6. Sampling assumptions – (Chapter 4 and 8) A look was made at evaluating the assumptions behind how the UTEX model estimates radionuclide "release" from or "sampling" within the simulated system. In particular, the effects of assuming a frozen sample (unphysical assumption) quantity versus a dynamic and decaying sample even as it is being collected (real effect) were considered and found not to greatly alter the resulting estimates. When considering the variation of radioxenon signatures as a function of sampling depth and position between fractures, the effect was minor.
7. Cavity and geology characterization – (Chapter 5) Effort was made to consider the effects of various layers of different rock geologies on the simulated UTEX transport. These effects were found to be somewhat subtle and not always intuitive. How various porosities and permeabilities influence noble gas transport by barometric pumping was characterized. Additionally, a simplified UNE cavity environment was considered and the effects of overpressurization of the cavity explored.
8. Soil-gas background estimates – (Chapter 6) Soil-gas background levels of radioxenon and ^{37}Ar were estimated and their sources characterized. Order of magnitude-wise, the resulting calculations are on par with similar results for radioxenon and 37Ar published by Hebel (2010) and Riedmann and Purtschert (2011) respectively. The apparent effects of geologic transport in UTEX were found to be minor in changing the radioactive decay equilibrium concentrations

except in the very shallow depths, which is consistent with other literature on the subject as well.

9. OSI considerations – (Chapter 7) An effort was made to model the actual act of soil-gas sampling in an OSI scenario. It was found that atmospheric infiltration could indeed be a significant problem and that tarping above a sampling site is one means of potentially countering it. The effectiveness of tarping for various shallow geological characteristics was considered in the context of a radius of influence, quantifying the size of the tarp necessary to reduce infiltration at the sampling point below a specified level.

8.2 MAJOR FINDINGS

Transport effects on radioxenon ambiguation

It is clear from the UTEX simulations of the sensitivity studies presented here that geological transport of xenon gas can significantly affect the isotopic ratios that are used to determine whether or not a clandestine nuclear test has taken place. This result is believed to be significant in that it has been previously proposed to use ratios of radioxenon isotopes to discriminate between nuclear explosion and peaceful nuclear activity sources (Kalinowski *et al.*, 2010). As demonstrated here, the evaluation of detected radioxenon by quickly filtering data based on a discrimination line to distinguish peaceful versus weapon nuclear sources can in many cases oversimplify the processes that bring such radionuclides from source to detector. This result is not altogether surprising given that transport processes have long been known to affect the *rate* at which subsurface gas migrates to the surface. Inclusion of radioactive decay and time-dependent

source modeling leads to a potential variability of radioxenon signatures due to mixing of sources from different times.

This work has demonstrated that a third decay bound should be considered when evaluating a potential explosion signature – it has been shown that it might be possible in the course of rapid atmospheric pressure fluctuations to temporarily evacuate local (near-fracture) regions of the subsurface of built-up radioxenon gas, whereupon xenon immediately produced from iodine decay can result in a separate, unique signature. As xenon from surrounding, un-evacuated regions subsequently diffuses in and mixes the signature begins to swing back towards the traditional non-fractioned decay bound. The net effect of this process is the *smearing* and further ambiguation of a generic radioxenon source signature, making it potentially harder to differentiate from nuclear reactor sources based solely on a single discrimination line.

Geologic and cavity sensitivities

Within the dual porosity framework of the UTEX model, the capability to simulate conceptually realistic heterogeneous geologic scenarios was demonstrated. It was found that the introduction of highly impermeable and low porosity zones in the modeled system results in an attenuation of the bulk air flow in those regions, which depending on the situation, can either enhance or inhibit vertical gas migration from a deep UNE source. Generally speaking, movement of radioactive gas from a deep underground source operates on two substantially different timescales. In the short term, higher porosity and more permeable mediums allow for a more rapid and efficient movement of noble gas in response to barometric fluctuations at the surface (as well as cavity overpressures and thermal convective processes). However, with regard to gas invading the upper levels of the bulk matrix medium, this more open geology is less

effective at trapping gas in those higher regions. The result of this difference is that on longer time scales, effects of barometric pumping are subdued in the more open geologies, as the UNE gas front is not as effectively built up towards the surface.

It has been demonstrated that potential UNE gas seepage is apparently significantly more susceptible to variability in the geology closer to the source than farther away. This is not entirely unintuitive, as gas being considered for transport in this context is radioactive so that its eventual transport to the surface is an inherent race against time. The faster the UNE noble gas can escape the lower regions of the geological system, the much higher probability that it can leak from the system on subsequent swings in the atmospheric pressure. This is likely especially true of the geologic conditions in the immediate vicinity of UNE cavity. How the cavity fills in and how the surrounding environment fractures and gets compacted following the initial event will have a large influence on how quickly noble gas can move upwards in the system. This is in addition to the sensitivity of outflows to the actual distribution of radioxenon, iodine, and radioargon gas in the early halo zone. These effects of the variability in the geology were found to be somewhat less pronounced in the long term process of barometric pumping than in the early time venting.

A cursory examination of the effects of a highly overpressurized post-UNE cavity state was also made. UTEX simulations of these cases indicated that the overpressurization does indeed lead to a substantial increase in the movement of UNE gas to the to the shallow depths in the short term time frame, but within a week's simulation time these induced outflows largely subsided. At later times, however, it was found that an initially overpressurized cavity might result in a lag in concentration buildup in the higher regions with the cumulative effects of barometric pumping. This is likely due to the earlier outflow of gas from the lower regions, which results in slightly

smaller inventory later. These effects, however, only appeared temporarily in the simulations and largely speaking the effects of overpressurizing the UNE cavity were minimal on the long term migration of radioxenon due to barometric pumping.

Lastly, regarding the isotopics of the resulting radioxenon outflows, the overpressurized cavity case was found to exhibit a substantial fluctuation at the very early times, corresponding to a removal of gas directly from the cavity environment that was void of iodine ingrowth. This fluctuation was short-lived, and beyond the first couple of days the xenon isotopics did not seem to be affected by the initial pressure in the cavity. Broadly speaking, it was found that regions within the geology that inhibit rapid movement of gas in response to atmospheric pressure fluctuations are also more likely to induce isotopic fluctuations through the trapping of upward-moving noble gas. By homogenizing the geology and essentially opening the system up to greater freedom of movement, the radioxenon ratios are less disturbed by movement through the geology.

On-site inspection concerns

A study was made to simulate the barometric effects of performing soil-gas sampling in the shallow subsurface as would occur as part of an OSI procedure. The capacity of surface pressure fluctuations (even without soil-gas sampling) to "imprint" an atmospheric concentration of radioxenon into the potential sampling region was considered and found to be a realistic possibility. The added effect of sampling in the shallow ground was confirmed to enhance the potential infiltration problem. Due to these combined effects, it is not unreasonable to expect that, if left unchecked, invasion of an atmospheric concentration of gas of >10% is possible at depths of up to 5 m or more.

Simulation of infiltration scenarios with the addition of a tarp above the sampling point show that such a practice can indeed be effective at inhibiting direct atmospheric

invasion at the sampling point. A radius of influence (ROI) was defined to estimate the area of tarp that would be necessary to limit infiltration to <1% (somewhat arbitrarily chosen) at the sampling point. A quick study was made to estimate this ROI and its dependence on major properties of the geology and depth of sampling. Similar to estimates by Carrigan *et al.*, (2012), it was found that utilization of a tarp of radius between 2-6 m would be required to prevent significant infiltration given a variety of different conditions.

8.3 APPLICABILITY OF UTEX MODELING

8.3.1 What UTEX does

The UTEX model as was set out in the early stages of this research is designed to:

- Simulate subsurface transport of environmentally unreactive gases
- Handle generalized time-dependent source terms of variable spatial distribution
- Simulate bulk advective flow driven by a fully user-specifiable pressure response
- Handle a system geometric model definable in terms of the handful of a handful of physical parameters as described in Chapters 2 and 3
- Account for radioactive decaying isotopes as well as generalized decay chains that include metastables
- Output simulated isotopic concentrations at every spatial mesh point for each time step in the simulation

8.3.2 Limitations and Assumptions of UTEX

Though a number of the underlying assumptions built into the UTEX model have been mentioned already or at least implied, it is important to state them explicitly to clearly define for what applications UTEX can be utilized – these are listed in Table 8.1.

The first five of these assumptions are basic to the double-porosity theory as a whole as laid out in Chapter 2 (Tang, *et al.*, 1981). Of these five, only the last one really restricts the transport modeling capabilities of UTEX. The last four assumptions listed in Table 8.1 are specific to the UTEX design and are not really restrictions to the model concept, but rather just represent current limitations that could be improved upon in the future.

Table 8.1 List of assumptions built into the UTEX model

Double-Porosity Assumptions	1. Fracture width is assumed to be much less than the length of the fracture, $\delta_f << L$. 2. Complete mixing across fracture width is assumed. 3. The matrix permeability largely inhibits bulk air flow , $k_m << 1$. 4. Vertical transport along fractures is assumed to be much faster than in the bulk matrix. 5. Isothermal transport is assumed; heat transfer could also apply, but this was beyond the scope of this work.
Modeling Assumptions	6. The modeled system is assumed to have a closed bottom boundary at some depth *L* corresponding to a water table or otherwise impenetrable medium. 7. Adsorption effects are not considered in the model; geologic water saturation is assumed to be small and its potential effects are assumed to be incorporated into specification of porosity and permeability values. 8. The model assumes the transport only of non-reactive gases; in the case of xenon, parent nuclides are assumed to remain stationary where initially emplaced.

8.4 RECOMMENDATIONS AND OUTLOOK FOR FUTURE WORK

In many respects, much of the work conducted in the course of this Ph.D. has been aimed at establishing a capability to model different aspects of noble gas transport and demonstrating the capacity through simple applications. These case studies have yielded insightful results, many of which are summarized in the preceding section on major findings. With that said prospects for future work fall roughly into three categories. First, there exist a number of possibilities for extending the UTEX model in terms of the model itself, its capabilities and its distributability. Second, the UTEX code could be used to conduct many of the studies presented here in more specific depth, as well as to undertake additional studies of topics not really considered in this work. Lastly, there is always a need for experimental verification of the physics being modeled numerically.

8.4.1 UTEX design extension

Code design

This first direction covers a very broad body of prospective work on the UTEX model that concerns addressing some of the limitations of the current model and expanding on its capabilities. However, before other significant modifications and extensions to the UTEX model are made, the current code should be further evaluated for efficiency and large scale deployment on parallel computing clusters, as it already pushes the limitations of desktop computing resources. These current limitations are:

- UTEX is written in MATLAB
- RAM requirements are determined by the size of the 2D system being modeled as well as the number of isotopes being tracked
- Single CPU core speed is the largest limiter of execution speed
- Current code largely does not utilize parallel computing capabilities

The greatest limitation of using MATLAB for the continued growth of UTEX is in its distributability; the software is not open source and quite expensive. UTEX future development will likely see an increase in the need for distributed computing power, which is something that may just not be feasible if a separate MATLAB license is required per node on a large computing cluster.

Options for tackling this potential shortfall in future work:

1. Stick with MATLAB environment – If the code is to remain in MATLAB, work should be done to optimize UTEX for multi-threaded processing on a single machine. This will require a great deal of additional modularization of the code as well as parallelizing the major numerical routines for utilization of the MATLAB parallel computing toolbox. This is probably the most straightforward option considered here. Revamping the code for increased modularity, multithreading and memory efficiency is probably significantly less time consuming and cheaper than building the code in a new environment. Another advantage of keeping the code in MATLAB is that any machine running the software can run the model. This is in addition to the user-friendly GUI and data analysis tools that come with it.
2. Utilize the Matlab code framework for use with Octave – Octave is another high-level programming language that was developed for use in numerical computing with Matlab compatibility in mind. For all intents and purposes, it can be regarded is an open-source "clone" of Matlab that, while somewhat different, could be used for large scale distributed computing without the licensing hassle. In this case, many of the pros of staying in a Matlab environment still apply; additionally, the capacity to deploy the model on a large scale for batch simulations can be achieved through the open-source alternative, Octave. Still, Octave differs from

Matlab in a few ways, which would likely require separate optimization of UTEX for use in Matlab as well as Octave. While minor inconvenience, there will exist a duplicity of certain development efforts going forward. Also, Octave is not as optimized for multithreading capability as Matlab, so it will likely remain slower per simulation than Matlab.

3. Port the UTEX code into a Fortran, C or similar language – Such a rewrite would facilitate a much broader, platform-independent distributability of the UTEX code. Pre-built numerical routines and libraries with years of development and optimization behind them could be incorporated to enhance execution speed. Large scale distribution would be straightforward. However, a complete rebuilding of the current UTEX model in one of these computer languages would be a very large undertaking, and additionally require subsequent re-vetting, re-verification, and re-optimization just to get the functionality of the new code to the point that it is at currently in Matlab. Also, whereas porting the software over to Fortran or C could increase speed and efficiency, this would be the expense of some amount of code transparency and user friendliness.

3D Modeling capability

UTEX currently simulates a 2D geological system using a rectangular mesh in an underlying double porosity framework. Transport of gas in the modeled system is broken into two degrees of freedom: vertical movement occurs only in fractures; horizontal movement takes place between the vertically running fractures; the two degrees of freedom are coupled at a fracture-matrix interface. While this simplified 2D system provides a good first approximation to true underground gas transport in a real geology, it remains a first approximation and limits the modeling capabilities to some extent

Incorporating an extended 3D geometry would facilitate modeling of even more realistic geologic systems in which previous underground detonations have been conducted and for which there potentially exists experimental data for radionuclide leakage. The current 2D geology modeled in UTEX should be regarded as an idealized, average representation of a larger system that is useful for establishing extremes in the mechanics of gas transport. A 3D model would allow for a better estimation of actual nuclide release concentrations, a more accurate representation of transport taking place in large pre-existing cracks that are not necessarily straight and vertical, and the ability to model specific event scenarios to produce data for comparison to actual field data. Simply restructuring the UTEX code to include an additional dimension on top of the 2D, simple double porosity system already modeled is neither very difficult to implement nor does it provide a whole lot more useful modeling capability. More useful would be enhancement of UTEX to a fully 3D model in which a geology is composed of non-regularly spaced and sized cracks within a heterogeneous geology and gas transports in all three degrees of freedom.

8.4.2 Case studies

Transport mechanisms

UTEX currently considers the transport of subsurface gas that is affected by the following mechanisms: diffusion, advection, and radioactive decay. Additional reaction mechanisms exist that can affect the rate of transport of subsurface gas, most notably adsorption, desorption and the effects of large thermal gradients (see below). Also, the current model altogether neglects the effect of soil moisture content. Even in dry, arid areas, moisture exists in the ground several meters below the surface and deeper. Additional considerations for natural ground water flow should be made, for the effect on

subsurface gas transport could be substantial. Adding modeling capability for all of these mechanisms would be well within the scope of future UTEX work.

Early post-UNE time studies

Largely due to the nature of the very simple system being modeled, UTEX currently is somewhat unsuited for modeling subsurface gas transport as would result from conditions just following a UNE. Effort was made in Chapter 5 to simulate some of the effects of the cavity and fractured bedrock on transport, as well as the influence of an overpressurized cavity. From these results as well as similar work done by Carrigan *et al.* (2012), it is clear that effects of high pressure and thermal gradients near a cavity are potentially important to gas transport in the first few hours to days following a UNE. Additional effects of a cavity collapse, highly fractured chimney, rapid vertical transport or venting through large fractures and potential mechanical containment measures could be examined in greater sensitivity studies than that presented in Chapter 5. Effects of thermal gradients, especially at early times due to the explosive heating of the detonation cavity as well as daily surface heating, would make interesting additions to the UTEX model, but this would add another driving force to the system in addition to the barometric pumping, and is thus beyond the present scope.

These suggestions would also be served better if UTEX is extended to include 3D environment modeling capabilities. Such early post-detonation effects have been shown in this work to be less likely to have immediate effects on radionuclide ratios, but can have a large effect on the distribution of radionuclides from which isotope fractionation may alter occur due to slower transport mechanisms. This would also lend the UTEX model useful to simulating noble gas releases within the first few days that have the greatest chances of being detected at IMS stations rather than just long-delayed releases relevant to OSI scenarios.

Larger sensitivity studies

Under the assumption that the above improvements have been implemented, a much desired task for future work would be to use UTEX to do even further work in estimating gas transport sensitivity on the large number of variables that go into modeling subsurface movement and release of gas. The ultimate goal would be that for a given geologic location (or even variety of potential locations) to establish a range of possible gas releases and ratios in the 3D model subject to varying weather, ground moisture, radionuclide source, and cavity conditions. Given a hypothetical event whose magnitude is constrained by seismic measurements in an area where the geology is "generally" known, the 3D UTEX model could be used to establish order of magnitude release bounds subject to the other variables within the model. A greater understanding of how various event parameters and environmental parameters affect gas transport and release can only improve understanding of how best to detect radionuclides released.

Additional OSI Science

On-site inspection scenarios still provide the most direct application of the results of the UTEX code. The current UTEX capability and potential future development would allow for greater examination of the CTBT concept of operations for OSI. There is potentially more work to be done in the assessment of atmospheric infiltration dangers in soil-sampling as well as characterizing both tarping as well as alternative solutions to the problem. Again, the capability of UTEX to be useful in modeling such scenarios has been established and demonstrated, but a large amount of work exists in covering sensitivities of such effects on environmental and OSI procedural parameters. Other tasks could be related to studying the material chosen for borehole backfilling, the process of de-wetting that occurs in materials like bentonite clay, optimizing the soil-gas sampling technique,

and examining the greater infiltration and sampling sensitivity to variations in the atmospheric pressure.

8.5 EXPERIMENTAL VERIFICATION

One reality of simulating subsurface gas transport and making estimates of leakage rates and isotopic characteristics is that such predictions are inherently difficult to verify experimentally. First of all (and fortunately), there are not many known incidents of underground nuclear explosions on which to test the major thesis of this work – that subsurface transport can potentially alter the isotopic signatures of UNE noble gases. Second, so many factors combine to create a real, physical system model and transport scenario that replicating such in a numerical model is an extremely tall task and small inaccuracies in the approximation can affect a large deviation in the compared estimates. As a result, transport modeling is a tool best used for order of magnitude type estimates with the larger aim of identifying important aspects of the physics and setting bounding cases on the potential results.

8.5.1 Possible Experiment Concept

The largest influence on fluctuations in the simulated radioxenon isotopic ratios presented in this work comes from the variable movement of a radioactive gas that is produced by a time-dependent source. The greatest potential for verifying such isotopic mixing effects experimentally would be in replicating as many of these characteristics as possible in a controlled environment. The most important points in the consideration of setting up such an experiment, even on a small scale, are:

- A mixed, radioactive gas source whose half-lives are different enough that their ratio of concentration should change "significantly" over the time frame of pressure fluctuation driving the system transport.
- A continuous geologic medium, preferably a rock or semi-impermeable soil medium in which fracture-matrix diffusion could be exhibited. Large gaps at potential rock-container interfaces would have to be minimized; otherwise they will become the dominant paths of transport rather than through the medium itself.
- A variable pressure source whereby the effects of fluctuating atmospheric pressure can be simulated. It is important that variable flow in both positive and negative direction can be induced in the system.
- And obviously a method for gas sampling and detection would be necessary to measure and quantify the transport effects.

Figure 8.1 shows a conceptual illustration of a possible approach to simulating small scale movement of radioactive gas through a geologic medium. The general idea of this concept is to emplace a large, bulk slab of geologic medium within a closed, controlled test system, through which transport of a tracer gas can be induced through manipulation of the pressure at the top of the system. If the medium does not contain a pre-existing fracture network, then it is conceivable that a system similar to that modeled by UTEX could be achieved artificially through the use of a very narrow tubing or similar mold around which a medium such as concrete could be poured and allowed to solidify. Either the tubing/mold could be withdrawn, baked out, or perforated tubing could be employed that is highly permeable and allows gas exchange with the surrounding rock medium.

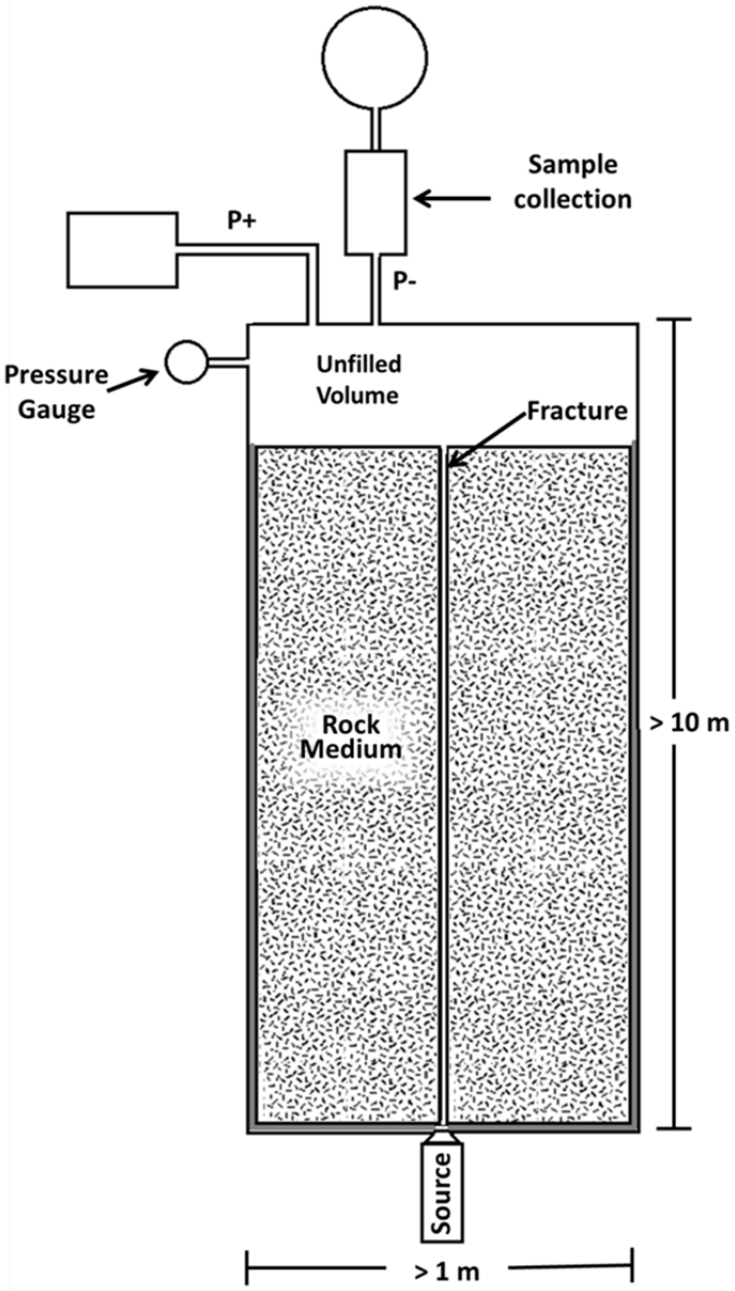

Figure 8.1 Conceptual illustration (not to scale) of a possible experiment to examine the effects of geologic transport on a time-dependent source signature.

At the bottom of this system, connected externally, would be a source, preferably of a radioactive gas such as iodine. This source gas would be released into the closed system and variable positive and negative applied pressures at the top of the system would induce advective vertical flow up the artificial fracture. Through successive upward and downward movements along the fracture, gas seepage into the surrounding bulk rock medium would occur, hopefully mirroring the barometric pumping effect. Sampling at the top of the system would then allow for the transported gas to be analyzed for alterations in isotopic signature.

Figure 8.2 depicts a schematic of the design concept illustrated in Figure 8.1, drawn to scale, to convey the relative size of the small narrow crack compared to the bulk size of the system as a whole. Small injections of nitrogen gas could be used induce pressure increases and a vacuum pump used to lower the upper system pressure. A charcoal trap could be connected in line with the vacuum to facilitate collection of xenon gas during *pressure lows*. Ideally, the source injected into the bottom of the system would not only be radioactive and variable in time, but also of mixed isotopes. For instance, both ^{131}I and ^{133}I could be used to provide a time-dependent source of radioactive ^{131}Xe and ^{133}Xe. It may also be possible to utilize a strong spontaneous fission source such as californium, ^{252}Cf.

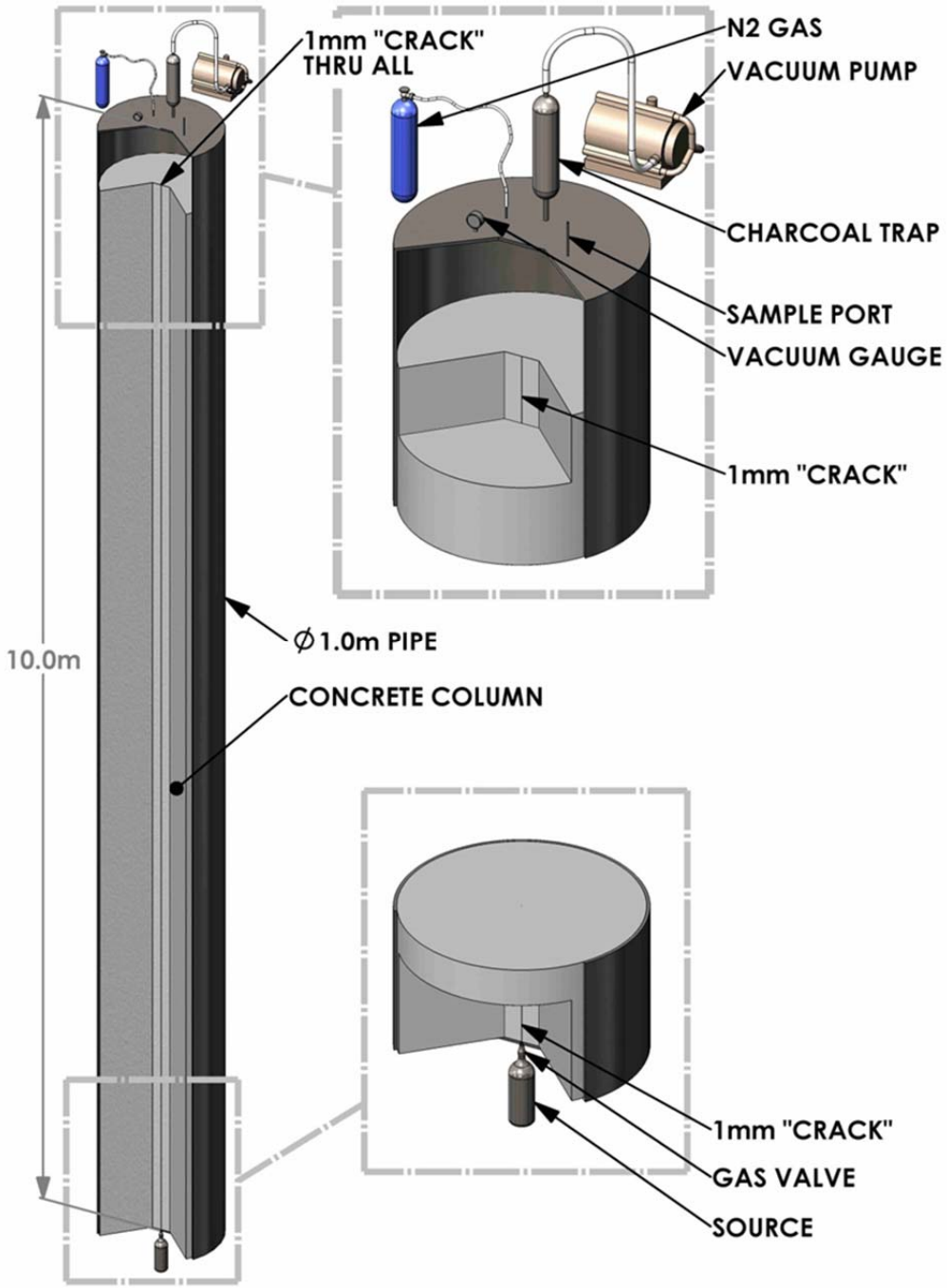

Figure 8.2 Scaled schematic of a possible experiment to examine the effects of geologic transport on a time-dependent source signature (illustration by R James Ewing, Pacific Northwest National Laboratory).

Such an experiment faces a large number of technical challenges, three major ones are:

- The rock-container interface must be gas tight; otherwise gas would trivially seep preferentially along the edges of the container. This could be facilitated through use of a rubber sealant or even a bentonite wrapper that expands to fill voids in the interface.
- The experiment scale suggested in Figures 8.1 and 8.2 are merely estimates. True geologic transport takes place over depths of hundreds of meters. Creating a closed system to simulate this must be only a fraction as deep. Still, constructing such a setup would be a tall task.
- Also because the system scale is so much smaller than a true geologic system, the size of induced pressure variations would have to be carefully considered. Too strong of pressure fluctuations would quickly deplete the fracture gas and overwhelm any potential effects of fracture-matrix interaction. Along this same line, a workable and detectable concentration range of source gas would have to be evaluated carefully.

One potential alternative, especially in a tabletop scale of an experiment, could be the use of non-radioactive tracer gas. One example might be the use of florescent dyes and tags, which are commonly used within the medical industry in place of radioactive tracers. The real importance of setting up such an experiment is that source gas in the system displays time-varying characteristics such that gas emanated at one time can be distinguished from gas emanated at other times. From this, the amount of source mixing that takes place in the course transport can be quantified and compared to numerical simulation.

Conducting such a test within a large scale geological environment would be very costly and more challenging, but potentially better demonstrative of the true transport processes. The difficulty is in fully characterizing the geologic medium as well as the assortment of experimental conditions. Ultimately, an experiment similar to the Non-Proliferation Experiment could be conducted with radioactive isotopes that are injected into the system at known, variable rates to simulate the ingrowth of radioxenon isotopes from iodine.

8.5.2 Infiltration studies

Atmospheric infiltration into the subsurface operates on the same mechanisms as subsurface leakage, and therefore studies of atmospheric infiltration can offer insight into the transport processes as a whole. The advantage of such a *reverse study* is that there are accessible locations around the world in the vicinity of medical isotope production plants and power reactors where time-varying radionuclide atmospheric concentrations are expected. If stack monitoring data could provide source release estimates, then it is possible that soil-gas sampling at shallow depths in the nearby regions could exhibit the effects of atmospheric infiltration due to surface pressure fluctuations.

Making use of such a scenario would largely depend on goal of the study being conducted. One such study would be to examine the correlation between infiltrating gas concentrations and source release, even in the context of fully simulating an on-site inspection soil-gas sampling scenario. The time lag between the source releases and elevated soil levels would provide meaningful field data on the infiltration process. Beyond this providing a framework for larger geologic transport in a UNE setting, such a study could yield insight into approaches for countering infiltration within the CTBT OSI concept of operations.

Appendix A: Table of Geologic Material Compositions

compositions are in ppm

		Rock			Soil	
Element		Wedepohl (1971)	Taylor (1964)	Mason (1966)	Vinogradov (1959)	Bowen (1966)
1	H	700	0	1400	0	0
3	Li	30	20	20	30	30
4	Be	2	2.8	2.8	6	6
5	B	9	10	10	10	10
6	C	320	200	200	20000	20000
7	N	20	20	20	1000	1000
8	O	472500	464000	466000	490000	490000
9	F	720	625	625	200	200
11	Na	24500	23600	28300	6300	6300
12	Mg	13900	23300	20900	6300	5000
13	Al	78300	82300	81300	71300	71000
14	Si	305400	281500	277200	330000	330000
15	P	810	1050	1050	800	650
16	S	310	260	260	850	700
17	Cl	320	130	130	100	100
19	K	28200	20900	25900	13600	14000
20	Ca	28700	41500	36300	13700	13700
21	Sc	14	22	22	7	7
22	Ti	4700	5700	4400	4600	5000
23	V	95	135	135	100	100
24	Cr	70	100	100	200	100
25	Mn	690	950	950	850	850
26	Fe	35000	56300	50000	38000	38000
27	Co	12	25	25	8	8
28	Ni	44	75	75	40	40
29	Cu	30	55	55	55	20
30	Zn	60	70	70	70	50

Element	Rock			Soil	
	Wedepohl (1971)	Taylor (1964)	Mason (1966)	Vinogradov (1959)	Bowen (1966)
31 Ga	17	15	15	15	30
32 Ge	1.3	1.5	1.5	1.5	1
33 As	1.7	1.8	1.8	1.8	6
34 Se	0.09	0.05	0.05	0.05	0.2
35 Br	2.9	2.5	2.5	2.5	5
37 Rb	120	90	90	90	100
38 Sr	290	375	375	375	300
39 Y	34	33	33	33	50
40 Zr	160	165	165	165	300
41 Nb	20	20	20	20	0
42 Mo	1	1.5	1.5	1.5	2
44 Ru	0.001	0	0.01	0.01	0
45 Rh	0.001	0	0.005	0.005	0
46 Pd	0.01	0	0.01	0.01	0
47 Ag	0.06	0.07	0.07	0.07	0.1
48 Cd	0.1	0.2	0.2	0.2	0.06
49 In	0.07	0.1	0.1	0.1	0
50 Sn	3	2	2	2	10
51 Sb	0.2	0.2	0.2	0.2	0
52 Te	0.002	0	0.01	0.01	0
53 In	0.5	0.5	0.5	0.5	5
55 Cs	2.7	3	3	3	6
56 Ba	590	425	425	425	500
57 La	44	30	30	30	30
58 Ce	75	60	60	60	50
59 Pr	7.6	8.2	8.2	8.2	0
60 Nd	30	28	28	28	0
62 Sm	6.6	6	6	6	0
63 Eu	1.4	1.2	1.2	1.2	0
64 Gd	8.8	5.4	5.4	5.4	0
65 Tb	1.4	0.9	0.9	0.9	0

	Rock			Soil	
Element	Wedepohl (1971)	Taylor (1964)	Mason (1966)	Vinogradov (1959)	Bowen (1966)
66 Dy	6.1	3	3	3	0
67 Ho	1.8	1.2	1.2	1.2	0
68 Er	3.4	2.8	2.8	2.8	0
69 Tm	0.6	0.48	0.5	0.5	0
70 Yb	0	0	0	0	0
71 Lu	0.6	0.5	0.5	0.5	0
72 Hf	3	3	3	3	6
73 Ta	3.4	2	2	2	0
74 W	1.3	1.5	1.5	1.5	1
75 Re	0.001	0	0.001	0.001	0
76 Os	0	0	0	0	0
77 Ir	0.001	0	0.001	0.001	0
78 Pt	0.005	0	0.01	0.01	0
79 Au	0.004	0.004	0.004	0.004	0
80 Hg	0.03	0.08	0.08	0.08	0.03
81 Tl	0	0	0	0	0
82 Pb	15	12.5	13	13	10
83 Bi	0.2	0.17	0.2	0.2	0
90 Th	11	9.6	7.2	7.2	5
92 U	3.5	2.7	1.8	1.8	1

Appendix B: FRAM advection scheme

To counter the spurious oscillations that occur in advection solutions resulting from large velocity gradients, the Filtering Remedy and Methodology (FRAM) developed by Chapman can be used to determine the advection terms in Equations (3.4) and (3.5). An outline of this scheme is as follows.

Crowley's so-called second order scheme is first used to calculate provisional values for the concentration by adjusting the advection to counter the leading temporal truncation error that grows large with sharp velocity gradients. Next, to determine acceptable concentration bounds, the local Lagrangian forms of the advective transport equations are solved, and the provisional values for the concentration are filtered to determine if these bounds are exceeded. If the bounds are exceeded then numerical diffusion is artificially introduced to counter the exceeding value. Finally, the advection terms as well as any artificial diffusion terms are added back to the tracer transport equations.

First a provisional value for the concentration is estimated using the 1D advection equation

$$\frac{\partial C}{\partial t} + u\frac{\partial C}{\partial y} = 0 \tag{B.1}$$

which in discretized form becomes

$$\frac{C_{ij}^{n+1} - C_{ij}^{n}}{\Delta t} + \frac{u}{2}\left(\frac{C_{i+1j}^{n} - C_{i-1j}^{n}}{\Delta y}\right) = 0\,. \tag{B.2}$$

To account for the error introduced by the leading term in the truncated error, an artificial diffusion term is introduced on the right side

$$\frac{C_{ij}^{n+1} - C_{ij}^{n}}{\Delta t} + \frac{u}{2}\left(\frac{C_{i+1j}^{n} - C_{i-1j}^{n}}{\Delta y}\right) = \frac{\partial}{\partial y}F \tag{B.3}$$

where

$$F = \varepsilon \frac{\partial C}{\partial y}. \tag{B.4}$$

Following the recommendation of Hirt (1968), the diffusion is made large enough to counter the oscillations by letting

$$\varepsilon = \frac{u\Delta y}{2} - \frac{u^2 \Delta t}{2} \tag{B.5}$$

By including Equations (B.5) and (B.4) in Equation (B.3) and solving for the *provisional* concentration, $C_{ij}^{n+1} \rightarrow \tilde{C}_{ij}^{n+1}$, the result is

$$\tilde{C}_{ij}^{n+1} = C_{ij}^{n} - \frac{u\Delta t}{2}\left(\frac{C_{i+1j}^{n} - C_{i-1j}^{n}}{\Delta y}\right) + \frac{u^2 \Delta t^2}{2\Delta y^2}\left(C_{i+1j}^{n} - 2C_{ij}^{n} + C_{i-1j}^{n}\right) \tag{B.6}$$

In areas of the mesh where $u\Delta t / \Delta y < 1$, Equation (B.6) is enough to stabilize the advection solution. However, in regions of particularly high pressure gradients, additional dissipation ε must be added. Consider now the Lagrangian equation for *C* or rather the flux, *uC*

$$\frac{d}{dt}(C) + C\frac{\partial u}{\partial y} = 0 \tag{B.7}$$

from which

$$C_{ij}^{*} = C_{ij}^{n} - C_{ij}^{n}\left(\frac{u_{i+1j}^{n} - u_{i-1j}^{n}}{2\Delta y}\right)\Delta t. \tag{B.8}$$

Equation (B.8) essentially says that the upper bound C_{ij}^{*} is represented by a pure translation $u\Delta t$ of the previous time concentration.

Now a filtering scheme can be established for the provisional concentration $\tilde{C}_{ij}^{n+1}$ by defining the minimum and maximum acceptable values for the provisional concentration by

$$\begin{aligned} C_{ij}^{-} &= \min\left(C_{i-1j}^{*}, C_{ij}^{*}, C_{i+1j}^{*}\right) \\ C_{ij}^{+} &= \max\left(C_{i-1j}^{*}, C_{ij}^{*}, C_{i+1j}^{*}\right) \end{aligned}. \tag{B.9}$$

If the provisional concentration $\tilde{C}_{ij}^{n+1}$ does not fall between these two values, then an additional artificial diffusive step ε is added. If a "gate" parameter is defined as

$$\chi_{ij} = \begin{cases} 0 & C_{ij}^{-} \le \tilde{C}_{ij}^{n+1} \le C_{ij}^{+} \\ 1 & \text{otherwise} \end{cases} \tag{B.10}$$

then the diffusive step can be written

$$\varepsilon_{ij} = \chi_{ij}\left(\frac{\left|u_{ij}^{n}\right|\Delta y}{2} - \frac{\left(u_{ij}^{n}\right)^{2}\Delta t}{2}\right) \rightarrow \varepsilon_{i\pm 1/2\,j} = \chi_{ij}\frac{\left|u_{ij}^{n}\right|\Delta y}{2}\left(1 \pm \frac{u_{ij}^{n}\Delta t}{\Delta y}\right). \tag{B.11}$$

The final filtered advection term then becomes

$$C_{ij}^{n+1} = \tilde{C}_{ij}^{n+1} + \frac{\Delta t}{\Delta y^{2}}\left[\varepsilon_{i+1/2\,j}\left(C_{i+1\,j}^{n} - C_{ij}^{n}\right) - \varepsilon_{i-1/2\,j}\left(C_{ij}^{n} - C_{i-1\,j}^{n}\right)\right]. \tag{B.12}$$

Appendix C: UTEX Benchmarking

C.1 Derivation of harmonic pressure response

The coupled pore-fluid diffusion equations are reiterated here (note that x in this derivation is vertical depth coordinate):

$$\frac{\partial p}{\partial t} = \frac{1}{A}\frac{\partial}{\partial x}\left(\alpha_f A \frac{\partial p}{\partial x}\right) - \frac{\phi_m}{\phi_f}\int_0^{\delta_m/2}\frac{\partial p}{\partial t}dy \tag{C.1}$$

$$\frac{\partial p}{\partial t} = \frac{\partial}{\partial y}\left(\alpha_m \frac{\partial p}{\partial y}\right). \tag{C.2}$$

Again, α_f and α_m are the pore-fluid diffusivities of the fracture and matrix respectively; assuming $p \ll p_0$ these diffusivities are approximately constant with depth and given by

$$\alpha_f = \frac{\left(\delta_f\right)^2}{12}\frac{p_0}{\mu\phi_f} \qquad \text{and} \qquad \alpha_m = \frac{k_m p_0}{\mu\phi_m}.$$

The integral in the fracture-matrix interaction term couples the pressure response within the fracture to the pressure response deeper within the bulk matrix at the point $(x, 0)$. Using the horizontal pressure equation (C.2) in this integral

$$\begin{aligned}\int_0^{\delta_m/2}\frac{\partial p}{\partial t}dy &= \int_0^{\delta_m/2}\frac{\partial}{\partial y}\left(\alpha_m\frac{\partial p}{\partial y}\right)dy \\ &= \alpha_m\left[\frac{\partial p}{\partial y}\right]_{y=0}^{y=\delta_m/2} \\ &= \alpha_m\left[\left(\frac{\partial p}{\partial y}\right)_{y=\delta_m/2} - \left(\frac{\partial p}{\partial y}\right)_{y=0}\right]\end{aligned}$$

Assuming a matrix slab width of δ_m, the system models a unit cell of half-slab width $\delta_m/2$. At this point within the matrix slab there is a reflective boundary condition; we therefore have $(\partial p/\partial y)_{y=\delta_m/2} = 0$. Assuming a constant fracture cross-sectional area of $A = \delta_f/2$ then Equations (C.1) and (C.2) become

$$\frac{\partial p}{\partial t} = \alpha_f\frac{\partial^2 p}{\partial x^2} + \frac{2\phi_m\alpha_m}{\delta_f\phi_f}\left(\frac{\partial p}{\partial y}\right)_{y=0} \tag{C.3}$$

$$\frac{\partial p}{\partial t} = \alpha_m \frac{\partial^2 p}{\partial y^2} \tag{C.4}$$

Separation of variables is employed to obtain an analytical solution to this coupled system of equations by looking for a pressure solution of the form

$$p(x, y; t) = X(x)Y(y)T(t) . \tag{C.5}$$

At the top of the fracture, $(x, y) = (0,0)$, the pressure should follow the surface pressure, taken to be harmonically varying,

$$p(0,0;t) = p_0 + \Delta p \cos \omega t .$$

Devoting attention only to the variation of pressure from the average p_0 does not change equations (C.3) and (C.4) for the pressure response. The boundary condition above then becomes

$$p(0,0;t) = X(0)Y(0)T(t) = \cos \omega t . \tag{C.6}$$

The boundary conditions at $x = L$ and $y = \delta_m/2$ are reflective, so $(dX/dx)_{x=L} = 0$ and $(dY/dy)_{y=\delta_m/2} = 0$.

Applying the separation of variables technique to Equation (C.4) gives

$$X(x)Y(y)\dot{T}(t) = \alpha_m X(x)T(t)Y''(y)$$

$$\frac{\dot{T}(t)}{T(t)} = \alpha_m \frac{Y''(y)}{Y(y)} = -\lambda_1{}^2 \tag{C.7}$$

Considering the left side of Equation (C.7) for the temporal dependence and using Equation (C.6) gives

$$T(t) = e^{i\omega t} \tag{C.8}$$

where the constant $\lambda_1 = i\sqrt{i\omega}$ has been identified. Then the second part of Equation (C.7) becomes

$$Y(y) = Y_1 e^{\lambda_2 y} + Y_2 e^{-\lambda_2 y} \tag{C.9}$$

where

$$\lambda_2 = \lambda_1 \sqrt{\frac{1}{\alpha_m}} = \sqrt{i}\sqrt{\frac{\omega}{\alpha_m}} .$$

Applying the first boundary condition to Equation (C.9):

$$Y(0) = Y_1 + Y_2 = 1$$
$$Y_2 = 1 - Y_1$$

then the second boundary condition gives

$$Y'\left(\frac{\delta_m}{2}\right) = \lambda_2 \left[Y_1 e^{\lambda_2 \frac{\delta_m}{2}} - Y_2 e^{-\lambda_2 \frac{\delta_m}{2}} \right] = 0$$
$$Y_1 e^{\lambda_2 \frac{\delta_m}{2}} = Y_2 e^{-\lambda_2 \frac{\delta_m}{2}}$$
$$Y_1 e^{\lambda_2 \delta_m} = Y_2 = 1 - Y_1$$
$$Y_1 = \frac{1}{1 + e^{\lambda_2 \delta_m}} \quad \text{and} \quad Y_2 = \frac{e^{\lambda_2 \delta_m}}{1 + e^{\lambda_2 \delta_m}} . \tag{C.10}$$

Plugging the coefficients Equation (C.10) back into (C.9), the *y*-independence can be written

$$Y(y) = \frac{1}{1 + e^{\lambda_2 \delta_m}} \left[e^{\lambda_2 y} + e^{\lambda_2 \delta_m} e^{-\lambda_2 y} \right]$$
$$= \frac{1}{1 + e^{\lambda_2 \delta_m}} \left[e^{\lambda_2 \frac{\delta_m}{2}} e^{\lambda_2 \left(y - \frac{\delta_m}{2} \right)} + e^{\lambda_2 \frac{\delta_m}{2}} e^{-\lambda_2 \left(y - \frac{\delta_m}{2} \right)} \right]$$
$$= \frac{\cosh\left(\left(\frac{\lambda_2 \delta_m}{2} \right) \left(1 - \frac{2y}{\delta_m} \right) \right)}{\cosh\left(\left(\frac{\lambda_2 \delta_m}{2} \right) \right)}$$

Finally, defining $\lambda_m = \frac{\lambda_2 \delta_m}{2} = \frac{\delta_m}{2} \sqrt{i} \sqrt{\frac{\omega}{\alpha_m}}$, then

$$Y(y) = \frac{\cosh \lambda_m \left(1 - \frac{2y}{\delta_m} \right)}{\cosh \lambda_m} \tag{C.11}$$

Now looking at Equation (C.3)

$$\frac{\dot{T}}{T} = \alpha_f \frac{X''}{X} + \frac{2\phi_m \alpha_m}{\delta_f \phi_f} \left(\frac{Y'}{Y} \right)_{y=0} = i\omega$$

where from Equation (C.11)

$$\frac{Y'}{Y} = \frac{-2\lambda_m}{\delta_m}\tanh\lambda_m\left(1-\frac{2y}{\delta_m}\right)$$

giving

$$\alpha_f\frac{X''}{X}+\left(\frac{2\phi_m\alpha_m}{\delta_f\phi_f}\right)\frac{-2\lambda_m}{\delta_m}\tanh\lambda_m = i\omega$$

$$\frac{X''}{X} = \frac{i\omega}{\alpha_f}+\frac{i\omega}{\alpha_f}\left(\frac{2\phi_m}{\delta_f\phi_f}\right)\frac{\sqrt{\alpha_m}}{\sqrt{i}\sqrt{\omega}}\tanh\lambda_m$$

$$\frac{X''}{X} = \frac{i\omega}{\alpha_f}\left[1+\frac{2\phi_m}{\delta_f\phi_f}\left(\frac{\delta_m}{2\lambda_m}\right)\tanh\lambda_m\right]$$

$$\frac{X''}{X} = \frac{i\omega}{\alpha_f}\left[1+\frac{\delta_m\phi_m}{\delta_f\phi_f}\frac{\tanh\lambda_m}{\lambda_m}\right] \qquad \text{(C.12)}$$

Finally letting

$$\lambda_f^2 = \frac{i\omega}{\alpha_f} \quad \text{and} \quad \lambda_{fm}^2 = \lambda_f^2\left[1+\frac{\delta_m\phi_m}{\delta_f\phi_f}\frac{\tanh\lambda_m}{\lambda_m}\right] \qquad \text{(C.13)}$$

the *x*-dependency can be written from Equation (C.12) as

$$X(x) = X_1 e^{\lambda_{fm}x} + X_2 e^{-\lambda_{fm}x}.$$

Similar to the *y*-dependence, the boundary conditions require $X(0) = 1$ and $X'(L) = 0$ so that following the same procedure as for *Y(y)* gives

$$X(x) = \frac{\cosh\lambda_{fm}\left(1-\frac{x}{L}\right)}{\cosh\lambda_{fm}} \qquad \text{(C.14)}$$

where λ_f becomes $\lambda_f = L\sqrt{i}\sqrt{\frac{\omega}{\alpha_f}}$. Combining Equations (C.8), (C.11) , and (C.14) the final analytical solution for the pressure response can be written

$$\frac{p(x,y;t)-p_0}{\Delta p} = \mathrm{Re}\left[\frac{\cosh\lambda_m\left(1-\frac{2y}{\delta_m}\right)}{\cosh\lambda_m}\frac{\cosh\lambda_{fm}\left(1-\frac{x}{L}\right)}{\cosh\lambda_{fm}}e^{i\omega t}\right] \qquad \text{(C.15)}$$

with Fourier numbers

$$\lambda_f = L\sqrt{i}\sqrt{\frac{\omega}{\alpha_f}}$$

$$\lambda_m = \sqrt{i}\,\frac{\delta_m}{2}\sqrt{\frac{\omega}{\alpha_m}}$$

$$\lambda_{fm}^2 = \lambda_f^2\left[1+\frac{\delta_m\phi_m}{\delta_f\phi_f}\frac{\tanh\lambda_m}{\lambda_m}\right]$$

C.2 DIFFUSION ANALYSIS OF UTEX CODE

As a test of the robustness of the UTEX numerical solution scheme for the actual transport equations, it is simplest to consider individual transport mechanisms as they are modeled by the code. The terms in the transport equations represent two physical transport mechanisms: diffusion and advection. A simple analysis of the diffusion transport in UTEX is considered here. Consider a very simple scenario as depicted below in Figure C.1 in which a single matrix cell is given an initial concentration, C_0, and the rest of the matrix is void of any contaminant. Now allow the system to diffuse throughout the matrix row only assuming the system is closed and bounded at the ends, $y = 0$ and $y = \delta_m$.

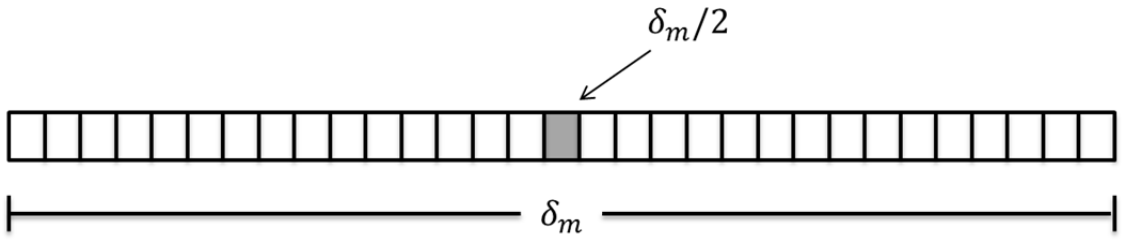

Figure C.1 Simple diffusion 1D diffusion scenario.

This is a scenario that is easily modeled in the UTEX code by forcing the mass-interaction terms and advection terms (and radioactive decay) to all be zero in the transport equations. Intuitively, we know that the concentration initially confined to the middle cell must diffuse outwards throughout the rest of the matrix row until a constant concentration is reached throughout.

The analogous analytical problem can be defined as such; assuming a concentration $C(y,t)$ defined on $[0,\delta_m]$, the diffusion of the gas follows

$$\frac{\partial C}{\partial t} = D\frac{\partial^2 C}{\partial y^2}.$$

The initial state of the system can be stated

$$C\left(y,0\right) = C_0\delta(\delta_m / 2)$$

with closed boundary conditions,

$$\left(\frac{\partial C}{\partial y}\right)_{y=0} = \left(\frac{\partial C}{\partial y}\right)_{y=\delta_m} = 0.$$

The solution to this familiar equation can be found through separation of variables and written in terms of a Fourier expansion as

$$C\left(y,t\right) = \frac{1}{2}D_0 + \sum_{n=1}^{\infty} D_n cos\left(\frac{n\pi y}{\delta_m}\right) e^{-D\left(\frac{n\pi}{\delta_m}\right)^2 t}$$

where

$$D_n = \frac{2}{\delta_m}\int_0^{\delta_m} C\left(y,0\right) cos\left(\frac{n\pi y}{\delta_m}\right) dy.$$

Substituting in the initial condition in the expression for D_n and simplifying leads to the solution for the concentration in the matrix row

$$C\left(y,t\right) = \frac{C_0}{\delta_m} + \frac{2C_0}{\delta_m}\sum_{n=1}^{\infty} cos\left(\frac{n\pi}{2}\right) cos\left(\frac{n\pi y}{\delta_m}\right) e^{-D\left(\frac{n\pi}{\delta_m}\right)^2 t}$$

Results

The results that follow in Figure C.2 and C.3 were obtained by running the numerical code using a mesh defined by $N \times M = 100 \times 200$ using time steps of size $\Delta t = 60$ s and a matrix width of $\delta_m = 1$ m. The initial concentration is taken as $C_0 = 5.252$ (arbitrary units). The analytical solution uses N = 10,000 steps to estimate the Fourier expansion.

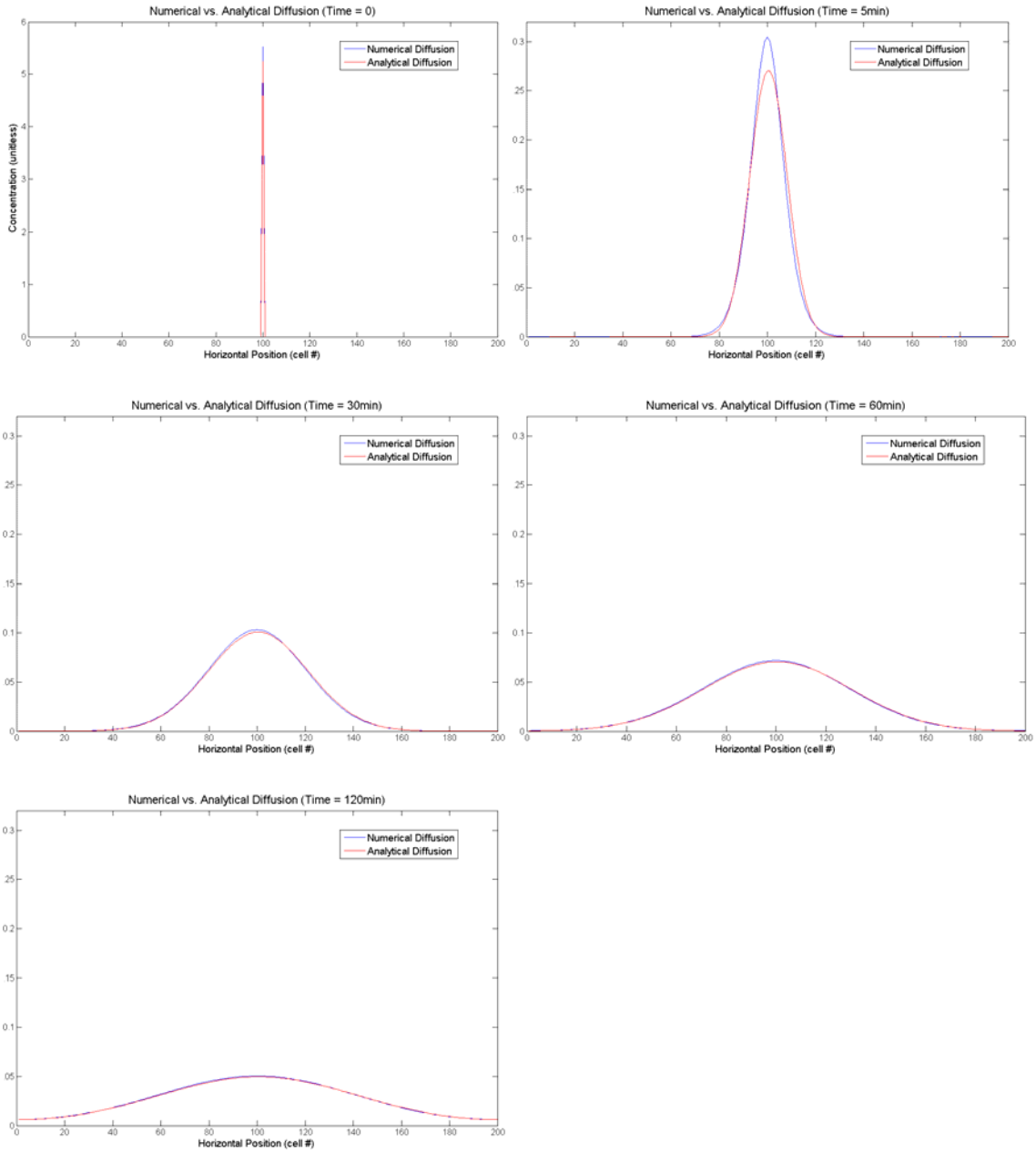

Figure C.2 Numerical UTEX and analytical diffusion solutions plotted against each other for comparison at various times up to 2 hours.

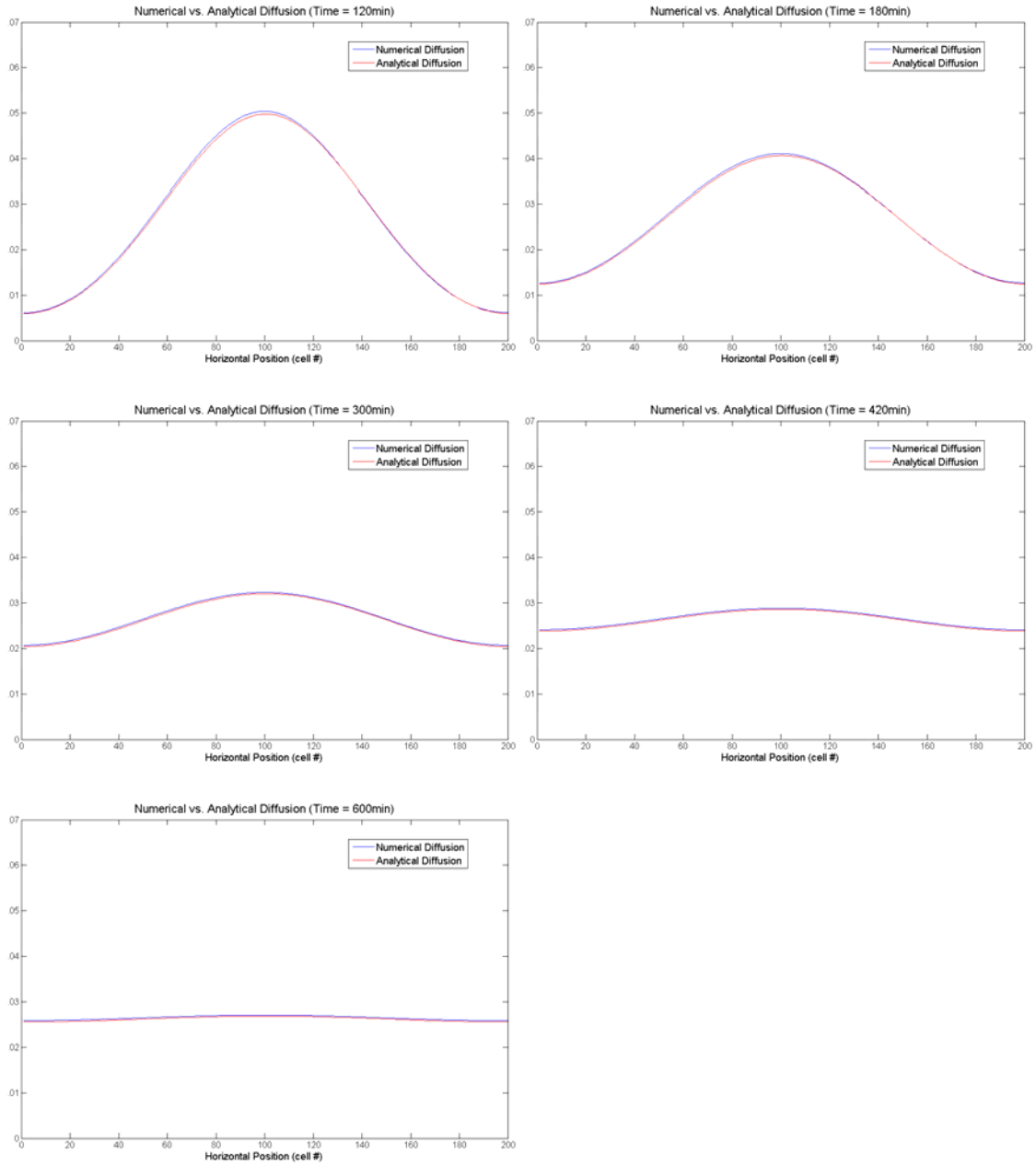

Figure C.3 Numerical UTEX and analytical diffusion solutions plotted against each other for comparison at various times, up to 10 hours.

C.3 ADVECTION ANALYSIS OF UTEX CODE

The second physical transport mechanism at work in the vertical transport model is the bulk flow of gas by advection. Unlike the diffusion within the system , which operates everywhere on the same scale since the diffusion coefficients for the radioxenon isotopes vary only a tiny amount, the advective flow is determined by the pressure gradients that exist in the system and varies over several orders of magnitude. Near the top of the system and at point closer to the fracture, the pressure response closely follows the changing surface pressure, thus at these points exist higher pressure gradients and therefore higher fluid velocities. During a simulation with the amplitude in pressure variation being $\Delta p = 5/30 p_0$, the maximum fluid velocity calculated within the system was $u_{max} \approx$ 4E-4 m/s. Since this Δp is a liberal estimate of the maximum pressure variation that could realistically be encountered, this maximum velocity serves as the ceiling for expected fluid velocities.

Removal of the diffusion and mass interaction terms from the transport equations leaves the 1-D advection equations of the form

$$\frac{\partial C(x,t)}{\partial t} = -\frac{1}{\phi}\frac{\partial}{\partial x}\left(C(x,t)u\right).$$

Generally, the fluid velocity $u = u(x,t)$ is a function of position in the system as determined by the pressure response at time, t. This makes an analytical solution very difficult for all but the simplest velocity distributions.

Of course, *the* simplest case is $u(x,t) = u_0$ so that the fluid velocity is a constant throughout the system for all times. Now instead of a complicated, largely intractable equation we have the simple linear advection equation

$$\frac{\partial C}{\partial t} = -\frac{u}{\phi}\frac{\partial C}{\partial x}$$

which has the rather obvious solution

$$C(x,t) = C_0\left(x - \frac{u}{\phi}t\right)$$

where $C(x,0) = C_0(x)$ is just the initial concentration distribution. In other words, the shape of $C_0(x)$ does not change but is shifted in position.

While this constant velocity scenario is somewhat uninteresting, it does serve well as an analytical test of the numerical advection portion of the transport code. Similar to the diffusion test before, assume an initial concentration distribution of the form $C_0(x) = C_0\delta(\delta_m/2)$. For a given flow velocity, u, the analytical solution for the concentration is just

$$C(x,t) = C_0\delta\left(\delta_m/2 - \frac{u}{\phi}t\right).$$

To test the numerical advection solution, a single cell within a horizontal matrix row was initially filled with an initial concentration of 5.252 Ci. Diffusion and decay constants were set to 0 and all interaction terms were forced to 0, so that in essence the matrix rows have closed boundaries. The pressure response function was turned off completely and the flow velocity throughout the system was set to a constant value for each simulation. Figure C.4 shows an example of the numerical solution versus the analytical solution for a specific time.

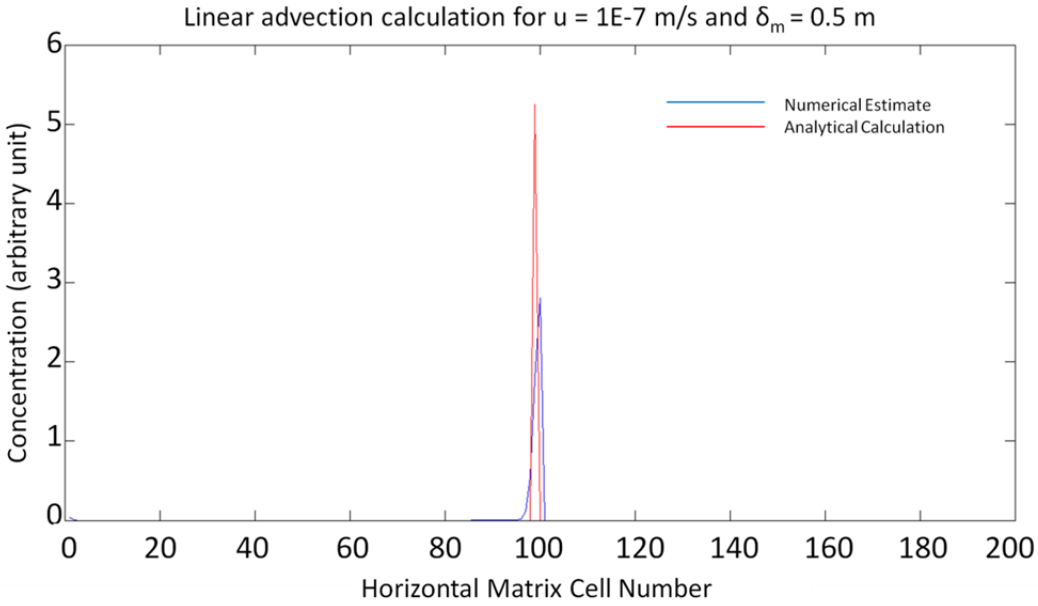

Figure C.4 Example comparison between numerical and analytical solution; the direction of flow is to the left.

This example exhibits the characteristics of where the error in the numerical solution comes into play. The red line plots the analytical solution, which shows a sharp peak at a single matrix cell with the full concentration, $C_0 = 5.252$. The blue line plots the numerical calculation, and is centered around the same matrix location as the analytical solution, however, the peak shows a forward spread in the direction of the fluid velocity. This is a depiction of *numerical diffusion*, which results from the fact that the numerical system is a discrete approximation of a continuous phenomenon. For a given flow $x = u\Delta t$ that is less than the mesh spacing Δx, the concentration in the finite difference scheme cannot be moved in a unit smaller than Δx. Instead the transport is approximated by placing some portion of the mass in the adjacent cell and leaving the rest in the original cell, so that the average transport equals $x = u\Delta t$. However, now there is a portion of the mass that has been *numerically diffused* a larger distance than $u\Delta t$. This

results in the spread of the initial concentration peak and is responsible for the error in the numerical approximation.

This concept is precisely that of the Courant Number, which is defined as the portion of mass that can be transported in a single time step,

$$C_r = \frac{u\Delta t}{\Delta x}.$$

Ideally the Courant Number should be as small as possible, say $C_r < 1$, to minimize numerical oscillations and the dispersion depicted above. An effect opposite of the above numerical diffusion is created when the fluid velocity results in a transport $x = u\Delta t$ that is much greater than Δx. In this case $C_r > 1$ and the numerical scheme suppresses transport because it allows mass to move only to adjacent cells and not multiple cells.

Appendix D: Variability of other isotopic ratios of radioxenon

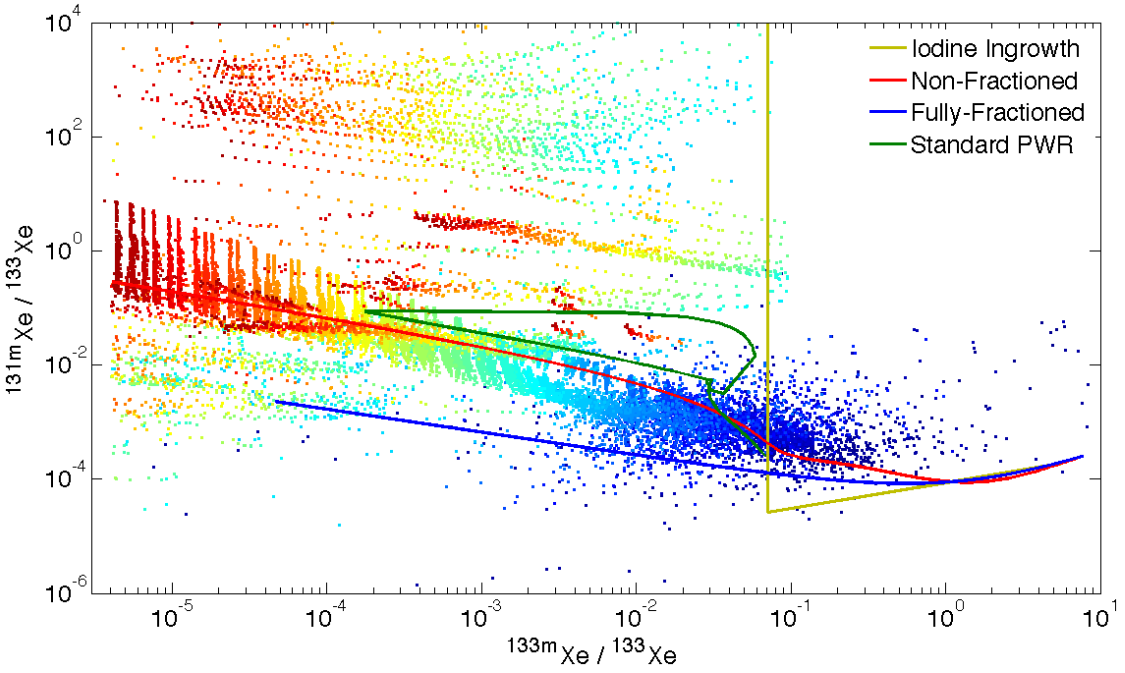

Figure D.1 Three isotope MIRC plot showing $^{131m}Xe/^{133}Xe$ vs. $^{133m}Xe/^{133}Xe$ for HEU fast pulse fission source term with standard PWR loop shown.

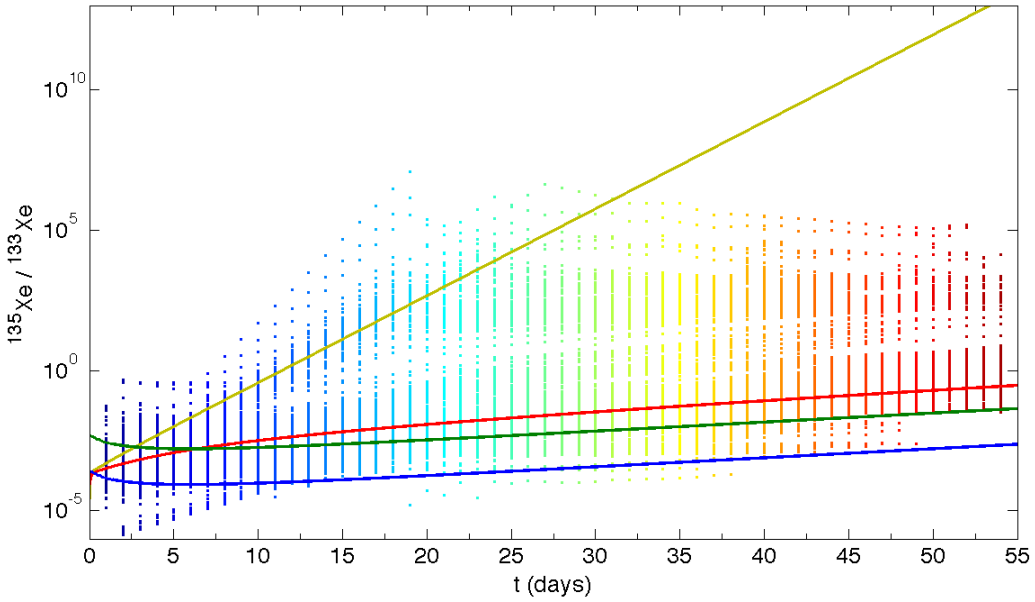

Figure D.2 Two isotope MIRC plot showing ^{131m}Xe/^{133}Xe vs. time for HEU fast pulse fission source term, with PWR signature (green) corresponding to a $t = 0$ release 90 days into standard operational cycle.

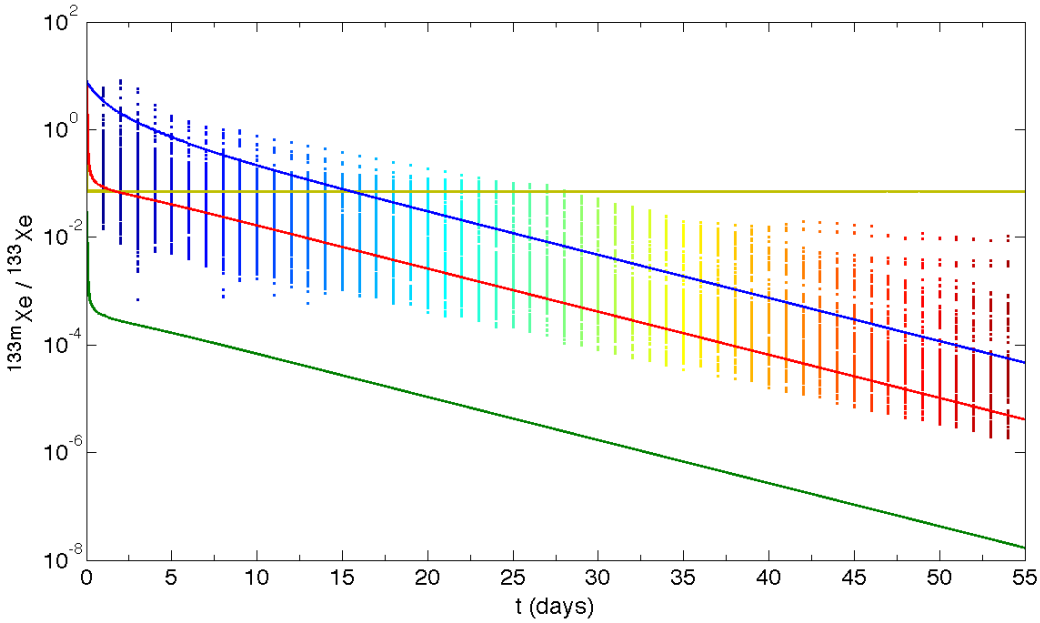

Figure D.3 Three isotope MIRC plot showing ^{133m}Xe/^{133}Xe vs. time for HEU fast pulse fission source term, with PWR signature (green) corresponding to a $t = 0$ release 90 days into standard operational cycle.

Appendix E: Elemental compositions and properties for geologies used in neutron flux profiling

Table E.1 Elemental compositions in concentrations of parts per million (ppm) utilized in neutron flux profiling, from Fabryka-Martin (1988).

	Z	A	Ultra-mafic	Basalt	Hi-Ca granite	Low-Ca granite	Clays, shales	Sand-stones	Carbon-ate
H,w	1	1.01	4000	4000	410	410	4600	9600	2000
Li	3	6.94	0.5	17	24	40	60	15	5
Be	4	9.01	0.2	1	2	3	3	0.5	0.5
B	5	9.01	3	5	9	10	100	35	20
C	6	12.01	100	100	300	300	10000	300	114000
N	7	14.01	6	20	20	20	60	20	20
O,rk	8	16	401200	397300	474600	482900	494000	437100	476700
O,w	8	16	35700	35700	3700	3700	41700	87000	18500
F	9	19	100	400	520	850	500	270	330
Na	11	22.99	4200	18000	28400	25800	660	3300	400
Mg	12	24.31	204000	46000	9400	1600	13400	7000	47000
Al	13	26.98	20000	78000	82000	72000	104500	25000	4200
Si	14	28.09	205000	230000	314000	347000	238000	368000	24000
P	15	30.97	220	1100	920	600	770	170	400
S	16	32.07	300	300	300	300	3000	240	1200
Cl	17	35.45	85	60	130	200	160	10	150
K	19	39.1	40	8300	25200	42000	22800	10700	2700
Ca	20	40.08	25000	76000	25300	5100	25300	39100	302300
Sc	21	44.96	15	30	14	7	10	1	1
Ti	22	47.87	300	13800	3400	1200	4500	1500	400
Cr	24	52	1600	2000	22	4.1	100	35	11
Mn	25	54.94	1620	1500	540	390	670	50	1100
Fe	26	55.85	94300	86500	29600	14200	33300	9800	3800
Co	27	58.93	150	46	7	1	20	0.3	0.1
Ni	28	58.69	2000	130	15	4.5	95	2	20
Se	34	78.96	0.05	0.05	0.05	0.05	0.6	0.05	0.08
Br	35	79.9	1	3.6	4.5	1.3	6	1	6.2
Rb	37	85.47	2	30	110	170	200	60	3
Sr	38	87.62	10	465	440	100	450	20	610
Zr	40	91.22	45	140	140	175	200	220	19
Mo	42	95.94	0.3	1.5	1	1.3	2	0.2	0.4
Ru	44	101.07	0.001	0.001	0.001	0.001	0.001	0.001	0.001
Te	52	127.6	0.001	0.001	0.002	0.002	0.01	0.002	0.02
I	53	126.6	0.5	0.5	0.5	0.5	1	1.7	1.2
Cs	55	132.91	0.1	1	2	4	12	0.5	0.5
Ba	56	137.33	0.4	330	420	840	800	50	10
Sm	62	150.36	0.5	5.3	8.8	10	6.5	10	1.3
Gd	64	157.25	0.5	5.3	8.8	10	6.5	10	1.3
Th	90	232.04	0.004	4	8.5	17	11	1.7	1.7
U	92	238.03	0.001	1	3	3	3.2	0.45	2.2

Table E.2 Physical properties of the geology types utilized in neutron flux profiling, from Fabryka-Martin (1988).

	Ultra-mafic	Basalt	Hi-Ca granite	Lo-Ca granite	Clays, shales	Sand-stone	Carbon-ate
porosity	0.1	0.1	0.01	0.01	0.1	0.2	0.05
grain density [g/cm^3]	3	3	2.7	2.7	2.6	2.6	2.8
bulk density [g/cm^3]	2.8	2.8	2.7	2.7	2.4	2.3	2.7
ppm H_2O	35700	35700	3700	3700	41700	87000	18500

Table E.3 Total neutron production rates as a function of depth (mwe) for the geology types utilized in neutron flux profiling, from Fabryka-Martin (1988).

Depth (mwe)	Ultra-mafic	Basalt	Hi-Ca granite	Lo-Ca granite	Clays, shales	Sand-stone	Carbon-ate
0.5	1513	1526	1526	1528	1520	1509	1503
1	1114	1128	1128	1129	1121	1109	1103
2	622	636	636	638	629	617	610
3	356	369	369	371	363	352	346
4	216	228	229	231	223	212	207
5	140	151	152	155	148	137	133
10	40.6	47.9	51.5	54.6	48.8	39.4	38.0
20	15.5	20.5	25.5	29.0	24.2	15.7	16.2
30	9.5	14.0	19.3	22.9	18.3	10.0	10.9
50	4.2	8.3	13.9	17.6	13.2	5.0	6.3
100	1.4	5.3	11.0	14.7	10.4	2.3	3.7
200	0.39	4.3	10.0	13.7	9.4	1.3	2.7
300	0.18	4.0	9.8	13.5	9.2	1.1	2.5
500	0.054	3.9	9.6	13.4	9.0	0.97	2.4
1000	0.011	3.9	9.6	13.3	9.0	0.92	2.4
2000	0.0053	3.9	9.6	13.3	9.0	0.92	2.4
3000	0.0049	3.9	9.6	13.3	9.0	0.92	2.4

Table E.4 Thermal neutron flux as a function of depth (mwe) for the geology types utilized in neutron flux profiling, assuming all neutrons are thermalized (see Table A.5), from Fabryka-Martin (1988).

Depth (mwe)	Ultra-mafic	Basalt	Hi-Ca granite	Lo-Ca granite	Clays, shales	Sand-stone	Carbon-ate
0.5	280764	184766	232698	224438	142636	188368	360451
1	206718	136509	171889	165847	105186	138505	264574
2	115440	77037	96937	93624	59020	77027	146340
3	66054	44659	56283	54499	34072	43888	82925
4	40095	27599	34892	33923	20965	26495	49706
5	25970	18260	23226	22714	13842	17065	31785
10	7524	5800	7856	8012	4581	4914	9117
20	2872	2480	3890	4261	2273	1960	3893
30	1758	1692	2945	3364	1719	1248	2621
50	786	1008	2121	2583	1235	625	1505
100	258	642	1677	2160	972	283	881
200	72	515	1520	2011	878	161	656
300	33	489	1488	1980	859	136	608
500	10	473	1469	1962	847	121	580
1000	2.1	468	1462	1956	843	115	570
2000	1	467	1462	1955	843	115	569
3000	0.92	467	1462	1955	843	188368	360451

Table E.5 Thermal and epithermal neutron flux breakdown in the deep lithosphere, from Fabryka-Martin (1988).

	U	Th	Neutron flux, n/cm^2/yr			Flux for 100%
Rock Type	ppm	ppm	Thermal	Epithermal	Total	thermalization
Ultramafic	0.001	0.004	0.86	0.08	0.95	0.90
Basalts	1	4	435	65	500	467
Hi-Ca granite	3	8.5	1155	574	1729	1462
Low-Ca granite	3	17	1544	799	2343	1955
Clays, shales	3.2	11	707	120	827	843
Sandstones	0.45	1. 7	109	7	116	115
Carbonates	2.2	1. 7	516	61	577	569

Table E.6 Thermal and epithermal neutron flux estimates used in soil-gas background calculations for the geologies listed in Table A.1.

Thermal Flux Profile (cm^{-2} yr^{-1})

Depth d(mwe)	Ultra-mafic	Basalt	Hi-Ca granite	Lo-Ca granite	Clays, shales	Sand-stone	Carbo-nate
0.5	265547	170208	183597	177386	119404	178784	323145
1	195518	125815	135713	131066	88061	131392	237145
2	109167	70938	76519	74066	49411	73101	131150
3	62482	41158	44395	43069	28516	41704	74390
4	37910	25431	27552	26817	17518	25117	44505
5	24571	16842	18288	17994	11626	16232	28595
10	7126	5343	6196	6339	3834	4668	8170
20	2720	2287	3068	3367	1901	1860	3483
30	1667	1562	2322	2658	1438	1185	2344
50	737	926	1672	2043	1037	592	1355
100	246	591	1323	1707	817	273	796
200	68	480	1203	1590	738	154	581
300	32	446	1179	1567	723	130	538
500	9.48	435	1155	1556	707	115	516
1000	1.93	435	1155	1544	707	109	516
2000	0.93	435	1155	1544	707	109	516
3000	0.86	435	1155	1544	707	109	516

Epithermal Flux Profile (cm^{2} yr^{-1})

Depth d(mwe)	Ultra-mafic	Basalt	Hi-Ca granite	Lo-Ca granite	Clays, shales	Sand-stone	Carbo-nate
0.5	24702	25433	91242	91795	20267	11482	38201
1	18188	18800	67445	67825	14947	8438	28035
2	10155	10600	38028	38328	8387	4695	15504
3	5812	6150	22063	22288	4840	2678	8794
4	3527	3800	13692	13877	2973	1613	5261
5	2286	2517	9088	9312	1973	1042	3380
10	663	798	3079	3280	651	300	966
20	253	342	1525	1742	323	119	412
30	155	233	1154	1376	244	76	277
50	69	138	831	1057	176	38	160
100	23	88	658	883	139	18	94
200	6.37	72	598	823	125	9.89	68.63
300	2.94	67	586	811	123	8.37	63.54
500	0.88	65	574	805	120	7.38	61.00
1000	0.18	65	574	799	120	7.00	61.00
2000	0.09	65	574	799	120	7.00	61.00
3000	0.08	65	574	799	120	7.00	61.00

Appendix F. Radionuclide background calculations

Table F.1 Calculated radioxenon production rates (top) and equilibrium concentrations (bottom) from spontaneous fission of the seven geologies in Table E.1.

	Xe Spontaneous Fission Production Rate, P_n [mBq/m^3/s]				
	Xe-131m	Xe-133	Xe-133m	Xe-135	Xe-135m
Ultramafic	7.31E-13	1.48E-09	1.02E-10	1.90E-08	1.01E-07
Basalt	7.31E-10	1.48E-06	1.02E-07	1.90E-05	1.01E-04
Hi-Ca granite	2.11E-09	4.29E-06	2.96E-07	5.50E-05	2.91E-04
Lo-Ca granite	2.11E-09	4.29E-06	2.96E-07	5.50E-05	2.91E-04
Clays/shales	2.00E-09	4.07E-06	2.80E-07	5.21E-05	2.76E-04
Sandstone	2.70E-10	5.48E-07	3.78E-08	7.02E-06	3.72E-05
Carbonate	1.55E-09	3.14E-06	2.17E-07	4.03E-05	2.13E-04

	Xe Spontaneous Fission Equilibrium Concentration [mBq/m^3]				
	Xe-131m	Xe-133	Xe-133m	Xe-135	Xe-135m
Ultramafic	1.09E-06	9.69E-04	2.79E-05	9.02E-04	1.33E-04
Basalt	1.09E-03	9.69E-01	2.79E-02	9.02E-01	1.33E-01
Hi-Ca granite	3.14E-03	2.80E+00	8.07E-02	2.61E+00	3.85E-01
Lo-Ca granite	3.14E-03	2.80E+00	8.07E-02	2.61E+00	3.85E-01
Clays/shales	2.98E-03	2.66E+00	7.65E-02	2.47E+00	3.65E-01
Sandstone	4.02E-04	3.58E-01	1.03E-02	3.33E-01	4.92E-02
Carbonate	2.31E-03	2.06E+00	5.92E-02	1.91E+00	2.82E-01

Table F.2 Calculated radioxenon production rates from n-induced fission for select depths of the seven geologies in Table E.1.

Total n-induced Fission Production Rates ($mBq/m^3/s$)

Depth (mwe)	Ultramafic					Basalt				
	Xe-131m	Xe-133	Xe-133m	Xe-135	Xe-135m	Xe-131m	Xe-133	Xe-133m	Xe-135	Xe-135m
0.5	6.07E-14	2.37E-11	1.65E-12	3.18E-10	1.91E-09	3.92E-11	1.56E-08	1.08E-09	2.09E-07	1.25E-06
1	4.47E-14	1.74E-11	1.21E-12	2.34E-10	1.41E-09	2.90E-11	1.15E-08	8.01E-10	1.55E-07	9.27E-07
5	5.62E-15	2.19E-12	1.52E-13	2.94E-11	1.77E-10	3.88E-12	1.54E-09	1.07E-10	2.07E-08	1.24E-07
10	1.63E-15	6.35E-13	4.42E-14	8.53E-12	5.13E-11	1.23E-12	4.89E-10	3.40E-11	6.57E-09	3.94E-08
100	5.62E-17	2.19E-14	1.52E-15	2.94E-13	1.77E-12	1.36E-13	5.41E-11	3.76E-12	7.27E-10	4.36E-09
1000	4.41E-19	1.72E-16	1.20E-17	2.31E-15	1.39E-14	1.00E-13	3.98E-11	2.77E-12	5.35E-10	3.20E-09
	Hi-Ca Granite					Lo-Ca Granite				
0.5	1.27E-10	5.62E-08	3.91E-09	7.54E-07	4.45E-06	1.25E-10	5.56E-08	3.86E-09	7.49E-07	4.41E-06
1	9.40E-11	4.16E-08	2.89E-09	5.57E-07	3.29E-06	9.24E-11	4.11E-08	2.85E-09	5.53E-07	3.26E-06
5	1.27E-11	5.60E-09	3.89E-10	7.51E-08	4.43E-07	1.27E-11	5.64E-09	3.92E-10	7.60E-08	4.47E-07
10	4.29E-12	1.90E-09	1.32E-10	2.54E-08	1.50E-07	4.47E-12	1.99E-09	1.38E-10	2.68E-08	1.57E-07
100	9.16E-13	4.05E-10	2.82E-11	5.43E-09	3.20E-08	1.20E-12	5.35E-10	3.71E-11	7.21E-09	4.24E-08
1000	8.00E-13	3.54E-10	2.46E-11	4.74E-09	2.80E-08	1.09E-12	4.84E-10	3.36E-11	6.52E-09	3.83E-08
	Clays/shales					Sandstone				
0.5	7.56E-11	3.02E-08	2.10E-09	4.06E-07	2.43E-06	1.51E-11	5.81E-09	4.04E-10	7.80E-08	4.70E-07
1	5.57E-11	2.23E-08	1.55E-09	2.99E-07	1.79E-06	1.11E-11	4.27E-09	2.97E-10	5.73E-08	3.45E-07
5	7.36E-12	2.94E-09	2.05E-10	3.95E-08	2.37E-07	1.37E-12	5.27E-10	3.67E-11	7.08E-09	4.26E-08
10	2.43E-12	9.71E-10	6.75E-11	1.30E-08	7.80E-08	3.93E-13	1.52E-10	1.05E-11	2.04E-09	1.23E-08
100	5.17E-13	2.07E-10	1.44E-11	2.78E-09	1.66E-08	2.29E-14	8.85E-12	6.16E-13	1.19E-10	7.16E-10
1000	4.47E-13	1.79E-10	1.24E-11	2.40E-09	1.44E-08	9.18E-15	3.54E-12	2.46E-13	4.76E-11	2.86E-10
	Carbonate									
0.5	1.57E-10	6.16E-08	4.28E-09	8.26E-07	4.96E-06					
1	1.15E-10	4.52E-08	3.14E-09	6.06E-07	3.64E-06					
5	1.39E-11	5.45E-09	3.79E-10	7.30E-08	4.39E-07					
10	3.96E-12	1.56E-09	1.08E-10	2.09E-08	1.25E-07					
100	3.85E-13	1.52E-10	1.05E-11	2.03E-09	1.22E-08					
1000	2.50E-13	9.83E-11	6.84E-12	1.32E-09	7.92E-09					

Table F.3 Calculated radioxenon production rates from all sources for select depths of the seven geologies in Table E.1.

Total Xe Production Rates from all sources (mBq/m^3/s)

Depth (mwe)	Ultramafic Xe-131m	Xe-133	Xe-133m	Xe-135	Xe-135m	Basalt Xe-131m	Xe-133	Xe-133m	Xe-135	Xe-135m
0.5	1.18E-06	9.84E-04	2.83E-05	9.17E-04	1.36E-04	1.15E-03	9.79E-01	2.82E-02	9.12E-01	1.35E-01
1	1.15E-06	9.80E-04	2.82E-05	9.13E-04	1.35E-04	1.13E-03	9.76E-01	2.81E-02	9.09E-01	1.34E-01
5	1.10E-06	9.70E-04	2.79E-05	9.03E-04	1.33E-04	1.09E-03	9.70E-01	2.79E-02	9.03E-01	1.33E-01
10	1.09E-06	9.69E-04	2.79E-05	9.02E-04	1.33E-04	1.09E-03	9.69E-01	2.79E-02	9.02E-01	1.33E-01
100	1.09E-06	9.69E-04	2.79E-05	9.02E-04	1.33E-04	1.09E-03	9.69E-01	2.79E-02	9.02E-01	1.33E-01
1000	1.09E-06	9.69E-04	2.79E-05	9.02E-04	1.33E-04	1.09E-03	9.69E-01	2.79E-02	9.02E-01	1.33E-01
	Hi-Ca Granite					Lo-Ca Granite				
0.5	3.33E-03	2.84E+00	8.18E-02	2.64E+00	3.91E-01	3.33E-03	2.84E+00	8.18E-02	2.64E+00	3.91E-01
1	3.28E-03	2.83E+00	8.15E-02	2.64E+00	3.89E-01	3.28E-03	2.83E+00	8.15E-02	2.64E+00	3.89E-01
5	3.16E-03	2.81E+00	8.08E-02	2.61E+00	3.86E-01	3.16E-03	2.81E+00	8.08E-02	2.61E+00	3.86E-01
10	3.15E-03	2.80E+00	8.07E-02	2.61E+00	3.85E-01	3.15E-03	2.80E+00	8.07E-02	2.61E+00	3.85E-01
100	3.15E-03	2.80E+00	8.07E-02	2.61E+00	3.85E-01	3.15E-03	2.80E+00	8.07E-02	2.61E+00	3.85E-01
1000	3.15E-03	2.80E+00	8.07E-02	2.61E+00	3.85E-01	3.15E-03	2.80E+00	8.07E-02	2.61E+00	3.85E-01
	Clays/shales					Sandstone				
0.5	3.09E-03	2.68E+00	7.71E-02	2.49E+00	3.68E-01	4.24E-04	3.62E-01	1.04E-02	3.37E-01	4.98E-02
1	3.06E-03	2.67E+00	7.69E-02	2.49E+00	3.67E-01	4.18E-04	3.61E-01	1.04E-02	3.36E-01	4.97E-02
5	2.99E-03	2.66E+00	7.66E-02	2.48E+00	3.65E-01	4.04E-04	3.58E-01	1.03E-02	3.34E-01	4.93E-02
10	2.99E-03	2.66E+00	7.65E-02	2.47E+00	3.65E-01	4.02E-04	3.58E-01	1.03E-02	3.33E-01	4.92E-02
100	2.98E-03	2.66E+00	7.65E-02	2.47E+00	3.65E-01	4.02E-04	3.58E-01	1.03E-02	3.33E-01	4.92E-02
1000	2.98E-03	2.66E+00	7.65E-02	2.47E+00	3.65E-01	4.02E-04	3.58E-01	1.03E-02	3.33E-01	4.92E-02
	Carbonate									
0.5	2.54E-03	2.10E+00	6.04E-02	1.95E+00	2.89E-01					
1	2.48E-03	2.08E+00	6.00E-02	1.94E+00	2.87E-01					
5	2.33E-03	2.06E+00	5.93E-02	1.92E+00	2.83E-01					
10	2.31E-03	2.06E+00	5.92E-02	1.91E+00	2.83E-01					
100	2.31E-03	2.06E+00	5.92E-02	1.91E+00	2.82E-01					
1000	2.31E-03	2.06E+00	5.92E-02	1.91E+00	2.82E-01					

Table F.4 Calculated ^{37}Ar production rates and equilibrium concentrations due to $^{40}Ca(n,\alpha)^{37}Ar$ neutron activation.

^{37}Ar Production rate (mBq/m3/s) by ^{40}Ca Activation

Depth (mwe)	Ultramafic	Basalt	Hi-Ca granite	Lo-Ca granite	Clays, shales	Sandstone	Carbonate
0.5	1.52E-05	4.50E-05	4.85E-05	9.82E-06	1.01E-05	9.65E-06	2.66E-04
1	1.12E-05	3.33E-05	3.58E-05	7.26E-06	7.47E-06	7.09E-06	1.95E-04
2	6.25E-06	1.88E-05	2.02E-05	4.10E-06	4.19E-06	3.95E-06	1.08E-04
3	3.58E-06	1.09E-05	1.17E-05	2.38E-06	2.42E-06	2.25E-06	6.12E-05
4	2.17E-06	6.73E-06	7.27E-06	1.48E-06	1.49E-06	1.36E-06	3.66E-05
5	1.41E-06	4.46E-06	4.83E-06	9.96E-07	9.86E-07	8.76E-07	2.35E-05
10	4.08E-07	1.41E-06	1.64E-06	3.51E-07	3.25E-07	2.52E-07	6.72E-06
50	4.22E-08	2.45E-07	4.42E-07	1.13E-07	8.79E-08	3.20E-08	1.11E-06
100	1.41E-08	1.56E-07	3.49E-07	9.45E-08	6.93E-08	1.47E-08	6.54E-07
500	5.42E-10	1.15E-07	3.05E-07	8.61E-08	5.99E-08	6.20E-09	4.24E-07
1000	1.10E-10	1.15E-07	3.05E-07	8.55E-08	5.99E-08	5.88E-09	4.24E-07
2000	5.32E-11	1.15E-07	3.05E-07	8.55E-08	5.99E-08	5.88E-09	4.24E-07
3000	4.92E-11	1.15E-07	3.05E-07	8.55E-08	5.99E-08	5.88E-09	4.24E-07

^{37}Ar Radioactive Equilibrium Concentration (mBq/m3) from ^{40}Ca activation

Depth (mwe)	Ultramafic	Basalt	Hi-Ca granite	Lo-Ca granite	Clays, shales	Sandstone	Carbonate
0.5	66.37	196.65	211.74	42.89	44.22	42.15	1160.73
1	48.87	145.36	156.51	31.69	32.61	30.97	851.82
2	27.28	81.96	88.25	17.91	18.30	17.23	471.09
3	15.62	47.55	51.20	10.41	10.56	9.83	267.21
4	9.48	29.38	31.77	6.48	6.49	5.92	159.86
5	6.14	19.46	21.09	4.35	4.31	3.83	102.71
10	1.78	6.17	7.15	1.53	1.42	1.10	29.35
50	0.18	1.07	1.93	0.49	0.38	0.14	4.87
100	0.06	0.68	1.53	0.41	0.30	0.06	2.86
500	0.0024	0.50	1.33	0.38	0.26	0.03	1.85
1000	0.0005	0.50	1.33	0.37	0.26	0.03	1.85
2000	0.0002	0.50	1.33	0.37	0.26	0.03	1.85
3000	0.0002	0.50	1.33	0.37	0.26	0.03	1.85

Table F.5 Calculated ^{37}Ar equilibrium concentrations due to muon interactions with potassium in natural geologies.

Ar-37 Equilibrium Concentration (mBq/m^3) from all K(μ,X·n) reactions							
Depth (mwe)	Ultramafic	Basalt	Hi-Ca granite	Low-Ca granite	Clay/shale	Sandstone	Carbonate
0.5	0.14	22.48	72.63	123.69	60.25	27.54	7.61
1	0.17	26.97	87.16	148.43	72.30	33.05	9.14
2	0.17	26.97	87.16	148.43	72.30	33.05	9.14
3	0.14	23.38	75.54	128.64	62.66	28.64	7.92
4	0.13	20.68	66.82	113.79	55.43	25.34	7.00
5	0.11	17.08	55.20	94.00	45.79	20.93	5.79
10	0.05	7.64	24.70	42.05	20.48	9.36	2.59
50	0.0033	0.54	1.74	2.97	1.45	0.66	0.18
100	0.0008	0.13	0.44	0.74	0.36	0.17	0.05
200	0.0002	0.03	0.09	0.15	0.07	0.03	0.01
300	0.0001	0.01	0.03	0.05	0.02	0.01	0.0030

Table F.6 Total estimated maximum ^{37}Ar equilibrium concentrations due to both ^{40}Ca neutron activation and muon interactions with potassium in natural geologies; note, this is the summation of results in Table F.4 (bottom) and Table F.5.

Total Ar-37 Equilibrium Concentration (mBq/m^3) from all sources							
Depth (mwe)	Ultramafic	Basalt	Hi-Ca granite	Low-Ca granite	Clay/shale	Sandstone	Carbonate
0.5	66.51	219.13	284.37	166.58	104.46	69.68	1168.34
1	49.03	172.34	243.67	180.12	104.91	64.02	860.96
2	27.45	108.93	175.41	166.33	90.60	50.28	480.22
3	15.76	70.93	126.74	139.05	73.22	38.47	275.13
4	9.60	50.06	98.60	120.28	61.92	31.26	166.87
5	6.25	36.54	76.29	98.35	50.09	24.76	108.50
10	1.83	13.82	31.84	43.59	21.90	10.46	31.93
50	0.19	1.61	3.67	3.46	1.83	0.80	5.05
100	0.06	0.82	1.96	1.15	0.66	0.23	2.90
200	0.02	0.58	1.47	0.53	0.35	0.07	2.09
300	0.01	0.52	1.39	0.43	0.29	0.04	1.93

Appendix G. Atmospheric infiltration

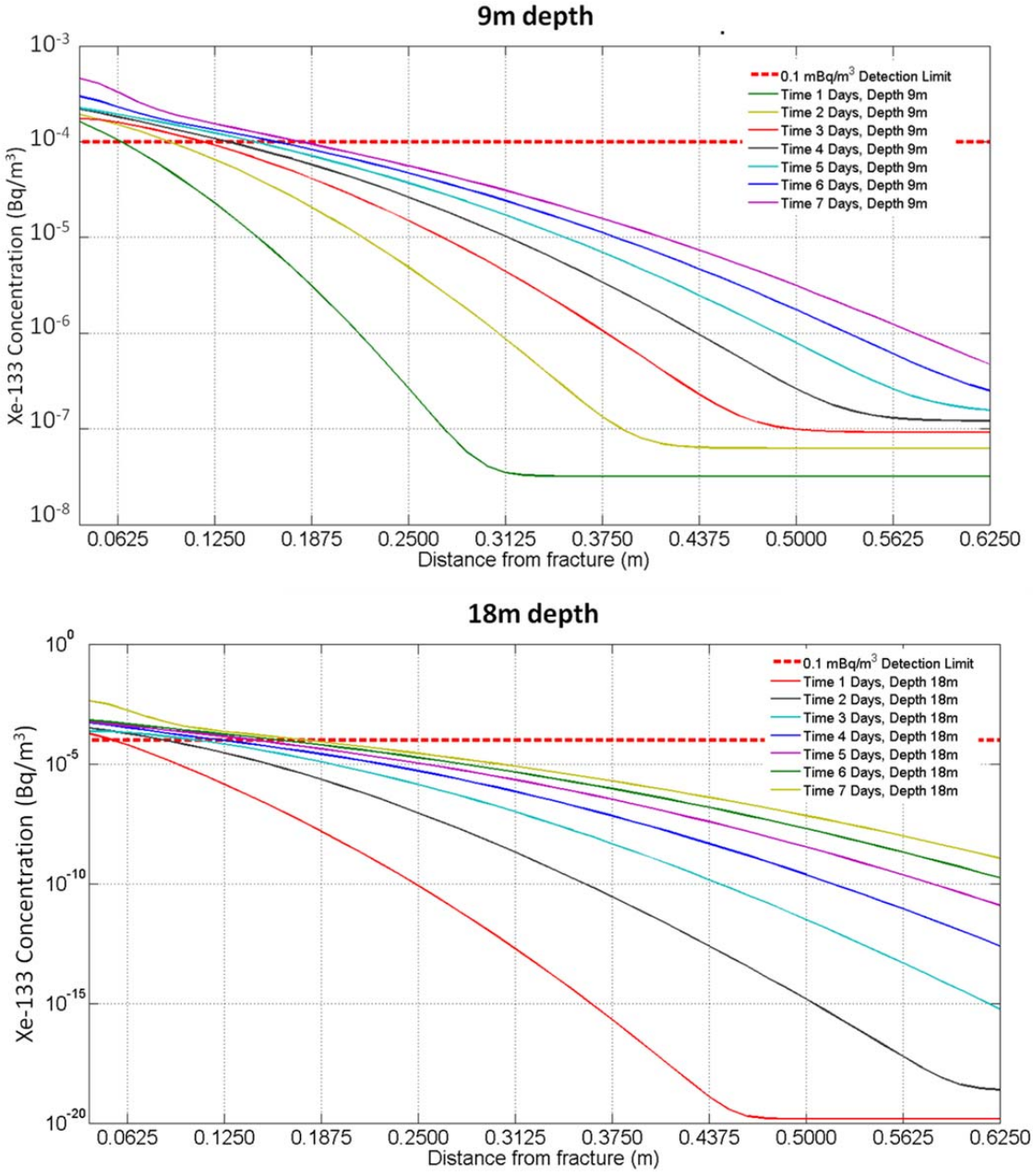

Figure G.1 Xe-133 concentration curves for each of days 1-7 as a function of distance from fracture at a depths of 9 m and 18 m due to simulated infiltration. The dashed line represents an approximate detection limit.

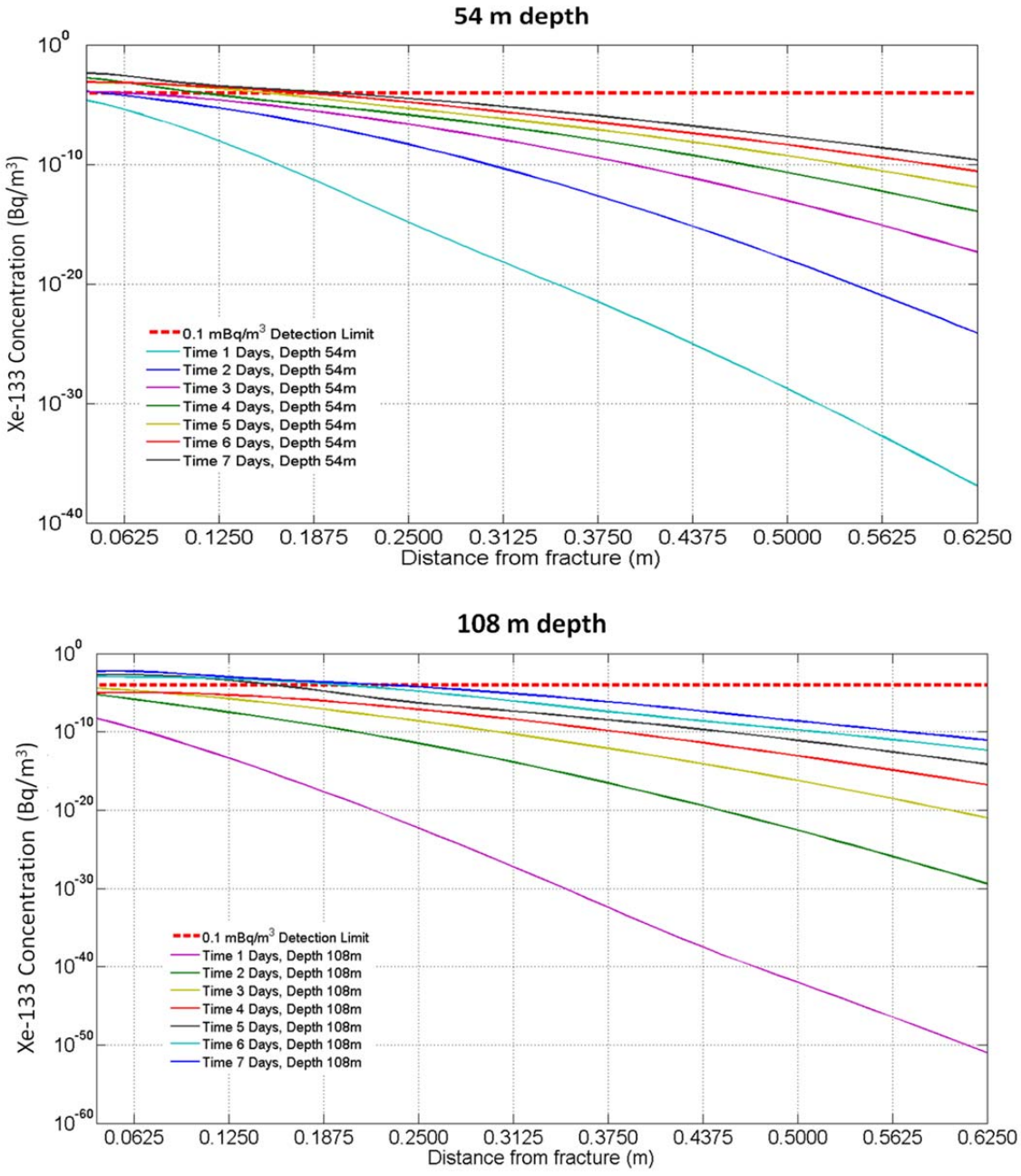

Figure G.2 Xe-133 concentration curves for each of days 1-7 as a function of distance from fracture at a depths of 54 m and 108 m due to simulated infiltration. The dashed line represents an approximate detection limit.

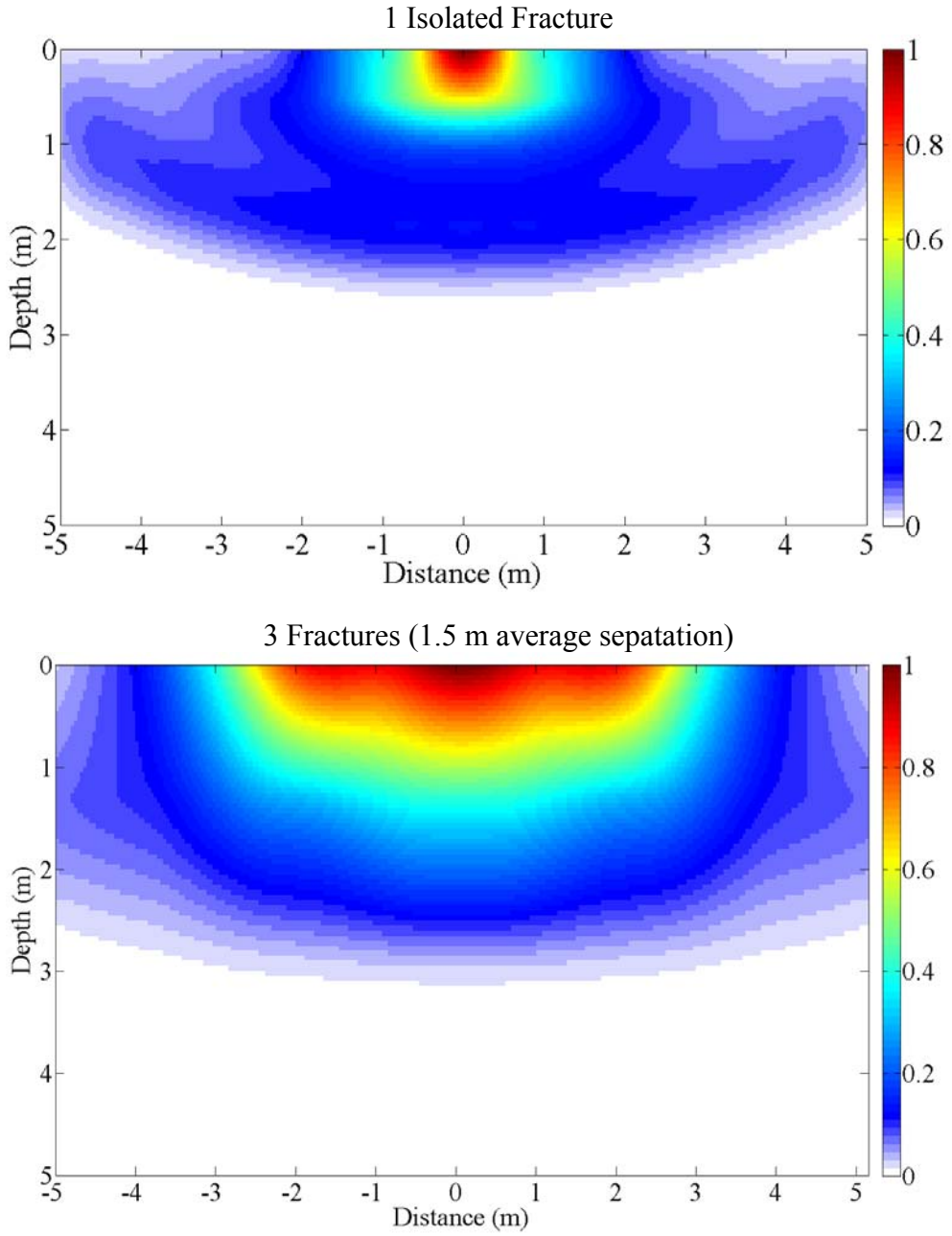

Figure G.3 Example of fracture position and orientation averaging applied to atmospheric infiltration down fracture. In the first plot (top), the results for only a single fracture averaged over possible angles ±90° from the vertical. In the second plot (bottom), the same average over angle but now with 3 fractures with average separation of 1.5 m.

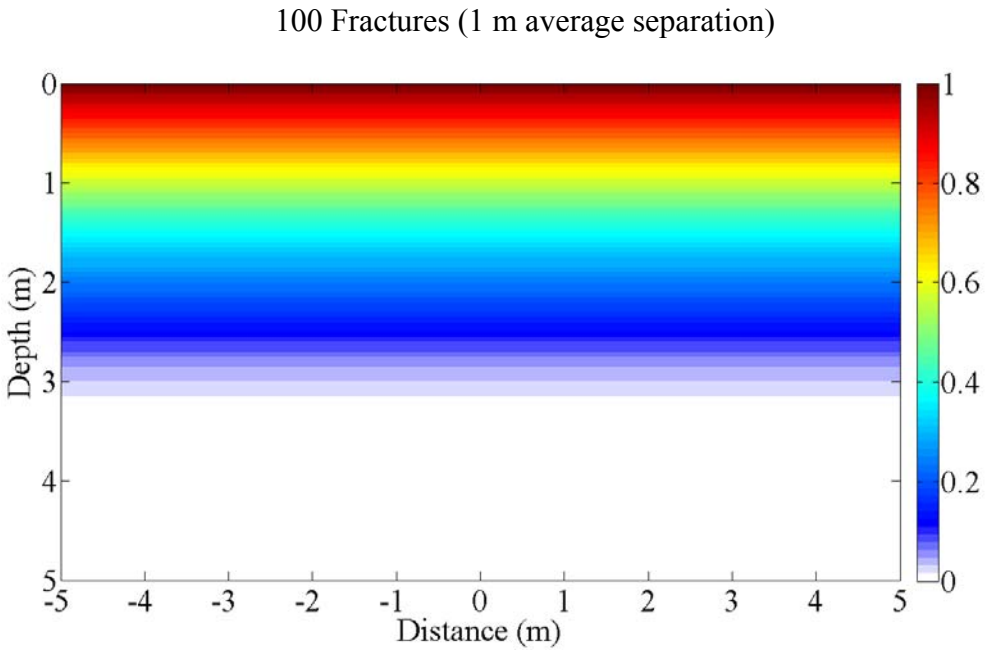

Figure G.4 Example of fracture position and orientation averaging applied to atmospheric infiltration down fracture with a "macroscopic" average perspective of the infiltration from averaging of 100 fractures separated by an average distance of 1 m, with random orientation.

References

Aalseth, C. E., Day, A. R., Fuller, E. S., Hoppe, E. W., Keillor, M. E., LeFerriere, B., . . . Williams, R. M. (2013). A new shallow underground gas-proportional counting lab—First results and Ar-37 sensitivity. *Applied Radiation and Isotopes*(0). doi: http://dx.doi.org/10.1016/j.apradiso.2013.03.050

Ackermann, M, Ajello, M, Allafort, A, Baldini, L, Ballet, J, Barbiellini, G, . . . Bellazzini, R. (2013). Detection of the Characteristic Pion-Decay Signature in Supernova Remnants. *Science*, 339(6121), 807-811.

Andrews, JN, Fontes, J-Ch, Michelot, J-L, & Elmore, D. (1986). In-situ neutron flux, ^{36}Cl production and groundwater evolution in crystalline rocks at Stripa, Sweden. *Earth and planetary science letters, 77*(1), 49-58.

Auer, LH, Rosenberg, ND, Birdsell, KH, & Whitney, EM. (1996). The effects of barometric pumping on contaminant transport. *Journal of Contaminant Hydrology, 24*(2), 145-166.

Bear, Jacob. (1972). *Dynamics of fluids in porous media*: Courier Dover Publications.

Bear, Jacob, Tsang, Chin-Fu, & De Marsily, Ghislain. (1993). *Flow and contaminant transport in fractured rock*: Academic Press.

Bell, MJ. (1973). ORIGEN: The ORNL isotope generation and depletion code: Oak Ridge National Lab., Tenn.(USA).

Biegalski, KM Foltz, Biegalski, SR, & Williams, Dwight L. (1999). Medical industry interference with ctbt monitoring of atmospheric radionuclides.

Bird, R Byron, Stewart, Warren E, & Lightfoot, Edwin N. (2006). *Transport phenomena*: Wiley.

Bowen, Humphrey John Moule. (1966). Trace elements in biochemistry. *Trace Elements in Biochemistry.*

Bowyer, TW, Abel, KH, Hubbard, CW, Panisko, ME, Reeder, PL, Thompson, RC, & Warner, RA. (1999). Field testing of collection and measurement of radioxenon for the Comprehensive Test Ban Treaty. *Journal of radioanalytical and nuclear chemistry, 240*(1), 109-122.

Boyer, Brian D. (2013). The IAEA and the International Safeguards System: Los Alamos National Laboratory (LANL).

Briesmeister, Judith F. (1986). MCNP-A general Monte Carlo code for neutron and photon transport. *LA-7396-M*.

Bruce, WF. (1980). Permeability of crystalline and argillaceous rock. *Int. J. Rock Mech. Min. Sci. & Geomeeh, 17*, 241-251.

Carrigan, C.R. (2009). *Using OSI Field Studies and Tests to Define Noble Gas Sampling and Analysis Requirements*. Paper presented at the International Noble Gas Experiment-2009 Conference, November 9-14, Daejeon, Korea.

Carrigan, Charles R, & Sun, Yunwei. (2012). Detection of Noble Gas Radionuclides from an Underground Nuclear Explosion During a CTBT On-Site Inspection. *Pure and Applied Geophysics*, 1-18.

Carrigan, CR. (1994). The non-proliferation experiment and gas sampling as an on-site inspection activity: A progress report: Lawrence Livermore National Lab., CA (United States).

Carrigan, CR, Heinle, RA, Hudson, GB, Nitao, JJ, & Zucca, JJ. (1996). Trace gas emissions on geological faults as indicators of underground nuclear testing. *Nature, 382*(6591), 528-531.

Carrigan, CR, Heinle, RA, Hudson, GB, Nitao, JJ, & Zucca, JJ. (1997). Barometric gas transport along faults and its application to nuclear test-ban monitoring: Lawrence Livermore National Lab., CA (United States).

Carrigan, CR, & Sun, Y. (2011). Issues Involving The OSI Concept of Operation For Noble Gas Radionuclide Detection: Lawrence Livermore National Laboratory (LLNL), Livermore, CA.

Carslaw, Horatio Scott, Jaeger, John Conrad, & Feshbach, Herman. (1962). Conduction of heat in solids. *Physics Today, 15*, 74.

Chadwick, M. B., Herman, M., Oblozinsky, P., Dunn, M. E., Danon, Y., Kahler, A. C., . . . Young, P. C. (2011). ENDF/B-VII.1 Nuclear Data for Science and Technology: Cross Sections, Covariances, Fission Product Yields and Decay Data. *Nuclear Data Sheets, 112*(12), 2887-2996. doi: DOI 10.1016/j.nds.2011.11.002

Chang, J. (2000). Table of Nuclides. from http://atom.kaeri.re.kr/ton/

Chapman, M, & Waisman, EM. (1985). A noise suppression algorithm for the numerical solution of Maxwell's equations. *Journal of Computational Physics, 58*(1), 44-58.

Chapman, Milt. (1981). FRAM—Nonlinear damping algorithms for the continuity equation. *Journal of Computational Physics, 44*(1), 84-103.

Charalambus, S. (1971). Nuclear transmutation by negative stopped muons and the activity induced by the cosmic-ray muons. *Nuclear Physics A, 166*(2), 145-161.

Chatwin, PC. (1975). On the longitudinal dispersion of passive contaminant in oscillatory flows in tubes. *Journal of Fluid Mechanics, 71*(03), 513-527.

Chazal, V, Brissot, R, Cavaignac, JF, Chambon, B, De Jésus, M, Drain, D, . . . Vagneron, L. (1998). Neutron background measurements in the underground laboratory of Modane. *Astroparticle Physics, 9*(2), 163-172.

Chen, Z-X. (1989). Transient flow of slightly compressible fluids through double-porosity, double-permeability systems—A state-of-the-art review. *Transport in Porous Media, 4*(2), 147-184.

CTBTO Preparatory Commission. (1996). Comprehensive-Nuclear-Test-Ban Treaty (CTBT). *Preparatory Commission for the CTBT Organization, Provisional Technical Secretariat, Vienna, Italy*.

CTBTO Prepatory Commission. (2010). Monitoring Technologies: How they work. Retrieved October, 2010, from http://www.ctbto.org/verification-regime/monitoring-technologies-how-theywork/seismic-monitoring/page-1

CTBTO Prepatory Commission. (2013). Status of signature and ratification. Retrieved May 27, 2013, from http://www.ctbto.org/the-treaty/status-of-signature-and-ratification/

Denny, MD. (1994). *Introduction and highlights*. Paper presented at the Proceedings of the Symposium on the Non-Proliferation Experiment (NPE): Results and Implications for Test Ban Treaties, MD Denny (editor), CONF-9404100, Department of Energy.

DeNovio, Nicole M, Bryant, Nathan, King, Chrissi B, Bhark, Eric, Drellack, Sigmund L, Pickens, John F, . . . Aly, Alaa. (2005). Phase II Contaminant Transport Parameters for the Groundwater Flow and Contaminant Transport Model of Corrective Action Unit 98: Frenchman Flat, Nye County, Nevada, Rev. No.: 0: Stoller-Navarro Joint Venture (SN), Las Vegas, NV.

Draxler, RR, & Rolph, GD. (2003). HYSPLIT (HYbrid Single-Particle Lagrangian Integrated Trajectory) Model. NOAA Air Resources Laboratory, Silver Spring, MD. *Access via NOAA ARL READY Website (http://www.arl.noaa.gov/ready/hysplit4.html)*.

Egnatuk, Christine M, Lowrey, Justin, Biegalski, Steven R, Bowyer, Theodore, Haas, Derek, Orrell, John, . . . Keillor, Martin. (2012). Production of 37 Ar in The University of Texas TRIGA reactor facility. *Journal of Radioanalytical and Nuclear Chemistry, 291*(1), 257-260.

England, TR, & Rider, BF. (1995). Evaluation and compilation of fission product yields 1993: Los Alamos National Lab., NM (United States).

Epstein, Norman. (1989). On tortuosity and the tortuosity factor in flow and diffusion through porous media. *Chemical engineering science, 44*(3), 777-779.

Fabryka-Martin, June Taylor. (1988). Production of radionuclides in the Earth and their hydrogeologic significance, with emphasis on chlorine-36 and iodine-129: Arizona Univ., Tucson, AZ (USA).

Feige, Y, Oltman, BG, & Kastner, J. (1968). Production rates of neutrons in soils due to natural radioactivity. *Journal of Geophysical Research, 73*(10), 3135-3142.

Flint, Lorraine E. (1998). *Characterization of hydrogeologic units using matrix properties, Yucca Mountain, Nevada*: US Department of the Interior, US Geological Survey.

Freeze, R Allan, & Cherry, John A. (1977). *Groundwater*: Prentice-Hall.

Gale, JE. (1982). Assessing the permeability characteristics of fractured rock. *Geol. Soc. Am., Spec. Pap.;(United States), 189*(CONF-790284-).

Garber, MS. (1971). A method for estimating effective porosity in a rubble chimney formed by an underground nuclear explosion. *US Geological Survey Research*, C207-C209.

Glasstone, Samuel, & Dolan, Philip J. (1977). The Effects of Nuclear Weapons: DTIC Document.

Glasstone, Samuel, & Edlund, Milton C. (1952). *The elements of nuclear reactor theory* (Vol. 47): van Nostrand New York.

Gringarten, Alain. (1984). Interpretation of tests in fissured and multilayered reservoirs with double-porosity behavior: Theory and practice. *Journal of petroleum technology, 36*(4), 549-564.

Grisak, GE, & Pickens, J-F_. (1980). Solute transport through fractured media: 1. The effect of matrix diffusion. *Water resources research, 16*(4), 719-730.

Groom, DE, & Particle Data Group. (2000). Eur. *Phys. Jour C, 15*, 1.

Haas, Derek A, Orrell, John L, Bowyer, Ted W, McIntyre, Justin I, Miley, Harry S, Aalseth, Craig E, & Hayes, James C. (2010). *The Science Case for 37Ar as a Monitor for Underground Nuclear Explosions*: Pacific Northwest National Laboratory.

Halford, Keith J, Laczniak, Randell J, & Galloway, Devin L. (2005). *Hydraulic Characterization of Overpressured Tuffs in Central Yucca Flat, Nevada Test Site, Nye County, Nevada*: US Department of the Interior, US Geological Survey.

Hannon, W J. (1985). Seismic Verification of a Comprehensive Test Ban. *Science, 227*, 251-257.

Hebel, Simon. (2010). Genesis and equilibrium of natural lithospheric radioxenon and its influence on subsurface noble gas samples for CTBT on-site inspections. *Pure and Applied Geophysics, 167*(4-5), 463-470.

Hirt, CW. (1968). Heuristic stability theory for finite-difference equations. *Journal of Computational Physics, 2*(4), 339-355.

Hwang, Shuen-Cheng, Lein, Robert D, & Daniel, A. (2005). Morgan (2005): Noble Gases. *Kirk-Othmer Encyclopedia of Chemical Technology*.

Johnson, Christine , & Biegalski, Steven. (2012, November 2012). *Background Radioxenon Soil Concentrations Due To Spontaneous Fission (poster*

presentation). Paper presented at the International Noble Gas Experiment - 2012, Mito City, Japan.

Kalinowski, Martin B, Axelsson, Anders, Bean, Marc, Blanchard, Xavier, Bowyer, Theodore W, Brachet, Guy, Pistner, Christoph. (2010). Discrimination of nuclear explosions against civilian sources based on atmospheric xenon isotopic activity ratios. *Pure and Applied Geophysics, 167*(4-5), 517-539.

Klingberg, FJ, Biegalski, SR, & Fay, AG. (2012). Radioxenon signatures from activation of environmental xenon. *Journal of Radioanalytical and Nuclear Chemistry*, 1-7.

Koning, AJ, & Rochman, D. (2011). TENDL-2010: TALYS-based Evaluated Nuclear Data Library, Nuclear Research and Consultancy Group (NRG), Petten, The Netherlands, Release Date: December 8, 2010.

Kurzweg, UH. (1985). Enhanced heat conduction in oscillating viscous flows within parallel-plate channels. *Journal of Fluid Mechanics, 156*(1), 291-300.

Lamarsh, John R. (2002). *Introduction to Nuclear Reactor Theory*: American Nuclear Society.

LANL, LLC (2011). Muon Radiography. *Research Quarterly* from http://www.lanl.gov/quarterly/q_spring03/cosmic_ray_muons.shtml

Le Petit, G, Armand, P, Brachet, G, Taffary, T, Fontaine, JP, Achim, P, . . . Pointurier, F. (2008). Contribution to the development of atmospheric radioxenon monitoring. *Journal of Radioanalytical and Nuclear Chemistry, 276*(2), 391-398.

Lowrey, J.D., & Osborne, A.G. (2011). *(unpublished) Notes - Discretized double porosity transport by simultaneous sparse matrix*. UT Austin.

Lowrey, J.D., Osborne, A.G., & Deinert, M.R. (not yet published). *Comparison of numerical solution methods for trigiagonal systems of equations describing subsurface mass transport driven by barometric oscillations*. UT Austin.

Lowrey, JD, Biegalski, SR, & Deinert, MR. (2012). UTEX modeling of radioxenon isotopic fractionation resulting from subsurface transport. *Journal of Radioanalytical and Nuclear Chemistry*, 1-6.

Lowrey, J. D., Biegalski, S. R., Osborne, A. G., & Deinert, M. R. (2013). Subsurface mass transport affects the radioxenon signatures that are used to identify clandestine nuclear tests. *Geophysical Research Letters*, *40*(1), 111-115.

Lowrey, Justin D. (2011). *Production and subsurface vertical transport of radioxenon resulting from underground nuclear explosions.* (Master's Thesis), University of Texas at Austin.

Martel, DJ, O'nions, RK, Hilton, DR, & Oxburgh, ER. (1990). The role of element distribution in production and release of radiogenic helium: The Carnmenellis Granite, southwest England. *Chemical geology, 88*(3), 207-221.

Mason, B. (1966). Principles of Geochemistry 3rd ed Wiley. *New York*.

McCord, John. (2007). Phase I contaminant transport parameters for the groundwater flow and contaminant transport model of Corrective Action Unit 97: Yucca Flat/Climax Mine, Nevada Test Site, Nye County, Nevada, Revision 0: Stoller-Navarro Joint Venture.

McNeill, JD. (1980). *Electrical conductivity of soils and rocks*: Geonics Limited.

Miall, Andrew D. (1990). *Principles of sedimentary basin analysis* (Vol. 633): Springer-Verlag New York.

Nelson, Ronald A, & Handin, John. (1977). Experimental study of fracture permeability in porous rock. *AAPG Bulletin, 61*(2), 227-236.

Neretnieks, Ivars, & Rasmuson, Anders. (1984). An approach to modelling radionuclide migration in a medium with strongly varying velocity and block sizes along the flow path. *Water Resources Research, 20*(12), 1823-1836.

Nilson, RH, & Lie, KH. (1990). Double-porosity modelling of oscillatory gas motion and contaminant transport in a fractured porous medium. *International Journal for Numerical and Analytical Methods in Geomechanics, 14*(8), 565-585.

Nilson, RH, Peterson, EW, Lie, KH, Burkhard, NR, & Hearst, JR. (1991). Atmospheric pumping: A mechanism causing vertical transport of contaminated gases through fractured permeable media. *Journal of Geophysical Research, 96*(B13), 21933-21921,21948.

Nitao, John J. (1998). Reference manual for the NUFT flow and transport code, version 2.0. *Lawrence Livermore National Laboratory*.

Perkins, Donald H. (2003). *Particle astrophysics*: Oxford University Press.

Poston, David I, & Trellue, Holly R. (1998). Users manual, version 1.00 for Monteburns, version 3.01: Los Alamos National Lab., NM (United States).

Purtschert, R, Riedmann, R, & Loosli, HH. (2007). *Evaluation of Argon-37 as a means for identifying clandestine subsurface nuclear tests*. Paper presented at the Proceedings of 4th Mini Conference on Noble Gases in the Hydrosphere and in Natural Gas Reservoirs, GFZ Potsdam, Germany.

Riedmann, Robin A, & Purtschert, Roland. (2011). Natural 37Ar concentrations in soil air: Implications for monitoring underground nuclear explosions. *Environmental science & technology, 45*(20), 8656-8664.

Ringbom, Anders, Elmgren, Klas, Lindh, Karin, Peterson, Jenny, Bowyer, Theodore W, Hayes, James C, . . . Williams, Richard. (2009). Measurements of radioxenon in ground level air in South Korea following the claimed nuclear test in North Korea on October 9, 2006. *Journal of radioanalytical and nuclear chemistry, 282*(3), 773-779.

Saey, Paul RJ. (2007). Ultra-low-level measurements of argon, krypton and radioxenon for treaty verification purposes. *Esarda Bulletin, 36*, 42.

Sinnock, Scott. (1982). Geology of the Nevada Test Site and nearby areas, southern Nevada *Sandia Report*.

Stacey, Weston M. (2007). *Nuclear reactor physics*: Wiley-VCH.

Sweeney, Jerry J. (1999). Case studies of geophysical search methods relevant to the continuation phase of an on-Site inspection: Lawrence Livermore National Laboratory (LLNL), Livermore, CA.

Swordy, SP. (2001). The energy spectra and anisotropies of cosmic rays. *Space Science Reviews, 99*(1-4), 85-94.

Tang, DH, Frind, EO, & Sudicky, Edward Allan. (1981). Contaminant transport in fractured porous media: Analytical solution for a single fracture. *Water resources research, 17*(3), 555-564.

Taylor, SR. (1964). Trace element abundances and the chondritic earth model. *Geochimica et Cosmochimica Acta, 28*(12), 1989-1998.

Vinogradov, Aleksandr Pavlovich. (1959). *The geochemistry of rare and dispersed chemical elements in soils* (Vol. 209): Consultants Bureau New York.

Wang, JSY, & Narasimhan, Thiruppudaimarudhur N. (1986). Hydrologic mechanisms governing partially saturated fluid flow in fractured welded units and porous non-welded units at Yucca Mountain: Lawrence Berkeley Lab., CA (United States).

Wedepohl, K. (1971). Environmental influences on the chemical composition of shales and clays. *Physics and Chemistry of the Earth, 8*, 305-333.

Widrow, Bernard, & Kollár, István. (2008). Quantization Noise: Roundoff Error in Digital Computation. *Signal Processing, Control, and Communications*, 485-528.

Wilson, Charles Richard, & Witherspoon, Paul Adams. (1970). *An investigation of laminar flow in fractured porous rocks*: Department of Civil Engineering, University of California.

Winograd, Isaac Judah, & Thordarson, William. (1975). Hydrogeologic and hydrochemical framework, south-central Great Basin, Nevada-California, with special reference to the Nevada Test Site.

Wohletz, Kenneth, Wolfsberg, Andrew, Olson, Alyssa, & Gable, Carl. (1999). Evaluating the Effects of Underground Nuclear Testing Below the Water Table on Groundwater and Radionuclide Migration in the Tuff Pile 1 Region of Yucca Flat: Numerical Simulations.

Xiang, YC, Gong, Jian, Li, Wei, Bian, ZS, Hao, FH, Wang, HX, . . . Xiong, ZH. (2008). Development of a system of measuring Ar-37 by spectrum method. *Acta Physica Sinica, 57*(2), 784-789.

Zuckerman, Lord. (1993). Prospects for a comprehensive test ban. *Nature: International weekly journal of science, 361*(6411), 392-396.

Vita

Justin David Lowrey was born in Dallas, Texas and is the son of John and Peggy Lowrey. He graduated valedictorian from Skyline High School of Dallas, Texas in 2002 and attended the University of Texas at Austin as an undergraduate student and graduated with highest honors in 2006, receiving Bachelors of Science degrees in Physics and Astronomy. He was a graduate student in high energy physics and a teaching assistant at the University of California at Santa Barbara for two years before transferring back to the University of Texas at Austin in 2009 to pursue study in nuclear engineering. Lowrey worked as a graduate research assistant at the Nuclear Engineering Teaching Lab in the Department of Mechanical Engineering at the University of Texas at Austin for three years and has worked as a Post-Masters Research Associate at Pacific Northwest National Lab for one year.

Permanent e-mail: jdlowrey9@gmail.com

This dissertation was typed by Justin David Lowrey.